

MINE SCHEDULE OPTIMIZATION WITH GEOTECHNICAL CONSTRAINTS

by

Negar Saeidi

Thesis submitted in partial fulfillment
of the requirements for the degree of
Master of Applied Science (M.Sc.) in Natural Resources Engineering

The School of Graduate Studies

Laurentian University

Sudbury, Ontario, Canada

© Negar Saeidi, 2015

THESIS DEFENCE COMMITTEE/COMITÉ DE SOUTENANCE DE THÈSE
Laurentian University/Université Laurentienne
Faculty of Graduate Studies/Faculté des études supérieures

Title of Thesis Titre de la thèse	MINE SCHEDULE OPTIMIZATION WITH GEOTECHNICAL CONSTRAINTS		
Name of Candidate Nom du candidat	Saeidi, Negar		
Degree Diplôme	Master of Applied Science		
Department/Program Département/Programme	Natural Resources Engineering	Date of Defence Date de la soutenance	September 28, 2015

APPROVED/APPROUVÉ

Thesis Examiners/Examineurs de thèse:

Dr. Dean Millar
(Supervisor/Directeur(trice) de thèse)

Dr. Lorrie Fava
(Committee member/Membre du comité)

Prof. Ming Cai
(Committee member/Membre du comité)

Dr. Mustapha Kumral
(External Examiner/Examineur externe)

Approved for the Faculty of Graduate Studies
Approuvé pour la Faculté des études supérieures
Dr. David Lesbarrères
Monsieur David Lesbarrères
Acting Dean, Faculty of Graduate Studies
Doyen intérimaire, Faculté des études supérieures

ACCESSIBILITY CLAUSE AND PERMISSION TO USE

I, **Negar Saeidi**, hereby grant to Laurentian University and/or its agents the non-exclusive license to archive and make accessible my thesis, dissertation, or project report in whole or in part in all forms of media, now or for the duration of my copyright ownership. I retain all other ownership rights to the copyright of the thesis, dissertation or project report. I also reserve the right to use in future works (such as articles or books) all or part of this thesis, dissertation, or project report. I further agree that permission for copying of this thesis in any manner, in whole or in part, for scholarly purposes may be granted by the professor or professors who supervised my thesis work or, in their absence, by the Head of the Department in which my thesis work was done. It is understood that any copying or publication or use of this thesis or parts thereof for financial gain shall not be allowed without my written permission. It is also understood that this copy is being made available in this form by the authority of the copyright owner solely for the purpose of private study and research and may not be copied or reproduced except as permitted by the copyright laws without written authority from the copyright owner.

Abstract

If a mining project consists of n stoping activities these can be scheduled in $n!$ ways according to the duration between the activities and their precedence. Mine schedule optimization manipulates the precedence relationships and the duration of the mining activities in order to maximize the Net Present Value (NPV). However, unexpected instabilities may impede or disrupt the schedule and thus reduce the profitability and so geotechnical aspects of the operation need to be taken into account.

The mine schedule optimization software considered in this work is the so-called Schedule Optimization Tool (SOT). This thesis reports the work for development of new geomechanical constraints for any mine scheduling tool to find the safest and the most profitable schedule, exemplified within the SOT framework.

The core hypothesis of this research is that there is a time-dependent aspect of the rock behaviour that leads to instability, a consequence of dependence of geotechnical instability upon the sequence and duration between stoping activities. There is evidence presented in this work that supports this hypothesis.

An automated procedure for timely and computationally efficient calculations of the instability metrics is presented. This can be applied to evaluate the geomechanical stability of any of the $n!$ schedules for excavating n stopes or applied to evaluate geomechanical stability of schedules arising in the schedule optimization process. However, in practice, the number of feasible schedules is much less than $n!$ due to the precedence constraints. The approach starts with computing n elastic stress fields induced after excavating each individual stope independently within an identical computational domain using Compute3D. The stress-time series of each

and/or every sequence of stoping are generated through superimposition of these pre-computed stress fields, and the time stamps of blasting for excavation are allocated corresponding to the stoping timetable. Different blasts are allowed to be timetabled at the same time. By means of Hooke's law and the 3D Kelvin-Voigt creep model the elastic strain time series and the viscoelastic strain time series are produced for the stress-time series. Based on the Mohr-Coulomb Failure criterion three (in)stability indicators are defined:

- i. 'Strength Factor' to evaluate state of stress at each stage of each schedule as a proportion of its strength
- ii. '*Strainth Factor*' to evaluate state of elastic strain at each stage of each schedule as a proportion of a limiting 'rupture' strain
- iii. '*Viscoelastic-strainth Factor*' to evaluate state of viscoelastic strain at each stage of each schedule as a proportion of a limiting 'rupture' strain.

To provide a perspective of the (in)stability condition in the computational domain for all the feasible sequences of stoping, 12 (in)stability metrics were defined and the results of each are illustrated in the form of '*(in)stability indicator diagrams*'. The overall methodology is applied to an example of excavating 6 open stopes.

Additionally, a methodology is theorized to evaluate the stability condition in the rock mass surrounding the stopes for a series of stoping and backfilling schedules. The methodology is based on pre-computing one additional stress field element for each stope, which represents the effect of the fill loading on the rock mass. The calculations for this approach are consistent with the time and computational efficiency of the original methodology. The computational effort

increases to $2n$ pre-computed stress fields rather than n : as problem sizes double, computational time doubles, rather than increases in polynomial or exponential time.

Keywords:

Mining schedule optimization, geomechanical stability, time-dependent rock deformability, excavation sequencing, superposition principle, 3D Kelvin-Voigt

Acknowledgement

First and foremost, I would like to thank my supervisor Professor Dean Millar for providing me with the opportunity of working on this research, and patiently guiding me through my studies. I have gained valuable experiences being a member of his research team and have always felt supported over the past two years.

Thanks to MIRARCO for financial support, office facilities and software licenses for this study. Thanks to Ontario Centers of Excellence (OCE) for the SOT+ project, Vale Canada and Datamine (CAE Mining), and the Connect Canada internship program for their financial support.

I would like to thank all my friends in Canada and Iran. Their company and support means a lot to me. I am forever thankful to my brothers, Salar and Shayan, for their support and encouragement from home, Karaj. Lastly, my heartfelt gratitude goes to my parents, Mina and Hamidreza, who taught me to love and strive for a better life.

Thank you all,

Negar Saeidi

Sudbury, Canada

12th August 2015

Table of Content

Abstract	iii
Acknowledgement	vi
List of Tables	xii
List of Figures	xv
Terminology.....	xxiii
1 Introduction.....	1
1.1 Underground Mining Scheduling.....	1
1.2 Schedule optimization methodologies	5
1.3 An example of schedule optimization – finding out when a project will be complete	9
1.4 An example of schedule optimization – finding out how much a project will cost.....	13
1.5 Schedule Optimization Tool.....	17
1.6 Scope and purpose of the thesis	20
1.7 Content of the thesis.....	22
2 A review of time-dependent rock response data.....	24
2.1 Analysis of elastic rock responses to differing stoping schedules	24
2.2 Time-dependent rock response data from closure measurements.....	29
2.3 Rock burst causality may be the time-dependent strength or the time-dependent deformation	33

2.4	Time-dependent behaviour of hard rocks from laboratory tests	34
2.5	Time-dependent behaviour of rock in low stress condition	38
2.6	Consideration of time-dependent responses of rock mass with support	40
2.7	Time-dependent rock response observed from seismic data records	41
2.8	Time-dependent rock behaviour in laboratory	42
2.9	Review of evidence of time-dependent rock response.....	43
3	A review of time-dependent rock deformability models: viscoelastic models.....	45
3.1	Introduction	45
3.2	Viscoelastic behaviours.....	47
3.3	Choices of viscoelastic models	49
3.4	Methods of measuring viscous coefficient.....	55
3.4.1	Static methods vs. dynamic methods	55
3.4.2	Laboratory determinations	55
3.4.3	Analysis of flow structures	56
3.4.4	Back analysis of observed response.....	57
3.4.5	A brief recap of the discussed methods of measuring viscosity	57
3.5	Viscoelastic approximation: Identification of most appropriate viscoelastic model	58
4	Key research questions and research hypothesis	63
4.1	When do instabilities occur?	64
4.2	Interaction between stoping schedule and time-dependent deformation	66

5	Methodology for automating geotechnical stability analyses for schedule optimization purposes.	70
5.1	Calculations of stress and elastic strain time histories for different stoping schedules .	75
5.2	Upgrading to 3D viscoelastically: 3D Kelvin-Voigt model.....	78
5.3	Assessment of geotechnical stability.....	84
5.3.1	3D Mohr-Coulomb failure criterion.....	85
5.3.2	Strength Factor.....	88
5.3.3	Strainth Factor.....	89
5.3.4	Viscoelastic Strainth Factor	90
5.4	Evaluating stability of each schedule	91
5.4.1	Choices of instability metrics.....	91
5.5	Automating the process	95
5.6	An estimation of the feasible number of sequences for the purpose of instability analysis.....	98
6	Application of the methodology to Lac du bonnet granite	102
6.1	Rock properties and field stresses	102
6.2	Meshing description	102
6.3	Computation of geomechanical response.....	104
6.4	Evaluation of stability metric	108
6.4.1	A simple example showing functionality of stability metrics	108
6.4.2	Methodology to produce the instability metric.....	109

6.4.3	Application of instability metrics on Lac du Bonnet granite	110
7	Stability analysis of a mine schedule including backfill activities	114
7.1	Effect of fill on the elastic stress distribution in the rock mass.....	114
7.1.1	Simulation set up.....	115
7.1.2	Simulation results.....	117
7.2	Stress distribution inside the fill.....	120
7.3	Conceptualization of the fill mechanics	121
7.4	Corollaries of the analysis of the effect of backfill on the surrounding rock mass	123
7.5	Integrating the backfill effect with the current superimposition methodology	124
7.5.1	Approaches for the stress field calculation around inclusions.....	124
7.5.2	The proposed approach for modeling backfill in the superposition procedure	126
7.5.3	Integration of the backfill effect with the current superimposition procedure	129
7.6	Summary	130
8	Conclusions and recommendations for future work	132
8.1	Summary and conclusions.....	132
8.2	Recommendation for future work	137
	References.....	141
A	Appendix 1: Stress distribution in sequences of excavations	148
B	Appendix 2: Fitting creep models to deformation data	154
C	Appendix 3: Examine3D batch mode processor.....	165

D	Appendix 4: AutoIt script	177
E	Appendix 5: MAT LAB script.....	183
F	Appendix 6: Permutation Processor.....	194
G	Appendix 7: The 12 ‘indicator diagrams’	197
	Curriculum Vitae	209

List of Tables

Table 1-1: List of the activities for a project of constructing a house from Hillier and Lieberman (2001), cost of activity and duration of the activities are included by the author.....	10
Table 1-2: Optimum time at which each activity should start to minimize duration of the house construction project is calculated with Simplex method.	13
Table 1-3: Optimum time at which each activity should start to minimize the cost of the house construction project to finish the project in 40 weeks is calculated with Simplex method.....	16
Table 2-1: Results for deviatoric stress (σ_d) arising from Phase2 analysis, at points A to G in two different sequences of excavation. Sequence 1: square (first), circle (second), diamond (third) and Sequence 2: square (first), diamond (second), circle (third). Principal stress fields are illustrated in Appendix 1, Stress is measured in MPa, and field stresses are $\sigma_1 = 100$ MPa and $\sigma_3 = 50$ MPa. $K = 0.5$	25
Table 3-1: Rheological models for unidimensional constitutive modeling. E is elastic module and η is viscosity module. Suffixes ‘‘h,’’ ‘‘k,’’ and ‘‘m’’ indicate module of Hooke, Kelvin, and Maxwell units (Ayden, <i>et al.</i> , 2013).	50
Table 3-2: Intuitive unidimensional creep models (except for (Ayden, <i>et al.</i> , 2003) the references to the citations in this table can be found in (Farmer, 1983)).	51
Table 3-3: Four rheological models are fitted to the data from Uniaxial compression test on Elsburg Quartzite from South African gold mine (Drescher and Handley, 2003)	59
Table 3-4: Four rheological models are fitted to the data from results of creep test on quartzite sample from Hartebeestfontein mine (Malan, <i>et al.</i> , 1997)	60
Table 3-5: Four rheological models are fitted to the data from results of creep test on lava from Hartebeestfontein mine (Malan, <i>et al.</i> , 1997)	60

Table 3-6: Four rheological models are fitted to the data from closure measurement from Deelkraal gold mine tabular stope (Malan, <i>et al.</i> , 1997)	61
Table 3-7: Four rheological models are fitted to the data from results of uniaxial creep test from Hartbeesfontein Mine quartzite (Bosman, <i>et al.</i> , 2000).....	61
Table 5-1: Possible choices of instability indicators and their pros and cons.	95
Table 6-1: Experimental results of rock testing on Lac du Bonnet granite (Yuannian and Fulvio, 2009).	102
Table 6-2: <i>In situ</i> field principal stress components' magnitudes and directions.	102
Table 6-3: Different choices of (in)stability metrics and their specifications.	112
Table 7-1: Deviatoric stress distribution around stopes showing effect of backfill on stress distributions for different values of R	119
Table 7-2: Deviatoric stress distribution inside fill. The rock mass elastic properties: Young's modulus=0.6 GPa, Poisson's ratio=0.26. The fill elastic properties: Young's modulus=0.6 GPa, Poisson's ratio=0.25.....	121
Table 7-3: The cons and pros of some of the methodologies suggested for stress analysis around inclusions.	126
Table B-1: Back-analyzed coefficients after fitting rheological models to the data presented in Figure B-2.	155
Table B-2: Back-analyzed coefficients after fitting rheological models to the data presented in Figure B-3.	156
Table B-3: Back-analyzed coefficients after fitting rheological models to the data presented in Figure B-5.	158
Table B-4: Back-analyzed coefficients after fitting rheological models to the data presented in Figure B-7.	160

Table B-5: Back analyzed coefficients after fitting rheological models to the data presented in Figure B-7. 162

Table B-6: back analyzed Burgers model coefficient based on the measured closure data from Deelkraal gold mine tabular stope reported by Malan *et al.* (1997). 163

Table B-7: Back-analyzed coefficients after fitting rheological models to the data presented in Figure B-7. 164

List of Figures

Figure 1-1: Schematic Gantt chart showing schedule of development and stoping activities. FS (Finish to Start) means the activity cannot start before its predecessor ends, although it may start later. SS (Start to Start) the activity cannot start until the predecessor starts, although it may start later. SF (Start-to-Finish) the activity cannot end before the predecessor starts, although it may end later. FF (Finish-to-Finish) means the activity cannot end before the predecessor ends, although it may end later (Gantt-Chart, 2012).....	2
Figure 1-2: Schematic presentation of a Network model of five activities. Nodes refer to the achievement of the activities, arcs refer to the duration of the activities and dashed line is the “dummy activity”.....	6
Figure 1-3: Search techniques on different optimization solution methods based on Sivanandam and Deepa (2008) from (Sharma, 2014)	7
Figure 1-4: The network model of the project of constructing a house from Hillier and Lieberman (2001). The blue line is showing “critical path”.....	11
Figure 1-5: The schematic relationship between costs of activity i , and duration of the activity i . Exemplified for activity D.	14
Figure 1-6: Flow chart of the SOT optimization process modified from (Maybee, <i>et al.</i> , 2010). 18	
Figure 2-1: Schematic stress time series in a sequence of excavations.	24
Figure 2-2: σ_1 (maximum principal stress) distribution after excavation of circular opening in sequence 1: square (first), circle (second), diamond (third). $K=0.5$	26
Figure 2-3: Deviatoric stress ($\sigma_d = \sigma_1 - \sigma_3$) at point D in the process of excavating new openings ($\times 100$).....	27
Figure 2-4: Typical time-dependent stope closure of the Ventersdorp Contact Reef at Western Deep Levels mine (now Mponeng mine) (Malan, 1999). This was for a closure station at a	

distance of 8.7 m from the face. Dashed lines have added by this author to emphasize differences between expected elastic only and viscoelastic deformation responses.	31
Figure 2-5: The effect of mining rate on the total amount of steady-state closure at a particular point in the stope (Malan, 2003).	32
Figure 2-6: An example of closure measurement in different geotechnical conditions (Malan, 2003).	33
Figure 2-7: Plot of creep rate versus axial stress for quartzite and lava (Drescher and Handley, 2003).	35
Figure 2-8: Post-failure relaxation curves for quartzite and lava (Drescher and Handley, 2003).	36
Figure 2-9: Graphs of compression test results on Hartebeestfontein Mine quartzite (Bosman, <i>et al.</i> , 2000).	37
Figure 2-10: Stand-up time for underground excavations after Bieniawski (1989). Black dots are tunnel examples and black squares are shallow underground mine examples.	39
Figure 2-11: An example of a tunnel being advanced with blocked steel sets being installed after each excavation. The load-deformation curves for the rock mass and the support system are given in the righth figure from Hoek and Brown (1980).	41
Figure 2-12: Magnitude-time chart for micro-seismic events at Big Bell mine (Beneteau, 2012).	42
Figure 2-13: Experimental Barnsley Hards Coal creep curve in two different scales (Millar and Jiao, 1994).	43
Figure 3-1: Creep curve under constant load Figure 3-2: Creep curve with recovery	48
Figure 3-3: The Bingham rheological model from Malan (1999).	49

Figure 3-4: Comparison of intuitive and rheological models with experimental responses: a) asymptotic response (intuitive models), b) response terminating with failure (intuitive models), and c) response terminating with failure (rheological models) (Ayden, <i>et al.</i> , 2013).....	52
Figure 3-5: Diagram of the three-dimensional viscoelastic rheological model (Picard, 2007). ...	53
Figure 4-1: The graphical representation of ‘chair leg analogy’ explaining relationship between instantaneous stress redistribution after excavation of each stope in a sequence of excavations and rock mass stability when elastic.....	65
Figure 4-2: Schematic strain-time curve showing deformations at a specific point in the rock mass.....	68
Figure 5-1: Application of principle of superposition to calculation of stress field after (a) excavation of a circle shaped and a square shaped opening (first circle and next square): (b) the stress field after excavation of circle opening is added to (c) the stress field after excavation of square shape opening and (d) <i>in situ</i> stresses are subtracted.	72
Figure 5-2: Boltzmann superposition principle based on Penny and Marriott (1971).	73
Figure 5-3: The resulting time series of stress and strain have a stepped appearance as elasticity redistributes stresses upon excavation. Presented data is from the example discussed in Chapter 6.....	78
Figure 5-4: The 3D Generalized Kelvin-Voight model for creep deformation is a combination of one 3D Kelvin-Voigt component (circled with a red line) in series with a Hookean element (spring) (Picard, 2007).....	79
Figure 5-5: Generalized Kelvin-Voigt, Kelvin-Voigt and Elastic rock mass deformation under constant load based on Goodman (1989).....	81
Figure 5-6: Results of least squares fitting different viscoelastic models to the data set of compression creep test on a quartzite sample from Hartbeesfontein Mine quartzite, South Africa reported by of Bosman <i>et al.</i> (2000). The right graph is the result of least squares fitting of 3D Kelvin-Voigt model to this data set.	83

Figure 5-7: Decastellated time series of strain as stresses redistribute upon excavations.	84
Figure 5-8: (a) Example of failure envelope in 3-dimensional stress space (from Benz <i>et al.</i> (2008)); (b) Representation of a stress state in principal stress space, (c) Representation of a stress state in the deviatoric plane (from Lee <i>et al.</i> (2012))......	86
Figure 5-9: Mohr-Coulomb failure criterion in the deviatoric plane from (Lee, <i>et al.</i> , 2012). ...	88
Figure 5-10: Strain-based Mohr-Coulomb failure criterion in the deviatoric plane.	90
Figure 5-11: Automated procedure for developing (in)stability metrics.	98
Figure 5-12: All the permutations of excavating four stopes.	99
Figure 5-13: Feasible sequences of excavating four stopes reduce substantially after applying constraints.	101
Figure 6-1: 6 designed stopes and their locations (lower right hand side). Stope meshes designed by Rhinoceros and imported into Examine3D for visualization, checking and mesh verification.	103
Figure 6-2: Time series of deviatoric stress and elastic/viscoelastic response of rock mass for grid point 6267 for two different sequences of excavations.	106
Figure 6-3: Time series of deviatoric stress and elastic/viscoelastic response of rock mass for grid point 7590 in sequence 145. Black arrow points out sensibility of viscoelastic strain in scheduling.	107
Figure 6-4: Presentation of (in)stability metric graphs' template.	110
Figure 6-5: Deviatoric stress distribution on the periphery of one stope from the stope model computed with Examine3D.....	111
Figure 6-6: (a) Metric 1: number of grid points with strength factor less than one; (b) Metric 2: number of grid points with strainth factor less than one; (c) Metric 3: Number of grid points with viscoelastic-strainth factor less than one.....	113

Figure 7-1: A sequence of excavating and backfilling two stopes in three stages. The figures on the left present the model geometry at each stage of excavations and the figures on the right present the deviatoric stress distribution at each stage of the excavation produced by Phase2.. 115

Figure 7-2: Modes of support of mine backfill: (a) kinematic constraint on surface blocks in de-stressed rock; (b) support forces mobilized locally in fractured and jointed rock; (c) global support due to compression of the fill mass by wall closure from Brady and Brown (1993). ... 122

Figure 7-3: Schematic presentation of Eshelby's inclusion problem. (a) is an unloaded homogeneous infinite medium of moduli (b) a region of this medium (the inclusion) is submitted to a free strain (c) deforming the inclusion to its original shape and size induces stress in the medium (Eshelby, 1957)..... 124

Figure 7-4: Stress distribution around a circular opening in a hydrostatic stress field (p), due to development of a fracture zone. p_i is the support pressure, a is the opening radius, r_e is the fractured zone radius, p_1 is the radial stress at the elastic interface and ϕ is the angle of friction for the fractured rock. 127

Figure 7-5: The additional element to complete superposition procedure. The far field boundary condition is equal to zero and the stress distribution on the periphery is uniform and hydrostatic. 129

Figure 7-6: The current superimposition procedure (a) is upgraded to the superimposition procedure (b) regarding to the backfill effect on the stress distribution. 130

Figure 8-1: Schematic presentation of an access tunnel and a stope excavated in a sequence of blasts: event -2, event -1, event0, event1, event2, event3..... 136

Figure 8-2: Schematic presentation of the 'viscoelastic strainth' compared to the 'strainth'. 'a' is the difference between the failure time for the elastic and the viscoelastic rock responses if the threshold is 'strainth', and 'b' is the difference between the failure time for the elastic and the viscoelastic rock responses if the threshold is 'viscoelastic-strainth'. 139

Figure A-1: σ_1 (maximum principal stress) distribution after the excavation of the square opening, $K = 0.5$	148
Figure A-2: σ_3 (minimum principal stress) distribution after the excavation of the square opening, $K = 0.5$	148
Figure A-3: σ_1 (maximum principal stress) distribution after the excavation of the circle opening, $K = 0.5$	149
Figure A-4: σ_3 (minimum principal stress) distribution after the excavation of the circle opening, $K = 0.5$	149
Figure A-5: σ_1 (maximum principal stress) distribution after the excavation of the diamond opening, $K = 0.5$	150
Figure A-6: σ_3 (minimum principal stress) distribution after the excavation of the diamond opening, $K = 0.5$	150
Figure A-7: σ_1 (maximum principal stress) distribution after the excavation of the square opening, $K = 0.5$	151
Figure A-8: σ_3 (minimum principal stress) distribution after the excavation of the square opening, $K = 0.5$	151
Figure A-9: σ_1 (maximum principal stress) distribution after the excavation of the circle opening, $K = 0.5$	152
Figure A-10: σ_3 (minimum principal stress) distribution after the excavation of the circle opening, $K = 0.5$	152
Figure A-11: σ_1 (maximum principal stress) distribution after the excavation of the diamond opening, $K = 0.5$	153
Figure A-12: σ_3 (minimum principal stress) distribution after the excavation of the diamond opening, $K = 0.5$	153

Figure B-1: Result of a uniaxial compression creep test of Elsburg Quartzite from Drescher and Handley (2003).	154
Figure B-2: Rheological models fitted to the first bit of measured strain from uniaxial compression creep test of Elsburg Quartzite from Drescher and Handley (2003).	155
Figure B-3: Rheological models fitted to the second part of the measured strain from uniaxial compression creep test on Elsburg Quartzite from Drescher and Handley (2003).....	156
Figure B-4: Graphs of compression test results on Hartebeestfontein Mine quartzite (Bosman, <i>et al.</i> , 2000).	157
Figure B-5: Rheological models fitted to the measured strain from UCS test on quartzite sample from Hartebeestfontein Mine sidewall.....	158
Figure B-6: Uniaxial creep tests on quartzite sample from Hartebeestfontein mine reported by Malan <i>et al.</i> (1997).....	159
Figure B-7: The rheological models fitted to the measured strain from the uniaxial creep tests on the quartzite sample from Hartebeestfontein mine under 107 MPa uniaxial compression load.	160
Figure B-8: Uniaxial creep tests on lava sample from Hartebeestfontein mine reported by Malan <i>et al.</i> (1997).....	161
Figure B-9: The rheological models fitted to the measured strain from the uniaxial creep tests, on the lava sample from Hartebeestfontein mine under 366 MPa uniaxial compression load.....	162
Figure B-10: The Burgers convergence model fitted to the underground closure measurements from Deelkraal gold mine (Malan, <i>et al.</i> , 1997).	163
Figure B-11: Rheological models fitted to the calculated strain from the measured closure data from Deelkraal gold mine reported by Malan <i>et al.</i> (1997).....	164
Figure C-1: The GUI (Graphical User Interface) of the 'Examine3D batch mode processor' VBA code.	176

Figure G-1: Indicator 1 - number of grid points with strength factor less than one.	197
Figure G-2: Indicator 2- number of grid points with strainth factor less than one.	198
Figure G-3: Indicator 3-number of grid points with viscoelasticstrainth factor less than one. .	199
Figure G-4: Indicator 4-Average strength factor over all grid points.	200
Figure G-5: Indicator 5-Average strainth factor over all grid points.....	201
Figure G-6: Indicator 6-Average viscoelasticstrainth factor over all grid points.	202
Figure G-7: Indicator 7-Minimum strength factor over all grid points.	203
Figure G-8: Indicator 8 - Minimum strainth factor over all grid points.	204
Figure G-9: Indicator 9 - Minimum viscoelasticstrainth factor over all grid points.....	205
Figure G-10: Indicator 10- Maximum strength factor over all grid points.....	206
Figure G-11: Indicator 10- Maximum strength factor over all grid points.....	207
Figure G-12: Indicator 12-Maximum viscoelasticstrainth factor over all grid points.	208

Terminology

The section defines key terms used in the context of mine design, mine planning and mine scheduling, as adopted in this thesis.

Activity: Each activity is an element of a project that is performed according to the *schedule*. An activity has a *duration*. The start and end of the activity are each an *event*.

Development activity: Development activities are generally the predecessors of the *stopping activities* in a *mine schedule*. Development activities are such as development of the ore access tunnel (e.g. crosscuts), ventilation raise and creation of other mine tunnels such as escape ways and travel ways.

Duration: The time to execute an *activity* is duration.

Event: A zero *duration* milestone defining the achievement of a defined outcome in an event. In this work, blast is referred to as an event.

Interval: The time lag between each two stopping *events* (blasts) is called interval. Each stopping *event* (blast) happens instantaneously.

Mine design: The mining area dimensions, and locations of the excavation area, supporting methods, machinery section and production planning in order to guide an efficient and economical production.

Mine planning: Mine planning is a multidisciplinary process involving different phases of mine's life from feasibility studies to production, such as geostatistical analysis, resource evaluation, mine design and scheduling.

Mine scheduling: Mine scheduling is the procedure of timetabling the start time and finish time of each *mining activity*.

Mining activity: Mining activities consist of *development activities* (those where infrastructure for the mine is created) and *stopping activities* (those involving removal of the ore). Activities have a start time and an end time. The time between the start time and the end time is called *duration*.

Schedule: The timetable for a series of *activities* that are planned to be done in a particular period is called schedule.

Sequence: The order in which activities occur is called a sequence, it consists of activities occurring in series or in parallel (activities happening simultaneously). The presented work only focuses on optimizing the order of *stopping activities* bounded by blast *events*. Practically, this involves deciding on the time of each *event*.

Stopping Activity: Stopping activities are the activities, which occur in between two *events* (blasts), such as mucking, hauling, hoisting, etc.

In this work, blasts are events which bund mining activities such as mucking, bolting, drilling and charging, each of which have finite duration. Blasts are assumed to create excavations instantaneously, redistributing stress instantaneously too. Time dependent response of the rock occurs concurrently with the mining duration.

1 Introduction

1.1 Underground Mining Scheduling

Underground mining consists of series of activities to extract ore from the host rock, such as developing excavations to gain access to the mineralized zone (development activities), extracting the ore (stopping), and transporting the material to the surface. The mentioned activities are defined in the process of mine planning followed by mine designing, which are two major steps in a mining project.

Underground mine designing is a complicated problem. Alford *et al.* (2007) mentioned that the complexity of the underground mine design is due to the infirmity in the understanding of the solution domain (feasible mine designs). However, improvements of optimization methods has eased developing different mine designs. Atae-pour (2005) reviewed methodologies for optimizing the geometry of the stope boundaries and their grounds of applicability. Such technique is adopted in this work by utilizing output of Mineable Shape Optimizer (MSO), a function in Studio3D, produced by Datamine, as a starting point. Topal *et al.* (2003) proved the improvements in the mine design at Kiruna Mine by comparing production prior to the introduction of an optimization model and production associated with an optimized design. Different optimization methodologies will be discussed further in this chapter.

After a mine design is available, mine scheduling provides a timetable for the mining activities over life of the mine. Gantt charts are widely used in mine scheduling to describe and monitor series of interdependent mining activities; these activities are linked together based on the start day and finish day of each activity and their predecessor and successor activities. This schedule

– which can be articulated as a Gantt chart – decides on the durations and sequence of mining activities subject to operational resources (e.g. equipment and personnel), mine development constraints (e.g. access precedence between excavations, ventilation raises or ore passes, etc), grade value of ore, operational costs and revenue.

Figure 1-1 shows possible types of links between activities. Whatever links exist between different activities, the start date of the first activity should correspond to the start day of the mining project and finish date of last activity should not exceed project deadline. These considerations can be applied to the Gantt chart by defining constraints such as SNET (Start No Earlier Than) which means the activity may not start before the given date and FNL (Finish No Later Than) which means the activity may not end later than the given date. The correct choices of constraints can enhance the schedule by reducing the overall duration of the project, so that the critical path can be found, or the minimum project cost can be found (Hillier and Lieberman, 2001).

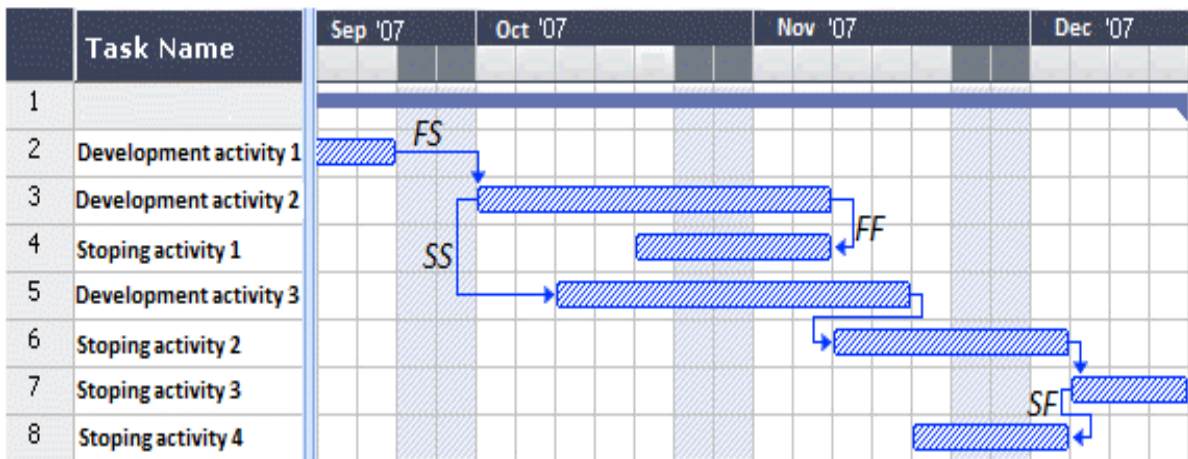


Figure 1-1: Schematic Gantt chart showing schedule of development and stoping activities. FS (Finish to Start) means the activity cannot start before its predecessor ends, although it may start later. SS (Start to Start) the activity cannot start until the predecessor starts, although it may start later. SF (Start-to-Finish) the activity cannot end before the predecessor starts, although it may end later. FF (Finish-to-Finish) means the activity cannot end before the predecessor ends, although it may end later (Gantt-Chart, 2012).

A well-planned schedule should support a high level of profitability. The underground mine schedule has to be resilient in the face of unexpected events which might impede or disrupt the schedule and cause additional cost to the mining project and consequently reduce profitability.

Creation of an underground excavation perturbs the *in situ* stress field, and this disturbance can induce stress concentrations around excavation areas. As the result of changes in the state of stress, rock masses deform to reach a new equilibrium, part of which may involve instability by various mechanisms, from gradual closure of an excavation to violent bursting of rock (Hoek and Brown, 1987). The high value production schedules could lead to a sequence of excavations, which increase the risk of geotechnical instabilities in the rock mass. The costs of such instabilities may be high. For example, mining at the Trout Lake Cu–Zn sulphide deposit, 5 km northeast of Flin Flon, Manitoba (Ordóñez-Calderón, *et al.*, 2009) showed that in deep mining, the cost of the failure amounted to the loss of revenue from the remaining ore and the development cost of access. For a more realistic evaluation of profitability of mining schedules, analysis of stability conditions in the rock mass should carefully integrate with mining scheduling procedures.

The stoping operation (removal of ore and transporting it to surface) forms the core of the mining process, requiring that the rock mass stability being controlled to ensure an efficient and economical ore recovery. Brady and Brown (1993) note that geomechanical considerations enable a predictive analysis for the rock response to different extraction and sequencing strategies to be undertaken and this is central to the topic of this thesis.

Mine schedule optimization is concerned with adjusting the timetabling of mining activities to maximize profitability of the project, articulated as its Net Present Value (NPV). The NPV of a

project is a measure of the net increase in wealth and is calculated by summation of present cash flows and present values of any future cash flows. A profitable project is a project with a positive NPV. The costs of stoping and development activities generally are based on the extracted tonnage or meters advanced respectively. What makes two individual stopes with the same size and similar production costs, in the same rock mass contribute differently to the NPV, is the grade of the ore, the way they are mined and the timing of the extraction. In general, the process of mine schedule optimization results in the ore mass with higher grade being reached sooner, and thus it contributes more strongly to the NPV (more revenue is produced, earlier with a lower present value factor, for roughly the same cost).

This search for the optimal schedule must take into account the amount of resource available to complete mining tasks. For example, development activity with a given fleet of equipment may mean that the total annual development advance is limited to a threshold value of development meters. Similarly, the production rate of ore may be limited by hoisting capacity (the skips installed may only allow a threshold to be hauled). Clearly, precedence constraints also need to be considered; stope access development must be completed before the corresponding stoping activity can start. In formal mathematical optimization parlance, such factors are called as constraints.

Practically, mine schedules can be disrupted by unexpected rock failure events. Stability of the rock mass is thus a key concern in underground mine schedule optimization, however, assimilating sequencing and timing constraints that aim to avoid or mitigate stress or displacement-related failures has proven very challenging. This work considers a generalized approach to address this challenge, articulated as the introduction of a new geotechnical constraint to the mine schedule optimization formulation.

1.2 Schedule optimization methodologies

There are a variety of methods and solutions proposed to solve optimization problems. Any of the optimization methods start with modeling the problem of interest and the constraints subjected, in a comprehensible and tractable way. Mathematical and graphical formulations are widely adopted ways for articulating optimization problems. These formulations provide an abstract statement of the large problem, by highlighting important cause and effect relationships. Simplifications and approximations, associated with developing the optimization model, are essential to keep the concept of the optimization problem valid and comprehensible. Correct formulation of the problem and its constraints is the pivotal step in the schedule optimization process. As stated by Hillier and Lieberman (2001) *“It is always difficult to extract a right answer from the wrong problem!”*

The mathematical formulation of an optimization problem usually consists of three parts (Hillier and Lieberman, 2001):

- i. Decision variables the quantities whose respective values need to be determined, e.g. time at which any of mining activities are scheduled;
- ii. Objective function expressed in the decision variables, which measures the relative performance of possible solutions, e.g. the NPV in underground mine schedule optimization problems;

and,

- iii. Constraints, which are limitations that need to be taken into account e.g. operational resources in underground mine schedule optimization problems.

For mine scheduling, the graphical part of formulation of the optimization problem visualizes all the activities involved in the project as a network, consisting of series of nodes referring to achievement of the activities; arcs referring to the duration of activities; and dashed arcs called “dummy activities” which simply define activity precedence. The network model of the optimization problem provides a graphical description, which displays each activity and its relation to other activities. The “Critical Path” in the network model is the path producing, simultaneously, the maximum and minimum duration of the project (Anderson, *et al.*, 1994).

Figure 1-2 is a schematic presentation of a Network model.

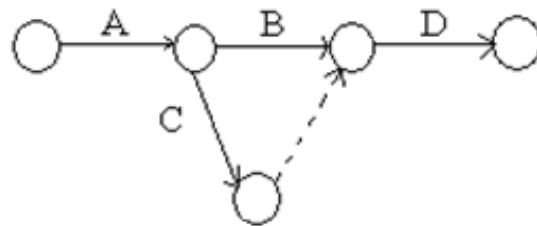


Figure 1-2: Schematic presentation of a Network model of five activities. Nodes refer to the achievement of the activities, arcs refer to the duration of the activities and dashed line is the “dummy activity”.

After formulation of the optimization problem, development of a procedure to find the solution to the problem is required. Figure 1-3 shows different solution methods for optimization problems in a tree diagram developed by Sharma (2014) based on Sivanandam and Deepa (2008).

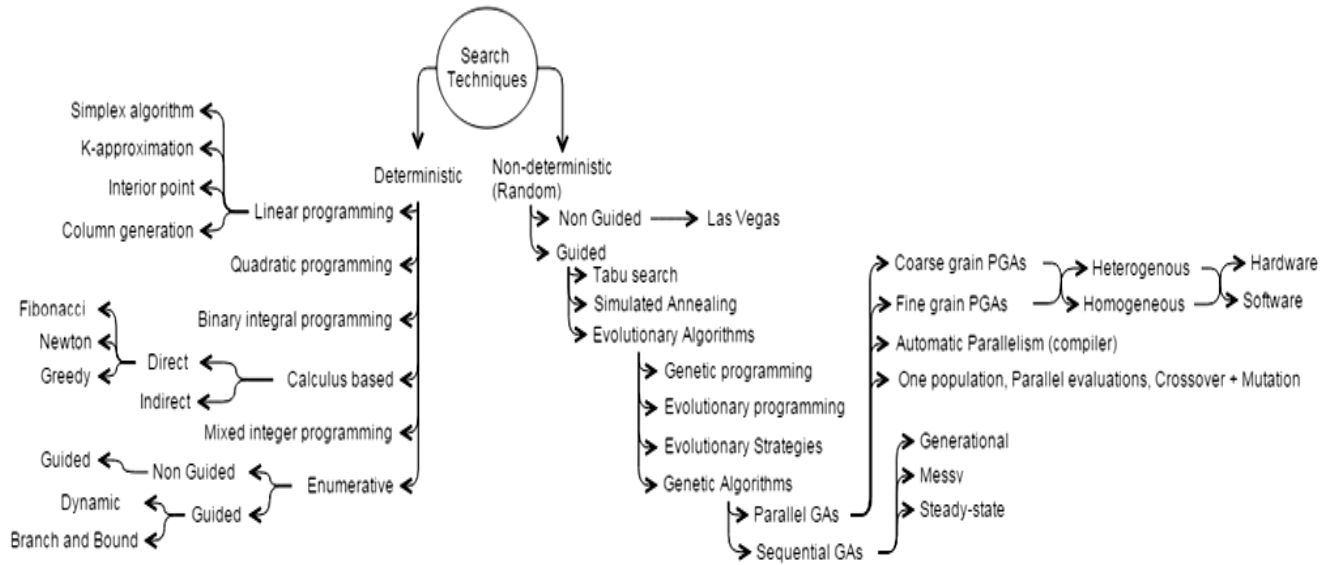


Figure 1-3: Search techniques on different optimization solution methods based on Sivanandam and Deepa (2008) from (Sharma, 2014)

Linear programming (LP), integer programming (IP) and quadratic programming (QP) are deterministic techniques that are used in solving optimization problems. Among these methods, linear programming (LP) is the most preferred, if applicable, because its solution methods guarantee optimality. Linear programming is a problem solving approach for optimizing a linear objective function, subject to linear constraints and real valued, positive decision variables and so application of the technique is restricted to problems with these characteristics. The most frequently used method to solve LP problems is called the Simplex algorithm (Hillier and Lieberman, 2001) however, it is not a practical solution for the case of an underground mine planning due to its iterative and slow solution for such large scale problems. Mine schedules are more likely to fit the integer programming (IP) techniques as they can cope with discontinuous objective functions.

However, the decision variables are integer. Mixed integer programming (MIP) techniques are more complex to solve compared to linear programming techniques and involve both real and

integer valued decision variables. The Branch and Bound algorithm (Anderson, *et al.*, 1994) is commonly employed to find the optimal answer for various integer and mixed integer linear optimization problems.

The abovementioned optimization techniques give the optimum solution of the problem however; they have limited scope of functionality in large-scale and complex optimization problems because, as soon as one of their fundamental assumptions is violated, the method of solution cannot be applied: for example, adoption of the NPV for the objective function in mine schedule optimization problems, make the problem nonlinear, and Simplex method, Branch and Bound are only applicable to linear optimization problems. For a large set of data and variables, the methods are either computationally long and give the optimum solution, or computationally time efficient and give a solution converging on the optimum solution. Underground mine scheduling optimization problems practically resolved under the second category.

A short-term planning mixed integer linear based software tool is developed by Zhanyou *et al.* (2009) to solve open pit and underground mine scheduling optimization problems. They formulated constraints based on linear programming techniques, which resulted in limiting the comprehensiveness of the problem. Nehring *et al.* (2010) proposed a mixed integer programming solution for solving mine production optimization problems. They also mentioned the impracticality of the computation time of the solution for long-term production schedules, such as those in underground mines.

Evolutionary algorithms are a range of problem-solving techniques that are commonly applied to large-scale, non-linear optimization problems, an example being underground mine schedule optimization. One type of evolutionary algorithm, a genetic algorithm, has been used by

multiple authors (e.g. Fava *et al.* (2011)) for mine schedule optimization. Winter *et al.* (1995) stated that it is a faster optimization method for large-scale optimization problems, compared to methods such as mixed integer programming. The non-deterministic nature of evolutionary algorithms in part refers to the uncertainty associated with the optimized solution to the optimization problem: it may not find the optimum, however a good or improved solution will be found, if one exists.

1.3 An example of schedule optimization – finding out when a project will be complete

In order to expand on the idea of the optimization analysis that arises in mining schedule optimization, this section describes an example of optimal scheduling of a series of activities required for construction a house based on an example from Hillier and Lieberman (2001). Table 1-1 lists out all these activities and their FS and SF precedence relations. A nominal duration for each activity is also available from Table 1-1. Activities precedence and their duration enable a network model of activities involved in the house construction project to be set out.

Table 1-1: List of the activities for a project of constructing a house from Hillier and Lieberman (2001), cost of activity and duration of the activities are included by the author.

Activity	Activity Description	Predecessors	Nominal duration of activity (weeks)	Duration of activity (weeks)		Cost of activity ($\$ \times \frac{1}{10^5 \$}$)	
				Max	Min	Min	Max
A	Excavate	-	2	3	1	5.5	6.5
B	Lay the foundation	A	4	4.5	3.5	6.55	6.65
C	Put up the rough wall	B	10	11	9	5.9	6.1
D	Put up the roof	C	6	8	4	3	5
E	Install the exterior plumbing	C	4	4.5	3.5	2.5	3.5
F	Install the interior plumbing	E	5	6	4	4	6
G	Put up the exterior siding	D	7	8	6	6.2	6.4
H	Do the exterior painting	E, G	9	10	8	6.5	6.6
I	Do the electrical work	C	7	9	5	6.2	7
J	Put up the wallboard	F, I	8	9	7	2.5	3.5
K	Install the flooring	J	4	5	3	4.5	5.5
L	Do the interior painting	J	5	6	4	0.4	0.6
M	Install the exterior fixtures	H	2	3	1	6.97	6.99
N	Install the interior fixtures	K, L	6	7	5	3	7

This is shown in Figure 1-4 where nodes refer to the activities' events (e.g. start/finish) and arcs refer to the activities themselves, each with a nominal duration. Each node (in Figure 1-4) is labeled from 1 to 14 and refer to the time at which either an activity starts or ends. The numbers typed to the left side of the arcs are the nominal duration of each activity and letters typed to the right side of the arcs are the activity labels presented in Table 1-1. The equations next to each of the activities show precedence relationships. As an example, activity *B* cannot start any time earlier than 2 weeks after activity *A* started. The highlighted path in blue is called "critical path" which is the longest path through the network and is equal to the estimated project duration. Dashed lines are "dummy activities" which are the activities introduced with zero duration and simply control activity precedence (Hillier and Lieberman, 2001).

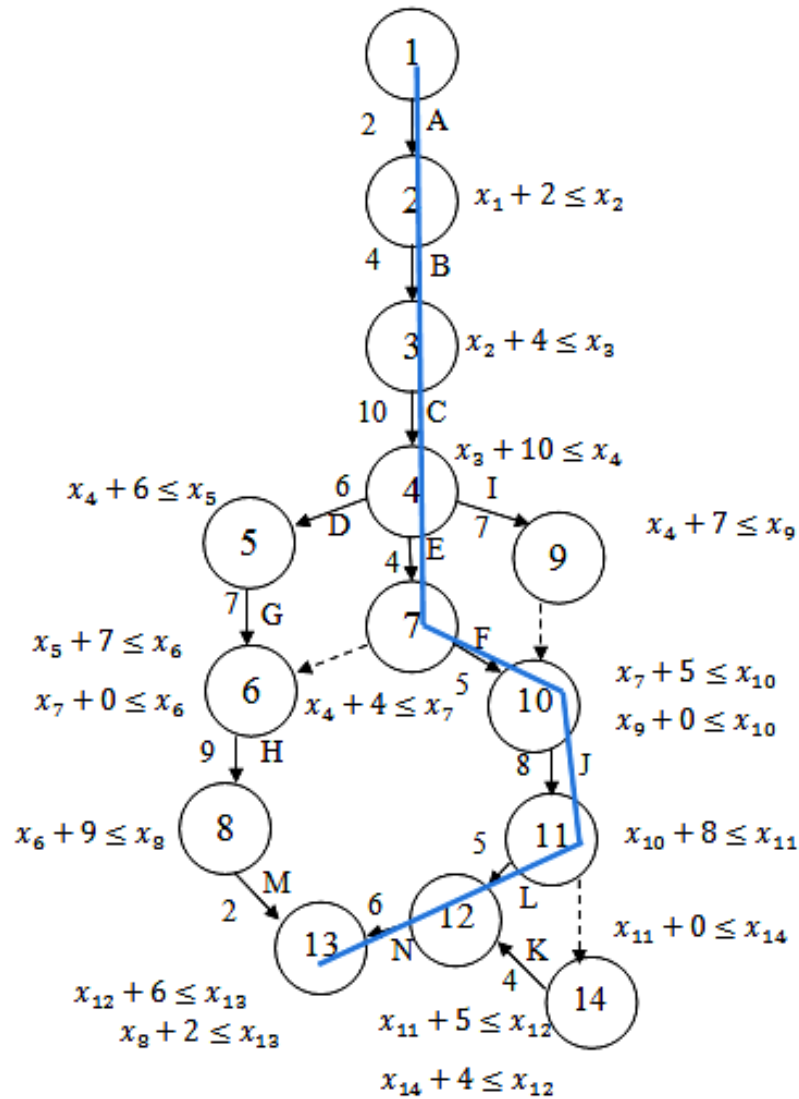


Figure 1-4: The network model of the project of constructing a house from Hillier and Lieberman (2001). The blue line is showing “critical path”.

The problem presented in Figure 1-4 is to schedule the abovementioned activities in order to minimize the total duration of the project. A Linear programming solver is preferred for this optimization problem because it is simple and the mathematical formulation of matches with the standard format of general linear programming problems, which is as follows:

Objective function: minimize $Z = \sum c_i x_i$

Subject to: $\sum a_i x_i \leq b_i$ and $x_i \geq 0$,

where x_i are decision variables, a_i, b_i and c_i are coefficients and $1 \leq i \leq N$ where N is the number of decision variables.

In the following, the optimization problem of minimizing the total duration of the building construction project is set out as a linear programming problem following the general form. The values of x_1 to x_{14} are decision variables and are the time at which each event occurs.

Objective function: minimize Z

$Z = x_{13}$ (time that the project is complete)

Subject to (precedence rules):

$$1x_1 - 1x_2 + 0x_3 + 0x_4 + 0x_5 + 0x_6 + 0x_7 + 0x_8 + 0x_9 + 0x_{10} + 0x_{11} + 0x_{12} + 0x_{13} + 0x_{14} \leq -2$$

$$0x_1 + 1x_2 - 1x_3 + 0x_4 + 0x_5 + 0x_6 + 0x_7 + 0x_8 + 0x_9 + 0x_{10} + 0x_{11} + 0x_{12} + 0x_{13} + 0x_{14} \leq -4$$

$$0x_1 + 0x_2 + 1x_3 - 1x_4 + 0x_5 + 0x_6 + 0x_7 + 0x_8 + 0x_9 + 0x_{10} + 0x_{11} + 0x_{12} + 0x_{13} + 0x_{14} \leq -10$$

$$0x_1 + 0x_2 + 0x_3 + 1x_4 + 0x_5 + 0x_6 + 0x_7 + 0x_8 - 1x_9 + 0x_{10} + 0x_{11} + 0x_{12} + 0x_{13} + 0x_{14} \leq -7$$

$$0x_1 + 0x_2 + 0x_3 + 0x_4 + 0x_5 + 0x_6 + 1x_7 + 0x_8 + 0x_9 - 1x_{10} + 0x_{11} + 0x_{12} + 0x_{13} + 0x_{14} \leq -5$$

$$0x_1 + 0x_2 + 0x_3 + 0x_4 + 0x_5 + 0x_6 + 0x_7 + 0x_8 + 1x_9 - 1x_{10} + 0x_{11} + 0x_{12} + 0x_{13} + 0x_{14} \leq 0$$

$$0x_1 + 0x_2 + 0x_3 + 0x_4 + 0x_5 + 0x_6 + 0x_7 + 0x_8 + 0x_9 + 1x_{10} - 1x_{11} + 0x_{12} + 0x_{13} + 0x_{14} \leq -8$$

$$0x_1 + 0x_2 + 0x_3 + 0x_4 + 0x_5 + 0x_6 + 0x_7 + 0x_8 + 0x_9 + 0x_{10} + 1x_{11} + 0x_{12} + 0x_{13} - 1x_{14} \leq 0$$

$$0x_1 + 0x_2 + 0x_3 + 0x_4 + 0x_5 + 0x_6 + 0x_7 + 0x_8 + 0x_9 + 0x_{10} + 1x_{11} - 1x_{12} + 0x_{13} + 0x_{14} \leq -5$$

$$0x_1 + 0x_2 + 0x_3 + 0x_4 + 0x_5 + 0x_6 + 0x_7 + 0x_8 + 0x_9 + 0x_{10} + 0x_{11} - 1x_{12} + 0x_{13} + 1x_{14} \leq -4$$

$$0x_1 + 0x_2 + 0x_3 + 0x_4 + 0x_5 + 0x_6 + 0x_7 - 1x_8 + 0x_9 + 0x_{10} + 0x_{11} + 0x_{12} + 1x_{13} + 0x_{14} \leq -2$$

$$0x_1 + 0x_2 + 0x_3 + 0x_4 + 0x_5 + 0x_6 + 0x_7 + 0x_8 + 0x_9 + 0x_{10} + 0x_{11} + 1x_{12} - 1x_{13} + 0x_{14} \leq -6$$

$$0x_1 + 0x_2 + 0x_3 + 0x_4 + 0x_5 + 1x_6 + 0x_7 - 1x_8 + 0x_9 + 0x_{10} + 0x_{11} + 0x_{12} + 0x_{13} + 0x_{14} \leq -9$$

$$0x_1 + 0x_2 + 0x_3 + 0x_4 + 0x_5 - 1x_6 + 1x_7 + 0x_8 + 0x_9 + 0x_{10} + 0x_{11} + 0x_{12} + 0x_{13} + 0x_{14} \leq 0$$

$$0x_1 + 0x_2 + 0x_3 + 0x_4 + 1x_5 - 1x_6 + 0x_7 + 0x_8 + 0x_9 + 0x_{10} + 0x_{11} + 0x_{12} + 0x_{13} + 0x_{14} \leq -7$$

$$0x_1 + 0x_2 + 0x_3 + 1x_4 - 1x_5 + 0x_6 + 0x_7 + 0x_8 + 0x_9 + 0x_{10} + 0x_{11} + 0x_{12} + 0x_{13} + 0x_{14} \leq -6$$

$$0x_1 + 0x_2 + 0x_3 + 1x_4 + 0x_5 + 0x_6 - 1x_7 + 0x_8 + 0x_9 + 0x_{10} + 0x_{11} + 0x_{12} + 0x_{13} + 0x_{14} \leq -4$$

and For $i=1$ to 14 $x_i \geq 0$

Solving the presented house-construction scheduling problem with ‘Simplex method’ (Millar, 2009) gives the answer of 44th week for the optimum duration of house-construction problem.

Table 1-2 presents the times of the 14 events and agree with those presented by Hillier and Lieberman (2001).

Table 1-2: Optimum time at which each activity should start to minimize duration of the house construction project is calculated with Simplex method.

Activity	A	B	C	D	E	F	G	H	I	J	K	L	M	N
Time (weeks)	0	2	6	16	20	25	22	29	25	33	33	38	42	44

1.4 An example of schedule optimization – finding out how much a project will cost

Mine schedule optimization problems take the costs associated with activities and the thresholds on available resources into account as part of the requirements for NPV maximization procedure. To illustrate these points, the analysis of Hillier and Lieberman (2001) is extended in the following.

Table 1-1 also contains information about minimum and maximum costs of each activity corresponding to the maximum and minimum duration of each activity. Based on the values of maximum and minimum duration and maximum and minimum cost for each activity presented in Table 1-1, a series of linear cost functions, expressed in terms of the activity durations augment the optimization model. Figure 1-5 presents a schematic representation of the relationship between costs of each activity and duration of each activity.

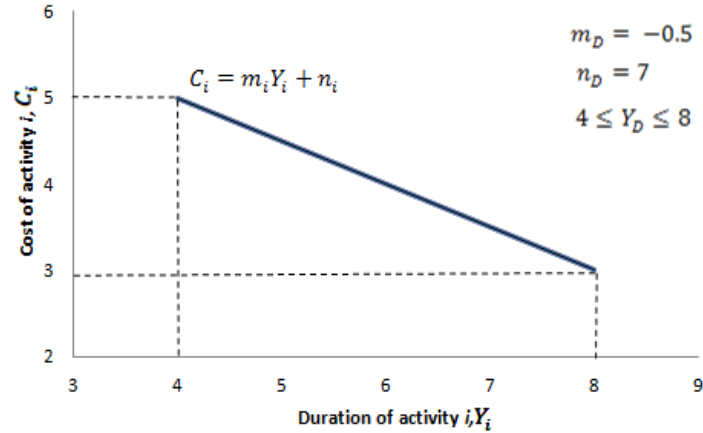


Figure 1-5: The schematic relationship between costs of activity i , and duration of the activity i . Exemplified for activity D.

The cost-time relationships in Table 1-1 define a new optimization problem where the objective is to minimize the cost of constructing the building, and this can also be solved using the Simplex method because the problem remains linear. In the following, the optimization problem for minimizing the total cost of the house construction project is formulated as a linear programming problem, with the decision variables now being the activities ($x_1 = \text{Activity A}$, $x_2 = \text{Activity B}$, ... ; $c_4 = -0.5$)

Objective function: minimize Z

$$Z = -0.5x_1 - 0.1x_2 - 0.1x_3 - 0.5x_4 - 0.1x_5 - 0.05x_6 - 0.1x_7 - 0.01x_8 - 0.2x_9 - 1x_{10} - 0.5x_{11} - 0.1x_{12} - 2x_{13} - 0.5x_{14} + 106$$

Subject to:

(precedence rules)

$$\begin{aligned} 1x_1 - 1x_2 + 0x_3 + 0x_4 + 0x_5 + 0x_6 + 0x_7 + 0x_8 + 0x_9 + 0x_{10} + 0x_{11} + 0x_{12} + 0x_{13} + 0x_{14} &\leq y_1 \\ 0x_1 + 1x_2 - 1x_3 + 0x_4 + 0x_5 + 0x_6 + 0x_7 + 0x_8 + 0x_9 + 0x_{10} + 0x_{11} + 0x_{12} + 0x_{13} + 0x_{14} &\leq y_2 \\ 0x_1 + 0x_2 + 1x_3 - 1x_4 + 0x_5 + 0x_6 + 0x_7 + 0x_8 + 0x_9 + 0x_{10} + 0x_{11} + 0x_{12} + 0x_{13} + 0x_{14} &\leq y_3 \\ 0x_1 + 0x_2 + 0x_3 + 1x_4 + 0x_5 + 0x_6 + 0x_7 + 0x_8 - 1x_9 + 0x_{10} + 0x_{11} + 0x_{12} + 0x_{13} + 0x_{14} &\leq y_9 \\ 0x_1 + 0x_2 + 0x_3 + 0x_4 + 0x_5 + 0x_6 + 1x_7 + 0x_8 + 0x_9 - 1x_{10} + 0x_{11} + 0x_{12} + 0x_{13} + 0x_{14} &\leq y_{10} \\ 0x_1 + 0x_2 + 0x_3 + 0x_4 + 0x_5 + 0x_6 + 0x_7 + 0x_8 + 1x_9 - 1x_{10} + 0x_{11} + 0x_{12} + 0x_{13} + 0x_{14} &\leq 0 \\ 0x_1 + 0x_2 + 0x_3 + 0x_4 + 0x_5 + 0x_6 + 0x_7 + 0x_8 + 0x_9 + 1x_{10} - 1x_{11} + 0x_{12} + 0x_{13} + 0x_{14} &\leq y_{11} \\ 0x_1 + 0x_2 + 0x_3 + 0x_4 + 0x_5 + 0x_6 + 0x_7 + 0x_8 + 0x_9 + 0x_{10} + 1x_{11} + 0x_{12} + 0x_{13} - 1x_{14} &\leq 0 \\ 0x_1 + 0x_2 + 0x_3 + 0x_4 + 0x_5 + 0x_6 + 0x_7 + 0x_8 + 0x_9 + 0x_{10} + 1x_{11} - 1x_{12} + 0x_{13} + 0x_{14} &\leq y_{12} \\ 0x_1 + 0x_2 + 0x_3 + 0x_4 + 0x_5 + 0x_6 + 0x_7 + 0x_8 + 0x_9 + 0x_{10} + 0x_{11} - 1x_{12} + 0x_{13} + 1x_{14} &\leq y_{14} \\ 0x_1 + 0x_2 + 0x_3 + 0x_4 + 0x_5 + 0x_6 + 0x_7 - 1x_8 + 0x_9 + 0x_{10} + 0x_{11} + 0x_{12} + 1x_{13} + 0x_{14} &\leq y_8 \end{aligned}$$

$$\begin{aligned}
0x_1 + 0x_2 + 0x_3 + 0x_4 + 0x_5 + 0x_6 + 0x_7 + 0x_8 + 0x_9 + 0x_{10} + 0x_{11} + 1x_{12} - 1x_{13} + 0x_{14} &\leq y_{13} \\
0x_1 + 0x_2 + 0x_3 + 0x_4 + 0x_5 + 1x_6 + 0x_7 - 1x_8 + 0x_9 + 0x_{10} + 0x_{11} + 0x_{12} + 0x_{13} + 0x_{14} &\leq y_6 \\
0x_1 + 0x_2 + 0x_3 + 0x_4 + 0x_5 - 1x_6 + 1x_7 + 0x_8 + 0x_9 + 0x_{10} + 0x_{11} + 0x_{12} + 0x_{13} + 0x_{14} &\leq 0 \\
0x_1 + 0x_2 + 0x_3 + 0x_4 + 1x_5 - 1x_6 + 0x_7 + 0x_8 + 0x_9 + 0x_{10} + 0x_{11} + 0x_{12} + 0x_{13} + 0x_{14} &\leq y_5 \\
0x_1 + 0x_2 + 0x_3 + 1x_4 - 1x_5 + 0x_6 + 0x_7 + 0x_8 + 0x_9 + 0x_{10} + 0x_{11} + 0x_{12} + 0x_{13} + 0x_{14} &\leq y_4 \\
0x_1 + 0x_2 + 0x_3 + 1x_4 + 0x_5 + 0x_6 - 1x_7 + 0x_8 + 0x_9 + 0x_{10} + 0x_{11} + 0x_{12} + 0x_{13} + 0x_{14} &\leq y_7
\end{aligned}$$

(minimum duration of activities)

$$\begin{aligned}
1 &\leq y_1 \\
3.5 &\leq y_2 \\
9 &\leq y_3 \\
4 &\leq y_4 \\
6 &\leq y_5 \\
8 &\leq y_6 \\
3.5 &\leq y_7 \\
1 &\leq y_8 \\
5 &\leq y_9 \\
4 &\leq y_{10} \\
7 &\leq y_{11} \\
4 &\leq y_{12} \\
5 &\leq y_{13} \\
3 &\leq y_{14}
\end{aligned}$$

(maximum duration of activities)

$$\begin{aligned}
y_1 &\leq 3 \\
y_2 &\leq 4.5 \\
y_3 &\leq 11 \\
y_4 &\leq 8 \\
y_5 &\leq 8 \\
y_6 &\leq 10 \\
y_7 &\leq 4.5 \\
y_8 &\leq 3 \\
y_9 &\leq 9 \\
y_{10} &\leq 6 \\
y_{11} &\leq 9 \\
y_{12} &\leq 6 \\
y_{13} &\leq 7 \\
y_{14} &\leq 5
\end{aligned}$$

(project deadline)

$$y_{13} = 40$$

and For $i=1$ to 14 $x_i \geq 0$.

After solving the problem using Simplex method the optimum set of durations of activities are obtained, x_i , from which the optimum start date for each activity, y_i , can be obtained – and the scheduling problem is solved, with least cost.

Solving this scheduling problem with ‘Simplex method’ (Millar, 2009) gives the answer of 57.44×10^5 \$ for the optimum cost if the house-construction project should take 40 weeks.

Table 1-3 presents the optimum duration of the 14 activities.

Table 1-3: Optimum time at which each activity should start to minimize the cost of the house construction project to finish the project in 40 weeks is calculated with Simplex method.

Activity	A	B	C	D	E	F	G	H	I	J	K	L	M	N
Duration of the activity (weeks)	0	1	4.5	13.5	17	21	17.5	23.5	18.5	28	28	32	31.5	40

The problem could be extended further by including additional constraints that reflect the availability of labour to construct the house, for example. Mining schedule optimization problems can be solved based on the same procedure, which includes listing out the activities and their relevant information such as: the duration of the activity, activity precedence and the cost functions of each activity. After formulating the objective function and constraints, a solution, which fits the mathematical presentation of the optimization problem, can be applied to find the optimum start date and finish date of the series of mining activities, which satisfies all the constraints. However, mining schedule optimization problems do not regularly fit into a linear programming standard because of their non-linear objective function (maximizing NPV) and potentially non-linear constraints for revenues and costs.

1.5 Schedule Optimization Tool

The schedule optimization process considered in this work is Schedule Optimization Tool (SOT), designed by the VPO group (Ventilation and Production Optimization) at MIRARCO (Fava, *et al.*, 2011). SOT assists with underground long-term mining planning. It conducts a search for the timetable, or schedule of a series of development and stoping activities, that aims to maximize the NPV (Net Present Value) of the mine project. Although SOT does not provide an exact optimality, it can solve problems that are intractable with exact optimization methods (because they have too many activities).

SOT formulates schedule optimization problems as follows:

Objective function:	Net Present Value of prospect extraction (maximize)
Decision variables:	Sequence of excavation activities (order)
Subject to (constraints):	Access precedence constraints between excavations Precedence milestones (e.g. no ore until ventilation system linked to stopes through development) Limits on operational resources (equipment, air, meters)

Figure 1-6 provides a simple flowchart of SOT algorithm. SOT studies different alternations of feasible sequences of activities and chooses the one with “*better economical performance*”.

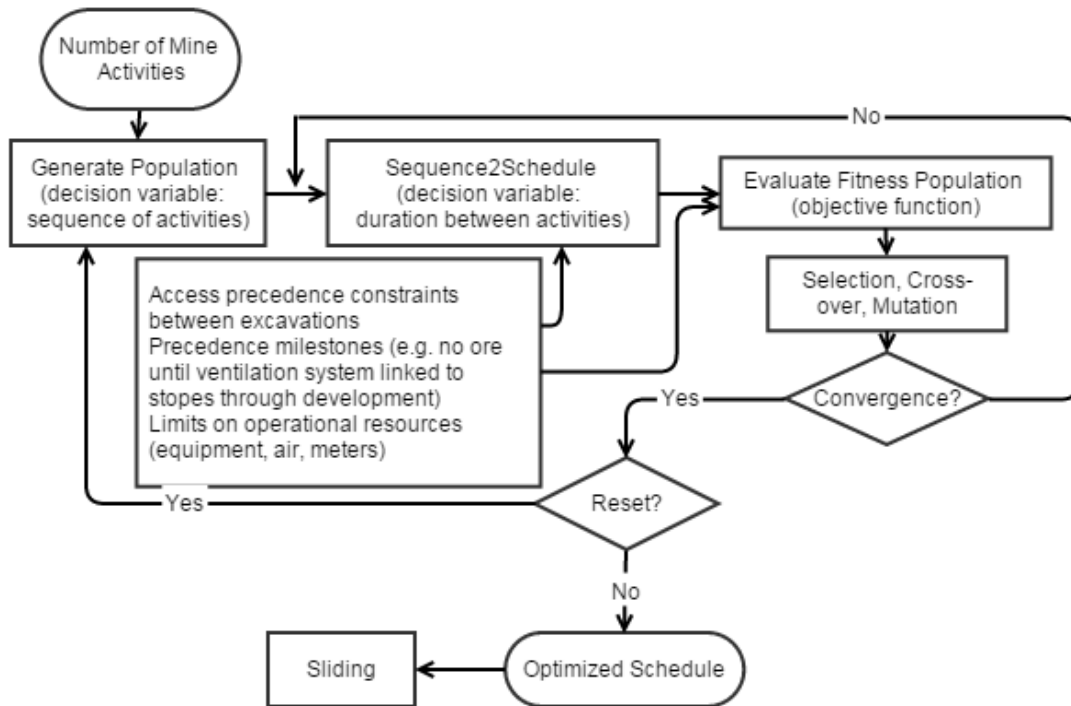


Figure 1-6: Flow chart of the SOT optimization process modified from (Maybee, *et al.*, 2010).

After the number of mine activities has been established, the ‘*General Population*’ models produces a set of randomly generated candidate solutions for the sequence of excavation, and these are subject to the problem constraints to ensure that they are feasible. ‘*Sequence2schedule*’ is the process which puts time labels on each activity in each sequence of activities and thus turns each sequence into a schedule. For each solution, the ‘*Evaluated Fitness*’ process calculates the NPV of the schedule. The processes of selection, crossover and mutation improve the pool of candidate schedules and these are re-evaluated in a process of evolutions. If the solution is converging to an asymptotic value and the number of repetitions of learning process have been exceeded, the best solution to that point is saved and the process can be ‘*reset*’ so that it starts from the beginning with a new randomly initialized set of candidates – to test for robustness. The solution from each ‘*reset*’ may be enter a final stage called “*sliding*” which

forces some activities with slack in the schedule, which are not required in the near future, to be deferred and this adds value to the schedule through the discounting process.

The capabilities of the existing optimization tool are being extended to a new mine scheduling optimization tool called SOT+ which will integrate geomechanical constraints and ventilation constraints to this automated optimization procedure. This thesis focuses on the development of geomechanical constraints integrating with SOT+. The objective is to add an additional constraint to the schedule optimization process, a “Threshold value of geotechnical stability metric”. Rock mechanics principles are to be incorporated into the schedule optimization process by defining instability risk metrics whether such metric will be integrated as an additional constraint or integrated as a penalty term in objective function.

To be a constraint, the geotechnical metric needs to be expressed in the decision variables, which are the activity sequence or order. The geotechnical metric could also be embedded into the objective function either as a straightforward penalty term, or the metric could be translated to costs arising from rock instability (cost of interruption of production). Integration of the geotechnical metric into SOT+, in either of the aforementioned ways, should produce mining schedules, which have lower geotechnical risk, as well as improved NPV.

Rather than being fully integrated into the optimization loop, geotechnical metrics could also be applied more as a check, rather than a constraint in the same way that *sliding* is applied post optimization). Highest NPV candidate schedules selected by the core SOT will have their geotechnical metric assessed. The module will thus accept or reject schedules generated by SOT based on the geotechnical evaluations. In this case, the final schedules generated by SOT+ will

be those with high NPVs, which are also geotechnically stable, but not necessarily the most geotechnically stable.

1.6 Scope and purpose of the thesis

The work reported herein extends prior efforts to establish the optimum sequence and timetable (schedule) of stoping and development activities, that maximize the Net Present Value of ore extraction. Excavation instabilities that interrupt stoping operations can cause delays to the mine schedule and appreciable loss of value. Geomechanical constraints on mine schedules, introduced with the aim of avoiding excavation instabilities, can be established for underground mine schedule optimization processes but, currently, this is done only rather crudely. The ultimate objective of this research is to produce a high value schedule for mine activities, which enhances the profitability of the mining process as well as reduces the risk of rock failure.

This thesis reports on an automated process that has been created and developed by the author for formulation of such geomechanical constraints in the decision variables. The requirements of the procedure were that it had to be time efficient and computationally efficient due to the large scale of the solution domain e.g. there is 'n!' different solutions available for excavation of 'n' stopes.

A core hypothesis of the work is that there is a time-dependent aspect of rock and rock mass deformability behaviour that, because the decision variables relate to time, is important mine schedule optimization. The work has led to an assumed causality model of rock instability. An excavation is created with a pre-existing *in situ* stress field and those stresses are immediately redistributed (at the speed of sound in the medium). The rock mass in which the excavation is made is presumed to have a viscoelastic constitutive behaviour, which is fundamental. Note that

this presumption should be directly compared with that of the overwhelming majority of most rock mechanics/geomechanical analyses of rock and rock masses: a presumption that the fundamental behaviour is initially elastic. In making a presumption of viscoelastic behaviour of rock and rock masses, it is not suggested that an elastic presumption is wrong. Nor is an explanation (in rock mechanic terms) of why a viscoelastic constitutive behaviour is presumed offered in this thesis. More practically, through the course of the work presented, it will become apparent that in making a presumption of a viscoelastic constitutive behaviour of rock and rock masses, it is easier to express the geotechnical instability metric and integrate it into the schedule optimization process.

This stated, the requirement that the schedule optimization process remain computationally tractable, has meant that the geotechnical numerical modeling undertaken relies on an assumption of elastic constitutive behaviour, and time dependency is confined to a type of ‘correction’ applied after the sequence of elastic analysis. If viscoelasticity had been assumed from the start these analyses would have just taken too long to complete.

Thus the approach presented here represents a compromise: an elastic stress and strain analysis is adopted which represents a straightforward approach for the purposes of development of a metric in order to guide the mine schedule optimization process, but will not account for the time-dependent deformation aspects which are thought to be important. Time stamps allocated to events corresponding to the excavation processes (blasting) permit the conversion of the sequence of elastic stress and elastic strain measurements into a time tabled, time series of stress fields. Time-dependent deformation responses are superimposed on the time series of elastic stress fields, and re-profiled with curve gradients related to a viscous parameter, characteristic of

rock. Stability metrics of the elastic and viscoelastic strain time series are calculated for every grid point within the domain of interest around the mining activities to be scheduled.

Various instability metrics have been developed on the basis that their requirement is that they should be capable of discriminating between different schedules on a geotechnical basis. As the work considers stress and strain tensors at every grid point within the domain at every step of sequence of excavation, applying in each of ‘n!’ schedules, where n is the number of mining activities, the nature of this part of the work can be clearly recognized as analysis and interpretation of ‘big data’. This work further considered 12 instability indicators.

1.7 Content of the thesis

Chapter 1 has introduced the topic of underground mine scheduling and explained methodologies adopted to optimize underground mining schedules. Section 1.3 of Chapter 1 has briefly reviewed the schedule optimization process considered in this work, the Schedule Optimization Tool (SOT); and its extension to a new mine plan optimization tool called SOT+.

Chapter 2 demonstrates how changes in sequence and timetable of a mining schedule may affect the stability of the surrounding rock mass, irrespective of whether time-dependent rock behaviour is presumed. It also presents and reviews evidence clearly showing significant time-dependent behaviour of rocks and rock masses observed, based on field and laboratory data – especially for ‘hard’ rocks. The potentially counterintuitive observation that rocks should be *a priori* presumed to exhibit viscoelastic behaviour rather than elastic behaviour arises from scrutiny of this evidence. Literature searches reveal a lack of support for this presumption in contemporary publications, but nevertheless, the work is guided by the data and concludes that time-dependency must be taken into consideration when optimizing for the safest mine schedule.

Chapter 3 discusses different forms of time-dependent rock responses, and categorizes choices for viscoelastic constitutive models. After introducing the different viscoelastic models and different methods of defining their parameter values, section 3.3 of this Chapter debates the best choice of viscoelastic model.

After the main review chapters, Chapter 4 presents the main hypothesis and research questions that have arisen in the course of the work. It is believed that there is a fundamental time-dependent aspect of rock mass behaviour that needs to be considered when studying rock stability, specially for scheduling. The key question that arises is whether there is a possible choice of activity sequencing and activity durations that can lead to the maximum stability of the rock mass during mining.

Chapter 5 details the methodology followed for development of stability metrics in a step-by-step fashion, where the methodology aims to manage the processes in a time and computationally efficient manner.

Application of the proposed methodology to a case study is described in Chapter 6, and in the section 6.3 some possible choices for (in)stability metrics are introduced and compared to each other.

Chapter 7 outlines a possible methodology to extend the analysis when stope backfill is scheduled in the stoping sequence.

Chapter 8 summarizes the contributions of this research and provides suggestions for future work.

2 A review of time-dependent rock response data

2.1 Analysis of elastic rock responses to differing stoping schedules

In this chapter, elastic stress analyses are conducted to demonstrate: i) how the sequence and interval of stoping events (blasts) can alter stress fields in the rock mass, and ii) how manipulations of sequence and interval can lead to avoidance of instability conditions at defined locations. Phase2 Software (available from Rocscience Inc) is used for stress field computations that illustrate these ideas. Appendix 1 presents computed principal stress fields around three phased excavations of different shape: square, circle, diamond, for two different sequences of excavations. The two sequences are, sequence 1: square (first), circle (second), diamond (third) and sequence 2: square (first), diamond (second), and circle (third). Field stresses are $\sigma_1 = 100$ MPa vertically and $\sigma_3 = 50$ MPa horizontally. The effect of the sequences of excavation assessed by ‘monitoring’ the instantaneous changes in the stress field at specific points, as each excavation is created in turn. Figure 2-1 presents a schematic profile of the ‘monitored’ stress field at one specific point in the rock mass as each excavation is created.

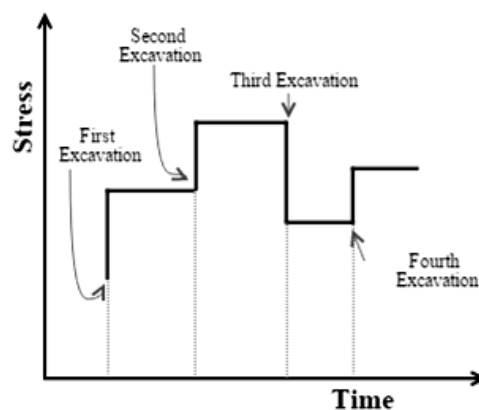


Figure 2-1: Schematic stress time series in a sequence of excavations.

For elastic media, excavation events create step changes in the stress-time profile for a given point, as suddenly excavated openings lead to sudden redistribution of stress. Due to this instantaneous response of an elastic medium, real time between excavations in the ‘time series’ of Figure 2-1 must be introduced externally. Without introduction of such time labels, the profile simply remains a sequence of stress and a sequence of strain values dictated by the order of excavations alone. Such a representation of the changes in stress and the changes in strain remains sufficient for a complete description of the evaluation of the stress field around the excavations, providing the rock remains elastic. If the rock is not, or does not remain, elastic, then the time labels introduced for the scheduling of the blasts take on much greater meaning and significance, as will be shown later in this chapter. For now, and initially, the discussion retains the ideal that the rock behaviour remains elastic only, in order to illustrate the effect of the order of mining activities on stability.

Table 2-1: Results for deviatoric stress (σ_d) arising from Phase2 analysis, at points A to G in two different sequences of excavation. Sequence 1: square (first), circle (second), diamond (third) and Sequence 2: square (first), diamond (second), circle (third). Principal stress fields are illustrated in Appendix 1, Stress is measured in MPa, and field stresses are $\sigma_1 = 100$ MPa and $\sigma_3 = 50$ MPa. $K = 0.5$.

			A(7,15)	B(21,19)	C(21,8)	D(15,2)	E(6,9)	F(1,1)	G(-5,20)
Sequence 1	Square	σ_d	76.67	52	52	53.67	79.33	35	55.33
	Circle	σ_d	59	59	62	93	132	48	59
	Diamond	σ_d	69.42	106.42	74.08	74.08	159.5	48.67	64.83
Sequence 2	Square	σ_d	76.67	52	52	53.67	79.33	35	55.33
	Diamond	σ_d	88	109.67	74.67	26.33	113.33	38	61.33
	Circle	σ_d	69.42	106.42	74.08	74.08	159.5	48.67	64.83

Table 2-1 reports deviatoric stress ($\sigma_1 - \sigma_3$) at seven points in the rock mass, A to G, marked as presented in Figure 2-2. Deviatoric stress is computed for each timetabled phase, to study the likelihood of failure caused by the excavation process deviatoric stress derives instability and deformation. Figure 2-2 presents the maximum principal stress distribution after excavation of the circular opening in sequence 1 (Table 2-1). The values of σ_1 are labeled at each of the points, A to G.

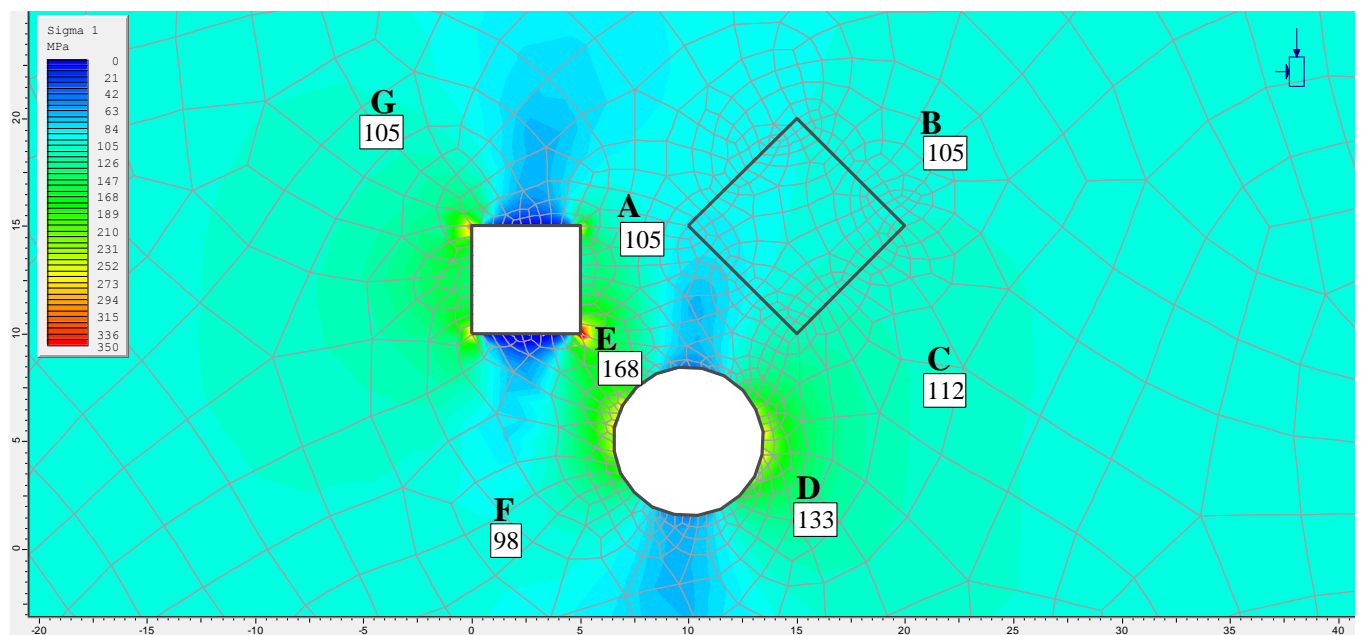


Figure 2-2: σ_1 (maximum principal stress) distribution after excavation of circular opening in sequence 1: square (first), circle (second), diamond (third). $K=0.5$.

In sequence 1, after excavating the square shaped opening, σ_1 (maximum principal stress) and σ_3 (minimum principal stress) at point D (15, 2) are approximately equal to 100 MPa and 50 MPa (Appendix 1). This suggests that the excavation has no effect on the state of stress at point D, as it lies outside the zone of influence of the square excavation. When the circular opening is excavated (assumed to be timetabled at the beginning of week 3), the state of stress at point D is changed, and it changes again in week 6 when the diamond shaped opening is excavated.

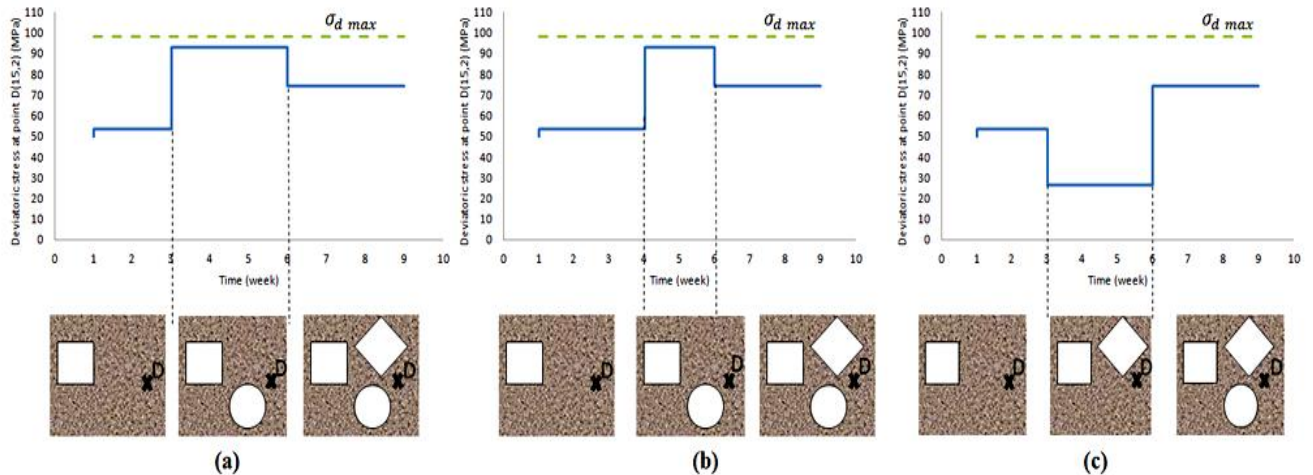


Figure 2-3: Deviatoric stress ($\sigma_d = \sigma_1 - \sigma_3$) at point D in the process of excavating new openings ($\times 100$).

The time series of deviatoric stress at point D is presented in Figure 2-3 for both sequences. Most importantly, it demonstrates that as new openings are excavated, deviatoric stress can reduce as well as increase at a given point, as new excavations are introduced. A notional (for elasticity only is assumed) strength for the medium is illustrated as a dotted line in Figure 2-3. The conventional interpretation is that if the deviatoric stress exceeds this threshold, the risk of instability at point D is high.

Figure 2-3a shows time series of deviatoric stress at point D for sequence 1. In Figure 2-3b, consideration is given to the effect of varying the duration between excavation events. Again, all excavations are assumed to be suddenly made to yield an instantaneous elastic deformation response as this is determined by the same elastic stress analysis as before. Figure 2-3b shows the circular opening excavated at week 4 (rather than week 3, as before) and the diamond opening excavated at week 5 (rather than week 6, as before). Nothing has changed significantly between Figure 2-3a and Figure 2-3b; the risk of failure is still the same, but this risk arises at a different time and for a different duration.

Figure 2-3c shows the deviatoric stress history at point D considering a different sequence of excavations (square, diamond, and then circle for Table 2-1). The deviatoric stress curve does not come close to the dashed green line, suggesting that the risk of instability is significantly reduced. Note also that the state at the start of the sequence and the end of the sequence are the same between Figure 2-3a and Figure 2-3c; elasticity requires that the end stress state must be the same, but clearly the loading path, hence the risk of failure is different.

Although analyzing stress change based on an elastic model is simplistic, the insight from the result is clearly very important for mining scheduling purposes. It showed that even if the rock is assumed to behave elastically only, the effect of a change in sequence and duration between stoping events (blasts) on the risk of instability is not negligible. Although the case analyzed in Phase2 to illustrate this finding has been arbitrarily defined, this finding is general and conceptually provides the central motivation for the work conducted and reported in this thesis.

If the timetable of stoping events is altered, the induced stresses at any given time during the excavation history will be altered too, and this means that rock mass deformation will depend on the specific schedule of stoping events.

Depending on the rock and ore constitutive behaviour, excavation-induced perturbations can take time to reach new equilibrium, this process can appear as either gradual time-dependent movements or deferred violent failures and rock bursts. In terms of mine safety, clearly it is preferable that deformation occurs in a non-violent fashion. A time-dependent rock response is defined as a continued deformation of the rock mass around an opening, when subjected to a constant stress (Malan, 1999). Considering time-dependent behaviour in rock masses comes to the fore when the principle objective of investigation is to determine timings of events and

activities, as is the case with mine scheduling. There are numerous examples of rock engineering and rock mechanics analysis that simplify the study so that time-dependent response is ignored as overlooked, despite its potential importance as a fundamental part of rock and rock mass behaviour and an important basis for explaining and predicting long-term stability of rock masses. The remaining part of this chapter reports on a literature review revealing the importance of consideration of time-dependent rock responses in mine scheduling.

2.2 Time-dependent rock response data from closure measurements

To avoid possible confusion, the two words ‘time-dependency’ and ‘creep’ are being defined in advance. According to Malan (1999), creep refers to continued deformation due to the constant applied stress and will be used exclusively to refer to the behaviour of laboratory-sized specimens containing no large-scale discontinuities. Time-dependency is more general and refers to large-scale openings and structures.

Even though the study of time-dependency has been assigned low importance in hard rock mining, there are several examples of closure data collected in hard rock underground mines, reviewed in the following, which indicate the importance of time-dependent behaviour of rock in deep mine environments.

Rock mechanics researchers working on South African gold mines have recognized the importance of time-dependent rock responses since the early fifties. Closure measurements demonstrated information about time responses of rock masses to perturbations induced by excavation, however sometimes they found it difficult to interpret the behaviour due to adherence of traditional methods for measuring closure (Malan, 1999). Typically, closure measurements were recorded with 24 hour to weeklong intervals between successive data points,

which led to large portions of closure data being missed. Nevertheless significant time-dependent deformation responses were noted and these have been isolated from excavation advance of nearby openings. As reported by Malan (1999): Roux and Denkhaus (1954) stated that time-dependent deformations of rock mass have significant effect on stability of the rock. Analysis done by Hodgson (1967) on closure data from East Rand Proprietary mines showed significant time-dependent closure behaviour which was explained as the result of migration of the fracture zone ahead of the excavation face. Adams and Jager (1980) studied fracture zone growth in progressive stoping activity and observed that postponing the advance of the stope face for two weeks could avoid the creation of new fractures. King *et al.* (1989) measured closure behaviour in a panel at Hartebeestfontein Mine. When blasting activity stopped in the panel (but probably continued in nearby panels, there is no report of this), the closure rate continued at a constant rate of 6 mm/day for 37 days. Only after this period did the rate gradually start to decrease. Gurtunca (1989) reported on the effect of backfill, based on the collected data from different panels in the Klerksdorp area, each of which exhibited varying closure rates, but as high as 30 mm/day. All mentioned examples clearly suggest a time-dependent response. What these causes have in common is that they are each in known high stress environments, that is, at great depth, and with appreciable stress concentration due to excavation geometry.

Malan's (1999) work presented continuous closure data collected from stopes of the Ventersdorp Contact Reef and the Vaal Reefs from South African gold mines, which showed significant time-dependent rock deformation responses and produced information for diagnosis of stress conditions leading to face bursting. The continuous closure data typically illustrated an instantaneous response at blasting time followed by a primary closure phase lasting approximately four or five hours and then a steady-state closure phase. The same pattern was

repeated after each blast and after induced mine seismic events; an example of such response is presented in Figure 2-4.

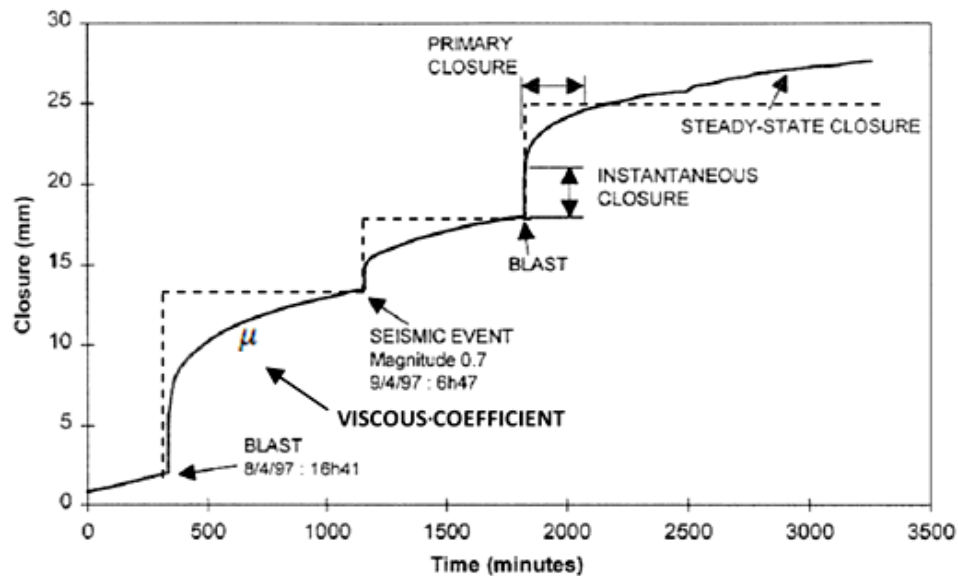


Figure 2-4: Typical time-dependent stope closure of the Ventersdorp Contact Reef at Western Deep Levels mine (now Mponeng mine) (Malan, 1999). This was for a closure station at a distance of 8.7 m from the face. Dashed lines have added by this author to emphasize differences between expected elastic only and viscoelastic deformation responses.

As later explained by Malan (2003), the rate of mining activities that is, the schedule of mining activities, that was largely ignored previously, was found to be an important factor in time-dependent deformation responses of rock mass around those deep, tabular-shaped excavations. After a study on the effect of mining rate on the total amount of steady-state closure at a particular point in the stope (an analogue to secondary creep behaviour as measured in the laboratory), it was concluded that the rate of steady state closure decreased as the number of blasts increased per week (presented in Figure 2-5). The increase in blasting activities corresponds to an acceleration of the mine schedule. This study did not consider the effect of mining rate on the instantaneous and primary closure phases.

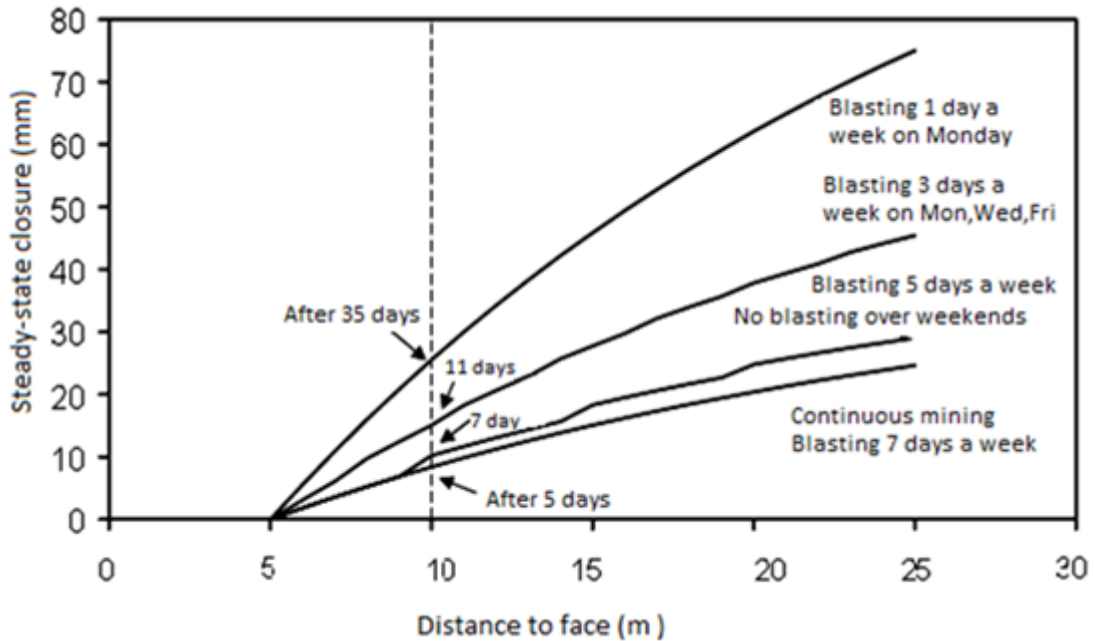


Figure 2-5: The effect of mining rate on the total amount of steady-state closure at a particular point in the stope (Malan, 2003).

Malan (2003) also reported that total rate of closure at the same point in the stope for a face advance of 5 meters with continuous mining (7 days a week) is 8.4 mm. He added that if the 5-meter face advance occurs with the rate of 5 days a week, mining time-dependent closure would be 10.2 mm. In addition, if blasting occurs 3 days a week, mining time-dependent closure would be 15.1 mm, and if there was 1 blast a week, mining time dependent-closure would be 25.5 mm. Malan (2003) defined the term ‘closure ratio’ as “*the ratio of the instantaneous blast closure to total closure following a blast.*” It can be concluded that for these cases, reducing the duration between two blasts can lead to lower values of closure ratio.

Researches on the deformation within South African gold mines also recognized the importance of different geotechnical conditions on closure profiles. Figure 2-6 presents 3 days of closure data from two different mine sites that are approximately of the same depth and measurements are done approximately at the same distance from the face. Closure behaviour of Ventersdorp

Contact Reef (hard lava) shows large instantaneous deformation after blasting followed by a low steady-state closure rate while Vaal Reef shows small instantaneous deformation after blasting followed by a high steady-state closure rate. Malan (2003) also reported that closure measurement at Ventersdorp Contact Reef hanging-wall (soft lava) indicated similar behaviour to Vaal Reef in Figure 2-6. The rate of closure of 0.46 mm/day calculated for Ventersdorp Contact Reef (hard lava) which shows higher risk of face bursting. Closure ratio is 0.04 for Ventersdorp Contact Reef (soft lava) and 0.06 for Vaal Reef. According to Malan and Napier (1999) a lower closure ratio suggests lower risk of violent failures such as strain bursting.

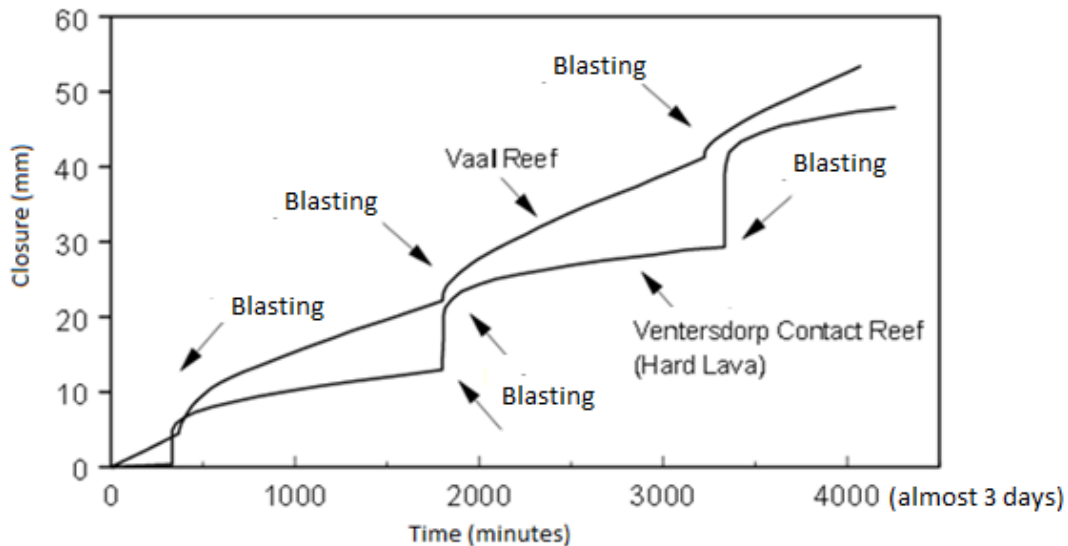


Figure 2-6: An example of closure measurement in different geotechnical conditions (Malan, 2003).

2.3 Rock burst causality may be the time-dependent strength or the time-dependent deformation

The importance of rock mass structure in studies of time-dependent behaviour of rock has been also mentioned by Kaiser and Morgenstern (1981). Their research aimed to develop a rheological model to study time-dependent behaviour of over-stressed hard rocks, specifically within the post-peak strength region of rock mass behaviour, to reveal a “time-dependent failure

process". The fundamental assumption of their work was that there is a connection between time-dependent behaviour of rock mass and the strength of that rock mass. They believed that there can be a long-term strength defined for most rocks below their failure point. Furthermore they argued that post-peak strength varies due to continuing changes in the rock structure as the result of stress redistribution and crack propagation. On these bases, they developed a time-dependent rheological model for time-dependent rock failure. Their results showed a reasonable consistency with laboratory tests.

Malan *et al.* (1997) also explained that after a blast, the existing fractures in the rock mass surrounding stopes would be subjected to an increase in mining induced stress. The fracture zone transfers stress to the more competent rock, which in turn causes formation of new fractures, which presents as a time-dependent process. Time-dependent behaviour of rock is important as it may explain why rock bursts do not always occur at blasting time. Kaiser and Morgenstern (1981) put forward time-dependent strength of rock masses as part of rock burst causality. Malan and his co-workers put forward that is due time-dependent deformation.

2.4 Time-dependent behaviour of hard rocks from laboratory tests

Laboratory creep tests can provide some constructive suggestions for the study of long-term stability of underground excavations. Drescher and Handley (2003) published results of their experiments on two typical types of hard rock at deep level gold mines of South Africa: Ventersdorp Lava and Elsburg Quartzite. They conducted uniaxial creep tests on intact samples of the lava and the quartzite that show similar creep rates occur at significantly different stress levels, Figure 2-7.

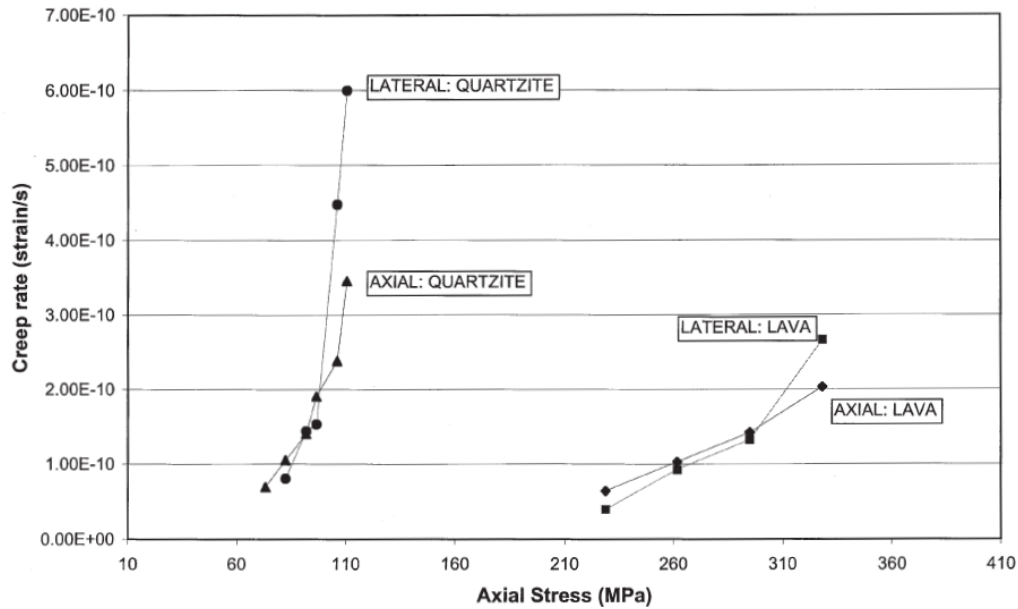


Figure 2-7: Plot of creep rate versus axial stress for quartzite and lava (Drescher and Handley, 2003).

Drescher and Handley interpreted this data with the suggestion that both lava and quartzite would present similar failure mechanisms despite their different structural, geological and physical properties. Figure 2-8 reproduced the results of their triaxial post-failure relaxation tests on both lava and quartzite samples. It shows the amount of stress relaxation in the quartzite being significantly more than that of the lava. The peak strength of lava is higher than that of the quartzite however, and the strain at failure is higher for the lava than that of the quartzite. It was concluded that at depth, lava is more prone to violent rock bursts compared to quartzite. Irrespective of whether this is true or not, it is more independent evidence of time-dependent behaviour of hard rock from laboratory testing if ‘hard’ rocks are subjected to sufficient stress, despite deformations being of a far smaller scale than for ‘soft’ rocks. Drescher and Handley (2003) claimed that first successful triaxial post-failure relaxation test on strong brittle rocks is reported by Malan and Drescher (2000) however, post-failure relaxation tests had been previously reported for softer rocks. Hudson and Brown (1973) conducted uniaxial compression tests and tested the strength of marble samples which are weaker than both quartzite and lava.

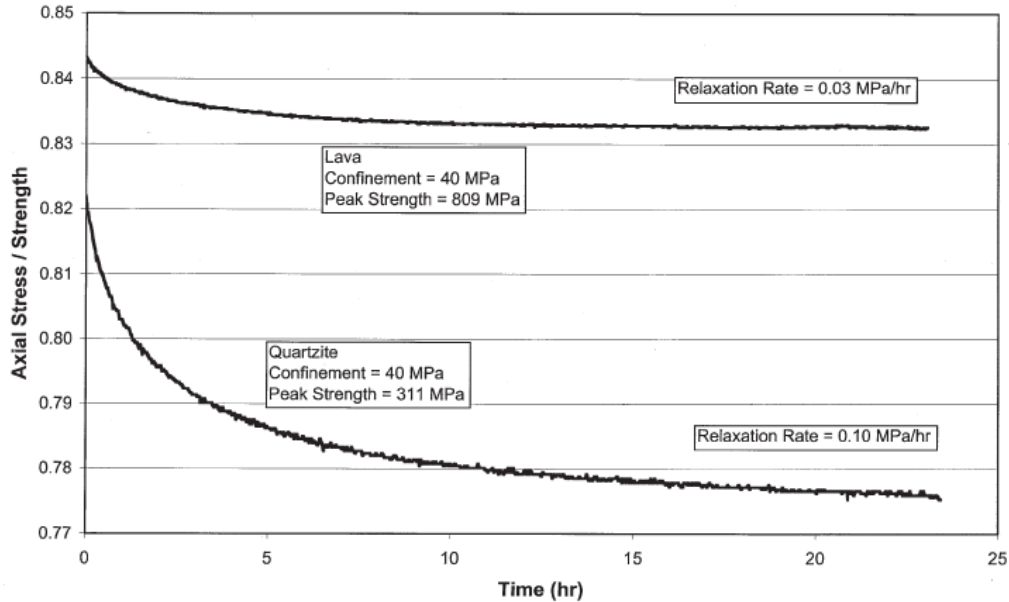


Figure 2-8: Post-failure relaxation curves for quartzite and lava (Drescher and Handley, 2003).

Time-dependent deformation of rock masses at the main access ways of Hartebeestfontein Mine interrupted the mining schedule by causing production delays and lead for further maintenance. This could have been prevented if a more complete understanding of the rock mass deformation was in hand. In an attempt to understand this massive time-dependent deformation of Hartebeestfontein Mine quartzite, Bosman *et al.* (2000) conducted a series of laboratory tests on samples taken from the mine site. The results from uniaxial compression tests (UCS) and Brazilian tensile strength (UTB) tests showed the behaviours of the quartzite samples from hangingwall and samples of the same quartzite from the sidewall of the access tunnel were quite distinct. The average UCS obtained for hangingwall samples was 180 MPa and the average UCS for the samples taken from the sidewall was 167 MPa (for 5 UCS tests on the two sets of samples). The average UTB of the hangingwall samples was 14.5 MPa and 18.5 MPa for the sidewall samples.

It is to be expected that samples of the same rock from different locations around the periphery of an opening have different character, especially in high stress environments: the samples may have suffered different degrees of damage. This was confirmed in the report from Bosman *et al.* (2000): fracture and density observations at the sampling locations led to expectation that the sidewall samples would present significantly lower strength than in laboratory test results, which was the case.

Aside from strength characterization, Figure 2-9 shows results of compression creep tests on similar samples. The steady state creep rate of 4.77×10^{-4} millistrain/hr calculated for the hanging wall samples compared to 7.5×10^{-4} millistrain/hr for the sidewall samples and demonstrated that the samples from the sidewall deformed at a different creep rate (58% greater) than the hanging wall samples. Further shear creep tests on both types of samples showed that the presence of water on the bedding contacts in the rock might increase their deformation rates in the access tunnel. Irrespective of the explanations of causality, the key point is that the above-mentioned laboratory tests are evidence showing that the same rock type can present different behaviour and that this behaviour is time dependent.

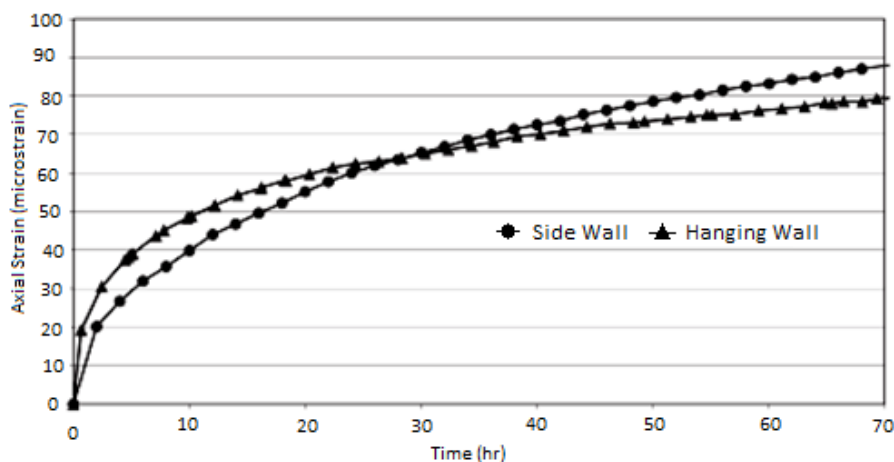


Figure 2-9: Graphs of compression test results on Hartebeestfontein Mine quartzite (Bosman, *et al.*, 2000).

2.5 Time-dependent behaviour of rock in low stress condition

Turning away from deep level, high stress mining environments, we turn to lower stress environments, and consider these in the context of rock classification schemes. According to Eberhardt (2009) the rock mass rating (RMR) scheme devised by Bieniawski between 1972 and 1973, and extended by others (e.g. Barton (2002) and Aksoy (2008)) summarised the empirically observed behaviour of 351 case studies of excavations principally from low stress environments, at very least of generally much lower stress environments than those of previous sections.

Palmstrom (2009) reinforces this ‘low stress’ nature in his observation that the RMR system has “no input parameter for rock stresses but stress up to 25 MPa are included in the estimated RMR value. Thus overstressing (rock bursting and squeezing) is not included.”

From the point of view of this work on mine scheduling, the debate on which parameters to include in the scheme or not, or the contest on how the parameters are to be quantified numerically, or how they should be treated arithmetically, matters very little. The reader is directed to Bieniawski’s original table that assists in interpretation of the rock mass classes of the low stress environment case studies summarized in the scheme. The rock mass classes are articulated in terms of a stand-up time (Figure 2-10).

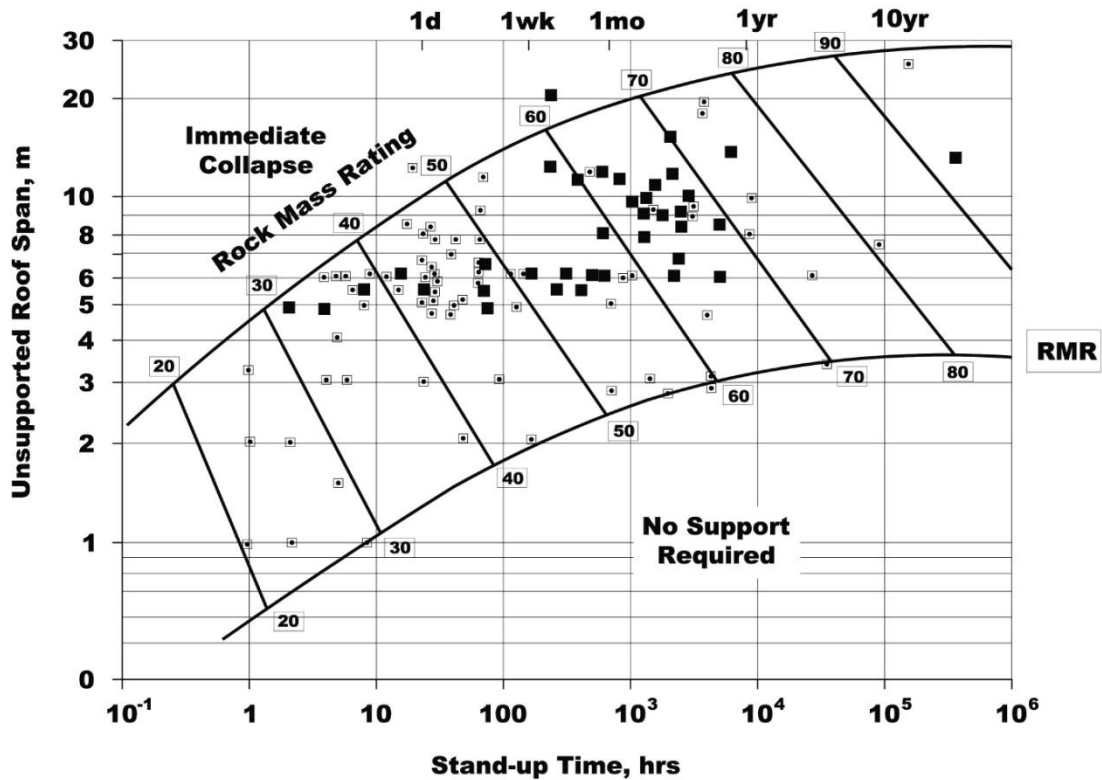


Figure 2-10: Stand-up time for underground excavations after Bieniawski (1989). Black dots are tunnel examples and black squares are shallow underground mine examples.

The indicated time range is between tens of years to minutes, and interpretation is complicated by a co-relation with excavation span, but nevertheless it concretely implies that the 351 case histories summarised, exhibited some manner of time-dependent rock response in that the excavation did not fall down as soon as it was made, it fell down after the stand-up time.

The very notion of a ‘stand-up time’ as used in Bieniawski’s rock mass rating classification (Bieniawski, 1989) thus suggests that there is general, or possibly fundamental, time dependency of excavation behaviour in rock, at these low stresses.

2.6 Consideration of time-dependent responses of rock mass with support

The stand-up time was originally proposed by Lauffer (1958) and its concept is that an increase in the span of the excavation reduces the time available for installing support. The concept has been modified by a number of authors, notably Pacher *et al.* (1974), and now is used referred to in the design and construction of excavations in rock generally and now forms part of the general tunneling approach known as the New Austrian Tunneling Method (Kolymbas, 2005). The NATM essentially generalizes the tactics to adopt for the installation of support in tunnels, as best exemplified in the diagrams and analysis for rock-support interaction presented in Hoek and Brown (1980) (presented in Figure 2-11).

In their development, Hoek and Brown initially explain the approach with reference to elastic behaviour of the rock. In this case, the relation between excavation step and deformation has no latency: there is no fundamental time-dependent behaviour implied. Instead, a type of pseudo-time arises, the pace of which is dictated entirely by the rate of tunnel advance, and hence the frequency with which a progression of stress field perturbations affect the deformation at the tunnel section (or chainage) at which installation of the support is being contemplated. Hence, the pseudo-time can be expressed as ‘distance from the face’. The idea of zero latency extends to the development of the methodology of Hoek and Brown to the situation when the periphery of the tunnel, or part of it, plastifies. Even in this case, there is no implied time-dependent constitutive response of the rock as is the case with the evidence from Bieniawski’s RMR.

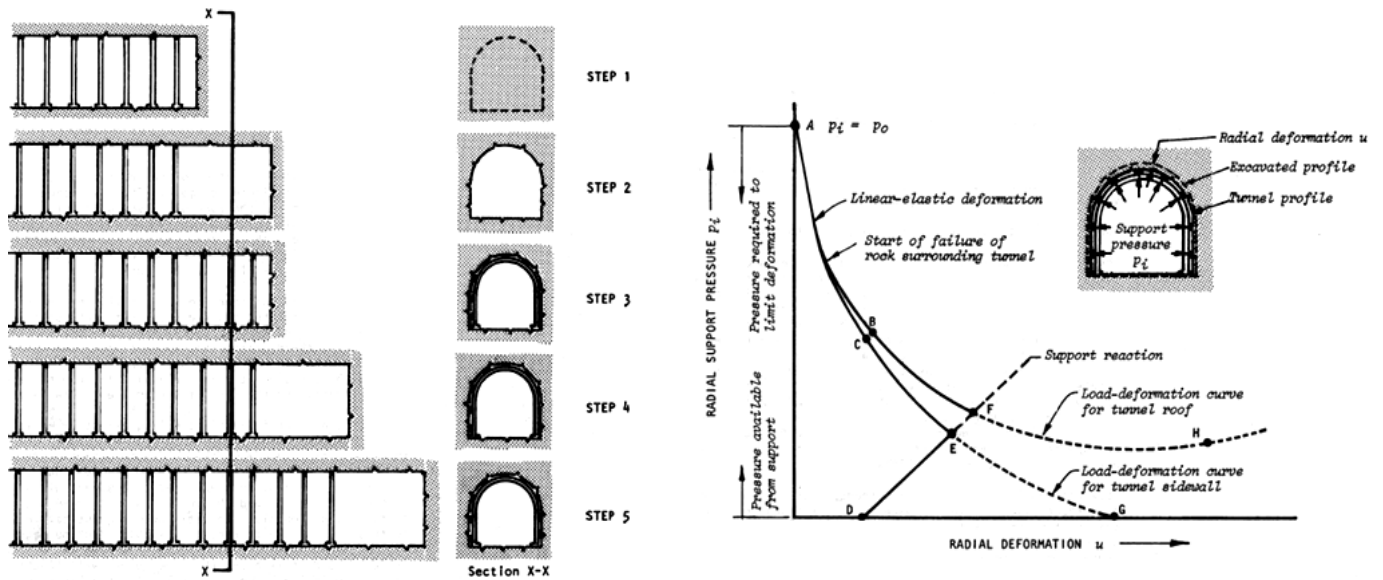


Figure 2-11: An example of a tunnel being advanced with blocked steel sets being installed after each excavation. The load-deformation curves for the rock mass and the support system are given in the right figure from Hoek and Brown (1980)

2.7 Time-dependent rock response observed from seismic data records

Mine seismicity data can also reveal a need to draw upon time-dependent rock behaviour to establish some kind of causality model for rock instabilities. To illustrate this point, Beneteau (2012) presents a magnitude-time chart for seismic events at the Big Bell mine collected over a three year period and this is reproduced in Figure 2-12. The record encompasses a one year period of mine shutdown when no or very little mining activity took place. The rate of seismic event occurrence during the production shutdown is low but, importantly, the mine was clearly still seismically active during this time. Without a model of seismicity causality that includes time-dependent rock constitutive behaviour, it is difficult to explain why these events occurred. When the mine was operational, it is clear from Figure 2-12 that the frequency of events increased and so if a seismicity causality model involving time-dependent behaviour has to be called upon to explain events during the shutdown, it is difficult to reject the same model to explain seismicity during mining operations.

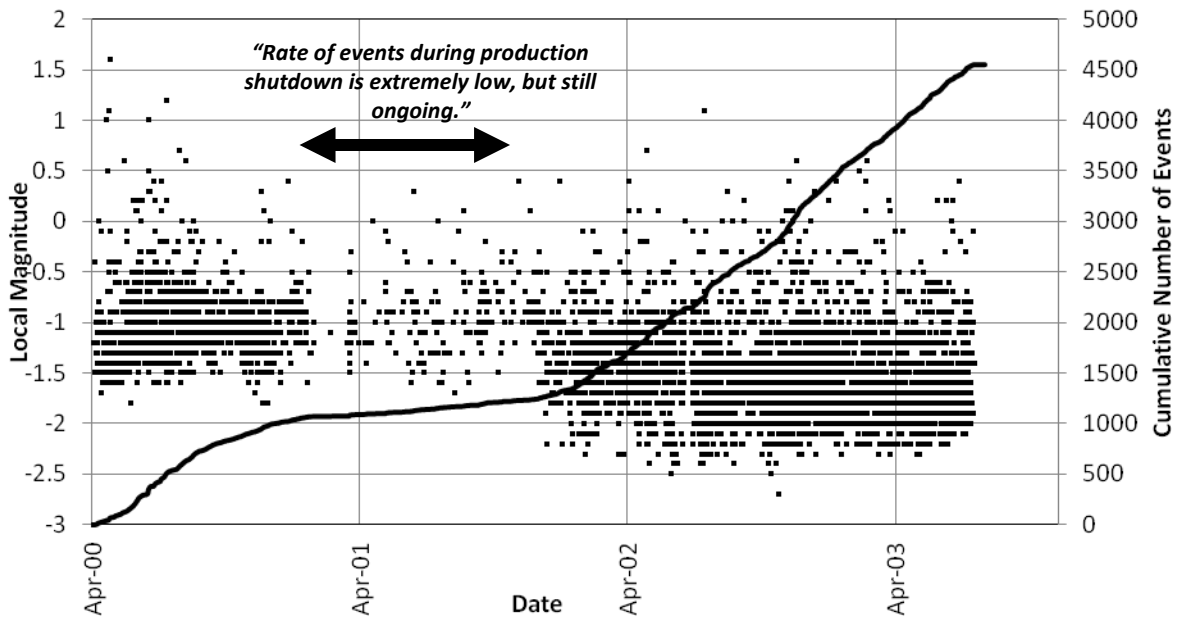


Figure 2-12: Magnitude-time chart for micro-seismic events at Big Bell mine (Beneteau, 2012).

2.8 Time-dependent rock behaviour in laboratory

Laboratory testing is the most frequent method of studying rock mechanical properties however; they do not necessarily reflect the behaviour that may be expected at scales requiring field measurements. Nevertheless, laboratory testing provides a controlled environment to permit measurement of the response of rock to stress induced in a controlled fashion, and is essential for effective mine design. Figure 2-13 is the creep curve for a sample of Barnsley Hards Coal obtained from Terry and Morgans (1958) as reported by Millar and Jiao (1994), plotted at two different scales. Both vertical axes refer to the displacement of the coal sample under constant load. The horizontal axis refers to the time of deformation. The solid line shows deformation on the left axis scale; the dots show the same deformation plotted upon the right axis scale. Clearly in this case, the rock appears to behave elastically over a length scale of 0.5 mm, developing a relatively large, near instantaneous, deformation at $t = 0$, with the displacement appearing to remain constant thereafter, and yielding a stepped profile (reminiscent of a step function; a

castellated appearance would result if followed by an unload stage). However, when the same deformation response is examined on an expanded scale, the time-dependent deformation and viscoelastic response is clearly revealed.

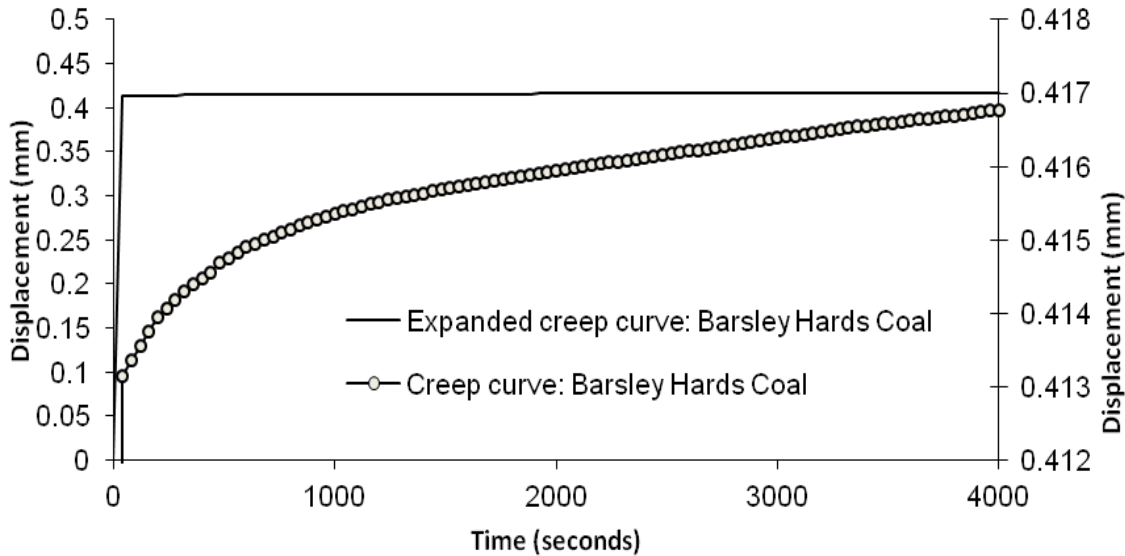


Figure 2-13: Experimental Barnsley Hards Coal creep curve in two different scales (Millar and Jiao, 1994).

2.9 Review of evidence of time-dependent rock response

Consideration of material behaviour is an unavoidable part of any engineering design process as mentioned by Kaiser and Morgenstern (1981). The evidence presented in this chapter clearly suggests that such considerations should extend to the mine scheduling part of mine design as well as the precursor excavation stability analysis part of mine design. This chapter presented abundant evidence of lagged responses of rock and ore masses, to excavation induced perturbation. It is put forward as sufficiently abundant to support the presumption of this work, that time-dependent constitutive behaviour should be considered the norm, rather than the exception, in mine excavation stability analysis.

Section 2.1 has clearly shown that even if analysis is confined to an assumption of purely elastic behaviour, the risk of excavation instability is dependent on the sequence of mine activities. Section 2.2 presented evidence of time-dependent deformation responses of the stopes in deep, high stress mining environments. Whether the underlying causality is related to progressive occurrence of damage to the rock, as suggested in Section 2.3, is of relatively little importance to this work. The overall effect is one that presents as viscoelastic (or viscoelastoplastic) at the mine scale. Section 2.4 presented evidence that the extent of visibility of a viscoelastic response will depend on structural and geological properties of individual rock types, and their environments. Section 2.5 turned away from high stress environments and drew upon evidence from rock mass classification schemes to demonstrate time dependency in low stress environments too. Section 2.6 showed how the analysis associated with the NATM and rock-support interaction may give rise to an apparent time-dependency, but the fact is that the rock mass need not be attributed any viscoelastic character at all, in these cases. Nevertheless they do confirm a dependency of rock instability on excavation sequencing. In contrast, Section 2.7 showed that some manner of time-dependent constitutive character must be invoked to explain seismicity in mines with no stoping or development activity being undertaken. Finally 2.8 showed that a rock may not exhibit viscoelastic deformation response depending on the scale at which these deformations are viewed. Overall the material in this chapter demonstrates unequivocally that time-dependency of rock deformation is ubiquitous. In the specific context of this work, excavation stability is dependent on both the sequence and the duration between stoping events.

3 A review of time-dependent rock deformability models: viscoelastic models

3.1 Introduction

As discussed in Chapter 2, changes in sequence and duration between stoping events (blasts) affect rock mass deformation even when the rock is assumed elastic. This effect would be much more noticeable if time-dependent constitutive behaviour of rock is assumed instead. Janakiraman (1967) highlighted that difficulties involved with design of underground spaces arising from the phenomenon of time-dependent rock response has been a prolonged concern. Time-dependent rock deformability under sustained load e.g. in between two stoping events, has been studied by numerous researchers namely Malan, Hodgson, King, Gurtunca and Kaiser. However, development of a comprehensive universally applicable rheological model for the time-dependent behaviour of the rock and rock masses has yet remained a challenge.

A practical time-dependent rock deformability model requires a comprehensive understanding of rock mass behaviour. The theory of linear viscoelastically provides a useful basis to approach study of time-dependent behaviour of rocks. However, development of this understanding has always been affected by the lack of information on mechanical characterization of the *in situ* rock.

Alfrey (1944) and Lee (1944) obtained a viscoelastic solution from an elastic solution of an elastic problem by replacing the elastic constants with parameters that were varying functions of time (Janakiraman, 1967). In 1961, Emery explained rock relaxation with rheological equations for a Kelvin solid and described the viscoelastic nature of rocks. Berry (1958) followed a similar

logic to study a steady state sinusoidal, forcing function; here again, a constant Young's modulus was substituted by one that was a function of time. These approaches all assumed that the viscoelastic constitutive response of rock was part of the intrinsic character of the rocks. Later Malan (1999) stated that viscoelastically is not suitable in studying time-dependency at the scale of South African gold mine stopes because the apparent time-dependency arises due to a time-dependent failure process associated with closure behaviour of rock masses, not fundamental viscoelastic behaviour. He developed a visco-elastoplastic constitutive model for studying time-dependent behaviour of zones ahead of the stopes. This model has proved to be more successful than viscoelastic models in simulating Ventersdorp Contact Reef closure behaviour with time-dependent behaviour. However, it was not successful in predictions of Hartebeestfontein Mine time-dependent closure, and this was thought to be because of existence of a major discontinuity in the surrounding rock mass (Malan, 1999). This indicates that assumption of some manner of time-dependent constitutive behaviour for rock should not supplant but should augment what is known about discontinuum mechanics in a rock-engineering context, but introduces more complexity.

In the scope of this research for the most profitable and the most geotechnically stable mine schedule, the author believes an assumption of linear viscoelastically is reasonable if the limitations are understood. It seems clear (e.g. Malan (1999), Kaiser and Morgenstern(1980)) that on a constitutive scale, time-dependent responses are somehow associated with the accumulation of damage to the rock or rock mass, but nevertheless on an engineering scale the response can be observed to be viscoelastic. In addition, an assumption of viscoelastically is unable to characterize failure or tertiary creep, so viscoelastically will always remain an approximation – but potentially a useful one. It remains a valuable tool in studying long-term

behaviour of rock masses at engineering scales because of its relative simplicity and because superposition principles remain valid. Mine schedules may involve excavation of hundreds of stopes such that an approach aiming to explicitly and completely model time-dependent behaviour of complete sequences, and the durations between these excavation activities, may be intensely impractical. So approximations may represent a useful step forward. This idea will be expanded upon later in Chapter 5, but for now, the discussion is focused on viscoelastic models.

3.2 Viscoelastic behaviours

The word “viscoelastic” means the simultaneous existence of viscous and elastic behaviour. The elastic behaviour is characterized by properties related to the Young’s modulus and the Poisson’s ratio of a purely elastic material. Viscous behaviour is characterized by the presence of ore or rock mass viscous parameters. Viscoelastic strain is associated with creep phenomenon. Generally, creep refers to the continuous deformation of a material under constant load or stress (Malan, 1999). In mine stoping, this behaviour can generally be observed with convergence measurements in between a blast and the next blast or the next seismic event, when the rock mass continues to deform with time until rupture, or yielding, or closure. Such behaviour is illustrated in Figure 3-1 with an idealized creep curve. The primary region is the early stage of deformation when time-dependent behaviour or the creep rate, decreases rapidly with time. Then it reaches a steady state condition of constant velocity, which is called the secondary creep stage and is followed by an accelerating phase (tertiary stage) which ends up with failure. If the sustained stress is released before the rupture occurs, an immediate elastic recovery equal to any initial elastic deformation results, followed by a period of slow recovery. The amount of the deformation recovery depends on length of time, the amount of stress applied, and this idea is illustrated in Figure 3-2.

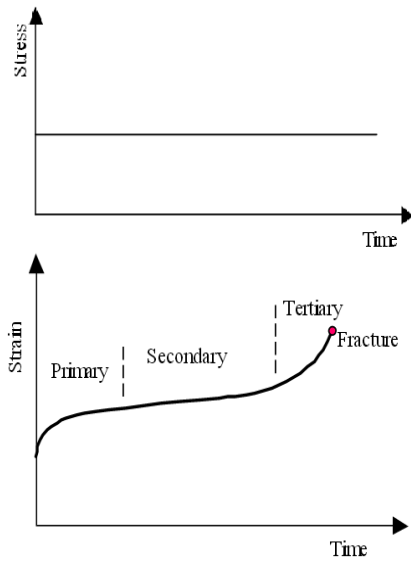


Figure 3-1: Creep curve under constant load (Chunhui, 2000)

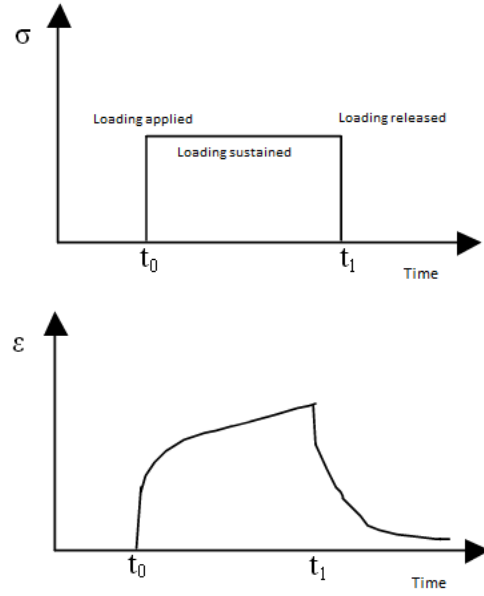


Figure 3-2: Creep curve with recovery.

Based on the statement by Barnes *et al.* (1989) who say: “*behaviour of a material depends on the time-scale of the experiment in relation to a natural time of the material*”; it is a little less unreasonable to assume that rock mass behaves viscoelastically, as it is to assume it behaves elastically. If the duration between stoping activities is long then rock mass will be more likely to appear viscous rather than elastic, where time is irrelevant, whereas if stoping activities occur quickly, rock mass would be more likely to appear to behave elastically rather than viscoelastically. Figure 2-13 showed that it is possible to consider either in the same response, depending on the scale of deformations of interest. So for, a general time scale, it can be argued that viscoelastic response is observed.

As explained in Chapter 2 there are some instances that laboratory tests reporting creep rate of an intact rock sample do not explain any symptoms of the large time-dependent deformations that are observed underground (e.g. Ventersdorp Contact Reef and Vaal Reef in South Africa (Malan and Napier, 1999)). It appears that the presence of rock mass structures and discontinuities can also lead to apparent viscoelastically. Expansion of fracture zones around stopes in progression

of excavations is mainly concluded based on the incremental number of microseismic events observed after each blast. Malan (1999) states that any model developed for simulation of time-dependent behaviour of the rock mass around deep underground hard rock excavations preferably should consider the fracture zone developed around excavations. This approach is achievable using rheological models that include a fuse in their mechanical scheme for example Bingham rheological model, Figure 3-3.

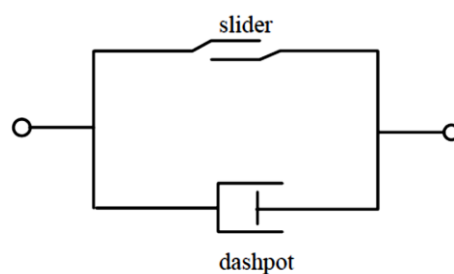


Figure 3-3: The Bingham rheological model from Malan (1999).

3.3 Choices of viscoelastic models

Irrespective of the cause of apparent viscoelasticity, the viscoelastic behaviour of rock can be modeled with a multiplicity of candidate rheological models conceptually deemed to comprise numbers of springs and dashpots; with the spring representing elastic deformation and the dashpot representing viscous deformation (Table 3-1). Some models simulate time-dependent behaviour of rock up to the failure point and some others simulate asymptotic responses to a definite value of strain. Irrespective of type, each spring/dashpot/fuse arrangement corresponds to an equation of a given form, a so-called constitutive model. These are functions fitted to data from creep tests and field measurements by adjusting values of parameters in the model. Constitutive models fall in to two broad categories as suggested by International Society of Rock Mechanics (ISRM) (Ayden, *et al.*, 2013): rheological models indicated in Table 3-1, and so-called ‘intuitive’ models indicated in Table 3-2.

Table 3-1: Rheological models for unidimensional constitutive modeling. E is elastic module and η is viscosity module. Suffixes “h,” “k,” and “m” indicate module of Hooke, Kelvin, and Maxwell units (Ayden, *et al.*, 2013).

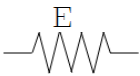
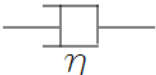
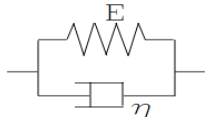
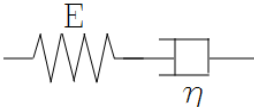
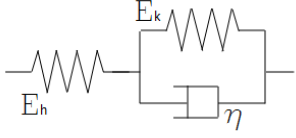
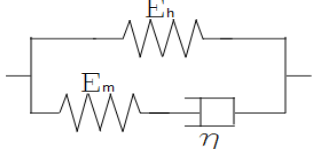
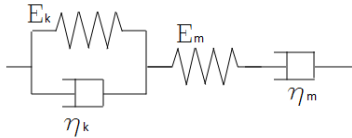
Model	Formula	Mechanical illustration
Hooke	$\varepsilon = \frac{\sigma}{E}$	
Newton	$\dot{\varepsilon} = \frac{\sigma}{\eta}$	
Kelvin-Voigt	$\varepsilon = \frac{\sigma}{E} \left(1 - e^{-t/t_T}\right); t_T = \frac{E}{\eta}$	
Maxwell	$\varepsilon = \frac{\sigma}{E} + \frac{\sigma}{\eta} t$	
Generalized Kelvin-Voigt	$\varepsilon = \frac{\sigma}{E_h} + \frac{\sigma}{E_k} \left(1 - e^{-t/t_T}\right); t_T = \frac{\eta}{E_k}$	 Hookean Kelvin-Voigt
Hill-Maxwell	$\varepsilon = \frac{\sigma}{E_h} \left[1 - \frac{E_m}{E_h + E_m} e^{-t/t_T}\right]; t_T = \frac{\eta}{E_k}$	
Burgers	$\varepsilon = \frac{\sigma}{E_m} + \frac{\sigma}{E_k} \left(1 - e^{-t/t_T}\right) + \frac{\sigma}{\eta_m} t; t_T = \frac{\eta_k}{E_k}$	 Kelvin-Voigt Maxwell

Table 3-2: Intuitive unidimensional creep models (except for (Ayden, *et al.*, 2003) the references to the citations in this table can be found in (Farmer, 1983)).

Proposed by	Formula	Comments
Andrade (1910,1914)	$\varepsilon = Bt^{1/\beta}$	Applicable to primary stage; $\beta = 3$;
Lomnitz (1956,1957)	$\varepsilon = A \ln(1 + \alpha t)$	Applicable to primary stage
Modified Lomnitz law	$\varepsilon = A + B \log(t) + Ct$	Primary and secondary stages
Norton's law	$\varepsilon = A\sigma^n t$ or $\varepsilon = A\sigma^n$	Applicable to secondary stage and n=4-5
Modified Norton's law	$\varepsilon = B \left\langle \frac{\sigma}{\sigma_{ct}} - 1 \right\rangle^n t$ or $\varepsilon = B \left\langle \frac{\sigma}{\sigma_{ct}} - 1 \right\rangle^n$	Applicable to secondary stage and σ_{ct} is the stress threshold to induce steady state creep response.
Griggs and Coles (1958)	$\varepsilon = A + Bt^2$	Applicable to tertiary stage
Ayden <i>et al.</i> (2003)	$\varepsilon = A \left(1 - e^{-t/t_r}\right) + B \left(e^{-t/t_r} - 1\right)$	Applicable to all stages creep leading to failure

Ayden *et al.* (2013) published three graphs (Figure 3-4) comparing experimental rock responses with models introduced in Table 3-1 and Table 3-2 and noted that any of the models can be adopted depending on the purpose of the user. The current author concurs with this notion, from first hand experience: Appendix 2 shows that various viscoelastic models fitted equally well (or equally poorly) to series of field measurements and laboratory experimental observations taken from literature.

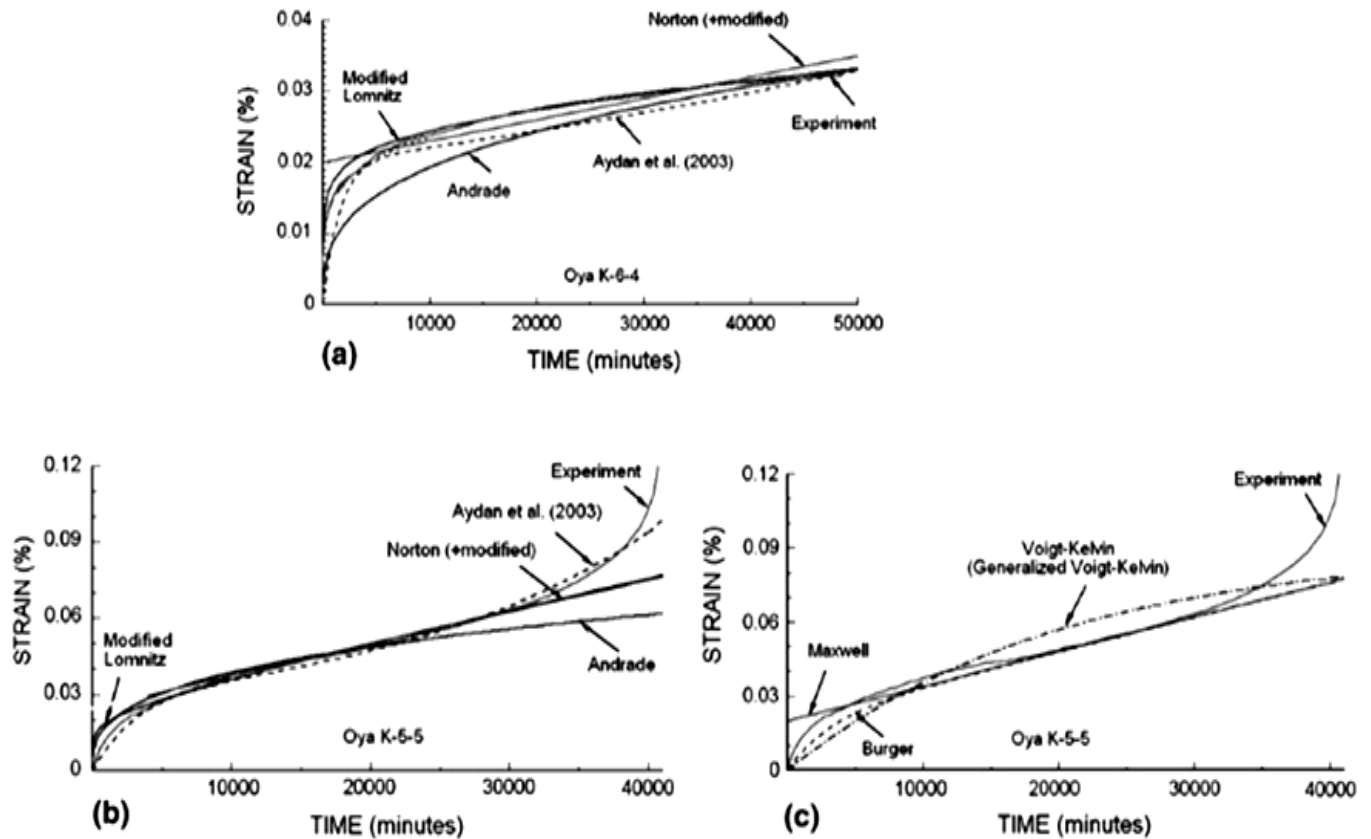


Figure 3-4: Comparison of intuitive and rheological models with experimental responses: a) asymptotic response (intuitive models), b) response terminating with failure (intuitive models), and c) response terminating with failure (rheological models) (Ayden, *et al.*, 2013).

All the models presented in Table 3-1 and Table 3-2 involve uniaxial loading conditions. However, Fafard *et al.* (2001) extended this approach for three-dimensional cases where time-dependent response of rock would be reported as a viscoelastic strain tensor series. The objective of their methodology was to develop a consistent three-dimensional viscoelastic model, compatible with the classical solid mechanics equations. Picard (2007) applied this model to carbon cathode solid materials. The viscoelastic behaviour of the carbon materials was simulated using a Generalized Kelvin-Voigt rheological model and the mechanical illustration of this model is presented in Figure 3-5.

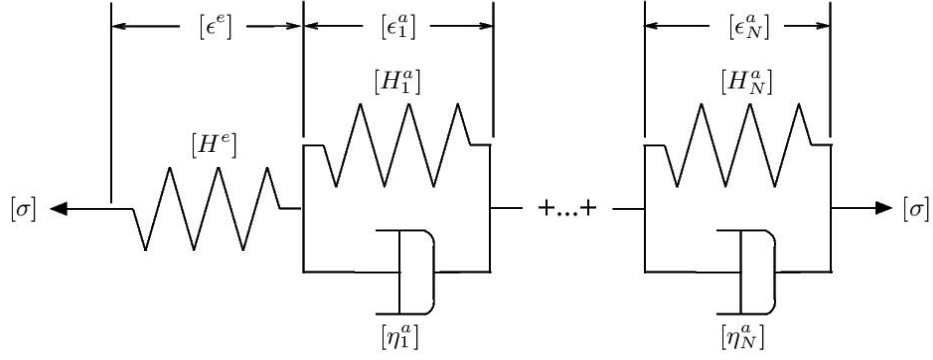


Figure 3-5: Diagram of the three-dimensional viscoelastic rheological model (Picard, 2007).

Picard (2007) calculated total strain with this proposed 3D rheological model under sustained load. The mathematical formulation of this model is as in Equation 3-1.

$$\{\varepsilon\} = [H^e]^{-1}\{\sigma\} + [X] \sum_{\alpha=1}^N \left\{ \begin{array}{c} F_{\alpha 1} \int_0^t e^{-\lambda_{\alpha 1}(t-\tau)} d\tau \\ \vdots \\ F_{\alpha 6} \int_0^t e^{-\lambda_{\alpha 6}(t-\tau)} d\tau \end{array} \right\} \quad [3-1]$$

where $[H^e]$ is defined with Hooke's law and parameters of Young modulus and the Poisson's ratio, $\{\sigma\}$ is the constant stress tensor, $[X]$ contain eigenvectors and λ_{α} s are eigenvalues for the system, N is number of Kelvin-Voigt components in the model and $\{F_{\alpha}\}$ is tensor of constants, t is time and τ is the duration of applying the constant load.

If this model is applied for an isotopic, homogenous material there would be just one time-dependent component placed in the model ($N=1$) and Equation 3-1 leads to Equation 3-2.

$$\{\varepsilon\} = [H^e]^{-1}\{\sigma\} + [X] \left\{ \begin{array}{c} F_1 \int_0^t e^{-\lambda_1(t-\tau)} d\tau \\ \vdots \\ F_6 \int_0^t e^{-\lambda_6(t-\tau)} d\tau \end{array} \right\} \quad [3-2]$$

where

$$[X] = \begin{bmatrix} 1 & -1 & -1 & 0 & 0 & 0 \\ 1 & 1 & 0 & 0 & 0 & 0 \\ 1 & 0 & 1 & 0 & 0 & 0 \\ 0 & 0 & 0 & 1 & 0 & 0 \\ 0 & 0 & 0 & 0 & 1 & 0 \\ 0 & 0 & 0 & 0 & 0 & 1 \end{bmatrix} \quad [3-3], \quad \lambda_1 = \dots = \lambda_6 = \frac{E_{H\alpha}^a \text{ (MPa)}}{E_{\eta\alpha}^a \text{ (MPa.S)}} \quad [3-4],$$

$$\{F\} = [X]^{-1}[\eta]^{-1}\{\sigma\} = \left\{ \begin{array}{l} -\frac{(2\nu-1)\sigma_1+(2\nu-1)\sigma_2+(2\nu-1)\sigma_3}{3E_{\eta\alpha}^a} \\ -\frac{(\nu+1)\sigma_1-2(\nu+1)\sigma_2+(\nu+1)\sigma_3}{3E_{\eta\alpha}^a} \\ -\frac{(\nu+1)\sigma_1+(\nu+1)\sigma_2-2(\nu+1)\sigma_3}{3E_{\eta\alpha}^a} \\ \frac{2(\nu+1)\tau_{12}}{E_{\eta\alpha}^a} \\ \frac{2(\nu+1)\tau_{13}}{E_{\eta\alpha}^a} \\ \frac{2(\nu+1)\tau_{23}}{E_{\eta\alpha}^a} \end{array} \right\} = \frac{1}{\text{MPa.S}} \quad [3-5].$$

$E_{\eta\alpha}^a$ is a viscous coefficient of the dashpot, $E_{H\alpha}^a$ is the stiffness of the spring and $\{F\}$ is a tensor defined based on the sustained stress tensor, Poisson's ratio and the viscous coefficient of the Kelvin-Voigt spring. For further details on calculation of these equations, see Fafard *et al.* (2001) and Picard (2007).

In contrast to the previously mentioned unidimensional rheological models (Table 3-1 and Table 3-2), the proposed 3D rheological model is expected to entirely recover strain if the sustained stress is removed. Picard (2007) calculated total strain with this proposed 3D rheological model under sustained load. The mathematical formulation of this model is as in Equation 3-2.

3.4 Methods of measuring viscous coefficient

3.4.1 Static methods vs. dynamic methods

The viscous coefficient is a key parameter in time-dependent deformation studies of rock mass behaviour. However, its value is not definite yet, even though there are multiple methodologies available to define it. These methodologies generally have two categories: static methods of determination and dynamic methods. The static methods are creep tests at constant stress, which is considered, applied instantaneously – as is broadly the case in a rock mass upon excavation after each blast. In practice, this assumption holds when the time required for input load to reach its steady value is infinitesimal relative to the duration that deformation is recorded. Most blasts are complete over milliseconds to seconds' time scales (observation periods are of the order of hours or days). The dynamic methods introduced varying stress as in compression/rarefaction of wave propagation and steady flow methods (Barnes, *et al.*, 1989). The static methods appear to be better suited to study time-dependent behaviour of rock in sequences of stopping activities (blasts). The dynamic methods appear better suited to studies of earthquakes and for micro- or mine seismicity.

3.4.2 Laboratory determinations

The most commonly used methodology for defining viscous coefficient in the rock mass is the laboratory creep test (Ulusay, 2014). As previously mentioned in Chapter 2, many researchers have undertaken series of laboratory creep experiments to determine values of viscosity, to inform simulations of the time-dependent behaviour of rock masses during the life of a mine. Creep parameters were back analyzed from laboratory test data using a time-dependent model. As reported by Janakiraman (1967), average values of viscous coefficient in Pa.s calculated from

series of monotonic creep tests range from 10^{14} to 10^{16} for halite, 10^{15} to 10^{16} for coal and 10^{21} for limestone. Back analysis were based on the theory of linear viscoelastically but it is not specified which viscoelastic model is conducted to back analyze creep tests results. He also reported 10^7 to 10^8 Pa.s viscosity for quartzite, granodiorite and argillite samples from forced vibration tests. Janakiraman (1967) suggested the modified Burger's model presented by Hardy (1959) as suitable for back analysis of force vibration test results, however, he did not mention if viscosity for quartzite, granodiorite and argillite were calculated using this model. Kumagai *et al.* (1978) conducted creep tests by bending two large beams of granite of a size of 215 cm × 12.3 cm × 6.8 cm. He reported $3 - 6 \times 10^{19}$ MPa.s after studying the general trend of the creep. The creep test measured granite sample behaviour for 20 years and it was reported that for the last ten years creep rate did not change. Kumagai *et al.* (1978) concluded that granite can present a viscous flow, and irrecoverable continuous steady deformation.

3.4.3 Analysis of flow structures

Another methodology to evaluate viscous coefficient of rock is through studying the structural geology of the rock mass to identify 'frozen in' flow behaviour, indicative of viscoelastic response at some time in the geological past. Here, the tectonic and geological history of the rock mass is studied to infer parameter values and is mostly applicable to soft and viscous rocks. Viscous parameters values of 10^9 to 10^{22} Pa.s are reported for salt in the Hormuz and Namakdan salt diapirs of the Persian Gulf (Mukherjee, *et al.*, 2007). The estimated viscosity of Tso Moriri Gneiss Dome, in the western Indian Himalayas was estimated of 7.5×10^{10} Pa.s (Mukherjee and Mulchrone, 2012). Newtonian behaviour was assumed for both of the examples.

In Twiss and Moores (1992) book on Structural Geology, a viscous coefficient of $10 - 25 \times 10^{20}$ Pa.s is reported for quartzite.

3.4.4 Back analysis of observed response

It is of considerable interest to calculate viscoelastic parameters through back-analyzing field measured data of time-dependent rock mass responses. This methodology has been frequently used to study the time-dependent behaviour of rock masses in South African Gold mines. Malan *et al.* (1997) reported $\mu_K = 250$ GPa.h and $\mu_M = 2300$ GPa.h after back analysis of closure measurement at a tabular stope at Deelkraal Goldmine based on Burger's rheological model. They also stated that the viscous coefficient is not a fundamental material constant; their results illustrate that there is a clear stress dependency with coefficient of viscosity: as applied stress increases, the viscous coefficient decreases.

3.4.5 A brief recap of the discussed methods of measuring viscosity

A viscous coefficient is a varying parameter depending on the loading condition, geological structure of the rock mass, the rheological model and measurement methodology adopted. Geological analyses underestimate the effect of induced stress. Laboratory tests, even when they aim to simulate field conditions, as are found in the real rock masses, do not always give an answer that can help with predicting rock mass behaviour. The author of this thesis believes that the viscous parameter calculated after back analysis of the field measurements is the most trustable, because the observed response of the rock mass is a manifestation of all of the above-mentioned effective factors for each particular case.

3.5 Viscoelastic approximation:

Identification of most appropriate viscoelastic model

If one elects to admit time-dependent deformation into an analysis, one is faced with a choice of viscoelastic model and calculation of viscoelastic constants for each of the models from a very large range of candidate models (Table 3-1 and Table 3-2 are not exhaustive). This highlights the complication involved in identification of an appropriate or most appropriate viscoelastic model. To overcome this challenge, the approach adopted in this work was that a comparative evaluation procedure was undertaken involving two steps. Firstly, mathematical formulations of linear viscoelastic models were fitted to various convergence time series taken from laboratory creep test data sets and field closure measurements; a least-square regression optimization process obtained values for the parameters of each model. Secondly, calculated values for the model parameters were compared to the literature values. The final decision was made based on an appraisal of reasonable consistency between calculated parameter values coefficients and those of the literature, as well as the least square regression.

This comparative study has different considerations for each individual deformation time series analyzed. Choices of viscoelastic models to fit to data sets are different, depending on the data set's deformation curves. For instance, if they go through three phases of creep curve this restricts the choices to models that accommodate tertiary creep. However, for the mine-scheduling objective it was preferred to avoid progression of deformation curves' to the tertiary creep stage, as we are ultimately searching for mine schedules when the risk of failure is low. This may give higher priority to the viscoelastic models that converged to a deformation value and have stayed in the primary and secondary creep stages. In the cases of uniaxial models, deviatoric stress (maximum principal stress minus minimum principal stress) is considered for

the input of the chosen mathematical model; and for 3D models, the deviatoric stress tensor was calculated by subtracting the hydrostatic stress tensor from the original stress tensor. Malan stated in his PhD dissertation (1999) referring to Lama and Vutuluri (1978) said that “*creep rate is dependent upon the magnitude of deviatoric stress and not the magnitude of the individual principal stresses.*” Stepped viscoelastic graphs, as in the case of closure measurements, after each blast, have been studied individually between each step, because each step is triggered with a different level of sustained deviatoric loading. Full details of evaluation of the different models for number of different examples of time-dependent behaviour data and laboratory creep tests are provided in Appendix 2. The results of this comprehensive analysis are summarized in Table 3-3 to Table 3-7.

Table 3-3: Four rheological models are fitted to the data from Uniaxial compression test on Elsburg Quartzite from South African gold mine (Drescher and Handley, 2003)

Kelvin-Voigt	μ_K (TPa.s)		E_K (TPa)		R-square	
	80		0.004		0.942568	
Generalized Kelvin-Voigt	μ_K (TPa.s)		E_K (TPa)		E (TPa)	R-square
	160		0.077		0.08	0.519712
Burgers	μ_K (TPa.s)	E_K (TPa)		μ_M (TPa.s)	E_M (TPa)	R-square
	200	0.09		290000	0.069	0.542653
Hill-Maxwell model	μ_K (TPa.s)		E_K (TPa)		E (TPa)	R-square
	22		0.0055		0.039	0.90719

Table 3-4: Four rheological models are fitted to the data from results of creep test on quartzite sample from Hartebeestfontein mine (Malan, *et al.*, 1997)

Kelvin-Voigt	μ_K (TPa.s)		E_K (TPa)		R-square	
	9000		1.03		0.87003	
Generalized Kelvin-Voigt	μ_K (TPa.s)		E_K (TPa)		E (TPa)	R-square
	9000		1.03		9.9	0.922805
Burgers	μ_K (TPa.s)	E_K (TPa)		μ_M (TPa.s)	E_M (TPa)	R-square
	800	1.2		900000	15	0.696062
Hill-Maxwell model	μ_K (TPa.s)		E_K (TPa)		E (TPa)	R-square
	9090		0.9		1.03	0.299143

Table 3-5: Four rheological models are fitted to the data from results of creep test on lava from Hartebeestfontein mine (Malan, *et al.*, 1997)

Kelvin-Voigt	μ_K (TPa.s)		E_K (TPa)		R-square	
	50000		1.5		0.971456	
Generalized Kelvin-Voigt	μ_K (TPa.s)		E_K (TPa)		E (TPa)	R-square
	50000		1.5		50	0.968445
Burgers	μ_K (TPa.s)	E_K (TPa)		μ_M (TPa.s)	E_M (TPa)	R-square
	70000	1.5		30000000	50	0.949185
Hill-Maxwell model	μ_K (TPa.s)		E_K (TPa)		E (TPa)	R-square
	99000		3		1.5	0.785852

Table 3-6: Four rheological models are fitted to the data from closure measurement from Deelkraal gold mine tabular stope (Malan, *et al.*, 1997)

Kelvin-Voigt	μ_K (TPa.s)		E_K (TPa)		R-square	
	120000		4		0.880602	
Generalized Kelvin-Voigt	μ_K (TPa.s)		E_K (TPa)		E (TPa)	R-square
	120000		4		60	0.935606
Burgers	μ_K (TPa.s)	E_K (TPa)		μ_M (TPa.s)	E_M (TPa)	R-square
	30000	11		541600	147	0.970602
Hill-Maxwell model	μ_K (TPa.s)		E_K (TPa)		E (TPa)	R-square
	9000000		190		3.1	0.87485

Table 3-7: Four rheological models are fitted to the data from results of uniaxial creep test from Hartbeesfontein Mine quartzite (Bosman, *et al.*, 2000)

Kelvin-Voigt	μ_K (TPa.s)		E_K (TPa)		R-square	
	150000		1.5		0.945959	
Generalized Kelvin-Voigt	μ_K (TPa.s)		E_K (TPa)		E (TPa)	R-square
	150000		1.5		60	0.947529
Burgers	μ_K (TPa.s)	E_K (TPa)		μ_M (TPa.s)	E_M (TPa)	R-square
	80000	2.5		1500000	60	0.96051
Hill-Maxwell model	μ_K (TPa.s)		E_K (TPa)		E (TPa)	R-square
	4100000		60		1.7	0.974192

It can be concluded that any of the models tried have equal potential to simulate and predict the viscoelastic response of the rock mass because each of the models fitted each of the data sets equally well (or equally poorly). It is also clear that different values can be calculated for the viscous coefficients of the same type of rock, depending on the rheological model assumed. While this idea suggests that any choices of values for viscous parameters in a rheological model can be considered 'right' providing such a fitting process has been undertaken, it is unhelpful in terms of trying to establish a most appropriate rheological model. Estimation of the parameter values is generally more trustable when the rheological model consists of fewer viscous elements (dashpots) and more elastic elements (springs). This is detailed in Chapter 5.

4 Key research questions and research hypothesis

Many mining problems are directly concerned with the conditions which may cause mine openings to collapse during the course of their usage. As earlier discussed in Chapter 2, stress distribution in the rock mass, and consequently the stability condition can be manipulated via the mining schedule. Although mine schedules consists of a wide range of activities, the discussion hereafter is confined to scheduling of stoping sequences for long term mine planning. The stepped profiles observed in Figure 2-3, are characteristic of assumptions of i) instantaneous excavation, and ii) linearly elastic rock constitutive behaviour, with instantaneous stress redistribution and corresponding deformation following excavation. As the two schedules of stoping that were chosen for explanation and illustration share the same initial stope and the same final stope, under these assumptions the state of stress at the end of the stoping schedule is the same.

The diagrams (Figure 2-3) show that as new openings are excavated, the deviatoric stress which drives instability can reduce as well as increase. For different stoping sequences; the stress path differs, despite starting and ending at the same states. Possible geomechanical instabilities associated with some of the sequences of excavations can add extra costs to the mining project. These issues are geomechanical aspects of the mine scheduling process which persist over the life of the mine; so they should be integrated with mine schedule optimization process.

Finding a methodology to integrate geomechanical considerations into mine schedule optimization processes is one of the challenges that this work addresses. Geotechnical stability metrics are developed and considered, which have the potential to guide mine schedule

optimization; these are thresholds defined either in terms of stress or strain. The metrics have to be capable of discriminating each schedule when studying all feasible schedules to excavate the stopes. This must be achieved with a reasonable amount of computational effort.

4.1 When do instabilities occur?

The relationship between instantaneous stress redistribution after excavation of each stope in a sequence of excavations and rock mass stability when elastic shall be explained as presented in Figure 4-1. The stress distribution in the elastic rock mass when no stope excavation has occurred yet equals to *in situ* stress. Figure 4-1 illustrates this condition through analogy between stope excavation and a chair loaded under the weight of a man sitting on it with his weight equally distributed on the four chair legs.

When one stope is excavated, stress instantaneously redistributes in the rock mass. If the stress distribution destabilizes the rock mass surrounding the excavation, failure will occur immediately after excavation is made if not Time-dependent behaviour. Figure 4-1 analogizes the stope excavation by removing one of the four chair legs (at time $t=0$) which causes instantaneous redistribution of the man's weight on the remaining three chair legs at time $t=0$ (this is also assumed in the Brady and Brown (1993)). Consequently the man on the chair either comfortably continues sitting on the chair or the chair will break immediately after chair leg is removed (at time $t=0$), and the man falls down. The key point about this analogy is that removal of chair leg (stopes excavation), stress redistribution and failure all happen at time $t=0$, if not time-dependent behaviour. This example will be referred to as 'chair leg analogy' in the forthcoming.

The study of rock mass stability in mine schedule optimization with an assumption of linear elasticity is thus principally concerned about sequences of stoping events and scheduled times of the events. Figure 2-3 showed that the sequence of excavation activities has the potential to direct when failure occurs even if the rock is assumed elastic.

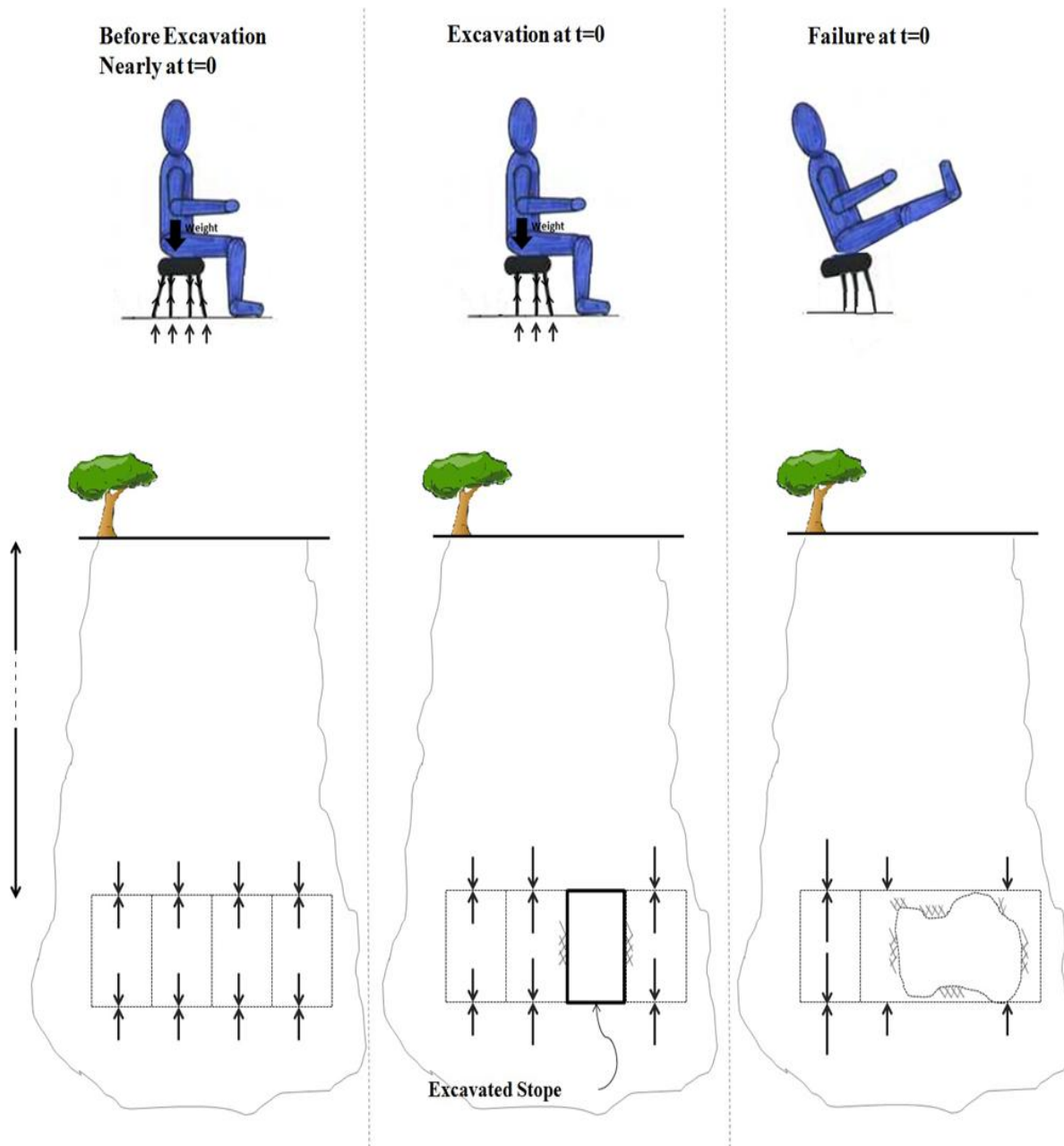


Figure 4-1: The graphical representation of ‘chair leg analogy’ explaining relationship between instantaneous stress redistribution after excavation of each stope in a sequence of excavations and rock mass stability when elastic.

As this work is principally concerned with the timing of excavations, and aims to develop a geomechanical instability indicator, a natural question for the work to be answered is:

When does instability occur?

Drawing upon the ‘chair leg analogy’ (rock is considered elastic as in most of rock mechanics analysis) failure occurs instantly after redistribution of stress (if the new stress distribution destabilizes rock mass). The key points are that if the rock is elastic, then stress redistribution occurs instantly after excavation, consequently the elastic displacement also occurs instantly and if the remaining structural elements are to fail, they will fail instantly too.

Chapter 2 discussed instances when displacement and failures occurred in a different manner, following what surely must still be considered as instantaneous redistribution of stress. Failure occurs after excavation. The ‘timing’ aspect of Figure 4-1 does not happen in practice. Thus the ‘timing’ aspect of an assumption of elastic behaviour of rocks and rock masses will fail to accurately predict the timing of instabilities relative to excavation processes.

The aggregate effect of the whole sequence of mine activities with the time stamps allocated for each activity may thus lead to time histories of elastic stress and strain fields which can build a good basis for a geomechanical constraint formulation. However, in order to rectify the situation where estimates of the timing of instability are erroneous, a ‘fix’ that considered some manner of viscoelastic response was necessary.

4.2 Interaction between stoping schedule and time-dependent deformation

When a time-dependent deformability response is assumed, the effect of a change in the duration between stoping events may become more dramatic. Instantaneous stress redistribution, as

explained with “chair leg analogy” must still hold, but when one of the chair legs are removed, the chair can fail in a range of time, if it is to fail. Mines’ report many instabilities that do not happen instantly after a blast or a seismic event, but which develop over time. Evidences supporting this idea of viscoelastic or viscoelastoplastic response were presented Chapter 2. However, any deviation at all from an assumption of linear elasticity for geomechanical numerical modeling, adopted to inform geomechanical constraint formulation, would rapidly lead to impractical levels of computational effort. For mine scheduling, the solution is not undertaking numerical modeling of mine sequences (and the times of excavation) using fully implemented 3D rheological models as the constitutive model. Instead, some manner of viscoelastic or viscoelastoplastic response is introduced coupled to elastic complete sequence modeling, as an approximation of reality.

A key assertion of this work is thus that the time-dependent behaviour of rock masses should be considered in mining schedule optimization. As it has special relevance for an optimization methodology that manipulates the sequence of events and the specific times at which individual stoping events are planned to commence and cease.

The nature of this assertion, for a proposed approximation has an extremely important corollary, illustrated in Figure 4-2. It shows a schematic strain-time curve showing deformations at a specific point in a rock mass, as sequence of mining activities are undertaken. The blue line in Figure 4-2 shows the expected response of the rock mass when it is considered to be purely elastic. Its stepped appearance is a result of instantaneous elastic deformations in response to instantaneous redistribution of stress, at the point of interest, as the excavations are produced. The green dashed line refers to a maximum permissible strain of the rock mass at the point of consideration (a rupture strain). The red line formally superimposes a time-dependent response

that asymptotically converges to the expected elastic deformation, as time after the excavation event, proceeds. At T1, a large stress perturbation occurs, which causes deformation in the rock mass. This deformation is presented with both an elastic assumption (blue line) and a time-dependent assumption (red line). At T2, another stress perturbation occurs, and this results in recovery of some portion of the deformation.

The outcome of the perturbation at T1 depends upon the choice of assumption about the rock behaviour. If rock mass is assumed elastic it fails, at T1. If time-dependent behaviour of rock mass is taken into account, the time interval to the next perturbation event is an important factor: if this interval is planned 'a' (in Figure 4-2), then the time-dependent response suggests that the threshold strain will be exceeded. On the other hand if the event schedule is modified (a management decision), so that the interval is 'b', then the time-dependent response suggests that exceeding the threshold (the dashed green line) will be avoided.

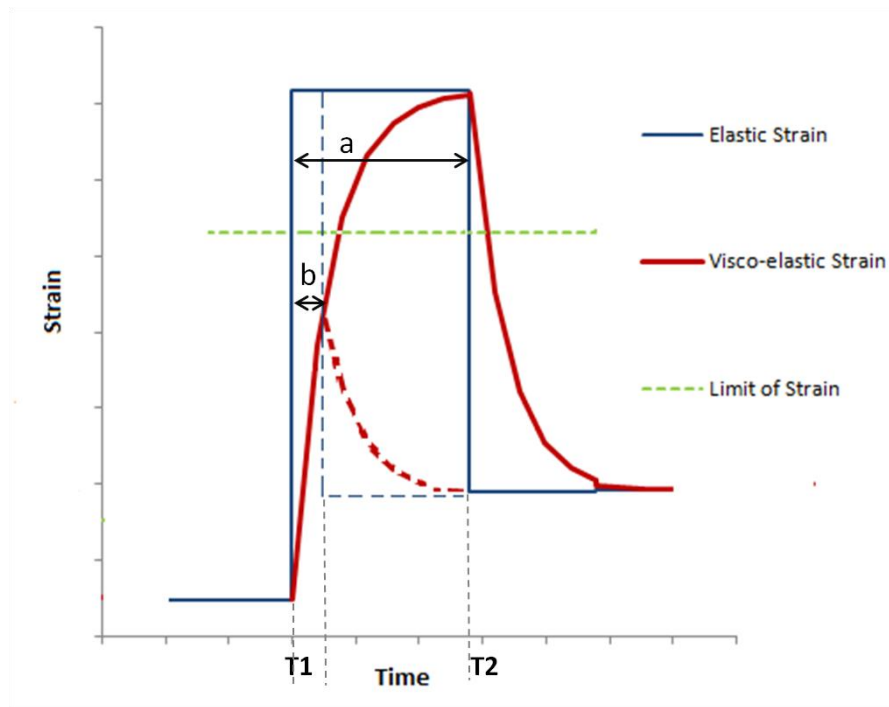


Figure 4-2: Schematic strain-time curve showing deformations at a specific point in the rock mass.

It can now be fully appreciated how the mine schedule optimization process, which adjusts the timing of mining activities, will interact with geomechanical instability process, when time-dependent deformability behaviour is taken into account. Clearly, the current conceptual construct goes beyond the observation that activity sequencing alone can reduce geotechnical risk, as that did not require assimilation of viscoelastic rock behaviour; the benefits would be realized with an assumption of elastic behaviour alone. Taking into account these ‘delayed’ deformations, the instability metric devised for the purposes of mine schedule optimization may be based on how ‘close’ the actual strain develops to a maximum limit of strain. The effectiveness of any such metric clearly will depend very strongly on, and may be undermined by, the value of the viscosity parameter effectively used to construct and superimpose the time-dependent portions of the strain curves (red lines). Higher values of viscosity require longer time spans to converge to the expected elastic deformation. Insufficient time lapses between scheduled excavation events do not allow the rock to converge on the elastic strain values, and the result is a strain time series that appears more continuous, with points of inflexion only apparent for dramatic stress redistribution.

Having now fully explained and supported the rationale for the approach to development of a geotechnical instability metric, the remaining chapters of this thesis report on the details of implementation and execution of the concepts.

5 Methodology for automating geotechnical stability analyses for schedule optimization purposes.

The work presented in this chapter consists of three main portions: elastic stress and elastic strain analysis, viscoelastic strain superimposition analysis and geotechnical stability assessment. These three components work together to produce (in)stability metric profiles of feasible stoping schedules for schedule optimization purposes.

The technique is presented with reference to an ore body consisting of just 6 stopes. There are $6!$ ($=720$) possible sequences of excavation to excavate the 6 stopes; in practice a mine may consist of a few hundred stopes to be excavated and so, the methodology must generalize to problem of this size. The large ‘geographical’ scale of mining operations creates interplay between the amount of detail required to represent the problem properly and the amount of time and the tools available to solve it in a timely fashion. Consequently, approaching the problem in a fashion where 720 separate evaluations of stress and strain field time series are undertaken with geomechanical numerical modeling of given mine sequences cannot be the solution either.

Instead, the methodology followed here is based on dividing the large-scale problem into a series of smaller problems, solving the smaller problems individually and then aggregating their solutions in an order corresponding to the proposed sequence to represent the solution to the large-scale problem.

Analysis of a different mine sequence requires no further numerical modeling; the results of the smaller problems are simply superimposed in a different order. The following explains how the methodology is planned to achieve a high level of time and computational efficiency.

The work starts with the assumption of linear elasticity for good reasons. Assumption of linear elasticity allows for application of the principle of superposition. Young (1989) states that: *“The effect produced on an elastic system by any final state of loading is the same whether the forces that constitute that loading are applied simultaneously or in any given sequence and is the result of the effects that the several forces would produce if each acted singly.”* Application of the principle of superposition permits a large complicated problem to be broken down into smaller and simpler problems, which are easier to solve. Summation of the solutions of small, subdivided problems together gives the solution of the original problem.

In the case of computing elastic stress fields for all the possible sequences of stope excavations: elastic stress fields induced by individual stope excavations can be calculated for each stope within a computational domain that is defined identically for each stope, and with each individual stope experiencing the same field stress conditions. It is assumed that each stope excavation happens with one blast and stress redistributes instantaneously after each blast. For each sequence of stopes, a sequence of stress fields applying throughout the domain may be expected. The sequence of stress fields, corresponding to a specific sequence of stoping, is then obtained by algebraically summing the pre-computed stress fields induced by each event (blast), in turn, stope-by-stope.

Figure 5-1 illustrates principle of superposition for calculation of stress fields in a sequence of excavating two openings: first, circular shaped opening is excavated and next a square-shaped opening is excavated.

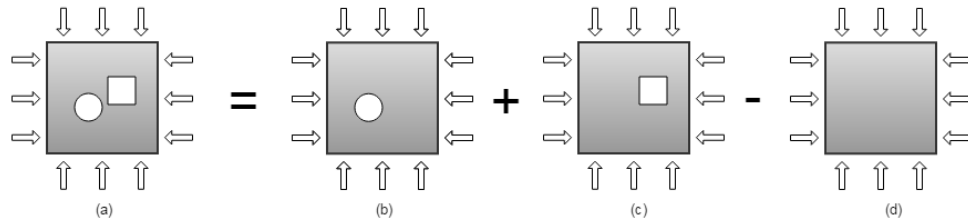


Figure 5-1: Application of principle of superposition to calculation of stress field after (a) excavation of a circle shaped and a square shaped opening (first circle and next square): (b) the stress field after excavation of circle opening is added to (c) the stress field after excavation of square shape opening and (d) *in situ* stresses are subtracted.

If a time label is allocated to each stope excavation according to a given mine schedule, this turns superimposed stress fields for each sequence of excavations into a stress field time series that results as consequence of the mining schedule. Each step in the stress field time series does not necessarily reflect the effect of one stoping event (blast); it is possible that same time label can be allocated to more than one stoping excavation (blast) according to the given mine schedule. In such a case, the stress fields time series is obtained by adding pre-computed stress fields of each of the concurrent stoping events (blasts) at once. The calculated stress fields time series may consist of steps arising from one stoping event (blast) or multiple simultaneous stoping events (blasts).

Hooke's law (e.g. Brady and Brown (1993), page 36) may be used to calculate elastic strain tensors from superimposed stress tensors for each stage of excavation. Considering the time labels allocated to each stoping event in the stress time series to apply also the resulting strain; leads to an elastic strain time series.

Even though an elastic strain time series does not reflect any viscous nature of a rock mass being modeled, it forms a basis for understanding the viscoelastic strain that may be according to different stoping schedules. In the linear viscoelastic regime, the Boltzmann principle of superposition, proposed by Ludwig Boltzman in 1874, says that time-dependent deformations

under sustained load are the function of loading history (Figure 5-2). The methodology is based on dividing the duration between two loading steps into equal time intervals and estimating the deformation with a stepped function along the time intervals. Calculating the integral of the estimated stepped functions result a function of time that presents viscoelastic deformation. The detailed mathematical formulation of the methodology is presented in Irgens (2008). The Boltzmann principle of superposition practically follows the same regulations as the general principle of superposition. Each loading step independently effects the total deformation, which can be calculated through the sum of each amount of deformation that occurred at each loading step (Chunhui, 2000).

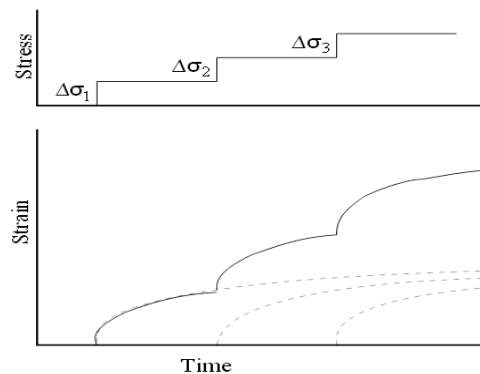


Figure 5-2: Boltzmann superposition principle based on Penny and Marriott (1971).

In the case of a stoping schedule: the loading steps arise due to each event in the schedule and stress field redistribution after each event. The viscoelastic rock mass deformation after each event is approximated by ‘draping’ it upon the elastic strain time series, with the knowledge of a viscous coefficient for the material. A viscoelastic model is chosen that converges asymptotically to the elastic value of strain defined in the elastic time series at each excavation step. Mine-by experiments equipped with suitable instrumentation to observe and monitor induced strains, coupled with a back-analysis technique, may be the most appropriate method through which to establish appropriate values for rock mass viscosity for such purposes.

The elastic stress, elastic strain and viscoelastic time series may each require a threshold value to define stability and thus to guide stability assessment of each stoping schedule. For this purpose, some manner of failure criterion may be introduced to establish such thresholds. Evaluation of rock mass stability based on comparing stress with strength in the rock mass surrounding an excavation is the norm in geomechanical analysis; and leads to calculation of a Strength Factor, with values of Strength Factor below unity implying instability.

In the approach reported here, strength factors are computed adopting the norm as an intermediate step, for reference. However the failure criterion is re-written as function of strain, the time-dependent quantity, rather than stress – ‘failure’ being considered the limiting condition of elastic behaviour – so that the state of strain can be compared with this limiting strain, and a so called ‘Strainth Factor’ can be defined. The ‘Strainth’ defines a threshold value of elastic strain compared with the state of strain throughout the stoping schedule, including, as an approximation, viscoelastic rock mass strain. The application of the strainth and strainth factor is thus extended to permit comparison of viscoelastic strain states that are time dependent, but converge on elastic values – and this is a more detailed description of the framework adopted as a basis for a geomechanical constraint formulation for mine schedule optimization.

Armed with knowledge of stopes’ geometry and the timing of each stopes’ excavation, the question arises of how the stress time series is calculated. Clearly it is possible to conduct a series of stress analyses for a single stope schedule ‘where the next stope to be excavated’ incrementally modifies the stress field arising due to all stopes that have been previously excavated. Such a procedure could be undertaken for every stoping schedule investigated, and this would be appropriate if it had to be assumed that the material had plastified at some stage during the prior excavations.

However, if it is instead assumed that the material remains elastic, and thus that the principle of superposition applies, the stress field time-series may be established by computing the stress field around each individual stope and superimposing the individual stress fields according to the order of excavating the stopes. The advantage of this latter approach is that in order to consider an alternative schedule of stoping, (as is typical for this work on schedule optimization) the individual stress fields do not need to be recomputed. Instead, the results of the stress analysis of the individual stopes just need to be superimposed in a different order. This implies highly computationally efficient arithmetic operation, so that the time series of interest, and thus the schedule's stability indicator, may be evaluated rapidly. Having explained the overall framework for geotechnical stability analysis for schedule optimization purposes, the following sub-sections of this chapter go on to explain each of the outlined steps, in detail.

5.1 Calculations of stress and elastic strain time histories for different stoping schedules

The general procedure used by most numerical methods to solve a given problem is to divide the problem into small components and then sum the influence of the components to approximate the behaviour of the whole system. Usually the method is chosen based on the program's capabilities and complexities, its cost, and its availability. This work uses the boundary element method (BEM) (Beer and Watson, 1994) for computation of stress distributions in the rock mass when each stope is excavated. BEM only discretizes the physical surfaces of the model and computes the field point stresses consistent with the defined surface tractions and far-field boundary conditions (Eberhardt, *et al.*, 1997). The boundary element method greatly reduces computational problem size in comparison to, for example, the finite element method where internal discretization of the medium is required. This makes BEM an extremely efficient tool

for the analysis of stope sequences (as suggested by Brady (1997), Bawden and Milne (1987), Beer (1988) and Grant *et al.*, (1993)). For the computations, the far field boundary should be placed sufficiently far from the locations of the proposed stopes that the specified *in-situ* field stresses may be taken to apply. The BEM assumes that rock mass is a homogeneous, isotropic, and linearly elastic medium. By utilizing the speed and efficiency of the boundary-element method to investigate 3D geometry related stress fields, a large number of geometries may be analyzed in a relatively short period.

The results of the boundary element calculations are highly sensitive to the surface mesh properties of the model (the discretization parameters). In adopting an inappropriate mesh size, it is possible to obtain misleading results (too few elements) or a long computation process (more elements than necessary). Consequently, a mesh size calibration process must be undertaken in advance to obtain the best balance between accuracy and speed. Mesh size calibration is repetition of a process of computing stress tensors around an excavation with a known stress field (possibly from an analytical solution) and monitoring convergence of results for different mesh sizes to the known values. When results started converging to known values with an acceptable tolerance, the mesh size with least computational duration would be chosen.

The BEM solver used in this work is Compute3D, which is part of the Examine3D package available from Rocscience Inc (Curran and Corkum, 1990-8). Due to automation limitations of this package (so that in future thousands of stoping and development activities can be considered similarly) boundary meshes for each stope were developed using an independent software package called Rhinoceros, distributed by Robert McNeel and Associates (McNeel, 2014). Meshes produced with Rhinoceros which can be readily automated, were checked and then accepted as equivalent to those of Examine3D (discretizes surfaces of stopes with 3 node

triangular elements). Rhinoceros mesh data were converted into the format required by Examine3D through a custom written computer program (the Visual Basic script that does this is provided in Appendix 3).

The resulting input files were uploaded to Compute3D which computed the stress fields induced, for each stope in turn, and saved the results as a MATLAB database. Stress field superimposition for the stope sequence was conducted within the MATLAB environment. The MATLAB script that does this is provided in Appendix 5. As a mine schedule not only considers the sequence of stoping but also the specific dates and times at which the activities are undertaken, having obtained the sequence of stress fields, a time series of stress fields is obtained simply by mapping the timestamps of the scheduled stoping times to the sequence. The elastic strain time series were calculated using Hooke's law (Equation 5-1) because linear elasticity is assumed, e.g. (Brady and Brown, 1993).

$$[\varepsilon] = [S][\sigma] \quad [5-1]$$

where $[\varepsilon]$ is strain tensor, $[\sigma]$ is stress tensor and $[S]$ is a 6×6 compliance matrix with elements are dependent on the of Young's modulus, E , and Poisson's ratio, ν .

Figure 5-3 presents an example of stress and strain history at one point as 6 stopes are being excavated one after each other with a *in situ* stress field with values $\sigma_1 = 40$ MPa ,090/00, $\sigma_2 = 30$ MPa ,000/00 and $\sigma_3 = 20$ MPa ,000/90. The green line in Figure 5-3 is the aggregated deviatoric stress at the field point shown with a red dot and the blue line refers to deviatoric strain. Equations for calculating deviatoric stress and deviatoric strain are explained in section 5.3. The green graph is generated by superimposing the precalculated stress components at the red dot

field point, each stopping step of the sequence. The blue line is generated from stress tensors with Equation 5-1. Arbitrary time labels have been introduced with units of days.

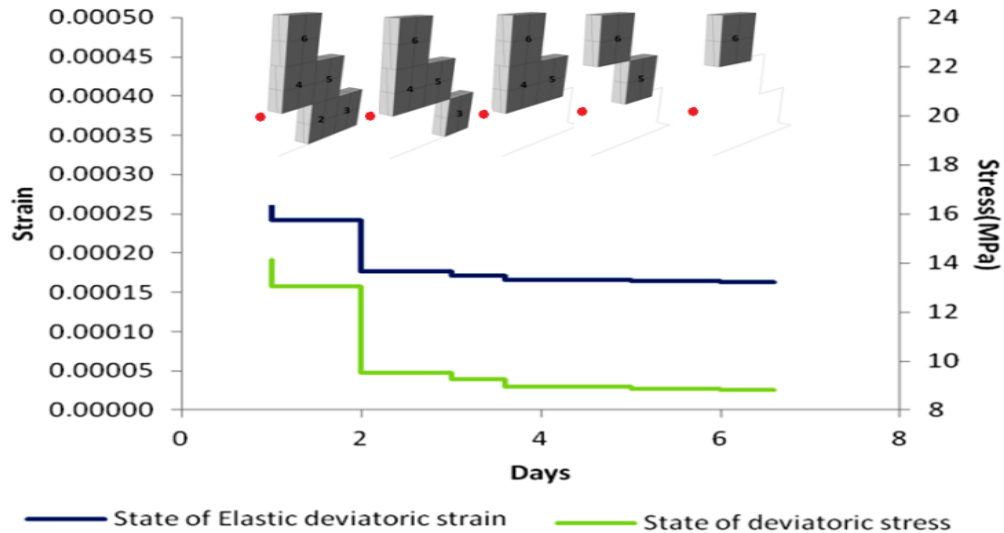


Figure 5-3: The resulting time series of stress and strain have a stepped appearance as elasticity redistributes stresses upon excavation. Presented data is from the example discussed in Chapter 6.

5.2 Upgrading to 3D viscoelastically: 3D Kelvin-Voigt model

As a result of the procedures of the previous section being applied, for each and every field point, a time series of elastic stress tensors is available. From these, an approximate viscoelastic response can be computed through adoption of a rheological model and knowledge of the stress perturbation arising through excavation, and the state of strain before excavation. This could be done using a viscoelastic numerical solver, but application of a suitable model as an approximation of viscoelastic response between excavation events is all that is assumed required to develop the required geomechanical stability indicator. The results of the BEM stress analyses are used instead and lead to a much more timely computational procedure.

In advance of the viscoelastic computations, a viscoelastic model must be chosen and values for its parameters must be established. For this work, a 3D Kelvin-Voigt model is used to approximate the viscoelastic response of rock mass. This model (Figure 5-4) is derived from 3D Generalized Kelvin-Voigt model as was detailed in Chapter 3.

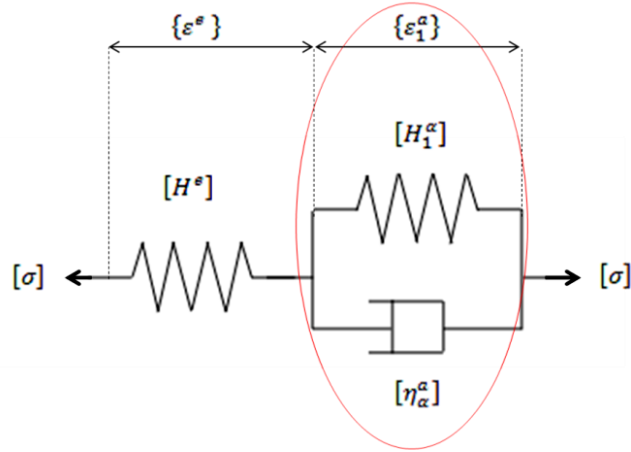


Figure 5-4: The 3D Generalized Kelvin-Voigt model for creep deformation is a combination of one 3D Kelvin-Voigt component (circled with a red line) in series with a Hookean element (spring) (Picard, 2007).

Equation 5-2 is the mathematical presentation of the 3D Kelvin-Voigt model obtained from the original 3D Generalized Kelvin-Voigt model developed by Picard (2007). Any term statement related to pure elastic deformation associated with the Hookean element is removed and the numbers of time-dependent parameters reduce to one.

$$\{\epsilon_1^{\alpha}\} = [X]F_{\alpha} \int_0^{\tau} e^{-\lambda_{\alpha}(t-\tau)} d\tau \quad [5-2]$$

where τ is duration between two stopping activities, t is time and also:

$$[X] = \begin{bmatrix} 1 & -1 & -1 & 0 & 0 & 0 \\ 1 & 1 & 0 & 0 & 0 & 0 \\ 1 & 0 & 1 & 0 & 0 & 0 \\ 0 & 0 & 0 & 1 & 0 & 0 \\ 0 & 0 & 0 & 0 & 1 & 0 \\ 0 & 0 & 0 & 0 & 0 & 1 \end{bmatrix} \quad [5-3], \quad \lambda_{\alpha} = \frac{[H_1^{\alpha}]}{[\eta_{\alpha}^{\alpha}]} \quad [5-4]$$

and

$$\{F_\alpha\} = \left\{ \begin{array}{l} -\frac{(2\nu-1)\sigma_1+(2\nu-1)\sigma_2+(2\nu-1)\sigma_3}{3\eta_\alpha^a} \\ -\frac{(\nu+1)\sigma_1-2(\nu+1)\sigma_2+(\nu+1)\sigma_3}{3\eta_\alpha^a} \\ -\frac{(\nu+1)\sigma_1+(\nu+1)\sigma_2-2(\nu+1)\sigma_3}{3\eta_\alpha^a} \\ \frac{2(\nu+1)\tau_{12}}{\eta_\alpha^a} \\ \frac{2(\nu+1)\tau_{13}}{\eta_\alpha^a} \\ \frac{2(\nu+1)\tau_{23}}{\eta_\alpha^a} \end{array} \right\} \quad [5-5]$$

where $[H_1^a]$ is the stiffness of the spring, $[\eta_\alpha^a]$ is a viscous coefficient for the dashpot, ν is Poisson's ratio and σ_1 , σ_2 and σ_3 are principal components of stress.

The Kelvin-Voigt model formulation adopted (Picard, 2007), is one of very few that describes viscoelastically in a fully 3D manner. This is of great importance in this work because the fundamental nature of the problem considered is 3D, and the stress analyses conducted are also 3D. The 3D Generalized Kelvin-Voigt model also satisfies this requirement but what makes 3D Kelvin-Voigt model superior for this work is the capability of the latter time-dependent rock response to converge on the elastic-only state of strain. Figure 5-5 illustrates this point by comparing the expected strain responses of 3D Generalized Kelvin-Voigt, 3D Kelvin-Voigt and elastic materials under the same constant loading.

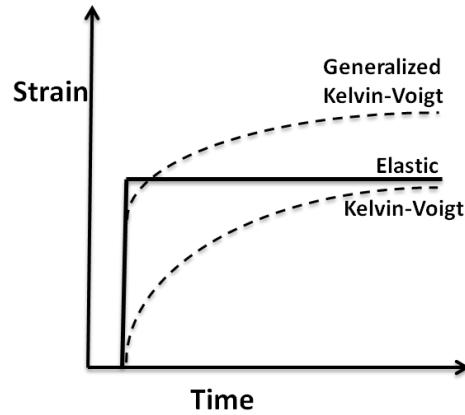


Figure 5-5: Generalized Kelvin-Voigt, Kelvin-Voigt and Elastic rock mass deformation under constant load based on Goodman (1989).

When the rock is assumed elastic, the rock mass deforms ‘instantaneously’ (with the perturbation propagation at the speed of sound in the material) corresponding to instantaneous stress redistribution. The Generalized Kelvin-Voigt model has an instantaneous deformation depending on the stiffness value of the spring ($[H^e]$ in Figure 5-4) and continues to deform time dependently under the applied load due to the Kelvin-Voigt component. If time-dependent rock response is simulated with the Kelvin-Voigt model, instantaneous deformations would be neglected and rock mass would just deform asymptotically to the elastic value of strain with time.

Whether or not the elastic state is achieved in practice during stability indicator computations depends on the value of the viscous parameter relative to the timing of the next stope excavation in the sequence. In this sense, the convergence of strain to the elastic state may be ‘interpreted’ before the next stress perturbation is introduced, but it is nevertheless assumed that the principle of superposition still applies for the next excavation step. The validity of this latter assumption requires detailed investigation, which requires further work, beyond the scope of this thesis.

However, as the objective of this work is to establish only an indicator of instability, that reflects time-dependent constitutive rock behaviour, as computationally expeditiously as possible, the choice of the Kelvin-Voigt over the Generalized Kelvin-Voigt model at least seems more consistent with the overall methodology being outlined. Importantly, as shown in Chapter 3, it has to be found that it is possible to curve-fit any viscoelastic model to any given observations of time-dependent deformation of rock, equally well. Given this, the stance that has been taken in this work has been a choice established principally on the basis of convenience, and the Kelvin-Voigt model more conveniently ‘fits’ with the elastic stress superimposition technique to establish the stress field time series. It presents the further conveniences that:

- i. There is one less viscoelastic model parameter to obtain a value for,
- ii. The Hookean element remaining in the Kelvin-Voigt model can be related to the conventional Young’s modulus of the material; because it asymptotically defines the elastic strain response, (the Hookean element has conventional ‘meaning’).

To illustrate this point Figure 5-6 shows the associated error when fitting 3D Kelvin-Voigt model to a set of time-dependent deformation data, compared to the errors associated with other proposed rheological models, which were previously discussed in Chapter 3. Figure 5-6(left) shows rheological models fitted to Bosman *et al.* (2000) results of a compression creep test on a quartzite sample from Hartbeesfontein Mine in South Africa. The various models approximately fit the data with their specific values for rheological parameters. Figure 5-6 (right) shows 3D Kelvin-Voigt model fitted to the same data set. The Hookean element is assigned the measured Young modulus of the quartzite sample of 70 GPa and the measured Poisson’s ratio is 0.2, based on the report from Bosman *et al.* (2000). The 3D Kelvin-Voigt viscous parameter has a value of 40 TPa.s, which is consistent with values from the literature discussed in Chapter 2.

Studying Figure 5-6, it is apparent that 3D Kelvin-Voigt model fits as well as the other viscoelastic models. For more details and examples of fitting viscoelastic models to time-dependent rock behaviours, the reader is directed to Appendix 2.

The formulation for implementation of the viscoelastic-strain time series from the elastic time series, while adopting the 3D Kelvin-Voigt viscoelastic model is presented in the MATLAB script set out in Appendix 5.

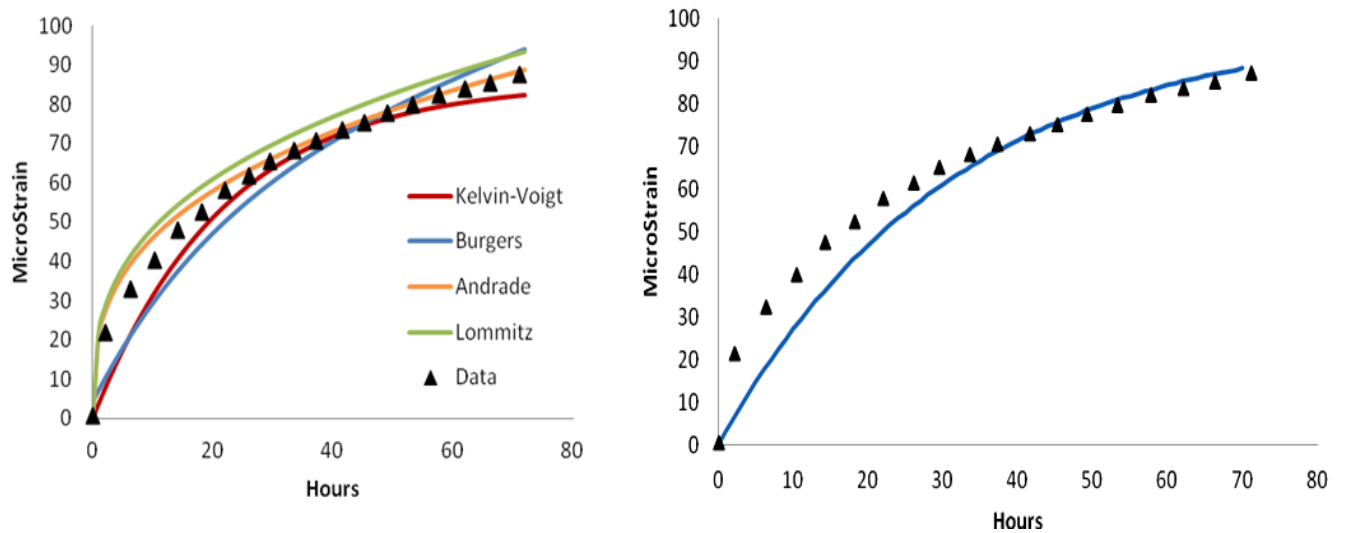


Figure 5-6: Results of least squares fitting different viscoelastic models to the data set of compression creep test on a quartzite sample from Hartbeesfontein Mine quartzite, South Africa reported by of Bosman *et al.* (2000). The right graph is the result of least squares fitting of 3D Kelvin-Voigt model to this data set.

The result of applying this MATLAB script to the schedule of stoping leading to the elastic response of Figure 5-3 is presented in Figure 5-7. As the process has reduced the rather castellated curve of the elastic response to a ‘smoother’ form, the process has been called ‘decastellation’, and the curve of Figure 5-7 is referred to as having been viscoelastically ‘decastellated’. This is principally to highlight that viscoelastically decastellated strain time series must be considered to be approximations of the genuine full 3D viscoelastic numerical analysis.

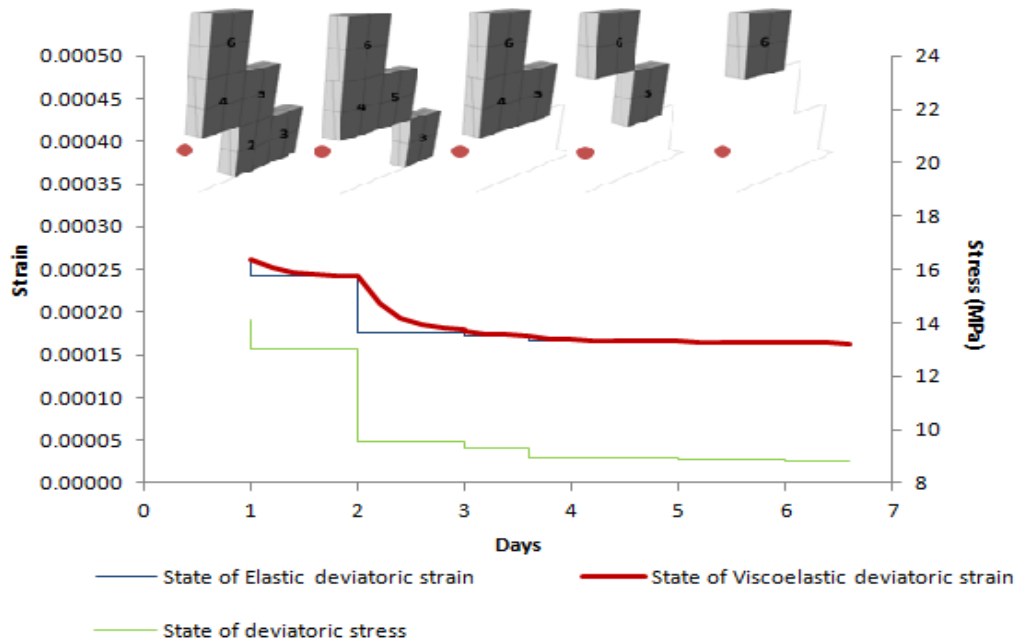


Figure 5-7: Decastellated time series of strain as stresses redistribute upon excavations.

5.3 Assessment of geotechnical stability

Assessment of geotechnical stability of a stoping schedule practically means defining and quantifying a measure of how ‘close’ a rock mass is to ‘failure’ as more stopes are excavated. For convenience, again, this measure should be defined within the framework of an established conventional failure criterion. Once the definition of the failure criterion has been established, the measure at each point within the rock mass can be calculated using the stress, strain or viscoelastic strain time series. This procedure can be automatically repeated for each considered location within the computational domain for each stoping sequence. This assessment builds the basis for a geomechanical constraint formulation to be adopted for evaluation of ‘goodness’ of each schedule for the purpose of mine schedule optimization.

The simplest and the best-known failure criterion is the Mohr-Coulomb criterion (e.g. Goodman, 1989), most routinely characterized as the linear envelope obtained from a plot of the applied stress within a material in the limiting condition during triaxial testing (Curran and Corkum,

1990-8). This criterion evaluates stability of rock mass in terms of stress. It calculates the maximum value of deviatoric stress, which would cause the rock to fail, given the current state of stress at a location in the rock. Taking the ratio between these two, a factor of stability known as strength factor is obtained. Higher values of strength factor indicate greater stability regions within the rock mass, while strength factors less than 1.0 represent zones of possible instability (Hoek and Brown, 1987). In the following, the Mohr-Coulomb failure criterion, conventionally expressed in terms of stress is re-written in terms of strain, based on knowledge that failure occurs at the upper limit of elastic behaviour. The failure criterion is written in this way because it makes no difference at all to instability indicator calculations for solely elastic behaviour and because a strain-based threshold is required for comparison with the viscoelastic response.

The strain threshold (a rupture strain) normalized by the state of strain defines a '*strainth factor*', in the same way that a strength factor is established. A viscoelastic *strainth factor* is also introduced in this work as the strain threshold normalized by the instantaneous viscoelastic strain. The following sections explain the procedure of development of these terms in detail.

5.3.1 3D Mohr-Coulomb failure criterion

When the Mohr-Coulomb failure criterion is considered in a 3-dimensional stress analysis, it appears as a polyhedral surface in σ_1 - σ_2 - σ_3 space, as presented in Figure 5-8a. Any point in the space that lies inside the area, which is surrounded by the failure envelope, indicates that rock is still stable. Figure 5-8b shows how a point in this principal stress space, in the form of P ($\sigma_1, \sigma_2, \sigma_3$) can be defined based on its distance from the origin of the plane passing through P that is perpendicular to the hydrostatic axis ($\sigma_1 = \sigma_2 = \sigma_3$), and the location of P within this plane. The plane containing P, which has a distance ξ from the origin, is generally referred to as

the deviatoric plane or Π -plane. The location of P within this plane may be characterized using the distance ρ and angle θ (see Figure 5-8b and Figure 5-8c).

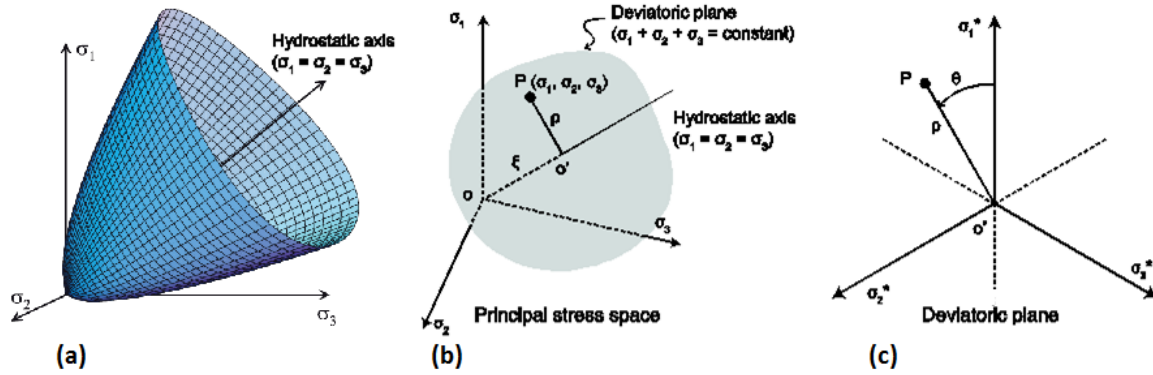


Figure 5-8: (a) Example of failure envelope in 3-dimensional stress space (from Benz *et al.* (2008)); (b) Representation of a stress state in principal stress space, (c) Representation of a stress state in the deviatoric plane (from Lee *et al.* (2012)).

Calculation of the stress threshold predicted by the 3D Mohr-Coulomb Failure Criterion requires principal stresses. Using the stress field time series explained in the previous section, principal stresses for any field point at any time (any excavation stage) within the calculation domain are given by the determinant presented in Equation 5-6 taken from Goodman (1989):

$$\begin{bmatrix} \sigma_{xx} - \sigma_i & \tau_{xy} - \sigma_i & \tau_{xz} - \sigma_i \\ \tau_{yx} - \sigma_i & \sigma_{yy} - \sigma_i & \tau_{yz} - \sigma_i \\ \tau_{zx} - \sigma_i & \tau_{zy} - \sigma_i & \sigma_{zz} - \sigma_i \end{bmatrix} \begin{bmatrix} l \\ m \\ n \end{bmatrix} = 0 \quad [5-6]$$

The determinant results in a cubic equation function of σ , the general stress tensor, as presented in Equation 5-7; in which the coefficients I_1, I_2 and I_3 are independent of the coordinate system, and are therefore called invariants, which means that the principal stresses for a given stress state are unique. The invariants are important in the development of the criteria that predict the onset of yielding. Since the principal normal stresses are roots of an equation involving the stress invariants as coefficients, their values are also invariant, that is, not dependent on the choice of the original coordinate system.

$$\sigma_i^3 - (\sigma_{xx} + \sigma_{yy} + \sigma_{zz})\sigma_i^2 + (\sigma_{xx}\sigma_{yy} + \sigma_{xx}\sigma_{zz} + \sigma_{zz}\sigma_{yy} - \tau_{xz}^2 - \tau_{xy}^2 - \tau_{yz}^2)\sigma_i - (\sigma_{xx}\sigma_{yy}\sigma_{zz} - \sigma_{yy}\tau_{xz}^2 - \sigma_{xx}\tau_{yz}^2 - \sigma_{zz}\tau_{xy}^2 + 2\tau_{xz}\tau_{yz}\tau_{xy}) = 0$$

$$I_1 = \sigma_{xx} + \sigma_{yy} + \sigma_{zz} \quad [5-7]$$

$$I_2 = \sigma_{xx}\sigma_{yy} + \sigma_{xx}\sigma_{zz} + \sigma_{zz}\sigma_{yy} - \tau_{xz}^2 - \tau_{xy}^2 - \tau_{yz}^2$$

$$I_3 = \sigma_{xx}\sigma_{yy}\sigma_{zz} - \sigma_{yy}\tau_{xz}^2 - \sigma_{xx}\tau_{yz}^2 - \sigma_{zz}\tau_{xy}^2 + 2\tau_{xz}\tau_{yz}\tau_{xy}$$

In a deviatoric plane, J_1 , J_2 and J_3 are first, second and third invariants of the deviatoric stress tensor, presented in Equation 5-8:

$$J_1 = I_1 = \sigma_{xx} + \sigma_{yy} + \sigma_{zz} \quad [5-8]$$

$$J_2^2 = \frac{1}{2} \left[(\sigma_{xx} - \sigma_{yy})^2 + (\sigma_{yy} - \sigma_{zz})^2 + (\sigma_{zz} - \sigma_{xx})^2 + 6(\tau_{xz}^2 + \tau_{xy}^2 + \tau_{yz}^2) \right]$$

$$J_3 = \det \begin{vmatrix} \sigma_{xx} - I_1 & \tau_{xy} & \tau_{xz} \\ & \sigma_{yy} - I_1 & \tau_{yz} \\ \text{sym.} & & \sigma_{zz} - I_1 \end{vmatrix}$$

The parameters, which are used to characterize the location of P ($\sigma_1, \sigma_2, \sigma_3$) within the stress space and its deviator plane are formulated as follows:

$$\xi = \frac{I_1}{3}, \quad \rho = \sqrt{2J_2}, \quad \theta = \frac{1}{2} \cos^{-1} \left(\frac{3\sqrt{3}J_3}{2J_2^{3/2}} \right).$$

Any value of $0 < \theta < \frac{\pi}{3}$ corresponds to the condition of $\sigma_1 > \sigma_2 > \sigma_3$, required by convention.

The ‘performance’ of various failure criteria are usually assessed by comparison in the deviatoric plane. Figure 5-9 the presents Mohr-Coulomb Failure criterion plotted in this deviatoric plane.

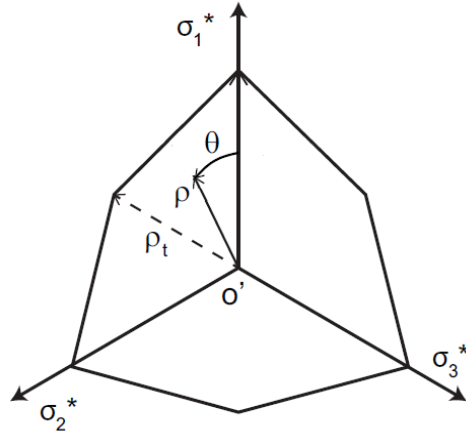


Figure 5-9: Mohr-Coulomb failure criterion in the deviatoric plane from (Lee, *et al.*, 2012).

5.3.2 Strength Factor

Stability assessment in the Mohr-Coulomb failure criterion is based on the ratio of the distance ρ which is interpreted as deviatoric stress and distance ρ_t which is the distance of the failure envelop to the center of deviator plane (as presented in Equation 5-9) and this is called the strength factor (Equation 5-10). Any value of strength factor below one corresponds to failure. The strength factor can be calculated for every point in the rock mass in every step of every stoping schedule.

$$\rho_t = \frac{\frac{I_1}{3} \sin \varphi + C \cos \varphi}{\cos \theta + \frac{\sin \theta \sin \varphi}{\sqrt{3}}} \quad [5-9]$$

where C is cohesion and φ is friction angle of the material.

$$\text{Strength Factor} = \frac{\rho_t}{\rho} \quad [5-10]$$

5.3.3 Strainth Factor

Any location in the rock mass at any step of stoping schedule can be represented with a point in a 3D strain space as well as stress space, and similarly, can be characterized in terms of strain invariants. Principal strains also can be calculated in the same way as principal stresses are calculated using Equations 5-6 to 5-8 by replacing σ is by ε and τ by $\frac{\gamma}{2}$ (Goodman, 1989).

The assumption of linear elasticity for the limiting state of failure allows one to define a strain based failure envelope to compare with rock deformation. This envelope is derived from the 3D Mohr-Coulomb failure criterion with Hooke's law and leads to Equation 5-11. This expresses the "distance of the failure envelope surface" from the center of deviator plane and the parameter has been called *strainth*.

$$\rho'_t = \frac{\frac{I'_1(1+\nu)}{3(1-2\nu)} \sin \varphi + \frac{C(1+\nu)}{E} \cos \varphi}{\cos \theta + \frac{\sin \theta \sin \varphi}{\sqrt{3}}} \quad [5-11]$$

where I'_1 is first strain invariant, ν is Poisson's ratio, E is Young's modulus, C is cohesion, φ is friction angle and θ is the angular departure of the strain state from ε_1^* -axis in the deviatoric plane, which is the projection of the ε_1 -axis in principal strain space (Figure 5-10).

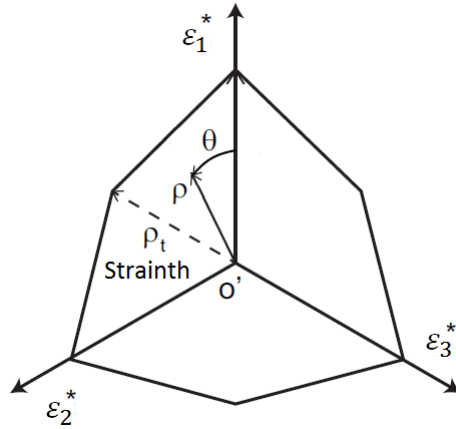


Figure 5-10: Strain-based Mohr-Coulomb failure criterion in the deviatoric plane.

Stability assessment is similarly based on the ratio of the distance ρ' , the deviatoric strain state – calculated as a function of second strain deviator invariants – and the distance ρ'_t (the strainth) which is the distance of the failure envelope to the center of deviator plane. The ratio has been called the *strainth factor* (Equation 5-12). Any value of *strainth factor* below one is indicative of instability.

$$\text{strainth factor} = \frac{\rho'_t}{\rho'} \quad [5-12]$$

For elasticity, *strainth factor* and strength factor are equal.

5.3.4 Viscoelastic Strainth Factor

In this work, the calculated strain based threshold value entitled *strainth* (Equation 5-11), is also used for evaluation of rock mass deformation when it behaves viscoelastically. Based on the values of principal strains calculated with Equation 5-1, the second deviator strain invariant, ρ' (Figure 5-10) can be calculated. The ratio of *strainth* and the just calculated ρ' , is the chosen (in) stability metric when the rock is assumed viscoelastic. This metric is called the *Viscoelastic-*

Strainth Factor (VSF). Any value of VSF below one indicates a risk of instability. The MATLAB script that evaluates the VSF is presented in Appendix 5.

5.4 Evaluating stability of each schedule

At this stage in the presentation, it has been shown how the condition of the rock body being excavated can be described using a strength factor, strainth factor or viscoelastic strainth factor. As it has been shown, rock stability can be both sequence dependent and time-dependent (Chapter 2). For the purposes of this work on mine schedule optimization, the *viscoelastic strainth factor* has been established for adoption as the core basis for (in)stability assessment.

However, establishment of the VSF is not, on its own, a suitable measure of instability. The VSF assess the instability at a single field point, at a single instant in time, within a spatial domain encompassing the whole stoping area to be excavated and within a time domain encompassing the whole stoping schedule. Somehow, the VSF must be integrated or aggregated over each field point of the whole spatial domain, and at each instant of time within the stoping schedule, to produce a single number that is indicative of the risk of instability of the schedule. In the next section, the process through which the stability indicators are developed and quantified so that they are indicative of the (in)stability of the mine schedule as a whole is explained.

5.4.1 Choices of instability metrics

For the purposes of development of a metric in order to guide a mine schedule optimization process, strength factor, strainth factor and VSF indicators are appraised (clearly, if the latter is to be dropped, then just strength factor needs to be examined). The choice of a suitable (in)stability metric should be aware of all locations (grid points) in the domain of the interest and

should reflect a conceptually traceable measure e.g. a representation of the average stability condition in the medium. The evaluated measure should be able to discriminate between different schedules effectively so that the most stable schedule can be certainly detected. Different arithmetic can be adopted to calculate a suitable (in)stability metric which satisfies the above-mentioned factors. This work undertakes such calculations based on the following four considerations:

- i. number of locations prone to instability risk in the domain,
- ii. average value of stability indicators for census field points in the medium,
- iii. searching for the value of maximum stability indicator in the medium,
- iv. searching for the value of minimum stability indicator in the medium.

As the result, 12 (in)stability metrics based on the combinations of the four arithmetic statements (max, min, average and number of grid points) and the three (in)stability indicators (strength factor, strainth factor and VSF) defined to identify the most appropriate measure for schedule optimization purposes. The 12 metrics are listed as follows:

1. **Number of grid points with strength factor less than one** – Any values of strength factor lower than one report instability. This metric evaluates strength factor over all grid points within the rock mass in every sequence of excavations stage-by-stage and counts number of grid points with strength factor less than one at each stage of each schedule.
2. **Number of grid points with strainth factor less than one** – This metric functions and produces results identical to the previous (in)stability except that it is evaluated based on rock deformation when the rock is assumed elastic.

3. **Number of grid points with viscoelastic-strainth factor less than one** – This metric evaluates viscoelastic-strainth factor over all grid points within the rock mass in every sequence of excavation stage-by-stage and counts number of grid points with viscoelastic-strainth less than one at each stage of each schedule. This metric is sensitive to time-dependent deformation of rock mass in different schedules.

These metrics are unable to distinguish a safe schedule from a safer schedule when stability indicator is greater than one at all grid points.

4. **Average strength factor over all grid points** – This metric calculates average of values of strength factor of all of the grid points in the domain of interest for each stage of each sequence of excavation. The schedule with the highest average strength factor would be the preferred schedule.
5. **Average strainth factor over all grid points** – This metric functions and produces results identical to that of the previous metric.
6. **Average viscoelastic-strainth factor over all grid points** – This metric calculates average of values of viscoelastic-strainth factor of all of the grid points in the domain of interest for each stage of each sequence of excavations. The schedule with the highest average viscoelastic-strainth factor would be the preferred schedule.

These indicators might give a wrong impression of the safety of a schedule because locations with the factor less than one can be masked by location with larger stability indicators, greater than one while calculating the average of them.

7. **Minimum strength factor over all grid points** – This metric evaluates strength factor over all grid points within the rock mass in every sequences of excavations stage-by-

stage and announces smallest value of Strength Factor at each stage of each schedule. The schedule with maximum minimum strength factor is the preferred schedule.

8. **Minimum strainth factor over all grid points** – This metric functions and results exactly the same as previous (in)stability metric due to assumption of elasticity.
9. **Minimum viscoelastic-strainth factor over all grid points** – This metric evaluates viscoelastic-strainth factor over all grid points within the rock mass in every sequence of excavation stage-by-stage and establishes the smallest value of viscoelastic-strainth factor at each stage of each schedule. The schedule with maximum minimum viscoelastic-strainth factor is the preferred schedule.
10. **Maximum strength factor over all grid points** – This metric evaluates strength factor over all grid points within the rock mass for every sequence of excavation stage-by-stage and establishes the largest value of strength factor at each stage of each schedule. Schedules with the lowest maximum strength factor not preferred.
11. **Maximum strainth factor over all grid points** – This metric functions and results exactly the same as previous (in)stability metric due to assumption of elasticity.
12. **Maximum viscoelastic-strainth factor over all grid points** – This metric evaluates viscoelastic-strainth factor over all grid points within the rock mass in every sequence of excavation stage-by-stage and establishes the largest value of strength factor at each stage of each schedule. The schedules with lower maximum strength factor are inferior.

The last three metrics do not give any information about grid points with stability indicator less than one.

5.4.2 The cons and pros of each of the instability metrics

Table 5-1 judges the practicality of each of these 12 (in)stability metrics as constraints to a schedule optimization purposes – choosing most stable schedule.

Table 5-1: Possible choices of instability indicators and their pros and cons.

Instability metrics	Duration & computation efficiency			Discrimination capability			Reflection of the domain		Time-dependency understanding	
	In-efficient	Average	Efficient	Well	reasonable	Weak	All-around	Partially	Yes	No
1			✓		✓		✓			✓
2			✓		✓		✓			✓
3			✓	✓			✓		✓	
4		✓			✓		✓			✓
5		✓			✓		✓			✓
6		✓			✓		✓		✓	
7			✓	✓				✓		✓
8			✓	✓				✓		✓
9			✓	✓				✓	✓	
10			✓			✓		✓		✓
11			✓			✓		✓		✓
12			✓			✓		✓	✓	

5.5 Automating the process

Figure 5-11 is a scheme showing how geotechnical analyses are merged in an automated process to study rock mass behaviour point-by-point and step-by-step for any stoping schedule. The scheme involves series of loops and some predefined processes. To start, stopes' geometries are required for passing to the BEM solver. For rectangular stopes, used in this proof of concept, this information is provided in an Excel work sheet that contains the coordinates of corners of each stopes in each row. More generally, decisions on stope's geometry may be established through an optimization procedure such as the Mineable Shape Optimizer (MSO), a function in Studio3D, produced by Datamine.

The next step is to discretize the geometry of these stopes; this includes deciding on mesh size, mesh type and full extent of the domain. Each stope has to be 'designed' individually within an

identical computational domain to allow for application of the principle of superposition of the stress states. As explained earlier, the limited automation functionality of Examine3D leads to the use of an independent mesh generation software package called Rhinoceros, distributed by Robert McNeel and Associates (McNeel, 2014). Rhinoceros mesh data files (one ‘*.raw’ file for each stope) were converted into the format required by Examine3D through a custom written computer program in Visual Basic (“Examine3D batch mode processor” see Appendix 3) that also added information on elastic rock properties, the far-field stress state and the locations where stress tensors should be reported, with one such file for each stage. The resulting input files for each stope were uploaded to Compute3D, which computed the stress fields induced by each stope individually and saved the results. The repeated runs of Compute3D were handled by AutoIt, a BASIC-like scripting language for automation in Windows. This permitted automation of the stress analysis process (the AutoIt script is provided in Appendix 4). Figure 5-11 highlights the AutoIt procedures within the overall process flowchart.

Procedures for stress field superimposition and additional geomechanical analyses are conducted within the MATLAB environment (stress field (*.res) files, are also required as input to the geomechanical analysis loop (Figure 5-11)). To apply principles of superposition, firstly a predefined order of stope excavation requires specification to add the stress fields in the correct order. For this purpose, each stope was labeled with a number from 1 to n , the number of stopes. Then all the possible permutations of those number labels (there are $n!$ ways of putting n number into orders) were listed with a custom written computer program in Visual Basic for Applications (“Permutation Processor” script is provided in Appendix 6). Each possible sequence (or schedule) of stope excavation (each blast) thus corresponds to a single permutation of the stope

labels. As the listing of permutation is done deterministically, this process defines an order to the possible stoping sequences such that it is possible to refer to the 'mth' stoping sequence uniquely.

The list of possible stoping schedules is input information for a process that aims to determine the stoping schedule that has the best value of instability metric – through exhaustive enumeration, simply for trialling purposes. It is not the intent that such an exhaustive enumeration process is adopted as a core part of the SOT schedule optimization tool. Rather the exhaustive enumeration procedure permits the best schedule from a geotechnical instability point of view to be established, so that the results that SOT yields when the instability metric is cast as a constraint within SOT's optimization procedure can be objectively assessed.

Again, for trialling purposes, a final database containing results of point-by-point and stage-by-stage geotechnical analysis for each schedule of stoping is established. The geotechnical constraint calculations are very fast because the stress states are pre-computed for each individual stope and then added, point-by-point, and stage-by-stage for each sequence evaluated. However for application at the scale of real mining activities for potentially hundreds of stopes, n , it is not practical to search for the best geotechnical stoping schedule through exhaustive enumeration. $n!$ permutations of stopeIDs is very large number of solutions in the solution space for finding the best sequence of n stopes.

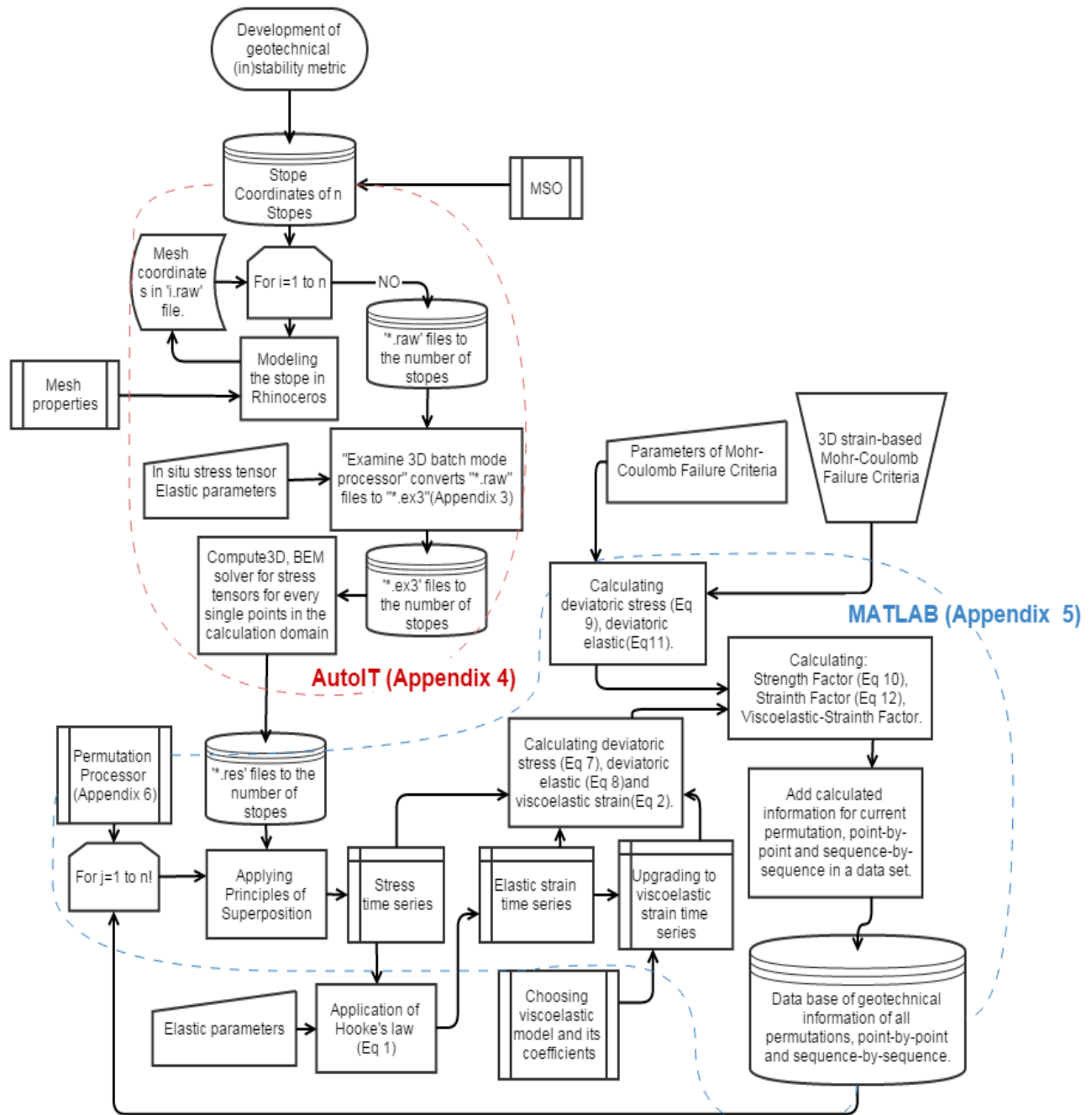


Figure 5-11: Automated procedure for developing (in)stability metrics.

5.6 An estimation of the feasible number of sequences for the purpose of instability analysis

SOT's optimization procedure to find the best schedule even now only 'visits' a small fraction of the set of accessible schedules when it solves / searches for the optimum stopping schedule.

Within SOT, precedence constraints apply which practically reduce the number of accessible solutions (feasible permutations of ‘ n ’ stope labels) substantially. Each precedence constraint defines relationships between two of the activities. For example this may be stated: excavate stope k before stope j . Therefore, for a schedule containing ‘ n ’ activities there can be $n \times (n - 1)$ different precedence constraints defined. Progressive application of each precedence constraint decreases number of the feasible solutions. In the following, the power of precedence constraints to decreasing the number of feasible permutations in the search space is illustrated for an example of excavating just four stopes!

The 24 ($4!$) different sequences of excavating 4 stopes are listed out in Figure 5-12 along with a presentation of the stopes’ geometry. Stopes are labelled from 1 to 4 (Figure 5-12). There are $12 (= 4 \times (4 - 1))$ different choices of precedence constraints available to apply to the original permutation list containing 24 different sequences of excavating the four stopes.

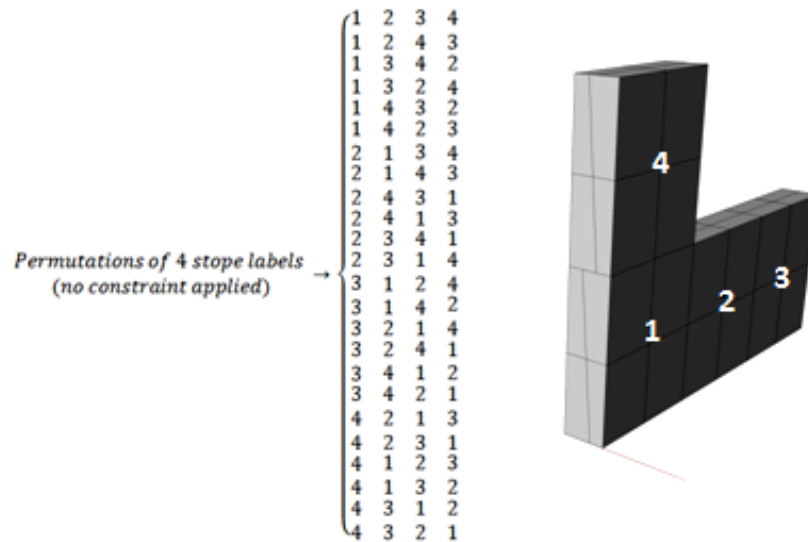


Figure 5-12: All the permutations of excavating four stopes.

Defining one constraint that obliges stope 3 to be excavated before stope 1, decreases the number of feasible permutations by half. This is illustrated in Figure 5-13a. Permutations which do not follow the constraint are crossed with red lines. At this stage 12 permutations are left in the solution domain. The second constraint is defined for excavation of stope 2 before stope 1 which reduces number of feasible solutions (sequences) to eight feasible solutions, as is presented in Figure 5-13b. Those permutations which do not follow the constraint are crossed with yellow lines. The third constraint chooses the sequences for which stope 3 is excavated before stope 4 and only leaves five feasible solutions. This is presented in Figure 5-13c and the permutations which do not follow the constraint are crossed with blue lines. And eventually number of feasible sequences reduce to only one sequence after defining the fourth constraint which forces excavation of stope 4 before stope 2. The rejected permutations are crossed with green lines and the only remaining solution is the circled permutation in Figure 5-13d.

Based on the above description and as presented in Figure 5-13 the most powerful precedence constraint is the first constraint, which reduces number of feasible solutions by half. Any precedence constraint applied afterwards will not be as effective because some of the permutations that could have been rejected after applying the new precedence constraint have already been rejected with the previous precedence constraint. In this example, application of only 4 constraints out of $12(= 4 \times (4 - 1))$ precedence constraints lead to reducing number of feasible sequences (permutations) to one.

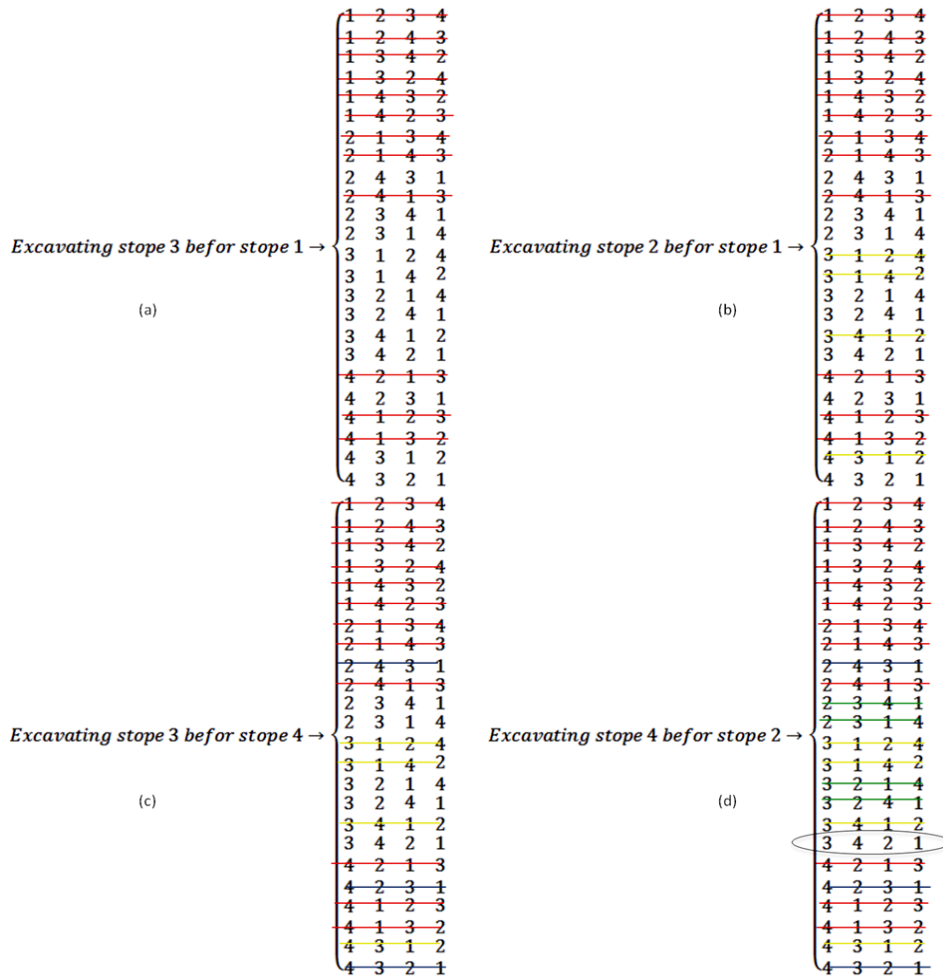


Figure 5-13: Feasible sequences of excavating four stopes reduce substantially after applying constraints.

For a mine scale size optimization problem involving excavating hundreds of stopes, using the proposed automation procedure described in section 5.4 within SOT would not visit all the ‘ $n!$ ’ number of schedules in the solution domain. The (in)stability constraint calculations will only be executed for each schedule that SOT visits – which is after the application of precedence constraints.

6 Application of the methodology to Lac du bonnet granite

6.1 Rock properties and field stresses

For the purposes of this illustrative example, the rock properties adopted were those of the Lac du Bonnet granite with values assumed from the work reported by Yuannian and Fulvio (2009) for the Underground Research Laboratory in Manitoba, Canada, as reported in Table 6-1.

Table 6-1: Experimental results of rock testing on Lac du Bonnet granite (Yuannian and Fulvio, 2009).

Property	Young's modulus (GPa)	Poisson's Ratio	Friction Angle (°)	Cohesion (MPa)	Tensile strength (MPa)
Value	69	0.26	59	30	9.3

The *in-situ* field stresses adopted for the illustrative example are presented in Table 6-2.

Table 6-2: *In situ* field principal stress components' magnitudes and directions.

Major principal stress		Intermediate principal stress		Minor principal stress	
Magnitude (MPa)	Dip Direction / Dip (°/°)	Magnitude (MPa)	Dip Direction / Dip (°/°)	Magnitude (MPa)	Dip Direction / Dip (°/°)
40	090/00	30	000/00	20	000/90

6.2 Meshing description

The stope model consists of 6 stopes which could be excavated in multiplicity (6!) different sequences. For the boundary element related computations, the far field boundary has been placed outside the zone of influence of the proposed stopes so that the specified *in-situ* field stresses (Table 6-2) may be taken to apply. Induced stresses were computed over a smaller portion of the computational domain, closer to the stoped areas with finer grid point spacing, for higher fidelity estimates. Figure 6-1 shows all 6 stopes considered and the dimensions of the domain and dimensions of stopes (all the stopes are assumed to have identical shape and size) in the Examine3D – Modeler environment.

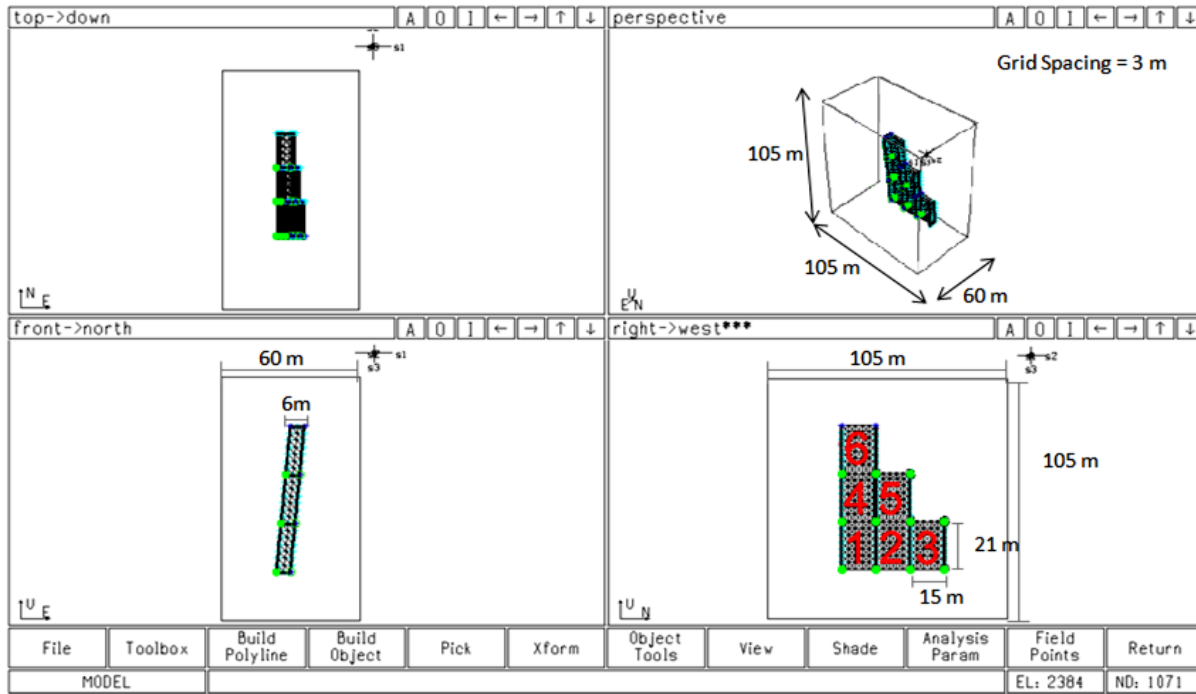


Figure 6-1: 6 designed stopes and their locations (lower right hand side). Stope meshes designed by Rhinoceros and imported into Examine3D for visualization, checking and mesh verification.

Rhinoceros 4.0 (McNeel, 2014) was used for meshing but mesh leakage was checked with Examine3D. Mesh sizes effect accuracy of the results and computation duration. The surfaces of the stopes, in Examine3D, were discretized by three-node triangular elements. Utilizing Rhinoceros 4.0 to produce a similar mesh, the Examine3D solver computes slightly different stress tensors at the element nodes; even though the mesh designed with Rhinoceros 4.0 is checked and accepted with Examine3D. This is because of the minor differences in the designed mesh from Rhinoceros 4.0 in comparison to that of Examine3D. This is illustrated in Appendix 7. As the Examine3D – Modeler is unable to operate with the AutoIt automation process Rhinoceros 4.0 that was used to do the stopes’ mesh design. In this regard, the differences associated with the results from the Rhinoceros 4.0 meshes and the Examine3D meshes were minimized by reducing the mesh size. Computational time had to be considered as well, since

time efficiency and computational efficiency of the analysis methodology is one of the main concerns of this work.

Consequently, the tradeoff between the degree of agreement and computational speed resulted in mesh size being set at 3 m. With this scheme, the final mesh design on the surface of each stope is presented in Appendix 7. Stress tensors calculated for each individual stope at 27216 grid points in the domain and at 144 node points on the surface of the stope and took 2 seconds with a PC running Windows 7, 32-bit, 2GB RAM and Intel (R) Core (TM) Duo CPU @ 2.16 GHz Processor. All BEM calculations necessary were thus completed in 12 seconds. As a check, the differences of calculated stress tensors when mesh is designed with Examine3D and designed with Rhinoceros 4.0 were computed and found to be nearly zero to all field points.

6.3 Computation of geomechanical response

When stress tensors at field points for each individual stope are computed (6 stopes so 6 individual stress fields), with the list of 720 different schedules of stoping events (all permutations of 6 stopeIDs from 1 to 6 as presented in Figure 6-1) and principle of superposition taken to hold, time series profiles of deviatoric stress for each sequence of stoping can be established for every location in the computational domain. Subsequently, elastic deviatoric strain time series are also calculated with Hooke's law and the assigned elastic properties from Table 6-1. The 3D Mohr–Coulomb failure criterion is applied to calculate strength (limit of deviatoric stress) and strainth (limit of deviatoric strain) at any locations in any sequences of stoping.

As mentioned earlier, a key assertion of this work is that the time-dependent behaviour of rocks and rock masses should be considered the norm, rather than a special consideration alone. Time-

dependent constitutive behaviour has special relevance for an optimization methodology that manipulates the sequence of stoping and the specific times that individual stoping activities are planned to commence and cease. Consequently, viscoelastic (deviatoric) strain time series were computed with the assumption of the 3D Kelvin-Voigt model and a viscosity of 40 TPa.s.

The time series presented in Figure 6-2 and Figure 6-3 show the expected response of the rock mass considering the rock mass to be both purely elastic (blue line) and viscoelastic (red line). The horizontal axis on each of these plots refers to the time at which stoping event is assumed to take place. The duration between excavations varies between 0.5 to 2 days. The stepped profiles are characteristic of the assumptions of instantaneous excavation and linearly elastic rock constitutive behaviour (with instantaneous stress redistribution following excavation). The green solid lines represent deviatoric stress and the dashed green lines are strength (limit of deviatoric stress); the blue solid lines represent elastic strain and the dashed blue lines are strainth (limit of elastic deviatoric strain). The viscoelastic strain curves, in red, exhibit time-dependent responses that converge on the elastic strain values.

Figure 6-2 shows the rock mass responses at grid point number 6267 for two different sequences of excavations: sequence 1 (1,2,3,4,5,6) on top and sequence 145 (2,3,1,4,5,6) on the bottom. The sequence IDs are according to the deterministic listing of 720 permutations of the 6 stoppe ID labels. As the two schedules of stoping that have been chosen (simply for explanation and illustration) share the same final stoppe, the state of stress at the end of the stoping schedule is the same for each schedule when it is assumed purely elastic. It is the same with strength and strainth. Comparison of these two sequences shows excavating stoppes according to a different schedule leads to a very different strain response at the same point whether elastic or

viscoelastic. Under these conditions, the instability metric devised for the purposes of mine schedule optimization may be based on how ‘close’ the actual strain develops to a maximum rupture strain. How this differs for the two schedules can be appreciated from the “closeness” of rock response curves to strength and strainth in two schedules at day 3. For sequence 145, there is a wide margin; for sequence 1, the margin is tight.

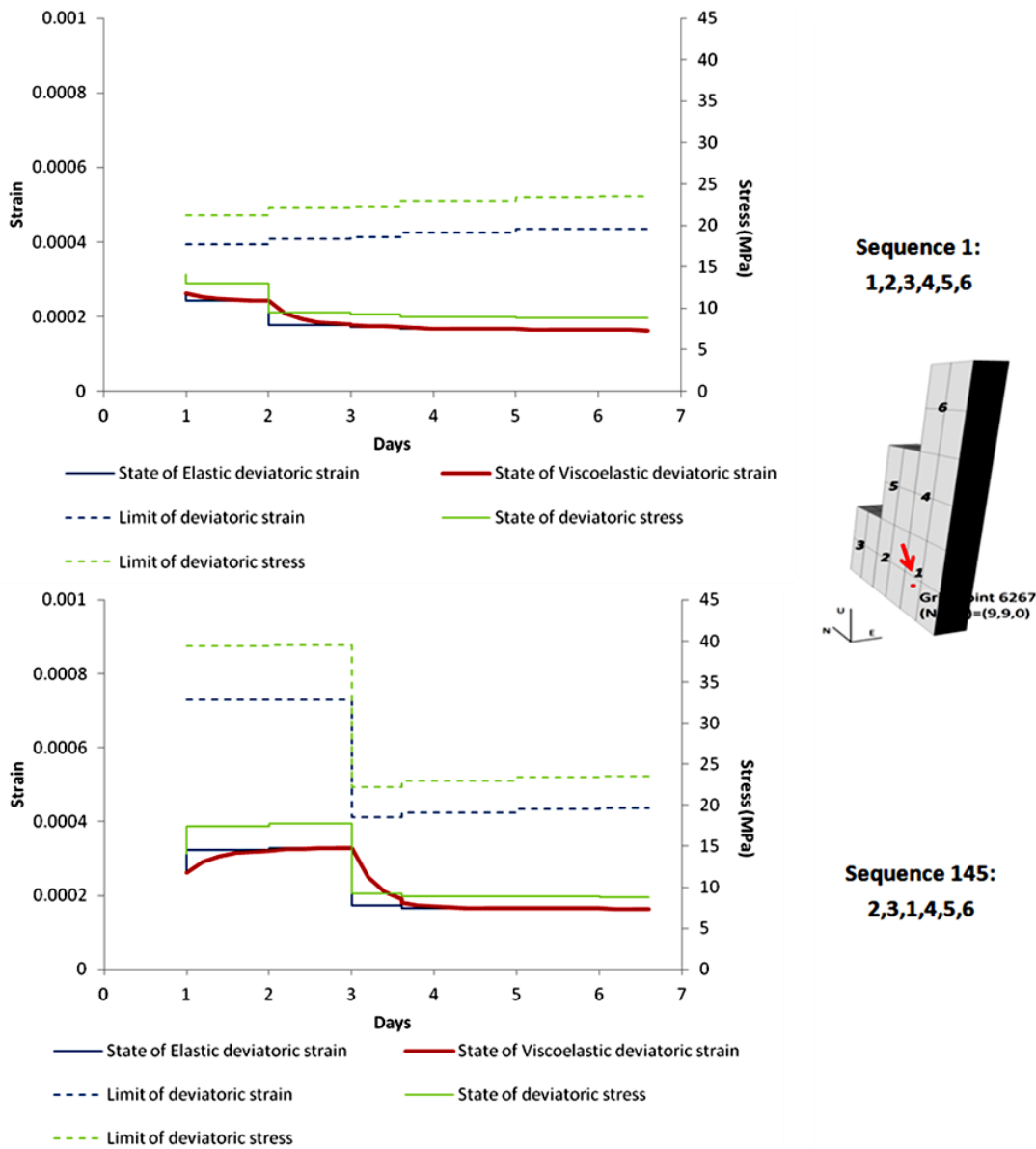


Figure 6-2: Time series of deviatoric stress and elastic/viscoelastic response of rock mass for grid point 6267 for two different sequences of excavations.

It is expected that different locations in the rock mass show different responses for the same sequence of excavations. Figure 6-3 the shows rock mass response in sequence 145 (2, 3, 1, 4, 5, 6) at a different grid point, grid point number 7590.

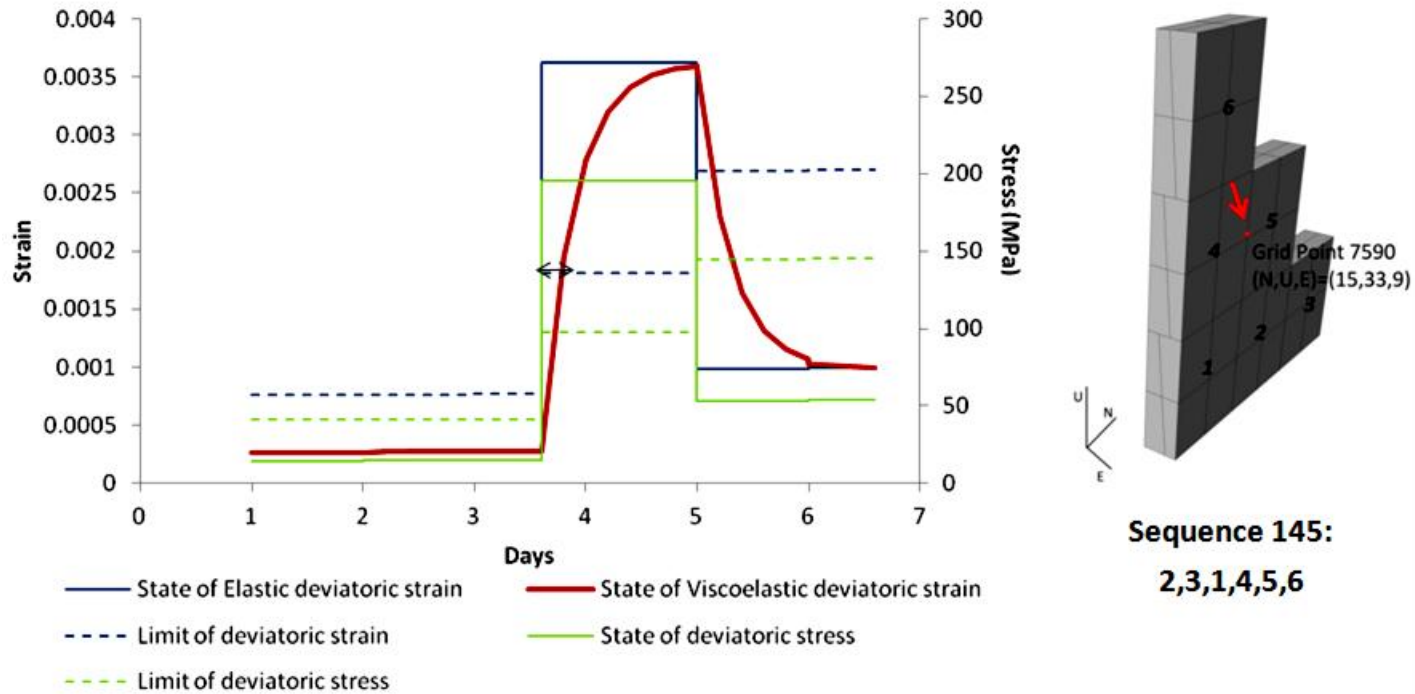


Figure 6-3: Time series of deviatoric stress and elastic/viscoelastic response of rock mass for grid point 7590 in sequence 145. Black arrow points out sensibility of viscoelastic strain in scheduling.

At day 3.5, a large perturbation occurs after excavation of stope 4, which causes deformation in the rock mass as presented with blue line if rock is elastic or with a red line if it is viscoelastic. Studying elastic and viscoelastic strain relative to strain rate leads to different decisions for mine scheduling. If rock is assumed to be elastic, rock will be unstabilized at grid point 7590, immediately after excavation of stope 4 at day 3.5, while the viscoelastic assumption, predicts failure for about a quarter of a day later. This point out the importance of decisions on duration between excavation activities. In current schedule, next perturbation occurs at day 5 when stope 5 is excavated; but if it was scheduled at any time before day 3.75, failure could be avoided if the

rock is viscoelastic. Grid point 7590 was specifically chosen to illustrate the concept explained in and around Figure 4-1 from numerical results.

Each of the time series just discussed applies to just one location in the rock mass. It is possible that a limited set of profiles from ‘representative’ locations within the computational domain may be used together to assess the superiority of one stoping schedule over another, but the approach being adopted in ongoing work is to use all locations within the domain so that a domain-wide indicator results.

6.4 Evaluation of stability metric

An automated procedure for production of such profiles provides a basis for (in)stability metrics to evaluate all schedules quickly; but a key aspect of the metric must be that it should be able to discriminate between schedules, and it should be able to indicate the superiority or inferiority of one schedule over another.

6.4.1 A simple example showing functionality of stability metrics

For a better illustration, some of the metrics are applied to geomechanical calculations presented in Figure 6-2 and Figure 6-3. Each of these statements can be applied based on any of the (in)stability indicators. For example when minimum measure of stability in the domain is considered, the safest schedule would be the one with the largest minimum value, this is a maxi-min criterion. If a maxi-min criterion is used to interpret the strength factors or strainth factors (they supposedly present same value), then it could perhaps be concluded that sequence 1 is superior to sequence 145; the minimum strength factors for grid points 6267 for sequence 1 is almost 1.5 at day 1 and for sequence 145 is almost 1.2 at day 3.5. The same can be concluded when studying viscoelastic-strainth Factor. Also (in Figure 6-2) the progressing of strength and

strainth factor as more stopes are excavated in sequence 1 is increasing; this is not observed in sequence 145. Consideration of average strength/strainth Factor will also distinguish between these two schedules at grid point 6267. Different results are expected if average VSF is considered since its values vary with time while strainth factor only varied when each excavation occurred. As presented earlier, different locations in the computation domain present different behaviours (e.g. grid points 6267 and 7590 in sequence 145). Some locations may be particularly prone to failure for example stope corners. Stability metric could be formulated to search for a schedule with minimum number of overstressed locations at each sequence of schedule. The strainth factor and VSF can give different answers as in the case discussed earlier for grid point 7590 at day 3.5 of sequence 145 (Figure 6-3).

What is presented above is a crude presentation of functionality of some choices of (in)stability metric to distinguish between schedules; an ideal evaluation of a schedule should be based on a wisely selected number of grid points in the rock mass.

6.4.2 Methodology to produce the instability metric

Different metrics might be applied individually or in series, also they might be applied only to selected grid points (referred to as census grid points); these are mainly procedural heuristics. Results of application of any of the metrics to census grid points using the geomechanical information database is presented with a new graphical device, which has been called an *indicator diagram*. Figure 6-4 is provided to illustrate the format of such diagrams. The horizontal axis refers to the time at which excavation activities occur. The vertical axis is the permutation index; each number on this axis refers to a different sequence of excavations based on the list produced with permutation processor (Appendix 4). The color bar on the right side of

the diagram is a legend which assigns different colors to different values of the metric e.g. for metric number 1, a blue color at any stage of any sequences of excavation means zero grid points with strength factor less than one. Each column shows results of application of a given indicator at each stage for all the different excavation schedules. These metrics are basically focused on changes in sequences rather than duration between excavation activities.

The indicator diagrams presented in Figure 6-4 are produced to support the scheduling of 6 stopes as there are 6 columns on the horizontal axis and 720 (=6!) schedules on the vertical axis.

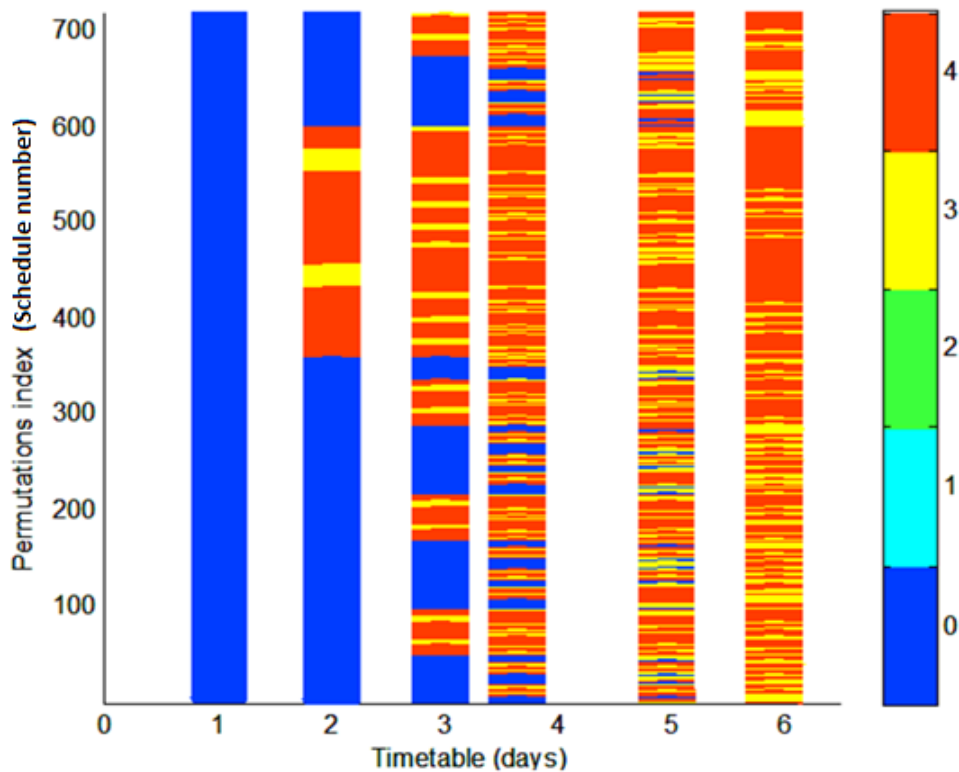


Figure 6-4: Presentation of (in)stability metric graphs' template.

6.4.3 Application of instability metrics on Lac du Bonnet granite

The stope model in this example consists of 27216 grid points. Computational efficiency makes evaluations at every grid point impractical. To reduce number of grid points, deviatoric stress distribution on the periphery of one individual stope when excavated with a blast was studied

and 26 grid points at the zones of both low stress concentration and high stress concentration were selected (presented in Figure 6-5).

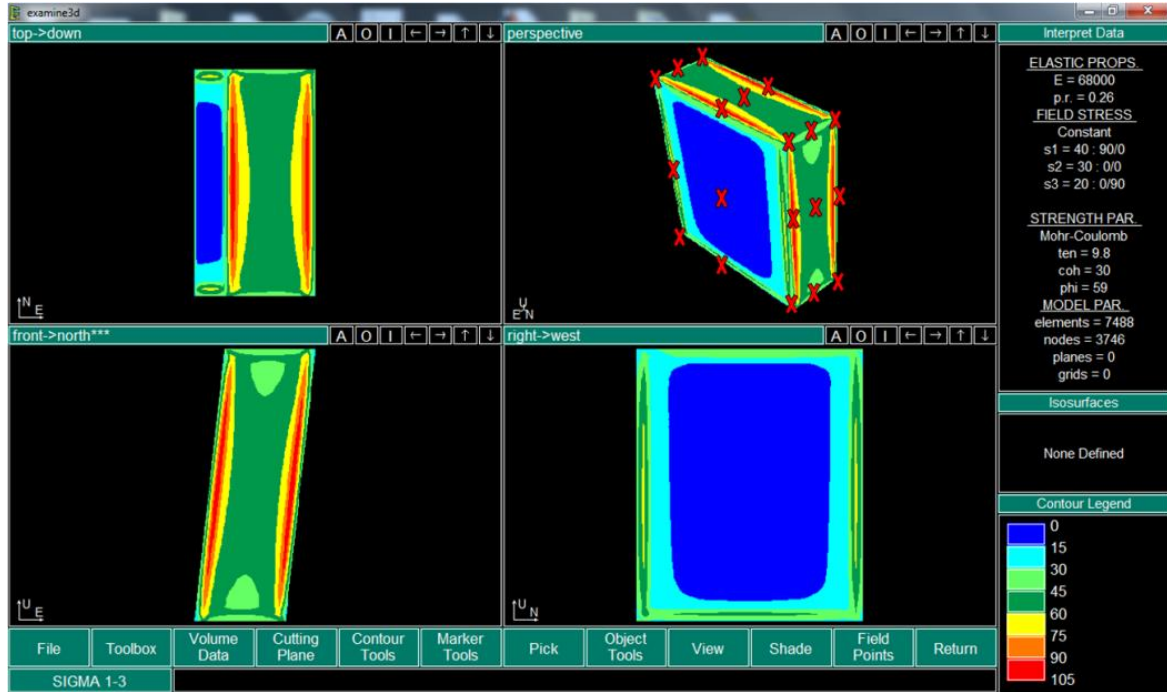


Figure 6-5: Deviatoric stress distribution on the periphery of one stope from the stope model computed with Examine3D.

In total, 111 census grid points around all 6 stopes were selected to be evaluated based on each of the (in)stability metrics. The resulting indicator diagrams arising from application of (in)stability metrics number 1 to 3 (Figure 6-6a, Figure 6-6b, Figure 6-6c) are discussed here. The rest are summarized in Table 6-3 with the remaining indicator diagrams provided in Appendix 7.

Table 6-3: Different choices of (in)stability metrics and their specifications.

(in)stability indicator	comments
Number of grid points with strength factor less than one	These three are calculated with a simple calculation procedure, which is also fast. However, they all are unable to distinguish a safe schedule from a safer schedule – when all census GPs are stable.
Number of grid points with strainth factor less than one	
Number of grid points with VSF Factor less than one	
Average strength factor over all grid points	These three require a longer calculation procedure compared to other metrics. They were potential to give the wrong impression of safety of a schedule; in the way that locations with the factor less than one can be covered with locations with large values of factors greater than one. These three may be good for discriminating between sequences of safe schedules.
Average strainth factor over all grid points	
Average VSF Factor over all grid points	
Minimum strength factor over all grid points	These three are easy and fast to calculate and are also discriminating.
Minimum strainth factor over all grid points	
Minimum VSF over all grid points	
Maximum strength factor over all grid points	These three are easy and fast to calculate; however, they do not care about unstable locations in the rock mass because they report the most stable location in the domain.
Maximum strainth factor over all grid points	
Maximum VSF over all grid points	

Figure 6-6a shows number of grid points with strength factor less than one, among 111 census grid points for all the different sequences of excavation. As more stopes are excavated, the number of grid points with strength factor less than one increase, in all sequence permutations – as expected. The metric, acts more discriminatively later on in the sequence. For example, at day 3.5 there are few sequences left with zero grid points with strength factor less than one.

Figure 6-6b shows number of grid points with strainth factor less than one among the 111 census grid points for all different sequences of excavation. As expected, using strainth factor (Figure 6-6b) and strength factor (Figure 6-6a) for the (in)stability metric gives exactly same indicator diagrams.

Figure 6-6c shows number of grid points with VSF less than one among 111 census grid points for all different sequences of excavation. There is more variation of color in this indicator diagram than those of Figure 6-6a and Figure 6-6b. This metric is acting much more discriminatively compared to other two metrics. For example at day 5, when there is only one stope left to be excavated in all different sequences, this metric has recognized a few sequences which still have zero grid points at risk of instability. Also in contrast to the assumption of linear elasticity, not all the sequences of excavation end with the same state. This example emphasizes the importance of consideration of time-dependent rock deformation in mine scheduling.

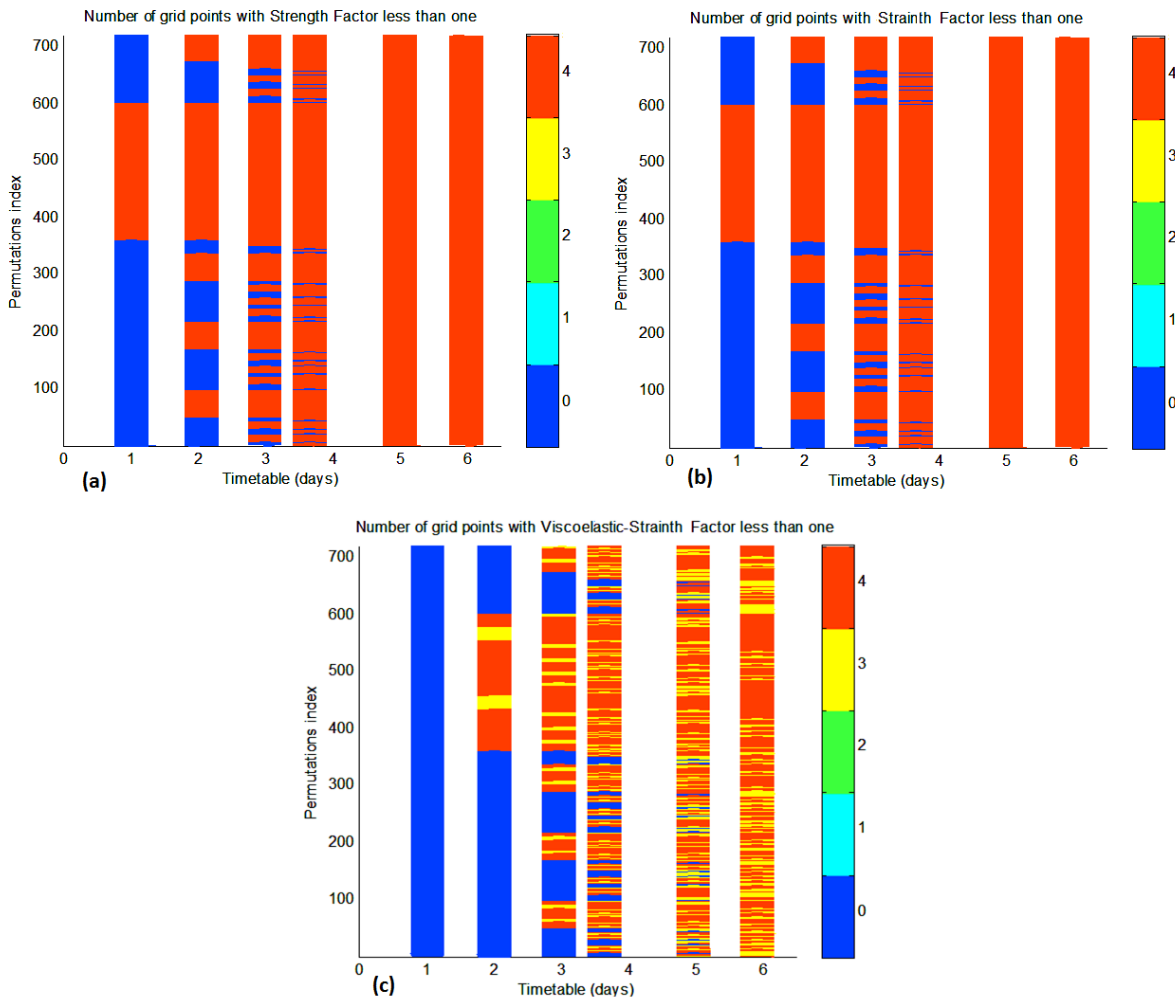


Figure 6-6: (a) Metric 1: number of grid points with strength factor less than one; (b) Metric 2: number of grid points with strainth factor less than one; (c) Metric 3: Number of grid points with viscoelastic-strainth factor less than one.

7 Stability analysis of a mine schedule including backfill activities

The methodology proposed in this thesis thus far, applies to the development of open stoping. However, backfilling is an undeniable part of any stoping procedure; backfilling is intended to enhance the stability condition in the surrounding rock mass. These circumstances motivated further development of the work presented in this thesis to accommodate the stabilizing effect of backfill within the development of (in)stability metrics.

The time limit of this M.A.Sc. program did not allow for full completion of this additional scope of work. Nevertheless, this chapter presents progress achieved to the date of submission on characterization and understanding of the problem, as well as an outline of a potential solution method.

7.1 Effect of fill on the elastic stress distribution in the rock mass

Backfilling is a passive support system; the fill emplaced inside the void is stress free and only becomes loaded when a perturbation (additional excavation) occurs in the rock mass. Figure 7-1 illustrates the sequence of excavating and backfilling two stopes in three stages, which are:

Stage 1: excavate the LHS stope,

Stage 2: backfill the LHS stope,

Stage 3: excavate the RHS stope to load the fill.

The fill is emplaced stress free in the excavated stope (LHS stope) and the stress distribution in the rock mass has remained undisturbed, compared to Stage 1. In Stage 2, the fill is not loaded until there is a further perturbation of the mining system through the ongoing excavation and the stress redistribution at stage 3. In this section, a series of numerical analyses are conducted to

examine the effect of the fill material on stress distribution in the rock mass at Stage 3 of the excavation.

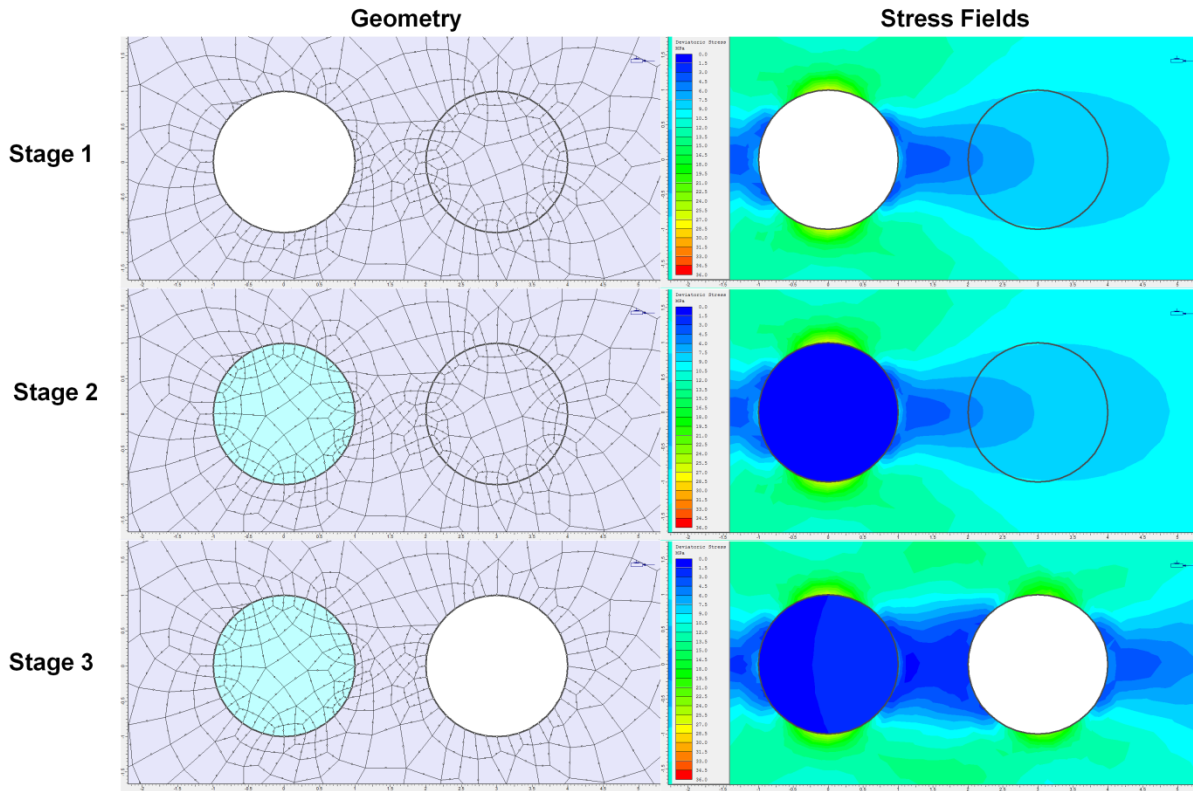


Figure 7-1: A sequence of excavating and backfilling two stopes in three stages. The figures on the left present the model geometry at each stage of excavations and the figures on the right present the deviatoric stress distribution at each stage of the excavation produced by Phase2.

7.1.1 Simulation set up

Brady and Brown (1993) state:

“Since Young’s modulus of a backfill is always low compared with that of a rock mass suitable for open stoping, the operational mode of the fill is unlikely to involve the global mobilization of support force in the fill mass.”

Numerical elastic stress analyses were undertaken to assess this statement in detail in the context of examining the effect of backfill emplacement on the elastic stress distribution of a rock mass.

The Young's modulus of the fill was assumed variable in this study, the central rationale for this being to assess the effect of the fill irrespective of the uncertainties is this key geomechanical parameter. Practically, simulations were run for different ratios of the Young's modulus of the surrounding rock mass ($E_{rockmass}$) to the Young's modulus of the backfill ($E_{backfill}$), and fill that was very stiff in comparison to the rock mass was also analysed for completeness.

For this purpose, series of excavating and backfilling sequences of two circular shape stopes were modeled in Phase2 (Figure 7-1). Each of the circular stopes is 2m diameter and is 1m apart; the stopes are located in each other's zone of influence. The meshing properties of the model are calibrated to match the computed stress distribution around a circular excavation with the analytical results from Kirsch equations (Kirsch, 1898). The *in situ* stress was set at 10 MPa uniaxial compression stress in x-direction, nil in y-direction and plain strain was assumed to apply.

The stress analysis was conducted for two different host rocks: a very stiff intact rock with the Young's modulus equal to 64 GPa (Lac du bonnet granite introduced in Table 6-1), and a rock mass with low stiffness equal to 0.6 GPa (the deformation modulus of a very weak rock, $RMR < 5$). The deformation modulus of the rock mass is calculated using the empirical relation (Equation 7-1) proposed by Serafim and Pereira (1983) for a very weak rock mass.

$$E_m = 10^{\frac{RMR-10}{40}} \quad [7-1]$$

where E_m is the mean deformation modulus measured in GPa (particularly in the range of 1-10 GPa) and RMR is the value of the rock mass rating, after Bieniawski (1989).

The stress distributions were computed for both host rocks across all three Stages with the backfill stiffness ranging from 0.6 GPa to 6000 GPa. The Poisson's ratio remained constant throughout: 0.26 for the rock mass and 0.25 for the fill. The tensile strength, cohesion and friction angle for the host rock and fill were set high enough to assure that neither plastified, so the solution remained elastic.

7.1.2 Simulation results

Table 7-1 presents the resulting deviatoric stress distribution at the last stage of the excavating and backfilling sequence for different ratios of R ($= \frac{E_{rockmass}}{E_{backfill}}$) to permit comparison with the deviatoric stress distribution when backfilling is not scheduled in the stoping sequence.

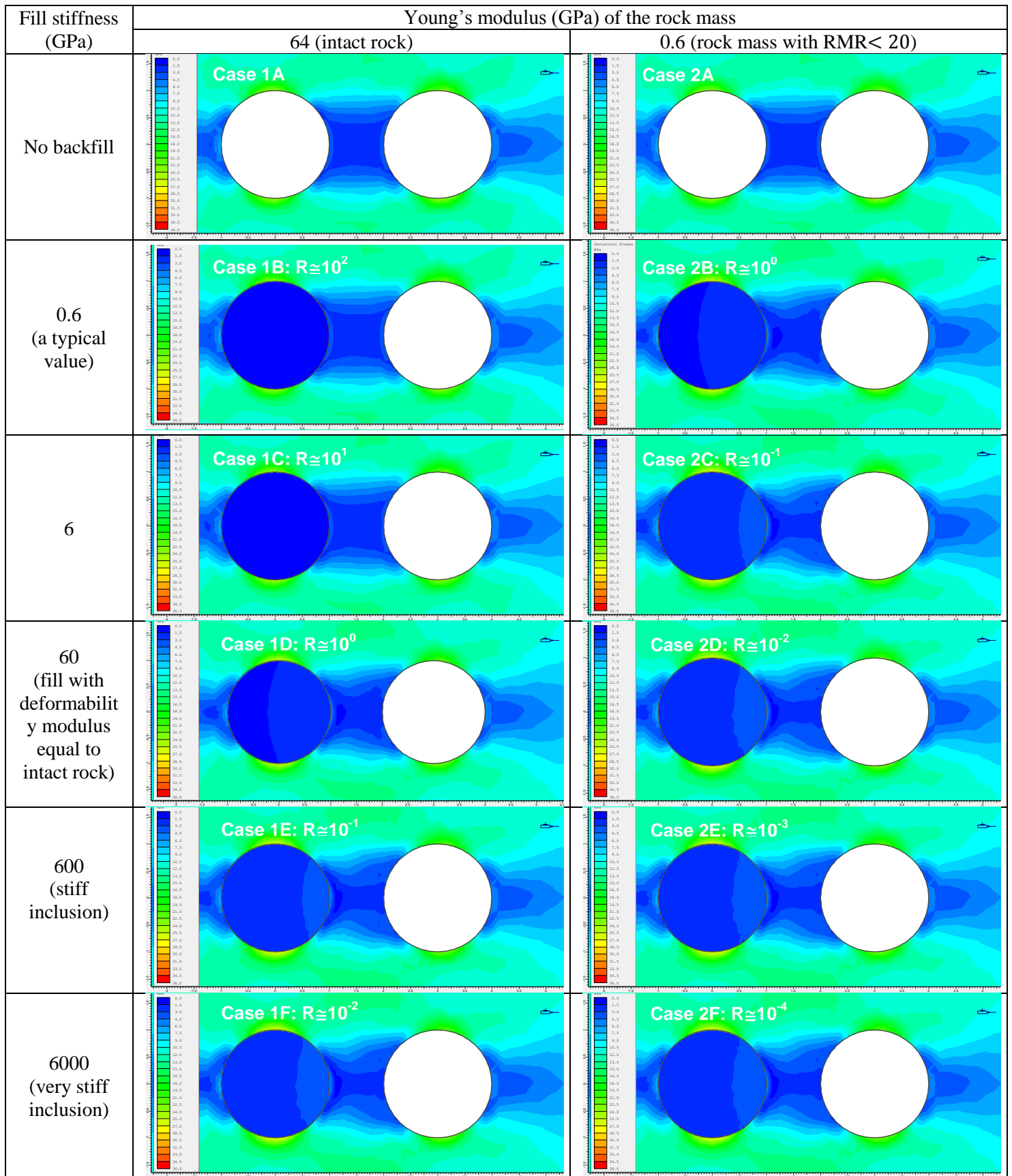
Under the conditions of the simulation, based on the results presented in Table 7-1 it can be observed that:

- i. Stress distribution around backfill depends on the ratio of the rock mass: backfill deformation moduli; R ($= \frac{E_{rockmass}}{E_{backfill}}$). Identical deviatoric stress distributions are recognizable for both the stiff rock mass and the compliant rock mass for the same values of R . As an example, compare 1D and 2B or 1E and 2C from Table 7-1.
- ii. Comparing the stress distribution around the backfilled stope (2B to 2F) and the open stope (2A), it can be observed that the backfill does not affect the stress distribution within the rock mass significantly, unless the back fill stiffness is greater than the rock mass stiffness ($R \leq 1$, cases 2C to 2F), which is a highly unlikely condition in the mining practice.

iii. The most likely situation in practice reflected in the cases reported in Table 7-1 is case 2B, where the rock mass stiffness and the fill stiffness are of the same order. Even in this case, when rock mass is stable, backfilling does not modify the stress distribution significantly, and only minor differences in stress contours are evident, and even then, mostly in the region between the two stopes. This finding is broadly consistent with the quote given earlier from Brady and Brown (1993); however, Table 7-1 suggests that the same conclusion may hold even when the stiffness ratios are close to unity.

Consequently, for the purposes of formulation of a geomechanical constraint to guide mine schedule optimization, it could be concluded that the effect of fill emplaced on the elastic stress distribution in the rock mass is negligible. However, before assuming this position definitively, in the remaining sections of this chapter, we present material that would be applicable if this conclusion was wrong.

Table 7-1: Deviatoric stress distribution around stopes showing effect of backfill on stress distributions for different values of $R (= \frac{E_{rockmass}}{E_{backfill}})$.



7.2 Stress distribution inside the fill

Within Table 7-1 it appears that the deviatoric stress distribution inside the fill is more or less homogenous. However, detailed inspection reveals minor variations, which are expanded upon in this section. One of the reasons for the modest fill response is that it is emplaced stress free, and only becomes loaded after excavation of another stope. Therefore, the discussion presented below which is relevant to the stope sequencing concerns of this thesis, refers to the stress field inside the fill after excavation of the second stope.

The fill material in the analysis presented in Table 7-1 remains elastic in all cases due to the values of strength parameters assigned: 100 MPa for tensile strength, 50° for friction angle and 300 MPa for cohesion in the Mohr-Coulomb failure criterion. From the results presented in Table 7-1, it is observed that for $R \geq 1$ (the case 1B and 1C from Table 7-1), deviatoric stress distribution inside the fill appears uniform and equal to zero. However, for the smaller values of R the stress field inside the fill are no longer uniform – sometimes a single contour crosses the fill area.

Table 7-2 presents the deviatoric stress distribution inside the fill when the Young's modulus of the rock mass and the stiffness of the fill are equal at 0.6 GPa (as in Case 2B of Table 7-1). In this new case, the strength parameters are progressively re-defined from a strong fill to a very weak fill. The results presented in Table 7-2 show that, in this example, the deviatoric stress field varies approximately linearly in the fill from 3 MPa to 0.6 MPa except when a very (unrealistically) weak fill material is considered, so that the deviatoric stress field is uniform inside the fill with a value of zero. It also can be observed that the deviatoric stress field in the pillar between the two excavated stopes remains identical for the stronger cases, indicating that

elasticity dominates. The exception is again for the very weak fill material: the deviatoric stress field between the two excavated stopes is symmetric and shows larger magnitudes of stress compared to the other cases in Table 7-2. The deviatoric stress distribution becomes symmetric because the fill cannot offer any reactive load at all – it is as if the first stope is unfilled.

Table 7-2: Deviatoric stress distribution inside fill. The rock mass elastic properties: Young's modulus=0.6 GPa, Poisson's ratio=0.26. The fill elastic properties: Young's modulus=0.6 GPa, Poisson's ratio=0.25.

Deviatoric Stress Field		Strength Parameters for M-C Failure criterion			
Strong Fill		Tensile strength (MPa)	100	Dilation angle (°)	–
		Friction Angle (°)	50	Friction angle (resid) (°)	–
		Cohesion (MPa)	300	Cohesion (resid) (MPa)	–
Weak Fill		Tensile strength (MPa)	0	Dilation angle (°)	–
		Friction Angle (°)	30	Friction angle (resid) (°)	–
		Cohesion (MPa)	0	Cohesion (resid) (MPa)	–
Very weak Fill		Tensile strength (MPa)	0	Dilation angle (°)	0
		Friction Angle (°)	0	Friction angle (resid) (°)	0
		Cohesion (MPa)	0	Cohesion (resid) (MPa)	0

7.3 Conceptualization of the fill mechanics

Brady and Brown (1993) put forward three different mechanisms to explain the interaction between the backfill material and the surrounding rock mass, which are presented in Figure 7-2.

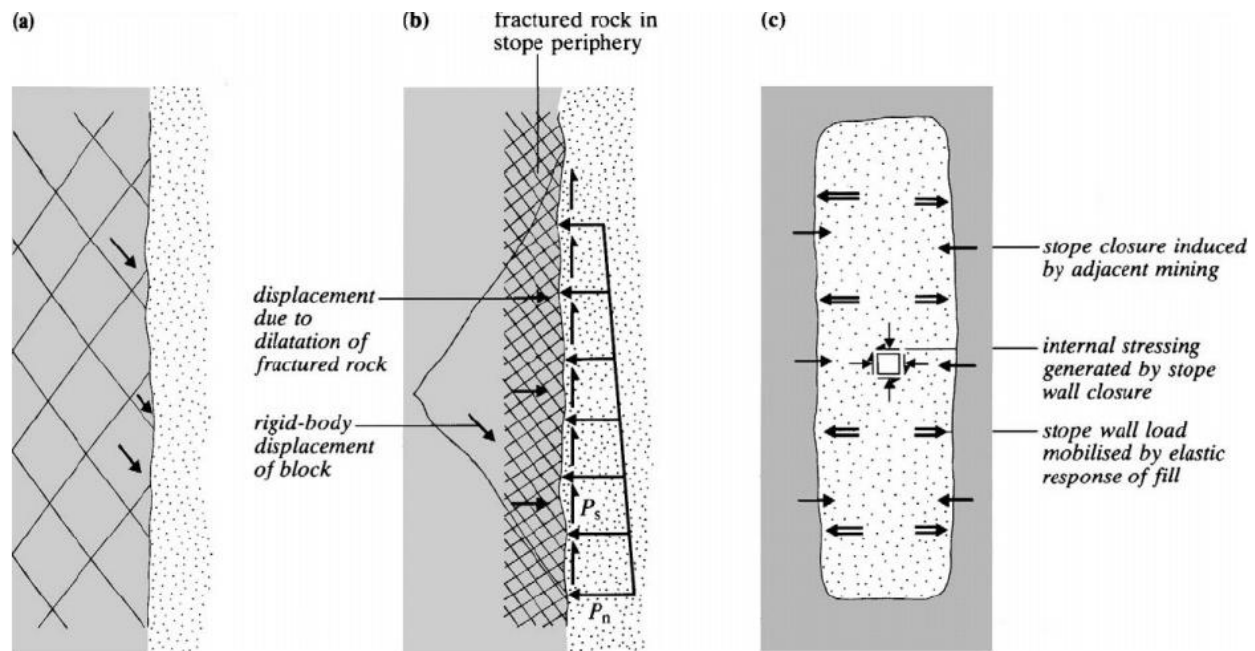


Figure 7-2: Modes of support of mine backfill: (a) kinematic constraint on surface blocks in de-stressed rock; (b) support forces mobilized locally in fractured and jointed rock; (c) global support due to compression of the fill mass by wall closure from Brady and Brown (1993).

The three mechanisms are as follows:

- i. Figure 7-2a shows the interaction of the fill material with the ‘key blocks’ of the surrounding rock mass. Without the fill, the ‘key blocks’ have potential to slide into the stope void. In such a case, backfill controls the displacement of the ‘key blocks’ by applying a kinematic constraint: there is simply no void for the ‘key block’ to slide into.
- ii. Figure 7-2b shows a condition in which the host rock on the periphery of the stope is highly fractured. The backfill maintains a small confining stress to the fractured and jointed rock mass by increasing friction and cohesion between the fractured pieces of rock. The small enhancement of confining stress makes the rock on the periphery strong enough to support itself.
- iii. Figure 7-2c is the case, in which a perturbation occurs in the rock mass and induces stress and consequently the rock mass deforms to reach a new equilibrium. The fill

reacts to the induced closure of the stope periphery and simply pushes back or impedes the progression of the closure of the stope's periphery.

All the three possible mechanisms of the backfill 'operations' show that, the fill tends to increase the stability of the surrounding rock mass. The important point to the note is that in all the cases, although the effect of the fill on the rock mass stress distribution is negligible (see section 7.1), the fill's principal effect is on the rock mass strength.

7.4 Corollaries of the analysis of the effect of backfill on the surrounding rock mass

- i. In the context of developing a metric for geomechanical instability in mine schedule optimization, fill would have little or no effect on the process of building up the stress time series using the principle of superposition, but the small tractions applied to the stope periphery from the fill may have a dramatic effect on the periphery strength and thus its stability. It is for this reason that it may be desirable to include even these apparently negligible effects of the fill loading on the rock mass stress distribution. This confirms part of the idea presented by Brady and Brown (1993) which says:

“Any conceivable, realistic support pressure at an excavation surface can have only a negligible effect on the elastic stress distribution in a rock mass.”

- ii. The magnitudes of the reaction pressures offered by the fill are such that the fractured zone that develops around the periphery of the stopes would occur whether fill is emplaced or not. However, the modest confining force offered from the fill on the peripheral fracture zone would increase the strength of the fractured rock to help the rock support itself.

- iii. Therefore, the effect of backfill still remains a concern due to the (in)stability evaluation elements of the proposed methodology (explained in Chapter 5).

The remainder of this chapter reports on the methodologies, which could possibly lead to integration of the backfill effect with the current automated procedure proposed for (in)stability evaluation for different stopping schedules.

7.5 Integrating the backfill effect with the current superimposition methodology

This section briefly reviews some of the proposed approaches to similar problems. Next, the methodology suggested by this author is explained.

7.5.1 Approaches for the stress field calculation around inclusions

Assuming that the rock mass is a continuous, homogenous, isotropic and linear elastic material, backfill can be interpreted as an inclusion embedded in an infinite medium, which produces an inhomogeneity.

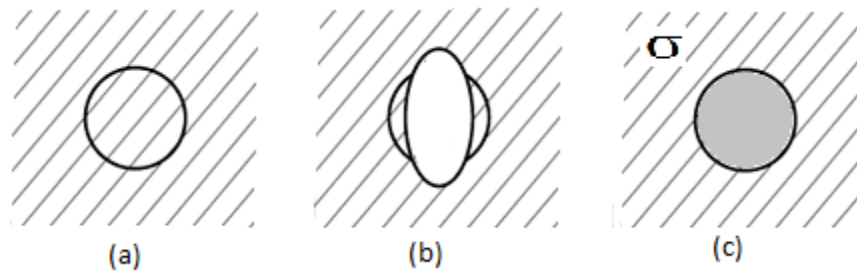


Figure 7-3: Schematic presentation of Eshelby's inclusion problem. (a) is an unloaded homogeneous infinite medium of moduli (b) a region of this medium (the inclusion) is submitted to a free strain (c) deforming the inclusion to its original shape and size induces stress in the medium (Eshelby, 1957).

Various analytical solutions have been proposed to study the stress distribution in and around inhomogeneities and some of them are briefly mentioned below:

- i. Brady and Brown (1993) considered the application of the principle of superposition to determine the effect of a uniform vertical support load on the stress distribution around the elliptical openings.
- ii. Deryugin and Lasko (2012) studied the stress distribution in an isotropic plane with a circular inclusion under uniaxial tensile stress.
- iii. Jin *et al.* (2009) corrected typo errors in the published equations proposed by Deryugin and Lasko (2012) and extended their work for the square shaped and rectangular inclusions.
- iv. Misseroni *et al.* (2014) employed a photoelastic methodology and validated analytical stress calculations near rectangular and rhombohedral inclusions embedded in the elastic plates.
- v. Zeng (2012) used the principle of superposition and Eshelby's inclusion phenomena (Figure 7-3) to study the inhomogeneities.

The seminal work to analyze the effect of an inclusion in the stress field of a homogenous matrix was done by Eshelby (1957) and all of the aforementioned work relates one way or another on the Eshelby's work. The schematic presentation of Eshelby's inclusion problem is presented in Figure 7-3.

The cons and pros of the abovementioned methodologies are presented in Table 7-3, following the detailed investigation of each one of them that was undertaken as part of the research.

Table 7-3: The cons and pros of some of the methodologies suggested for stress analysis around inclusions.

The methodology	Positive points	Negative points
Brady and Brown (1993)	Useful explanatory example	Uniaxial support loading Unclear description of the method
Deryugin and Lasko (2012)	Can be used to compute stress fields for use in the superposition methodology, if the inclusion material is not stress free when emplaced	The solution is for uniaxial tensile stress only. Stress distribution inside the inclusion (fill) is uniform. Inclusion is not emplaced stress free so it is insensitive to further perturbations. It is a plain stress solution.
Jin <i>et al.</i> (2009)	Considers polyhedral inclusion shapes	Inclusion is not emplaced stress free so it is insensitive to further perturbations
Misseroni <i>et al.</i> (2014)	Informative, instructive and practical examples that can be used to verify analytical methods	It is not a computer analysis technology. Considers a stiff inclusion whereas in this mine scheduling application, stiffness of the fill is never greater than the rock mass Young's modulus.
Zeng (2012)	Explains the inhomogeneity condition based on the Eshelby's transformation problem (1957)	Too complex to include in the methodology

7.5.2 The proposed approach for modeling backfill in the superposition procedure

To briefly reiterate, for clarity, a sequence of excavating and backfilling two stopes consists of three stages (Figure 7-1):

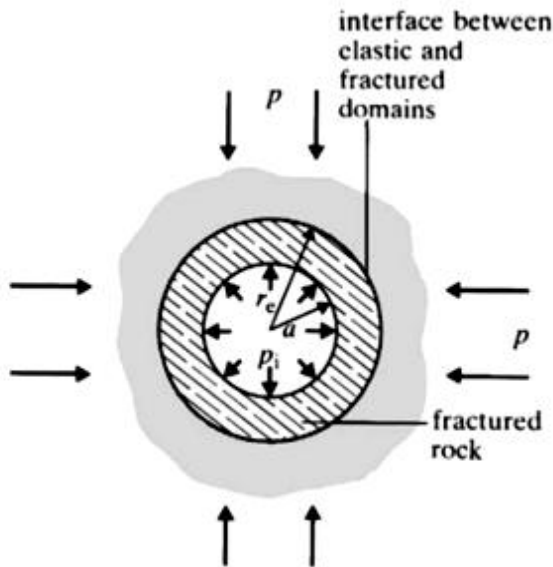
- i. Excavating stope 1: The stress field redistributes in the rock mass and consequently rock mass deforms to reach a new equilibrium.
- ii. Backfilling stope 1: The stress free fill material emplaces in the rock mass and the field stresses remain unchanged. The weight of the fill is ignored.
- iii. Excavating stope 2: The stress field redistributes and consequently rock mass deforms to reach a new equilibrium. The fill in stope 1 becomes loaded (modestly).

The displacement on the periphery of the fill material is equal to the displacement of the rock mass on the periphery of the stope 1 (a condition of the strain compatibility required for a continuum, irrespective of whether it is homogeneous or not). Under the displacement equality condition, a set of tractions arises on the periphery of the stope 1. The stress field in the rock

mass arising from these tractions may be superimposed on the stress fields for the two excavated stopes to account for the effect of the fill.

Two approaches are proposed to estimate tractions on the near-field boundary of the fill:

Approach one:



$$p_1 = p_i \left(\frac{r_e}{a} \right)^{d-1}$$

$$d = \frac{(1 + \sin \phi_f)}{(1 - \sin \phi_f)}$$

Figure 7-4: Stress distribution around a circular opening in a hydrostatic stress field (p), due to development of a fracture zone. p_i is the support pressure, a is the opening radius, r_e is the fractured zone radius, p_1 is the radial stress at the elastic interface and ϕ_f is he angle of friction for the fractured rock.

Brady and Brown (1993) described an example of a circular opening excavated in a hydrostatic *in situ* stress field (Figure 7-4). A ring shaped fracture zone develops on the periphery of the opening as the internal support pressure is reduced. Assuming that the rock stability condition is defined with the Mohr-Coulomb failure criterion, the stress distribution on the interface surface between fractured zone and the elastic domain, p_1 , can be established in terms of the radius of the failed zone (r_e) and the internal support pressure (p_i) and the friction angle of the fracture zone (cohesion of the rock in the fracture zone is assumed lost). For the detailed solution, the reader is directed to the page 219 of Brady and Brown (1993).

In the automated methodology proposed in this thesis requiring that the principle of superposition hold, the fracture zone developing on the periphery of the excavation cannot be considered (because it represents localized plasticity). However, inspired by Brady and Brown (1993) methodology, the strength properties of the fill could replace the strength properties of the fragmented rock; so that stress distribution on the elastic (stope periphery) boundary can be calculated.

For instance, assuming an extreme case where the Young's modulus of the surrounding rock mass is equal to the deformation modulus of the fill, and a very weak rock mass, the deviatoric stress on the periphery of the elastic domain based on Brady and Brown (1993) could be established as follows.

With the strength parameters of, tensile strength (σ_t) = 0 MPa, Cohesion = 0 MPa and Friction angle (ϕ_f) = 30°, the strength of the fill material is assumed purely frictional. Based on the Mohr-Coulomb failure criterion the limiting deviatoric stress within the fill material would be:

$$\sigma_1 = \frac{(1+\sin \phi_f)}{(1-\sin \phi_f)} \sigma_3 \rightarrow \sigma_1 = \frac{(1+\sin 30)}{(1-\sin 30)} \sigma_3 \rightarrow \sigma_1 = 3\sigma_3$$

and $\sigma_d = \sigma_1 - \sigma_3 = 3\sigma_3 - \sigma_3 = 2\sigma_3$.

These would be the values of tractions applied to the periphery, in a second BEM model of an individual stope.

Approach two:

Assume that the fill is such a weak material, that it cannot sustain a shear stress, so that it behaves effectively as a compressible fluid. Under these conditions the stress distribution on the

periphery of the fill would be uniform and hydrostatic, magnitude unknown, but likely to be small. The magnitude of p could be assigned a constant plastic residual strength of order of 1 to 3 MPa (Brady and Brown, 1993).

7.5.3 Integration of the backfill effect with the current superimposition procedure

The current superimposition procedure is as Figure 7-6a. The knowledge of the fill boundary condition based on the second approach, presented in the previous section, leads to defining a component stress field to accumulate with the previously calculated stress fields. This component is a backfilled stope embedded in the rock mass. The boundary condition of this additional component is presented in Figure 7-5. The near-field boundary condition is uniform and equal to p , normal to the periphery of the fill, because the fill material is assumed to behave as a compressible fluid. The far-field boundary condition is set to zero. The stress fields for the case presented in Figure 7-5 can be computed with Examine3D, by assignment of values for the field stresses and the surface tractions in the '*.ex3' files produced by the VBA macro listed in Appendix 3.

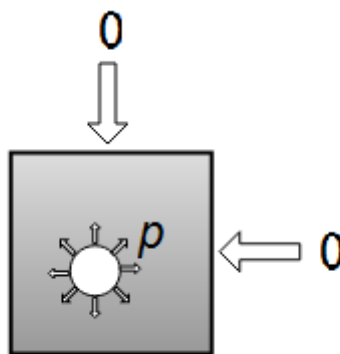


Figure 7-5: The additional element to complete superposition procedure. The far field boundary condition is equal to zero and the stress distribution on the periphery is uniform and hydrostatic.

The proposed procedure to model the fill effect only needs one additional BEM calculation for each stope. Regardless of the timing of the backfill emplacement otherwise governed by the schedule, the stress distribution on the boundary of the fill material would be equal to p because this represents a plastic strength that can never get higher, irrespective of the number of perturbing excavations. Thus for n stopes, $2n$ individual stress fields should be computed with the BEM, in total. The computed stress field arising from the plastic tractions on the stope periphery adds to the other stress fields after a stope is scheduled to be backfilled and one further stope is excavated. The current superimposition procedure presented in Figure 7-6a is upgraded to Figure 7-6b. This methodology simply integrates the effect of backfill with the current proposed automated procedure and does not significantly penalize the time and computational efficiency of the methodology ($2n$ BEM analyses rather than $n!$).

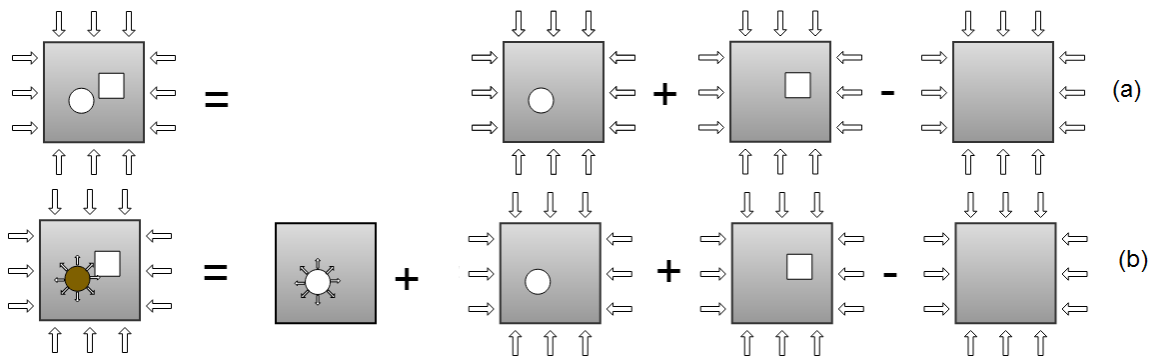


Figure 7-6: The current superimposition procedure (a) is upgraded to the superimposition procedure (b) regarding to the backfill effect on the stress distribution.

7.6 Summary

The backfill effect is missing in the current stability analysis presented in this work. Although the effect on the stress distribution is small, the effect on strength of the rock mass is significant. Various solutions have been reviewed to establish the stress distribution in the inhomogeneities that the filled stopes constitute, embedded in the rock mass. The work in this chapter theorized a

technique to complete the proposed automation process for development of (in)stability metrics to accommodate the effect of backfill. Ultimately, the solution reduced to one more BEM computation undertaken per slope in the scheduling sequence, where tractions equal to the plastic strength of the fill are applied to the slope periphery, within a medium with zero field stress. Implementation of the proposed procedure and proof of its efficacy remain future work.

8 Conclusions and recommendations for future work

Schedule Optimization Tool (SOT) assists with the long-term underground mining schedule optimization and maximizes the NPV of the mining project subject to changes in the precedence and duration between mining activities. SOT is being extended to SOT+, which updates the schedule optimization constraints according to the ventilation and the geomechanical aspects of mining project. This thesis reported an approach for development of the geomechanical constraints to be integrated with SOT+, exclusively for the scheduling of the stoping sequences.

In this chapter, a summary of the steps towards the development of the geomechanical constraints along with the conclusions and the suggested future works are presented.

8.1 Summary and conclusions

This work started with a numerical analysis of the elastic stress distribution in different sequences and timetables of stoping activities, defined in a hypothetical schedule. The induced stress fields after each stope excavation (each stope assumed excavated with one blast) distributed instantaneously. With the assumption of linear elasticity, the consequent deformation after each perturbation (stope excavations) correspondingly occurred instantaneously. This scope of the work lead to the conclusion that based on the settlements of the sequence and the duration between stoping events, the (in)stability conditions in the rock mass surrounding the stopes periphery can be postponed or even avoided. This is detailed in Saeidi *et al.* (2014).

A core hypothesis of the work was that there is a time-dependent aspect of the rock behaviour, which leads to unexpected instability conditions, a consequence of dependence of geotechnical instability upon the sequence and duration between stoping events. Mine seismicity data, creep

test data and stope convergence data, presented in Chapter 2, all supported the idea that the deformation response of the surrounding rock mass to the excavation activities is time dependent. The reasons that this behaviour occurs are not explained in detail in this work. It is just assumed as an accepted fact at the scale of modeling undertaken.

Based on the mentioned notations, the target was set for studying the rock mass (in)stability conditions in all the stoping schedules ($n!$ sequences for excavating n stopes) hoping that the work could lead to sensible definition of an appropriate geomechanical stability indicator on which to base the constraints, in order that the high value schedules were also those for which geotechnical risks were reduced or avoided. The work reported, developed an automated procedure for the formulation of such a geomechanical constraint. Thus, the approach presented in this thesis represented a compromise, exemplified by a step-by-step procedure to define the geomechanical constraint in the case of a schedule of 6 stopes:

1. The elastic stress fields induced by the individual stoping activities were computed for each excavation activity independently within an identical computational domain to that of all the others. The boundary element tool, Examine3D was adopted for the stress field computations while Rhino 4.0 was adopted for the mesh design. The Rhino outputs were manipulated to a readable format for Compute3D using a VBA code provided in Appendix 3. This whole procedure executed in an automated fashion, the script for which is presented in Appendix 4.
2. The resulting stress fields are stored in a database. The instability risk for a specific sequence of the stoping activities is assessed through progressive superimposition of the stress fields drawn from the pre-computed database. For the specific locations within the computational domain, the aggregate effect of the sequence of stoping events lead to the

stress-time histories having a stepped appearance, a result of the near instantaneous response of an elastic medium to the excavation perturbations. The elastic deformation responses were computed through the application of Hooke's law to the stepped stress time histories.

3. The time-dependent deformation responses were allowed for by the re-profiling the stepped stress time histories through application of a viscoelastic rheological model with the appropriate values of the coefficients. Based on the material provided in Chapter 3, the challenge for simulation of the time-dependent behaviour of the rocks reduces to the choice of the coefficients (detailed in Saeidi and Millar (2015)) for any rheological model. The 3D Kelvin-Voigt model from Picard (2007) was adopted for defining the time-dependent deformation responses since it conveniently 'fit' with the elastic stress superposition techniques, was one of the very few that describes viscoelastically in a fully 3D manner, and required just a single viscous parameter to do this.
4. The time history graphs (stress time histories, elastic strain time histories and viscoelastic-strain time histories) formed the basis for a geomechanical constraint formulation adopted for the mine schedule optimization procedure. For this purpose (in)stability indicators were introduced for each of the three types of time histories to report the instability with any value below unity. The (in)stability indicators are entitled: '*Strength Factor*' (when studying stress time series), '*Strainth Factor*' (when studying elastic strain time series) and '*Viscoelastic-strainth Factor*' (when studying viscoelastic strain time series).
5. For a comprehensive evaluation of all the locations in the computational domain, 12 '*instability diagrams*' were generated to represent a statistical metric of each of the three

(in)stability indicators for different schedules of stoping. The 12 '*instability diagrams*' varied in terms of maximum, minimum and average of the (in)stability indicator either among all locations or at a specified set of grid points, with instability indicator value below unity within the computation domain. The procedure of the formulation of the 3 indicators and 12 metrics is detailed in Chapter 5 and the MATLAB script for the entire arithmetic is presented in Appendix 5.

6. The choice of the (in)stability metrics recommended are those base on the '*Viscoelastic-strainth Factor*' , but the simpler indicators are also available for less advanced analysis. The resulting '*instability diagrams*' are presented in Appendix 7.

The proposed procedure allowed for instability calculation of 720 (=6!) possible sequences of excavating the 6 stopes as an example. This took a few seconds with a PC running Windows 7, 32-bit, 2GB RAM and Intel (R) Core (TM) Duo CPU @ 2.16 GHz Processor. However, at the scale of the mining activities for potentially hundreds of stopes, n , it is not practical to search for the best geotechnical stoping schedule through exhaustive enumeration. The ' $n!$ ' permutations is a very large number of the solutions in the solution space in which to find the best sequence of n stopes with this method. But, SOT's optimization procedure to find the best schedule, even now, only 'visits' a small fraction of the set of the accessible schedules, because of the precedence constraints that apply. These practically reduce the number of feasible solutions (schedules) substantially. This is explained in section 5.6.

In the presented work, conceptually each stope is assumed to be excavated with one-blast while in reality stopes are excavated with multiple blasts. This does not interfere with applicability of the proposed methodology since each step in the calculated stress time series arises from an

event (blast) and a complete stoping process can comprise the blasting of several rounds in the stope. In effect, Figure 6-1 could be apply equally to a mining district with six stopes, or a single stope with six rounds – depending on scale. Figure 8-1 shows that development activities can be treated similarly too.

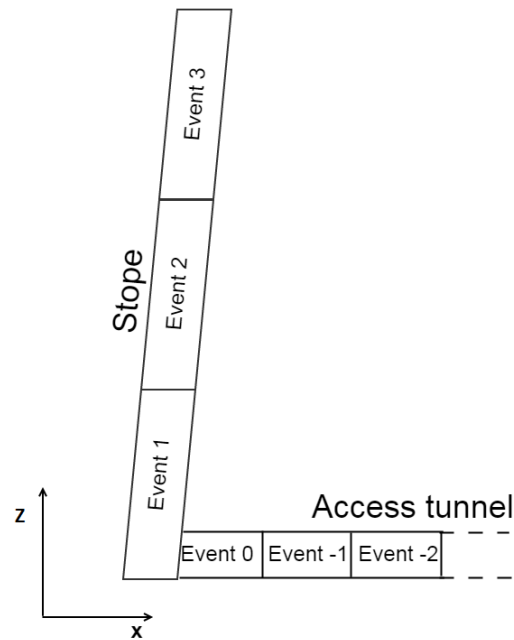


Figure 8-1: Schematic presentation of an access tunnel and a stope excavated in a sequence of blasts: event -2, event -1, event0, event1, event2, event3.

The stope presented in Figure 8-1 is scheduled to be excavated in a sequence of 3 blasts. For the purpose of calculating the stress field induced after excavation of this stope, each blast can be considered as an event with zero duration and their stress fields aggregate in the sequence: event 1, event 2, event 3 corresponding to the event schedule. As the result, the effect of the stope excavation would be presented with three steps in the time series.

Additionally, Figure8-1 presents an access tunnel, which has been progressively excavated in a sequence of blasts: event -2, event -1, event 0, scheduled prior to stope excavation. Even though the excavation of access tunnels is classified as development activity, their effect on stress fields

can be monitored using principle of superposition. Similarly, the effect of each of these blasts on the stress redistribution can be aggregated to the other stress fields at differing or similar time labels depending on the schedule. The proposed methodology thus far, applied for (in)stability evaluations of open stoping schedules. Chapter 7 reported an investigation on the effect of backfilling activities on the stress distribution and (in)stability conditions in the rock mass. It concluded that the fill has a negligible effect on the process of calculating the stress time series using the principle of superposition but a significant effect on the strength, *strainth* and *VSF* of the surrounding rock mass. In this regard, for the purposes of the (in)stability indicators evaluated in this work, an approach was theorized to integrate, through superimposition, the effect of fill loading on the stress distribution in the rock mass. The theorized methodology involved computing the stress field around a stope geometry with a traction free far field boundary condition and a uniform and hydrostatic near field boundary condition, of a magnitude equal to the plastic fill strength. These stress fields can also be computed with Exmine3D and accumulated with the previously computed stress fields.

The procedure described in this thesis results in a timely and computationally efficient calculation procedure, which develops the instability metrics for evaluation of the geomechanical stability for every feasible sequence of excavating a series of stopes if required. Even when the fill effect is considered, the computational effort only increases to ' $2n$ ' rather than ' $n!$ ' for the ' n ' stopes. The results of the analysis reported in the form of '*indicator diagrams*', which reveals the most geomechanically stable schedule.

8.2 Recommendation for future work

The author of this thesis recommends further work in three areas:

Scope1:

For the purpose of fulfilling geotechnical considerations in SOT+ optimization process, the 12 defined (in)stability metrics have to be formulated in the form of constraints to integrate with the SOT+ optimization algorithm. As the result, the high value schedule, which increases the profitability of the mining project as well as decreasing the risk of rock failure, would be obtained.

Scope2:

One of the productions of this work was a threshold value for the rock mass deformation, '*Strainth*'. This threshold is certainly a valid measure if the rock is purely elastic however, it may be an estimated measure when the rock is viscoelastic. There are two suggestions for checking the validation of the '*Strainth*' threshold for viscoelastic deformation:

- i. To generate the threshold curves similarly as viscoelastic strain curves by manipulating 'Strength' with the 3D Kelvin-Voigt model and its relevant viscous coefficients. This would produce a viscoelastic threshold, supposedly called '*Viscoelastic Strainth*';
- ii. To feed the viscoelastic strain tensors, from the 3D Kelvin-Voigt model, into the strain-based Mohr-Coulomb failure criterion and calculate the viscoelastic threshold, '*Viscoelastic Strainth*'.

For either of the ways, the new threshold is expected to be present a different interpretation of the stability condition of the timetable of the stoping activities. Figure 8-2 is a schematic explanation of this new threshold when evaluating stability conditions at one point in the rock mass. The information on the time axis refers to the time at which a new opening adjacent to the

point of consideration is excavated. The blue line shows the expected response if the rock mass is purely elastic. The red line refers to a maximum permissible strain of the rock mass at the point of consideration, '*Strainth*', calculated from the strain-based 3D Mohr-Coulomb failure criterion. The dashed blue line refers to the viscoelastic strain and the dashed red line is the hypothetical '*Viscoelastic Strainth*'. After a large perturbation (presented in Figure 8-2), the assumption of linear elasticity predicts a failure immediately after the perturbation occurs, while the viscoelastically shows a time gap arises between the time at which the perturbation occurs and the time at which the failure occurs. This gap is expected to be 'a' units of time if the measure of (in)stability is '*strainth*', and 'b' units of time if the measure of (in)stability is '*viscoelastic-strainth*'. Repeated assessment of times 'a' and 'b' from numerous case studies will verify the accuracy of the framework proposed.

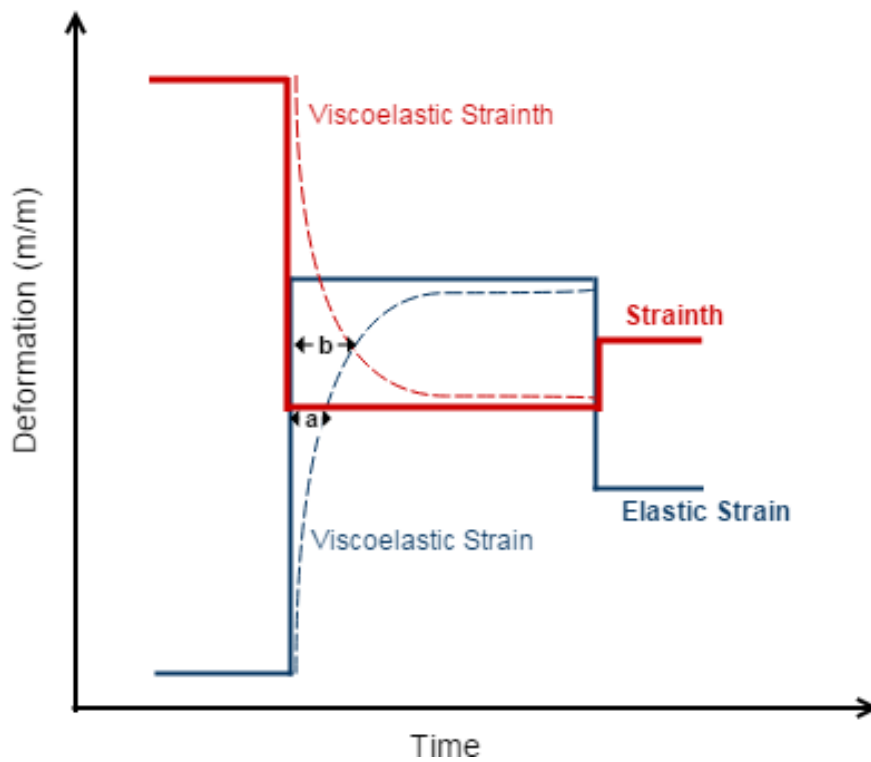


Figure 8-2: Schematic presentation of the 'viscoelastic strainth' compared to the 'strainth'. 'a' is the difference between the failure time for the elastic and the viscoelastic rock responses if the threshold is '*strainth*', and 'b' is the difference between the failure time for the elastic and the viscoelastic rock responses if the threshold is '*viscoelastic-strainth*'.

Scope3:

The theorized methodology presented in Chapter 7 seems a legitimate guide to study the effect of fill on the stress distribution and strength of the rock mass, for the sequences of stoping and backfilling that assumes the framework of superposition principle. However, implementation of the proposed procedure and the proof of its efficacy remain future work. The case study presented in Chapter 6 is suggested to be analyzed with the updated methodology so that the results can be compared with the '*indicator diagrams*' presented in Appendix 7.

References

- Adams, G., Jager, A., 1980. Petroscopic observations of rock fracturing ahead of stope faces in deep-level gold mines. *African Institute of Mining and Metallurgy*, Volume 80, Issue 6, pp. 204-209.
- Aksoy, C. O., 2008. Review of rock mass rating classification: historical developments, applications, and restrictions. *Journal of Mining Science*, Volume 44, Issue 1, pp. 51-64.
- Alford, C., Brazil, M., David H., L., 2007. Optimisation in underground mining. In: A. Weintraub, C. Romero, T. Bjørndal & R. Epstein, eds. *Handbook of operations research in natural resources*. Volume 99 of the series of International Series In Operations Research amp; Mana: Springer US, pp. 561-577.
- Alfrey, T., 1944. Non Homogeneous stresses in viscoelastic media. *Quarterly Applied Mathematics*, Volume 2, pp. 113-119.
- Anderson, D. R., Sweeney, D. J., Williams, T. A., 1994. *An introduction to management science*. 7th ed. St. Paul: West publishing company.
- Ataee-pour, M., 2005. A critical survey of the existing stope layout optimization techniques. *Journal of Mining Science*, Volume 41, Issue 5, pp. 447-466.
- Ayden, O., Tokashiki, N., Ito, T., Akagi, T., Ulusay, R., Bilgin, H. A., 2003. An experimental study on the electrical potential of non-piezoelectric geomaterials during fracturing and sliding. South Africa, 10th ISRM Congress.
- Ayden, O., Tokashiki, N., Ozbay, U., Kwasniewski, M., Shariar, K., Okuno, T., Ozgenoglu, A., Malan, D. F., Okada, T., 2013. ISRM suggested methods for determining the creep characteristics of rock. In: *The ISRM suggested methods for rock characterization, testing and monitoring*. Ankara-Turkey: Springer-Verlag Wien, pp. 115-129.
- Barnes, H., Hutton, J., Walters, K., 1989. *An introduction to rheology*. 3rd ed. Amsterdam: Elsevier Science Publishers.
- Barton, N., 2002. Some new Q-value correlations to assist in site characterisation and tunnel design. *Int Journal of Rock Mech & Min Sci*, Volume 39, Issue 2, pp. 185-216.
- Bawden, W. Milne, D., 1987. Geomechanical mine design approach at Noranda Minerals. Montreal, A.A. Balkema, Rotterdam, 6th ISRM International Congress on Rock Mechanics, pp. 799-803.
- Beer, G., Watson, J., 1994. *Introduction to finite and boundary element methods for engineers*. Chichester: Willey and Sons.

- Beer, G., 1988. Application of 3-D boundary element and coupled analysis in geomechanics: Case Studies. Rotterdam: Innsbruck, A.A. Balkema., Proceedings of the 6th International Conference on Numerical Methods in Geomechanics, pp. 2209-16.
- Beneteau, D., 2012. A study relating Time-Between-Events (TBE) to seismic source mechanisms in hard rock mining. Sudbury, Ontario: M.Sc. Thesis Laurentian University, Bharti School of Engineering.
- Benz, T., Schwab, R., Kauther, R., Vermee, P., 2008. A Hoek-Brown criterion with intrinsic material strength factorization. International Journal of Rock Mechanics and Mining Sciences, Volume 45, Issue 2, pp. 210-222.
- Berry, D., 1958. Stress propagation in viscoelastic bodies. Mechanics and Physics of Solids, Volume 6, Issue 3, pp. 177-185.
- Bieniawski, Z., 1989. Engineering rock mass classifications. London: John Wiley & Sons.
- Bosman, J., Malan, D., Drescher, K., 2000. Time-dependent tunnel deformation at Hartbeesfontein Mine. The journal of South African Institute of Mining and Metallurgy, Volume 100, Issue 6, pp. 333-340.
- Brady, B., Brown, E., 1993. Rock Mechanics: for underground mining, 3rd ed. Dordrecht: Kluwer academic publisher.
- Brady, B., 1997. An analysis of rock behaviour in an experimental stoping block at the mount Isa Mine, Queensland, Australia. International Journal of Rock Mechanics and Mining Sciences & Geomechanical Abstracts, pp. 59–66.
- Chunhui, W., 2000. University of Minnesota. [Online] Available at: <http://www.me.umn.edu/labs/composites/Projects/Polymer%20Heat%20Exchanger/Creep%20description.pdf> [Accessed 12 6 2015].
- Curran, J., Corkum, B., 1990-8. Examine3D- User's Manual Version 4.0. Toronto: Rocscience Inc.
- Deryugin, Y. Y., Lasko, G. V., 2012. Field of stress in an isotropic plane with circular inclusion under tensile stress. " *Engineering*, Volume 4, Issue 9, pp. 583-589.
- Drescher, K., Handley, M., 2003. Aspects of time-dependent deformation in hard rock at great depth. The journal of South African Institute of Mining and Metallurgy, Volume 103, Issue 5, pp. 325-336.

Eberhardt, E., 2009. Rock Engineering practice and design. Lecture 3: Rock mass classifications and empirical design. University of British Columbia- Geological Engineering: ISRM Edition.

Eberhardt, E., Stead, D., Reeves, M., Connors, C., 1997. Design of tabular excavations in foliated rock: an integrated numerical modeling approach. *Journal of Geotechnical and Geological Engineering*, Volume 15, Issue 1, pp. 47–85.

Emery, C., 1961. The measurement of strains in mine rocks. Rolla, Missouri, Int. Symp. on Mining Research.

Eshelby, J., 1957. The determination of the elastic field of an ellipsoidal inclusion, and related problems. London: The Royal Society.

Fafard, M., Boudjelal, M., Bissonnette, B., Cloutier, A., 2001. Three-dimensional viscoelastic model with nonconstant coefficients. *(ASCE) Journal of Engineering Mechanics*, Volume 127, Issue 8, pp. 808-815.

Farmer, I., 1983. Engineering behaviour of rocks. 2nd ed. London: Chapman and Hall.

Fava, L., Millar, D., Maybee, B., 2011. Scenario evaluation through Mine Schedule Optimisation. In *Proceedings of the 2nd International Seminar on Mine Planning*, Gecamin, Santiago, pp. 1-10

Gantt-Chart, 2012. Gantt.com. [Online] Available at: <http://www.gantt.com/creating-gantt-charts.htm> [Accessed 10 July 2015].

Goodman, R. E., 1989. Introduction to rock mechanics, New York: John Wiley & Sons.

Grant, D., Potvin, Y., Rocque, P., 1993. Three dimensional stress analysis techniques applied to mine design at Golden Giant Mine. Montreal, McGill University, 1st Canadian Symposium on Numerical Modelling Applications in Mining and Geomechanics.

Gurtunca, R., 1989. Results of a classified tailings monitoring program at Vaal Reefs., COMRO (now CSIR Miningtek) Internal Report: no. 614.

Hardy, H. R., 1959. Time-dependent deformation and failure of geologic materials, *Quart. Col. School of Mines*, Volume 54, Issue 3, pp. 134-175.

Hillier, F. S., Lieberman, G. J., 2001. Introduction to operations research. 7th ed. Dubuque: McGRAW-HILL.

Hodgson, K., 1967. The behaviour of the failed zone ahead of a face, as indicated by continuous seismic and convergence measurements, Transvaal and Orange Free State Chamber of Mines Research Organisation: Chamber of Mines Research Report No 31/67.

Hoek, E., Brown, E., 1980. *Underground excavation in rock*. London: Institution of Mining and Metallurgy.

Hudson, J., Brown, E., 1973. *Studying the time-dependent effects in failed rock*. New York, proceeding of Fourteenth symposium on Rock Mechanics, American Society of Civil Engineers.

Irgens, F., 2008. *Continuum Mechanics*, Berlin:Springer.

Janakiraman, C. S., 1967. *Determination of viscosity of rocks by a dynamic resonance technique*. Vancouver: M.Sc. Thesis, University Of British. [Online] Available at: <https://Circle.Ubc.Ca/Handle/2429/36279> [Accessed 30th August 2014].

Jin, X., Keer, L. M., Wang, Q., 2009. *New Green's function for stress field and a note of its application in quantum-wire structures*. *International Journal of Solids and Structures*, Volume 46, Issue 21, pp. 3788-3798.

Kaiser, P., Morgenstern, N., 1981. *Phenomenological model for rock with time-dependent strength*. *International Journal of Rock Mechanics and Mining Sciences & Geomechanics*, Volume 18, Issue 2, pp. 153–165.

King, R., Jager, A., Roberts, M., Turner, P., 1989. *Rock mechanics aspects of stoping without back-area support*, COMRO (Now CSIR Miningtek) Research Report No. 17/89.

Kirsch, G., 1898. *Die Theorie der Elastizitat und die Bedurfnisse der Festigkeitslehre*. *Zantralblatt Verlin Deutscher Ingenieure*, Volume 42, pp. 797-807.

Kolymbas, D., 2005. *The New Austrian Tunnelling Method*. In: *Tunnelling and Tunnel mechanics: a rational approach to tunnelling*. Austria: Springer-Verlag Berlin Heidelberg, pp. 171-175.

Kumagai, N., Sasajima, S., Ito, H., 1978. *Long-term Creep of Rocks*. *J. Soc. Mat. Sci. (Japan)*, Volume 27, pp. 157.

Lama, R., Vutukuri, V., 1978. *Handbook on mechanical properties of rocks – testing techniques and results - Volume III*. Germany: Trans Tech Publications.

Lauffer, H., 1958. *Gebirgskla sifizierung für den stollenbau*. *Geo. Bauwesen*, Volume 24, Issue 1, pp. 46-51.

Lee, E., 1955. *Stress analysis in viscoelastic bodies*. *Quarterly Applied Mathematics*, Volume 13, Issue 2, pp. 183-190.

- Lee, Y. K., Pietruszczak, S., Choi, B.-H., 2012. Failure criteria for rocks based on smooth approximations to mohr-coulomb and hoek-brown failure functions. *International Journal of Rock Mechanics and Mining Sciences*, Volume 56, pp. 146-160.
- Malan, D., Napier, J., 1999. The effect of geotechnical conditions on the time-dependent behaviour of hard rock in deep mines. 37th U.S. Rock Mechanics Symposium. pp. 903-910.
- Malan, D. F., Drescher, K., 2000. Modelling the post-failure relaxation behaviour of hard rock. Seattle, proc. of the fourth North American Rock Mechanics Symposium. pp. 909-917.
- Malan, D. F., 1998. An investigation into the identification and modelling of time-dependent behaviour of deep level excavations in hard rock. Johannesburg: PhD Thesis Faculty of Engineering, University of the Witwatersrand.
- Malan, D., 1999. Time-dependent behaviour of deep level tabular excavations in hard rock. *Rock Mechanics and Rock Engineering Springer-Verlag*, Volume 32, Issue 2, pp. 123-155.
- Malan, D., 2003. Guidelines for measuring and analyzing continuous stope closure behaviour in deep tabular excavations. Braamfontein, The Safety in Mines Research Advisory Committee (SIMRAC).
- Malan, D., Vogler, U., Drescher, K., 1997. Time-dependent behaviour of hard rock in deep level gold mines. *The Journal of the South African Institute of Mining and Metallurgy*, Volume 97, Issue 3, pp. 135-148.
- Maybee, B., Fava, L., Dunn, P.G., Wilson, S., Fitzgerald, J., 2010. Toward optimum value in underground mine scheduling. *Canadian Institute of Mining and Petroleum*, Volume 1, Issue 3, pp. 176-182.
- McNeel, 2014. Rhinoceros Users Guide. [Online] Available at: <http://www.Rhino3d.Com/Support>. [Accessed 30th August 2014].
- Millar, D., Jiao, Y., 1994. On the use of genetic algorithms in modelling the deformability behaviour of rock. *Riccione, IV convegno dei giovani ricercatori in geologia applicata*, Volume 1, pp. 25-43.
- Millar, D., 2009. Linear programming.xla (Version 1.1), Renewable Energy Laboratory, Camborne school of Mines:University of Exeter, Cornwall Campus.
- Misseroni, D., Dal Corso, F., Shahzad, S., Bigoni, D., 2014. Stress concentration near stiff inclusions: Validation of rigid inclusion model and boundary layers by means of photoelasticity. *Engineering Fracture Mechanics*, Volume 121–122, pp. 87–97.

- Mukherjee, S., Mulchrone, K., 2012. Estimating the viscosity of the Tso Morari Gneiss Dome, western Indian Himalaya. *International Journal of Earth Sciences*, Volume 101, Issue 7, pp. 1929-1947.
- Mukherjee, S., Talbot, C., Koyi, H. A., 2007. Estimation of viscosity of natural salts of the Hormuz- and the Namakdan salt diapirs in the Persian Gulf. *Annual Transactions Of The Nordic Rheology Society*, Volume 15. pp. 189-201.
- Nehring, M., Topal, E., Little, J., 2010. A new mathematical programming model for production schedule optimization in underground mining operations. *Journal of the South African Institute of Mining and Metallurgy*, Volume 110, Issue 8, pp. 437-446.
- Ordóñez-Calderón, J., Lafrance, B., Gibson, H. L., Schwartz, T. and Pehrsson, S. J., 2009. Preliminary results from a stratigraphic and structural investigation of the Trout Lake volcanogenic massive sulphide deposit, Flin Flon, Manitoba. *Manitoba Innovation, Energy and Mines, Manitoba Geological Survey*, pp. 37-46.
- Pacher, F., Rabcewicz, L., Golser, J., 1974. Zum der seitigen Stand der Gebirgsklassifizierung in Stollen-und Tunnelbau. Salzburg, Austria, In proceedings of the XXII Geomach Colloq.
- Palmstrom, A., 2009: Combining the RMR, Q, and RMI classification systems. [Online] Available at: http://www.rockmass.net/files/combining_RMR-Q-RMi.pdf [Accessed 14th August 2015].
- Penny, R., Marriott, D., 1971. *Design for creep*. 1st ed. London: McGRAW-HILL Book Company (UK) Limited.
- Picard, D., Fafard, M., 2011. Three-dimensional constitutive viscoelastic Model for isotropic materials. In: *Thermodynamics - Physical Chemistry of Aqueous Systems*. InTech, pp. 328-350.
- Picard, D., 2007. *Modélisation et Caractérisation Du Fluage / relaxation de materiaux une base de carbone présente DANS LES revêtements cathodiques des cuves de électrolyse de laaluminuam*. Quebec City, Quebec: PhD Thesis Laval University.
- Roux, A., Denkhaus, H., 1954. An investigation into the problem of rockbursts, an operational research project. *Chem. Metall. Min. Soc. S. Afr*, Volume 55, Issue 5, pp. 103-124.
- Rudnicki, J., 2011. Eshelbys technique for analyzing inhomogeneities in geomechanics. *Vienna, Mechanics of Crustal Rocks*, Springer, Volume 533, pp. 43-72.
- Saeidi, N., Millar, D., 2015. Response of ore masses to stope sequence variations. Montreal, QC, The 13th international ISRM congress.

Saeidi, N., Millar, D., Fava, L., Cai, M., 2014. Towards mining schedule optimisation constrained by geomechanics. Sudbury, ON, Canada, Seventh International Conference on Deep and High Stress Mining.

Serafim, J. L. and Periera, J. P., 1983. Considerations of the geomechanical classification of Bieniawski. Proc. Int. Symp. on Engineering Geology and Underground Construction, Lisbon, Volume 1, Issue II, pp. 33–42.

Sharma, V., 2014. Long term schedule optimization of an underground mine under geotechnical and ventilation constraints using SOT, Sudbury, Ontario: M.Sc. Thesis Laurentian University, Bharti School of Engineering.

Terry, N., Morgans, W., 1958. Measurement of the static and dynamic elastic moduli of coal. Fuel, Volume 37, pp. 201-6.

Topal, E., Kuchta, M., Newman, A., 2003. *Extensions to an efficient optimization model for long-term production planning at LKAB's Kiruna Mine*. Application of Computers and Operations Research in the Minerals Industries, South African Institute of Mining and Metallurgy.

Winter, G., Periaux, J., Galan, M., Cuesta, P., 1995. Genetic algorithms in engineering and computer science, Chichester: Willey and Sons.

Young, W. C., 1989. ROARK's formulas for stress and strain. 6th ed. Singapore: McGRAW-HILL.

Yuannian, W., Fulvio, T., 2009. Modeling Lac du Bonnet granite using a discrete element model. International Journal of Rock Mechanics & Mining Sciences, Volume 46, Issue 7, pp. 1124–1135.

Zeng, T., 2012. Modélisation multi-échelle des comportements plastiques et viscoplastiques des géomatériaux polycristallins: Université LILLE I - Sciences et Technologies, Laboratoire de Mécanique de Lille (UMR CNRS 8107) Ecole Doctorale Régionale Sciences Pour l'Ingénieur Lille Nord-de-France.

Zhanyou, H., Cai, W., Benfield, F., 2009. A mixed integer linear programming based short term planning tool. in: Application of Computers and Operations Research (APCOM 2009). Canadian Institute of Mining Metallurgy and Petroleum (CIM), Vancouver, Canada, Volume 1, pp. 1–10.

A Appendix 1: Stress distribution in sequences of excavations

1. The stress distribution in the sequence of excavating: firstly, square shaped opening, secondly circle shaped opening, and lastly diamond shaped opening

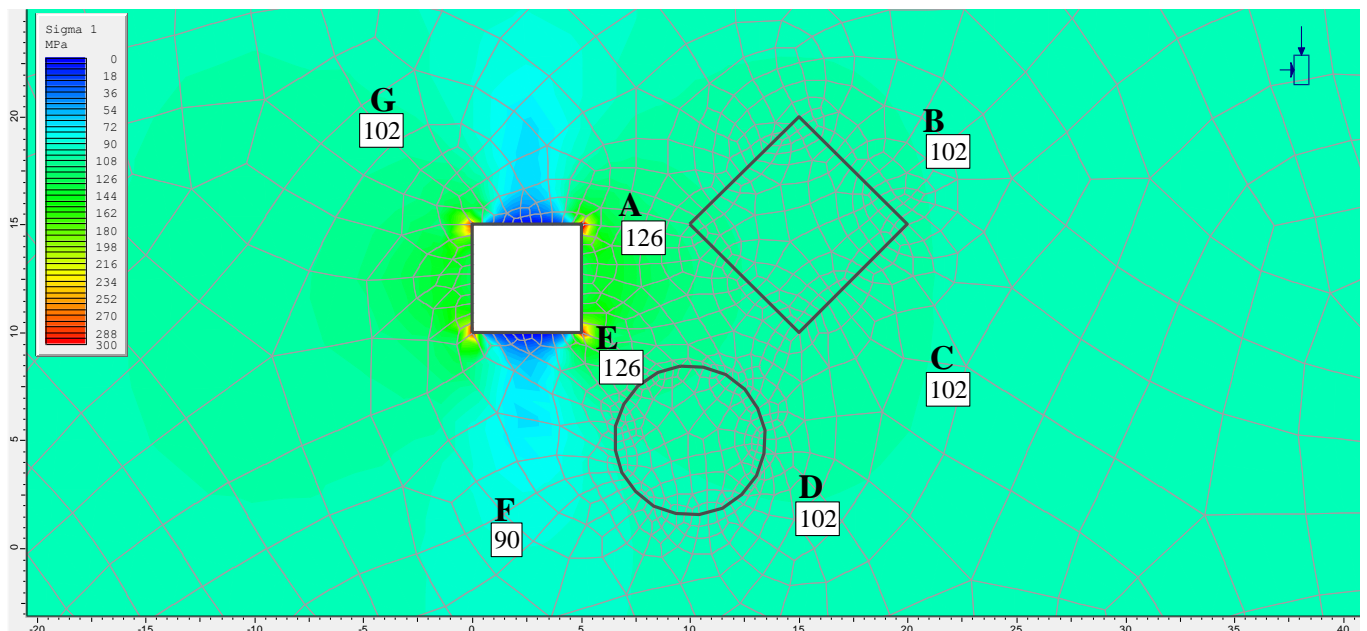


Figure A-1: σ_1 (maximum principal stress) distribution after the excavation of the square opening, $K = 0.5$

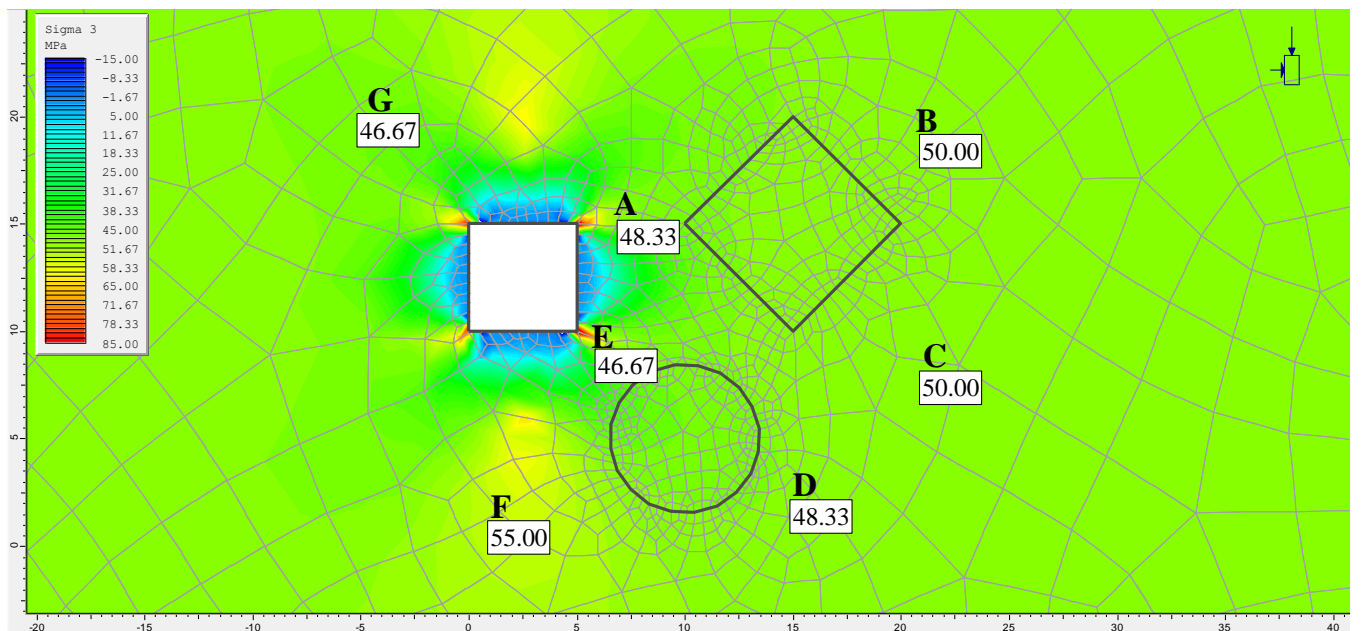


Figure A-2: σ_3 (minimum principal stress) distribution after the excavation of the square opening, $K = 0.5$

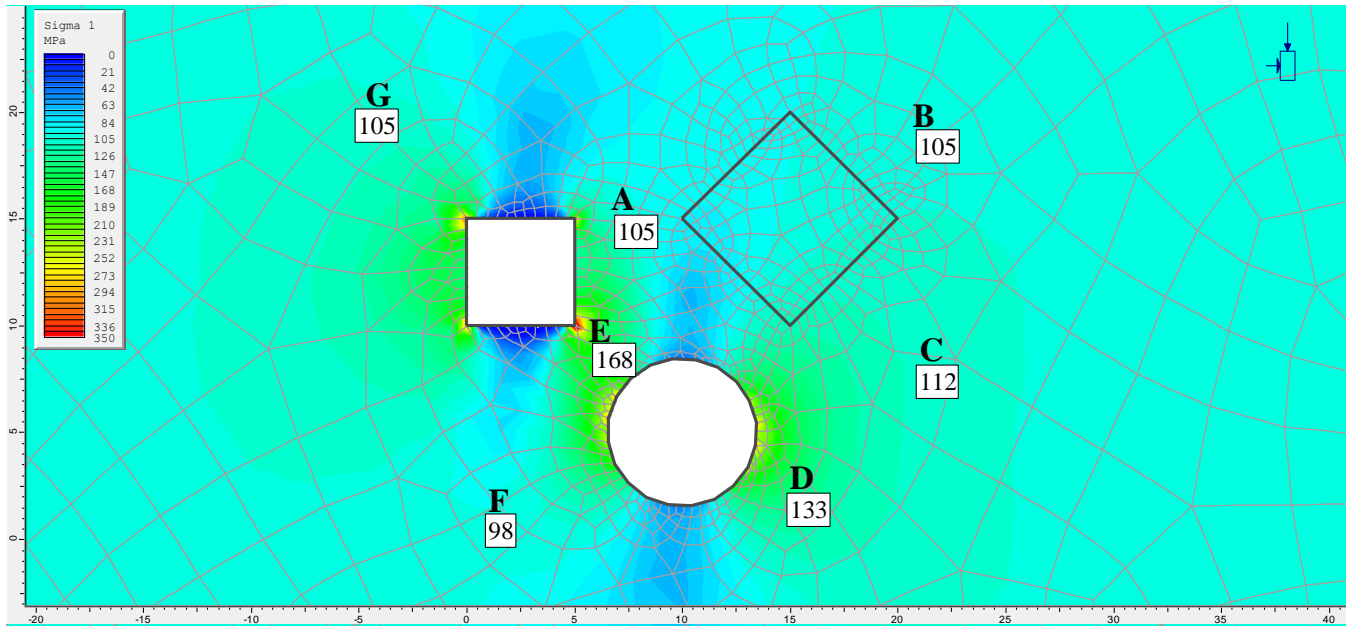


Figure A-3: σ_1 (maximum principal stress) distribution after the excavation of the circle opening, $K = 0.5$

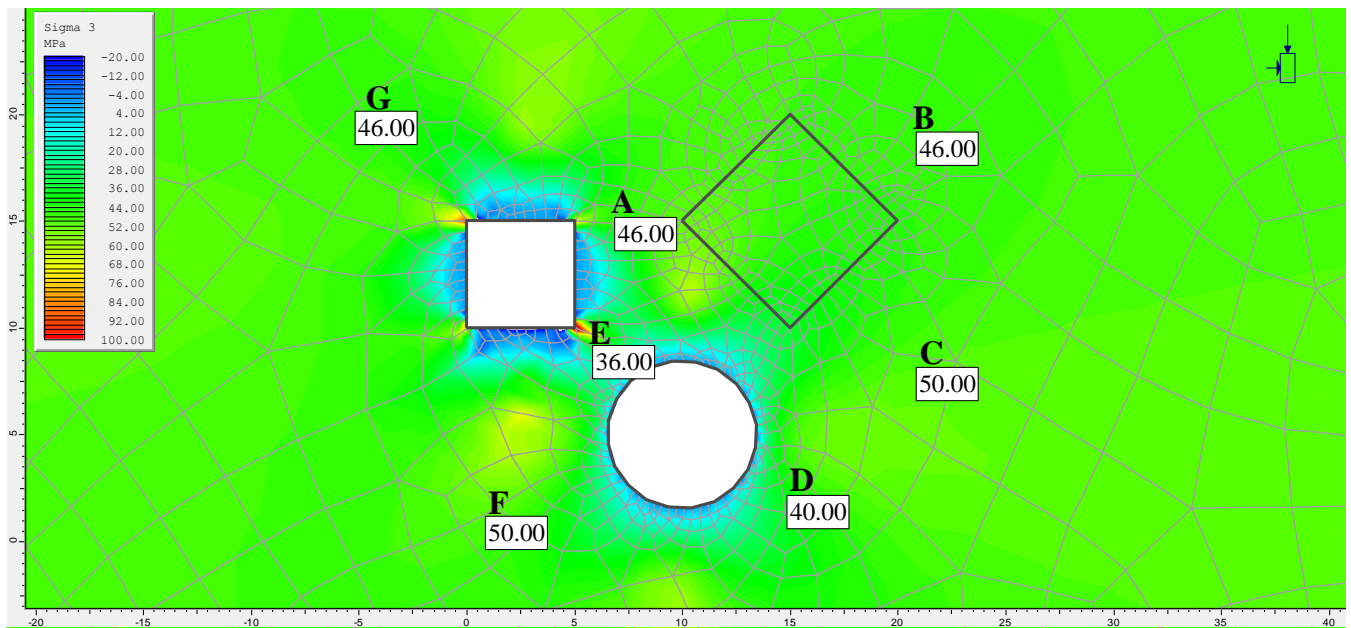


Figure A-4: σ_3 (minimum principal stress) distribution after the excavation of the circle opening, $K = 0.5$

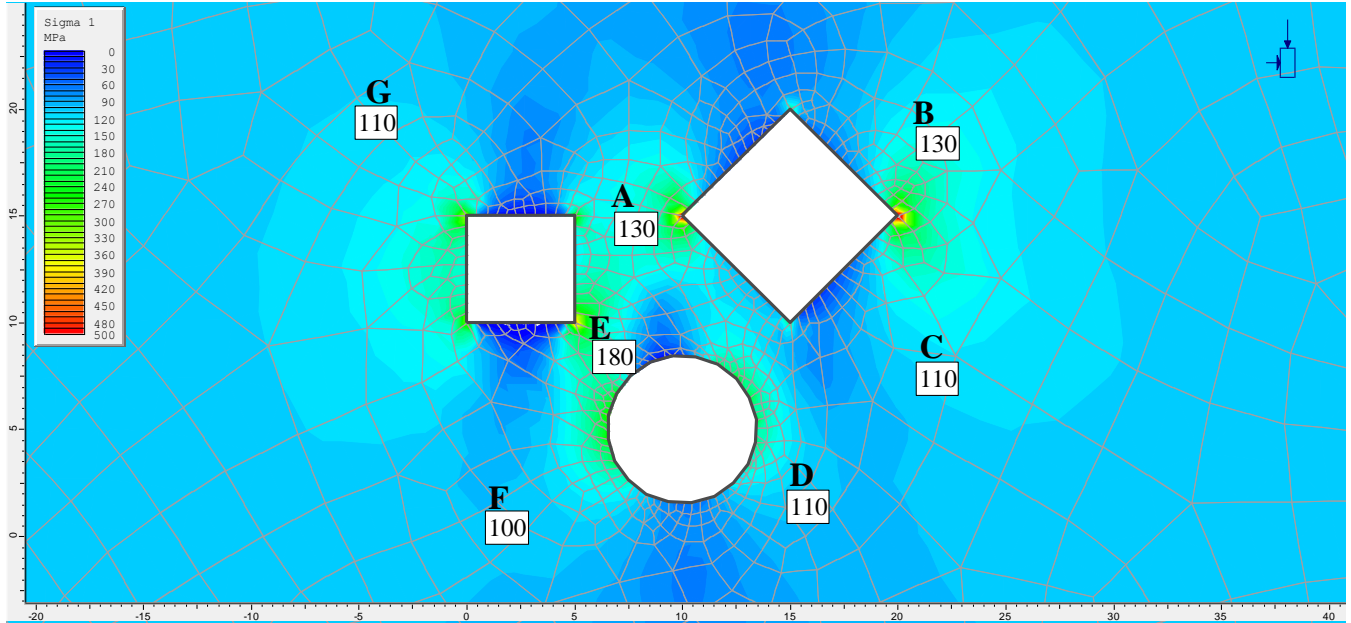


Figure A-5: σ_1 (maximum principal stress) distribution after the excavation of the diamond opening, $K = 0.5$

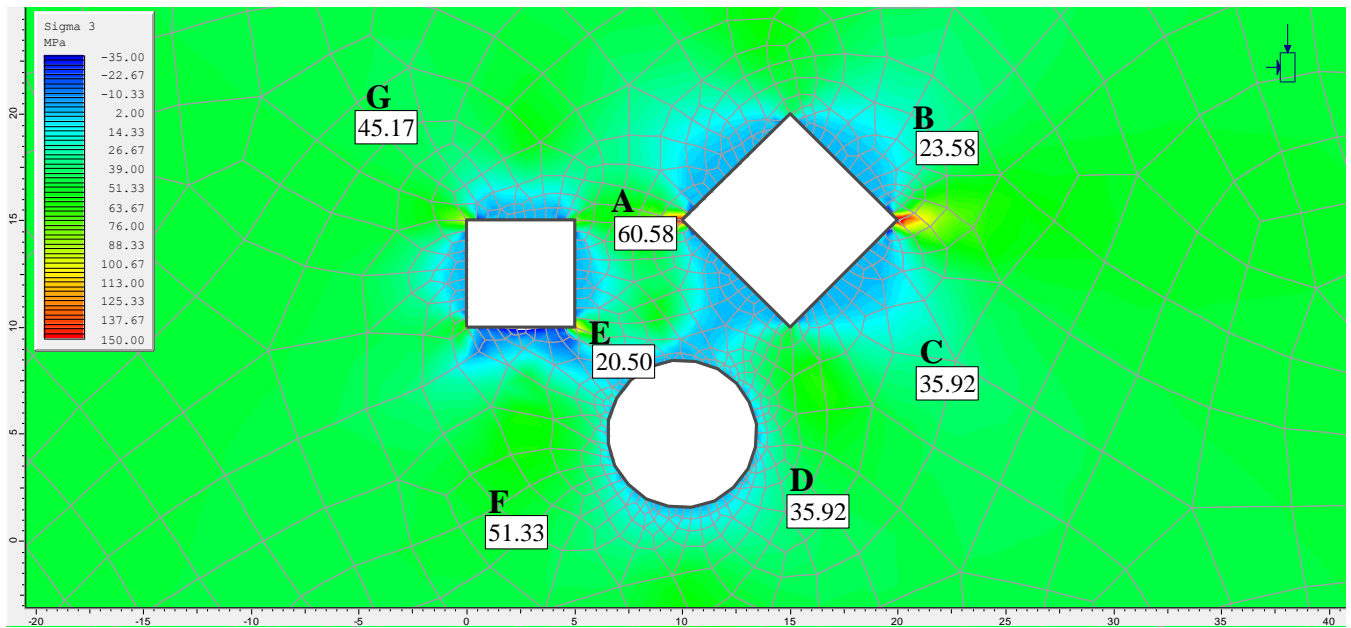


Figure A-6: σ_3 (minimum principal stress) distribution after the excavation of the diamond opening, $K = 0.5$

- The stress distribution in the sequence of excavating: firstly, square shaped opening, secondly diamond shaped opening, and lastly circle shaped opening

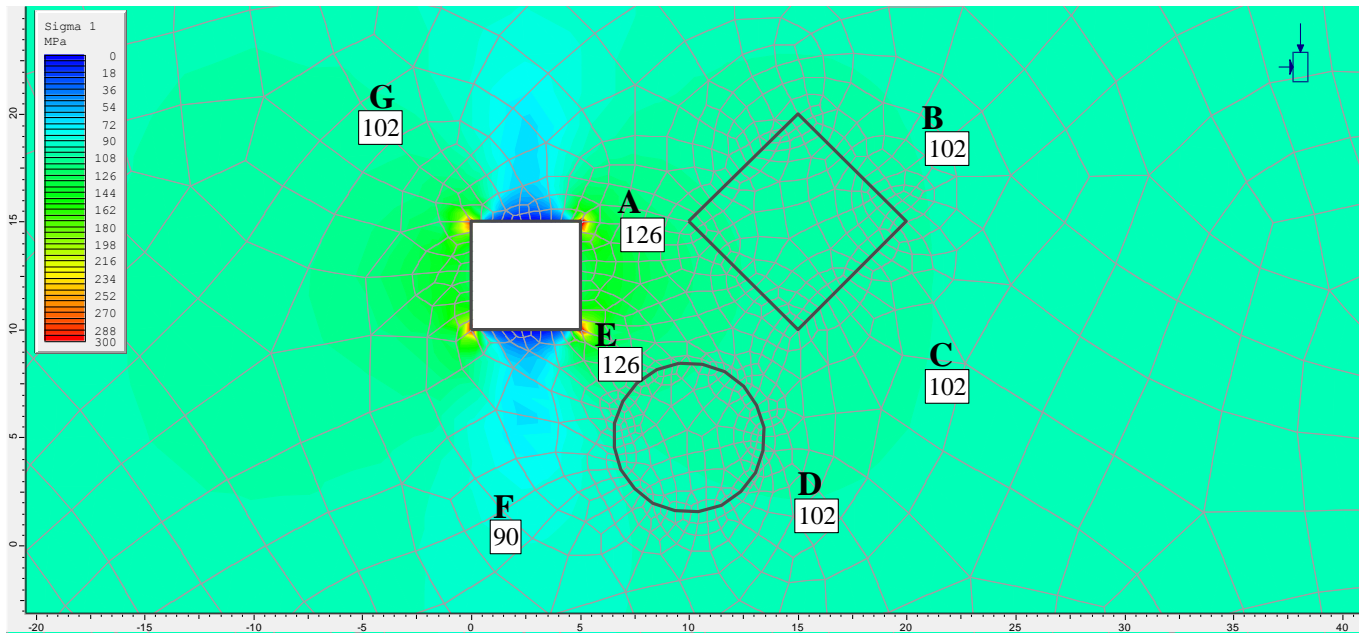


Figure A-7: σ_1 (maximum principal stress) distribution after the excavation of the square opening, $K = 0.5$

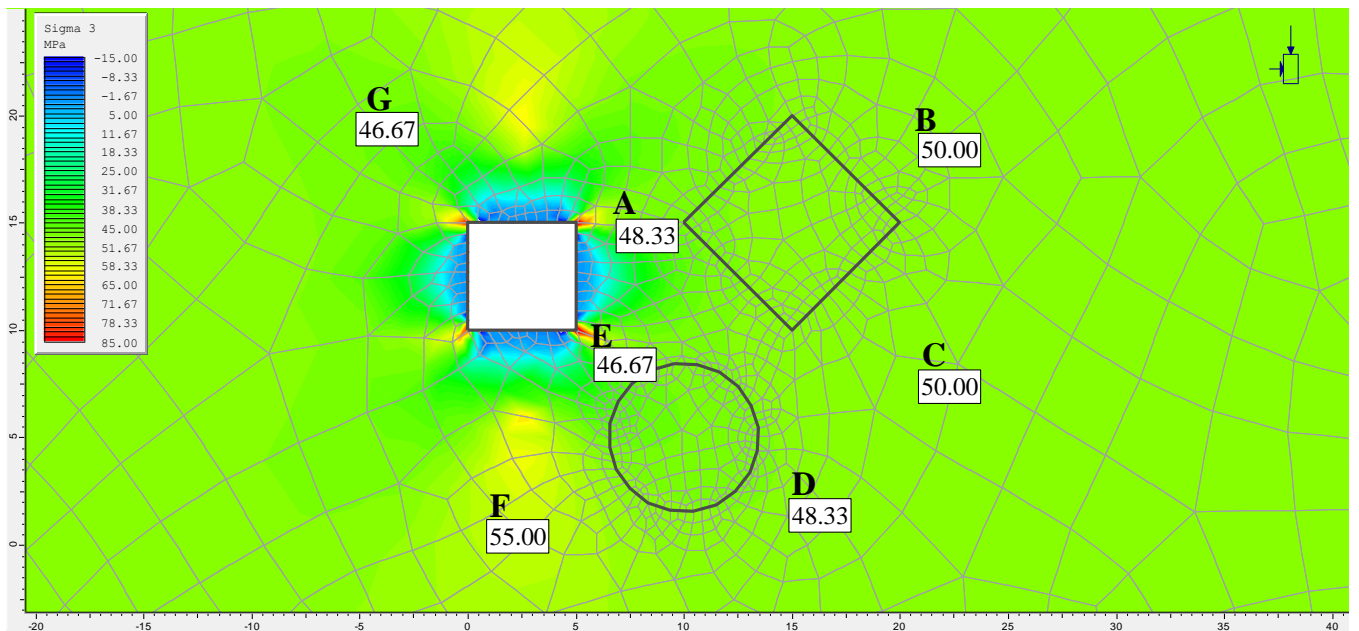


Figure A-8: σ_3 (minimum principal stress) distribution after the excavation of the square opening, $K = 0.5$

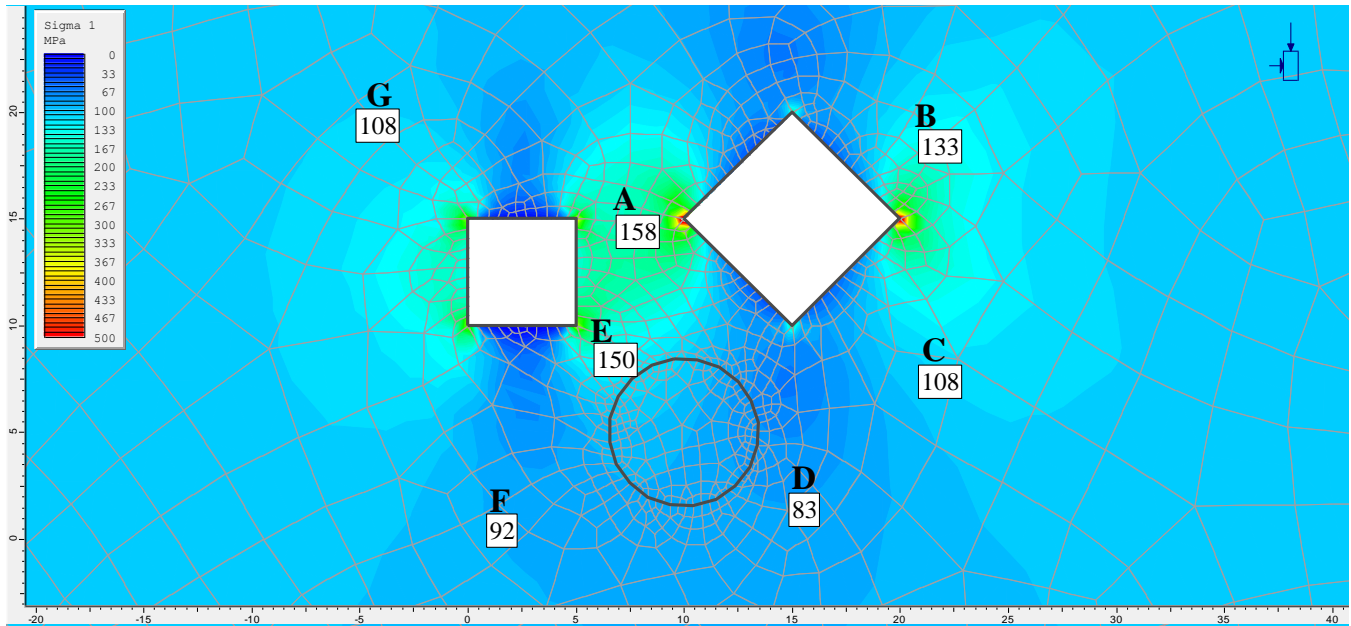


Figure A-9: σ_1 (maximum principal stress) distribution after the excavation of the circle opening, $K = 0.5$

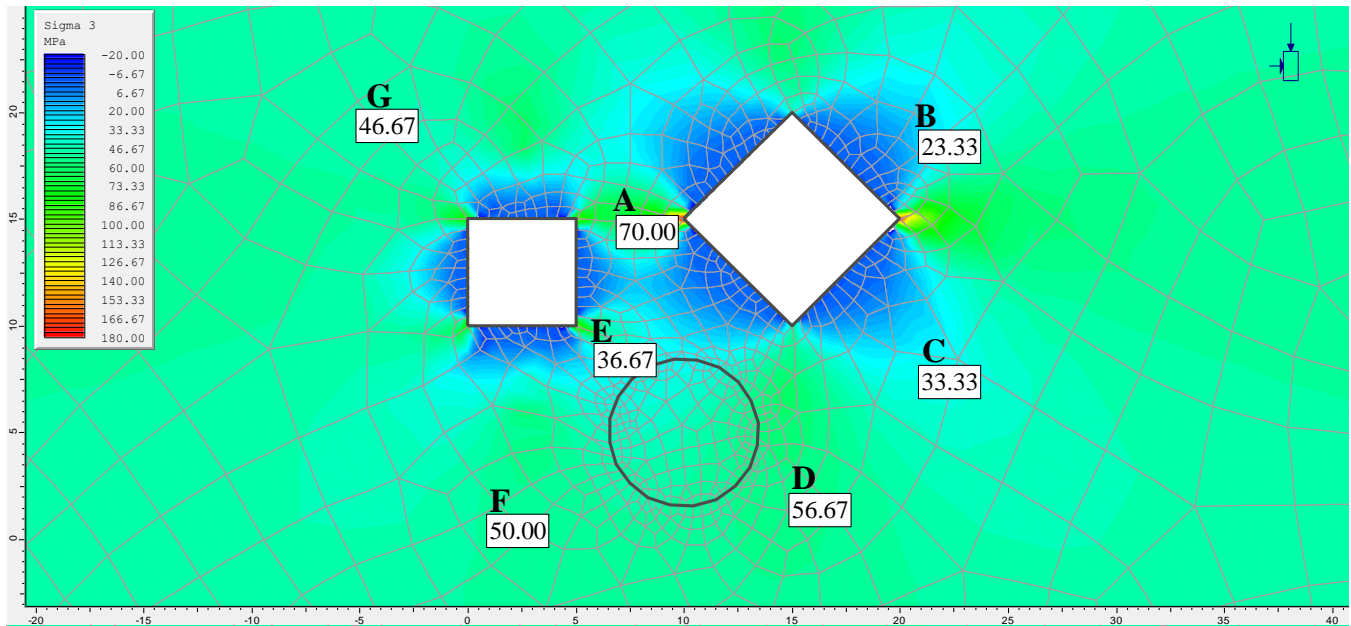


Figure A-10: σ_3 (minimum principal stress) distribution after the excavation of the circle opening, $K = 0.5$

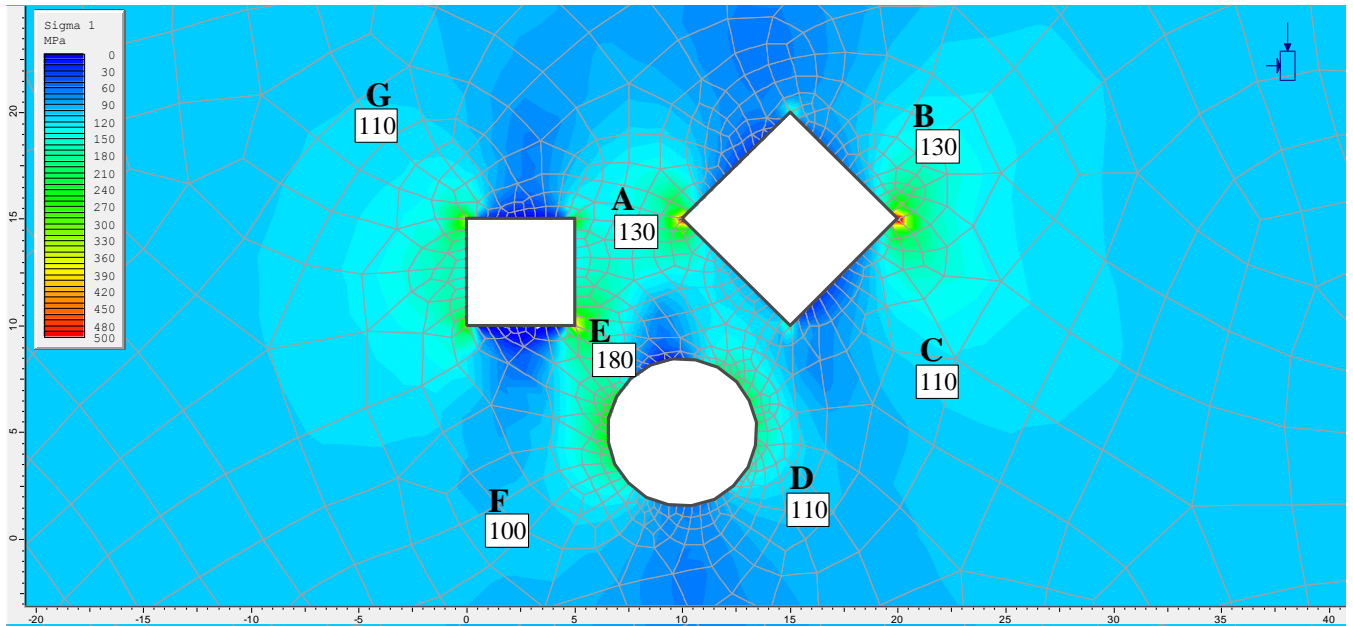


Figure A-11: σ_1 (maximum principal stress) distribution after the excavation of the diamond opening, $K = 0.5$

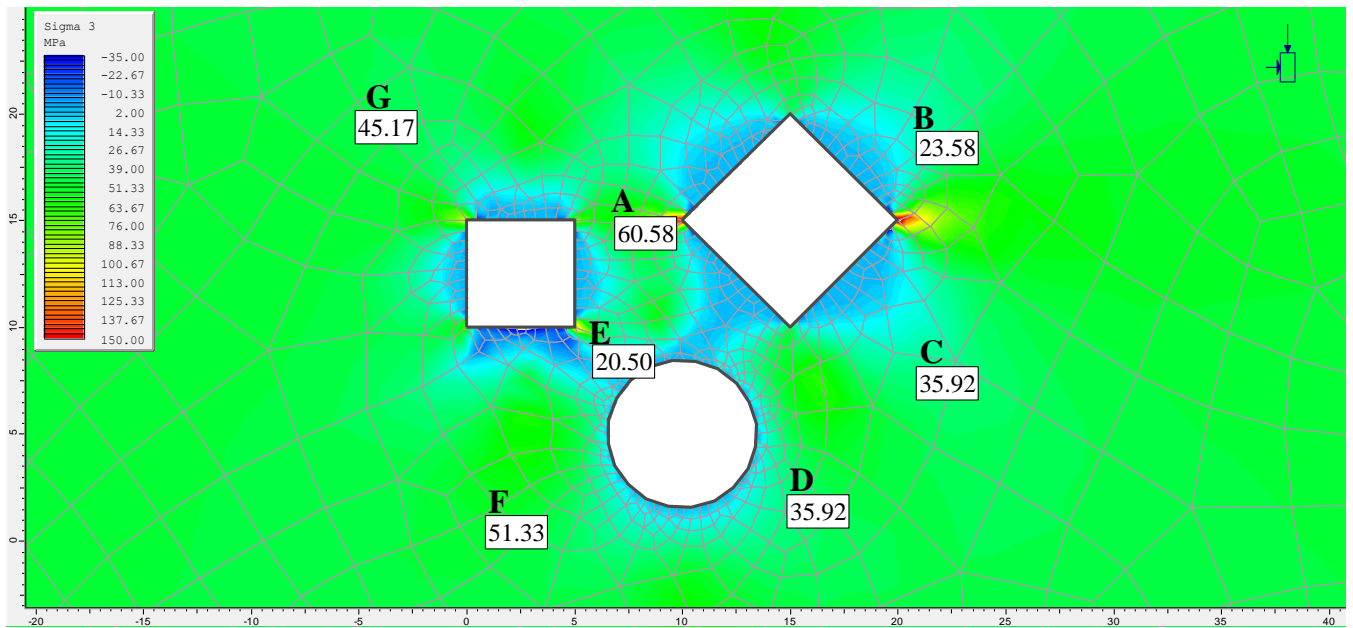


Figure A-12: σ_3 (minimum principal stress) distribution after the excavation of the diamond opening, $K = 0.5$

B Appendix 2: Fitting creep models to deformation data

1. Uniaxial compression test on Elsburg Quartzite from South African gold mine

Figure B-1 shows the results of the axial deformation measurements during a uniaxial compression strength test on Elsburg Quartzite from the deep level gold mines in South Africa. The quartzite specimen is loaded in steps. The loading started with 73 MPa uniaxial compressions stress, which is approximately 60% of the expected failure load as reported by Drescher and Handley (2003). The loading increased by almost 5% every 48-hours until the specimen failed.

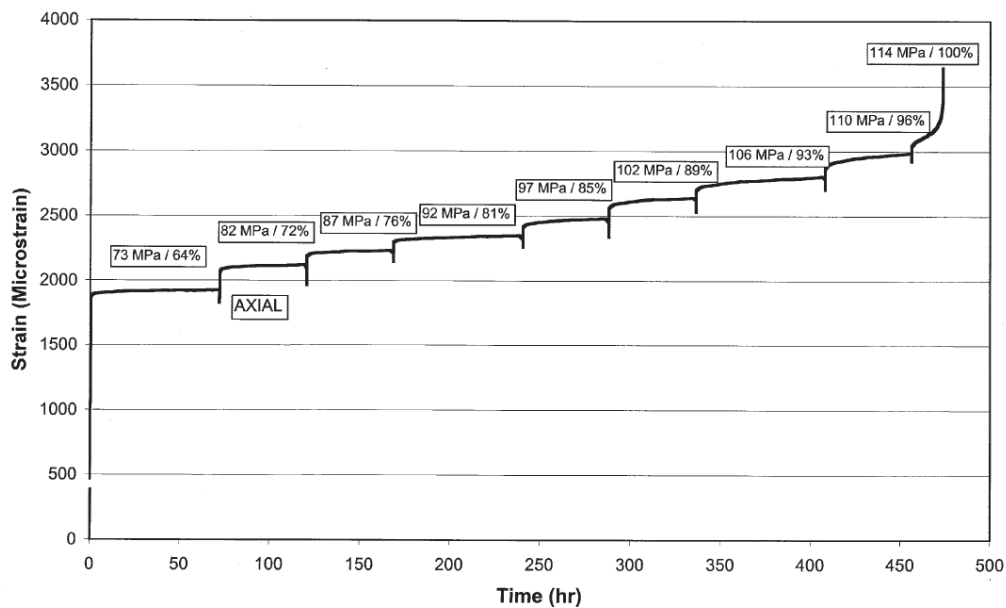


Figure B-1: Result of a uniaxial compression creep test of Elsburg Quartzite from Drescher and Handley (2003).

The first step of the axial strain measurement of the Elsburg Quartzite is digitized. At this step the specimen is loaded under 73 MPa uniaxial compression stress for 70 hours. The Excel solver was used to fit each of the four rheological models: Burger, Kelvin-Voigt, Generalized Kelvin-Voigt and Hill-Maxwell to the data. Figure B-2 is showing the best fit of each of the four rheological models along with the original data.

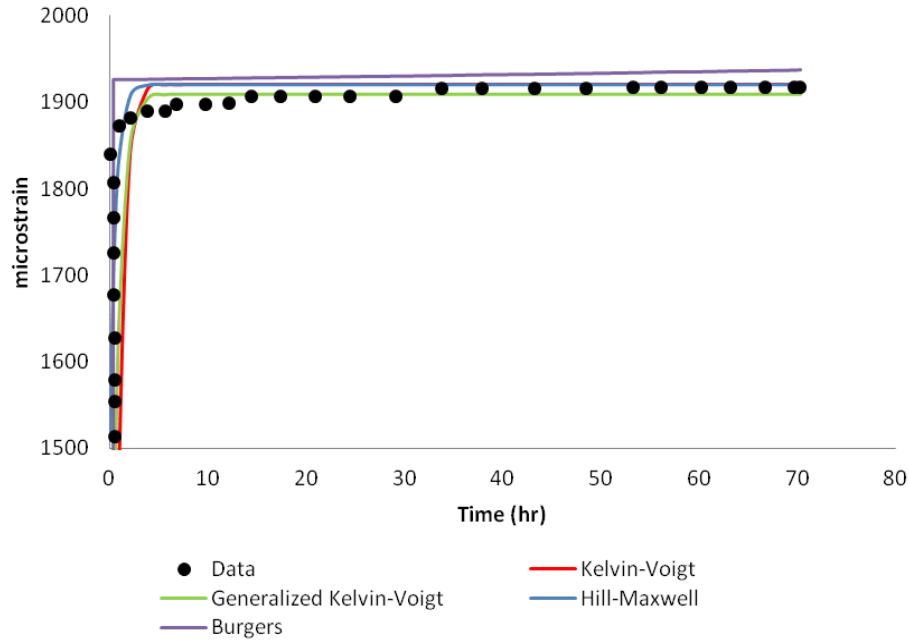


Figure B-2: Rheological models fitted to the first bit of measured strain from uniaxial compression creep test of Elsburg Quartzite from Drescher and Handley (2003).

The R-square and the coefficients of each of the rheological models are computed with the Excel solver and are presented in Table B-1.

Table B-1: Back-analyzed coefficients after fitting rheological models to the data presented in Figure B-2.

Kelvin-Voigt	μ_K (MPa.s)		E_K (MPa)		R-square
	90007880.33496		38000.6623640392		0.407708
Generalized Kelvin-Voigt	μ_K (MPa.s)		E_K (MPa)	E (MPa)	R-square
	200000000		76453.387357633	76453.387357633	0.597704
Burgers	μ_K (MPa.s)	E_K (MPa)	μ_M (MPa.s)	E_M (MPa)	R-square
	3000000	85453.3873577	1600000000000	68113.387358	0.8
Hill-Maxwell model	μ_K (MPa.s)		E_K (MPa)	E (MPa)	R-square
	22000000		10194.51266542	38000.387357633	0.184222

Figure B-3 presents the results of the similar analysis on the second step of the Elsburg Quartzite strain curve. At this step the specimen is loaded under 82 MPa uniaxial compression stress for 48 hours. Table B-2 provides the back analysed coefficients and the minimum R-square for each of the models.

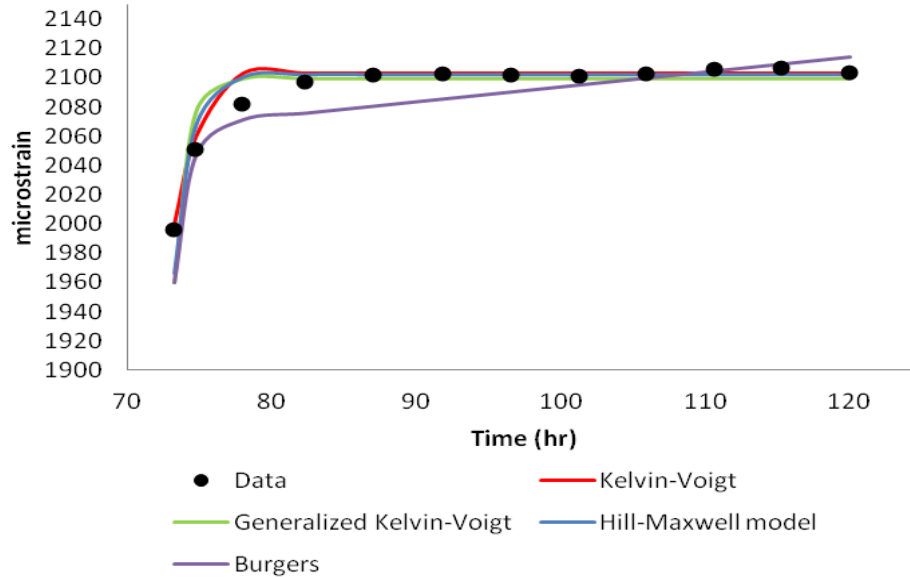


Figure B-3: Rheological models fitted to the second part of the measured strain from uniaxial compression creep test on Elsburg Quartzite from Drescher and Handley (2003).

Table B-2: Back-analyzed coefficients after fitting rheological models to the data presented in Figure B-3.

Kelvin-Voigt	μ_K (MPa.s)		E_K (MPa)		R-square	
	80000880.33496		38990.9539357827		0.942568	
Generalized Kelvin-Voigt	μ_K (MPa.s)		E_K (MPa)	E (MPa)	R-square	
	160000000		77178.500591081	79104.84043937	0.519712	
Burgers	μ_K (MPa.s)	E_K (MPa)	μ_M (MPa.s)	E_M (MPa)	R-square	
	200000000	93430.565838	290000000000	69015.35782	0.542653	
Hill-Maxwell model	μ_K (MPa.s)		E_K (MPa)		E (MPa)	R-square
	22000000		5545.3873576339		39000.387357633	0.90719

2. Uniaxial creep test on quartzite samples from Hartebeestfontein mine

To understand the squeezing condition in the tunnels of the Hartebeestfontein Mine, five uniaxial compressive strength tests and Brazilian tensile strength tests were conducted on the quartzite samples from the sidewalls and hanging walls of the Hartebeestfontein mine in South Africa. Bosman *et al.* (2000) reported the uniaxial compression strength of the sidewall samples for 167 MPa. Figure B-4 presents the results of a uniaxial strain measurement during a compression creep test for about 70 hours on quartzite samples from side wall and hanging wall of the Hartebeestfontein mine. Since there is no information provided for the load that was applied in the UCS test, the author of this thesis decided for the value of 147 MPa uniaxial compression load, a little below the strength.

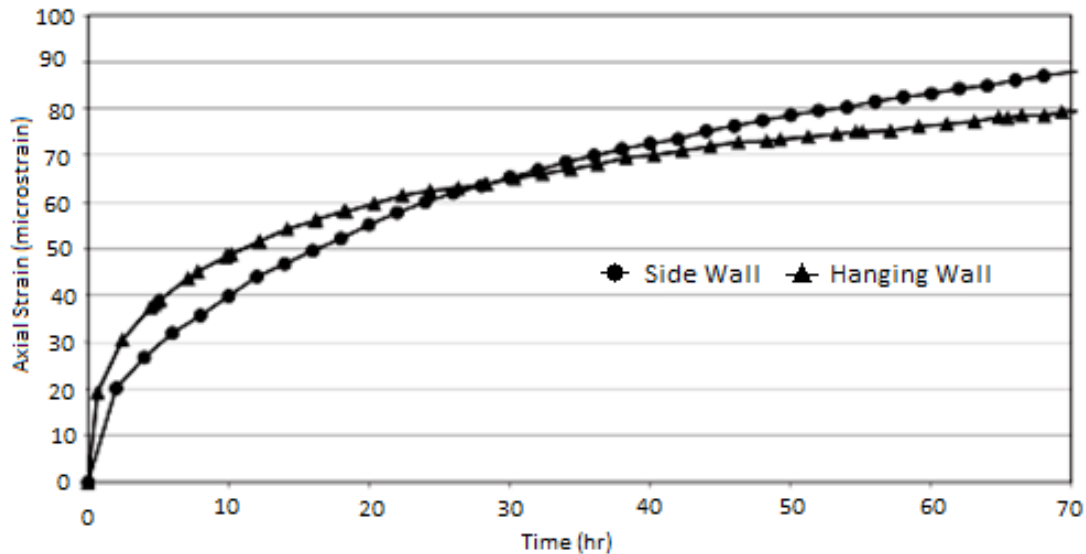


Figure B-4: Graphs of compression test results on Hartebeestfontein Mine quartzite (Bosman, *et al.*, 2000).

Excel solver was used to fit each of the four rheological models: Burger, Kelvin-Voigt, Generalized Kelvin-Voigt and Hill-Maxwell to the data. Figure B-5 is showing the best fit of each of the four rheological models along with the experimental data.

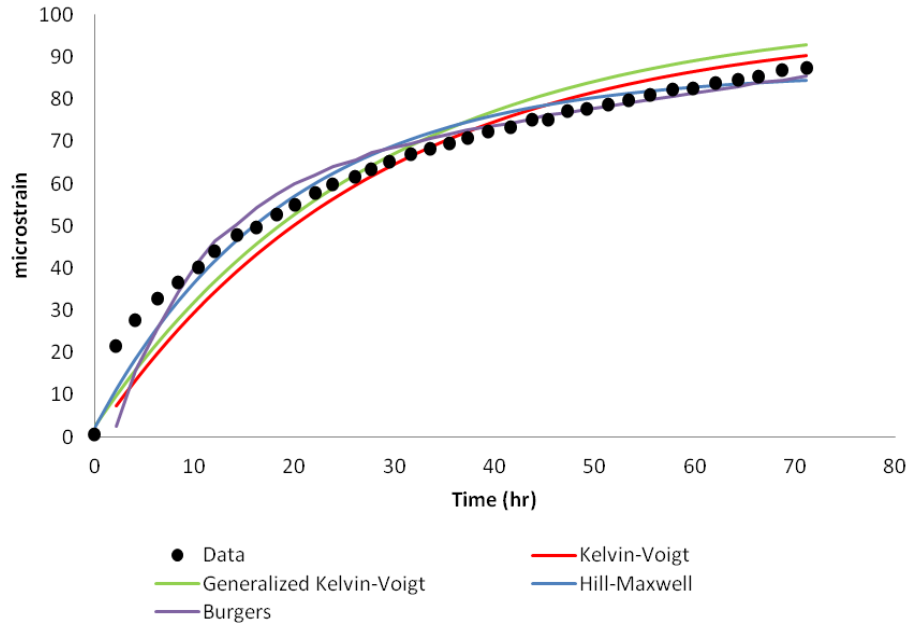


Figure B-5: Rheological models fitted to the measured strain from UCS test on quartzite sample from Hartebeestfontein Mine sidewall.

Table B-3 provides the back analysed coefficients for each of the models with the minimum R-square.

Table B-3: Back-analyzed coefficients after fitting rheological models to the data presented in Figure B-5.

Kelvin-Voigt	μ_K (MPa.s)		E_K (MPa)		R-square
	150000000000		1500000		0.945959
Generalized Kelvin-Voigt	μ_K (MPa.s)		E_K (MPa)	E (MPa)	R-square
	150000000000		1500000	60000000	0.947529
Burgers	μ_K (MPa.s)	E_K (MPa)	μ_M (MPa.s)	E_M (MPa)	R-square
	80000000000	2500000	1500000000000	60000000	0.96051
Hill-Maxwell model	μ_K (MPa.s)		E_K (MPa)	E (MPa)	R-square
	4100000000000		60000000	1700000	0.974192

3. Creep test on the quartzite sample from Hartebeestfontein mine

Figure B-6 shows the results of a series of creep test on a quartzite samples from Hartebeestfontein gold mine in South Africa reported by Malan *et al.* (1997). The quartzite specimen is loaded under 88, 91, 99 and 107 MPa uniaxial compression stress for about a day.

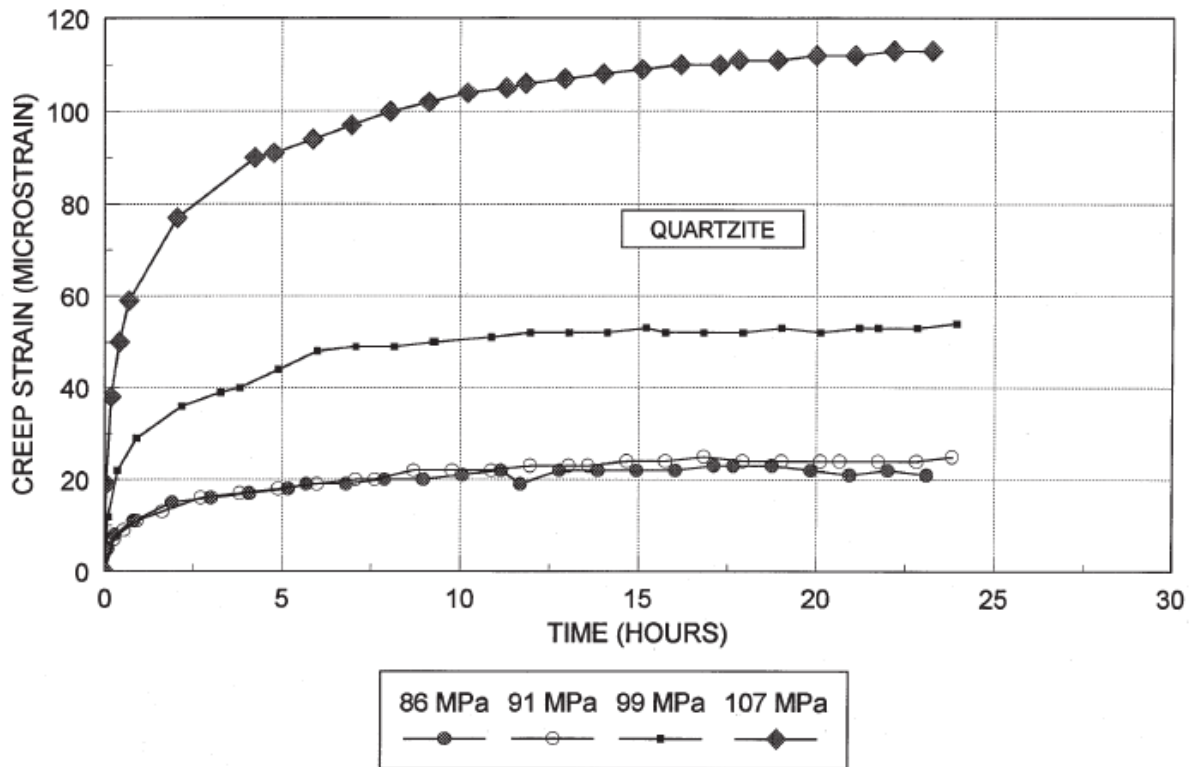


Figure B-6: Uniaxial creep tests on quartzite sample from Hartebeestfontein mine reported by Malan *et al.* (1997).

The Excel solver was used to fit each of the four rheological models: Burger, Kelvin-Voigt, Generalized Kelvin-Voigt and Hill-Maxwell to the measured data from the uniaxial creep tests under 107 MPa uniaxial compression load. Figure B-7 is showing the best fit of each of the four rheological models along with the measured data.

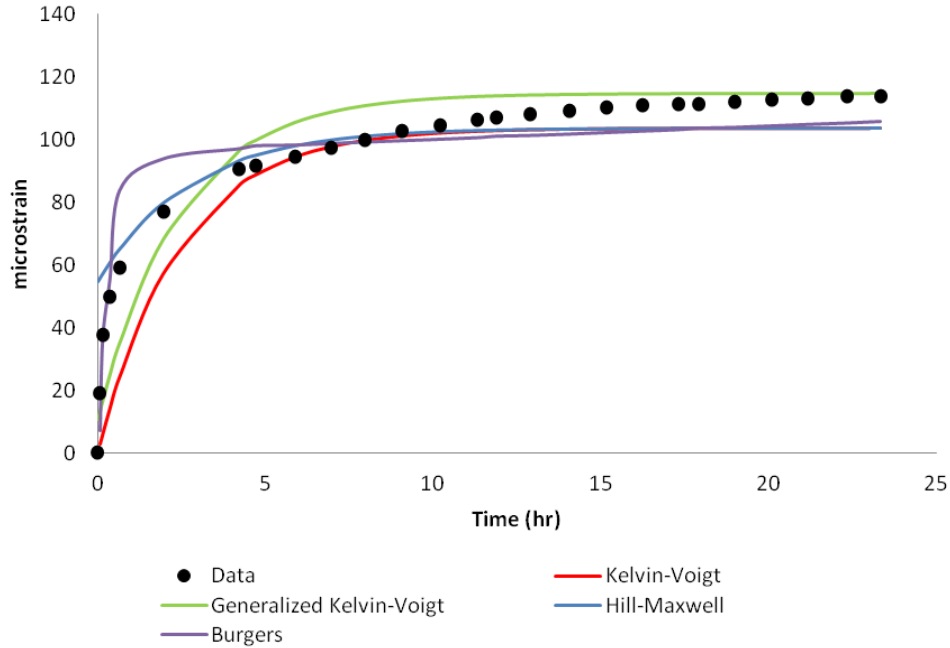


Figure B-7: The rheological models fitted to the measured strain from the uniaxial creep tests on the quartzite sample from Hartbeestfontein mine under 107 MPa uniaxial compression load.

Table B-4 provides the back analysed coefficients for each of the models and the minimum R-square.

Table B-4: Back-analyzed coefficients after fitting rheological models to the data presented in Figure B-7.

Kelvin-Voigt	μ_K (MPa.s)		E_K (MPa)		R-square	
	9000000880.33496		1030293.30952024		0.87003	
Generalized Kelvin-Voigt	μ_K (MPa.s)		E_K (MPa)	E (MPa)	R-square	
	9000000880.33		1030293.30952	9930293.3095202	0.922805	
Burgers	μ_K (MPa.s)	E_K (MPa)	μ_M (MPa.s)	E_M (MPa)	R-square	
	800000000	1200000	900000000000	15000000	0.696062	
Hill-Maxwell model	μ_K (MPa.s)		E_K (MPa)		E (MPa)	R-square
	9090000880.3349		930293.30952025		1030293.3095202	0.299143

4. Creep test on lava from Hartebeestfontein mine

Figure B-8 shows results of a series of creep tests on a lava sample from Hartebeestfontein gold mine in South Africa reported by Malan *et al.* (1997). The lava specimen is loaded under 265, 296, 331 and 366 MPa uniaxial compression stress for about three days.

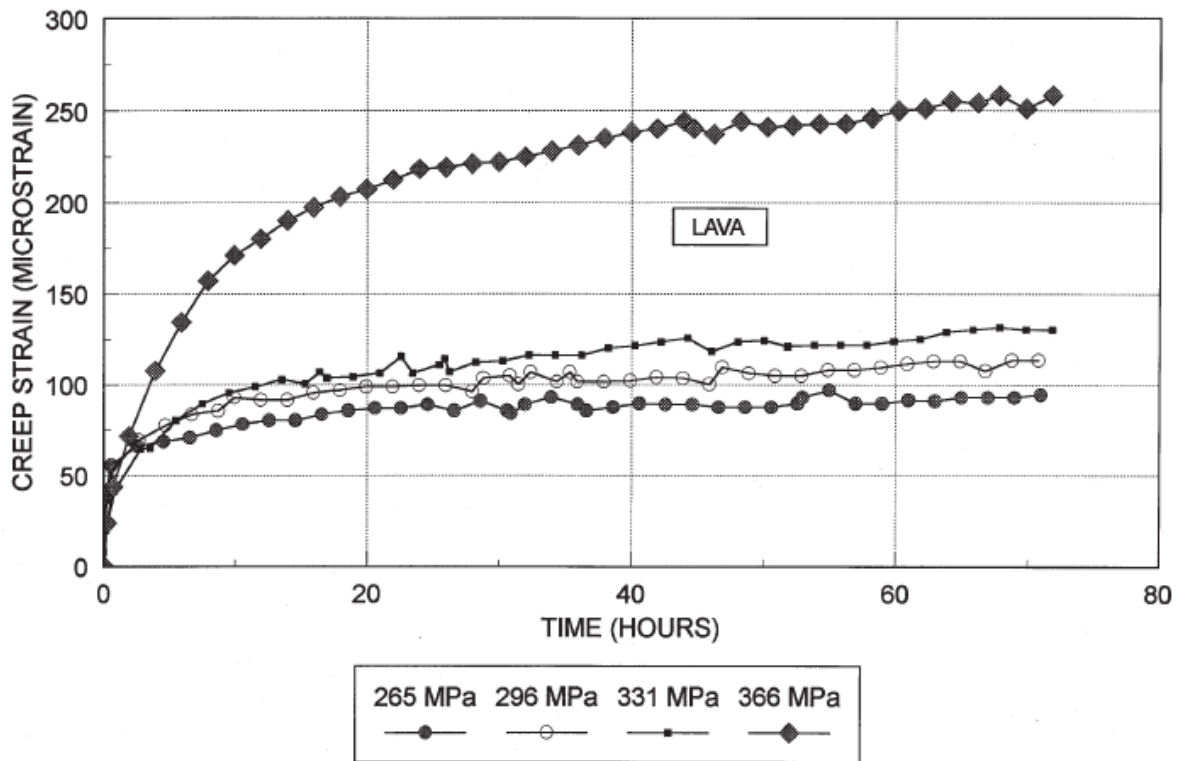


Figure B-8: Uniaxial creep tests on lava sample from Hartebeestfontein mine reported by Malan *et al.* (1997).

The Excel solver used to fit each of the four rheological models: Burger, Kelvin-Voigt, Generalized Kelvin-Voigt and Hill-Maxwell models to the measured data from the uniaxial creep tests under 366 MPa uniaxial compression load. Figure B-9 is showing the best fit of each of the four rheological models and the measured data.

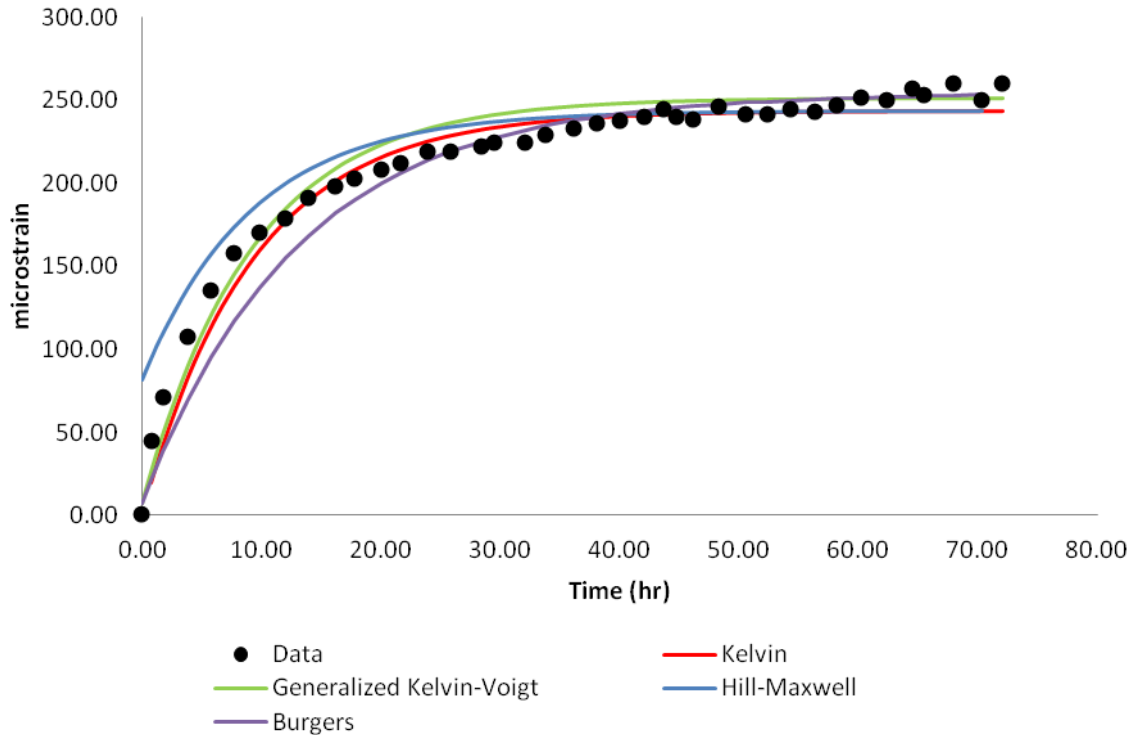


Figure B-9: The rheological models fitted to the measured strain from the uniaxial creep tests, on the lava sample from Hartebeestfontein mine under 366 MPa uniaxial compression load.

Table B-5 provides the back analysed coefficients for each model and their minimum R-square.

Table B-5: Back analyzed coefficients after fitting rheological models to the data presented in Figure B-7.

Kelvin-Voigt	μ_K (MPa.s)		E_K (MPa)		R-square
	50000000000		1500000.30952024		0.971456
Generalized Kelvin-Voigt	μ_K (MPa.s)		E_K (MPa)	E (MPa)	R-square
	50000000000		1500000	50000000	0.968445
Burgers	μ_K (MPa.s)	E_K (MPa)	μ_M (MPa.s)	E_M (MPa)	R-square
	70000000000	1500000	3000000000000	50000000	0.949185
Hill-Maxwell model	μ_K (MPa.s)		E_K (MPa)	E (MPa)	R-square
	99000000000		3000000	1500000	0.785852

5. Closure measurement from a tabular stope of Deelkraal gold mine

Malan *et al.* (1997) reported that the closure data, measured from a 200 m span stope in Deelkraal Gold Mine in South Africa. The measured data is back analyzed by fitting the Burgers' model to the data set (Figure B-10) assuming uniaxial stress equals to 147 MPa as reported by Malan *et al.* (1997). The back analyzed values for the Burgers model coefficients are presented in Table B-6.

Table B-6: back analyzed Burgers model coefficient based on the measured closure data from Deelkraal gold mine tabular stope reported by Malan *et al.* (1997).

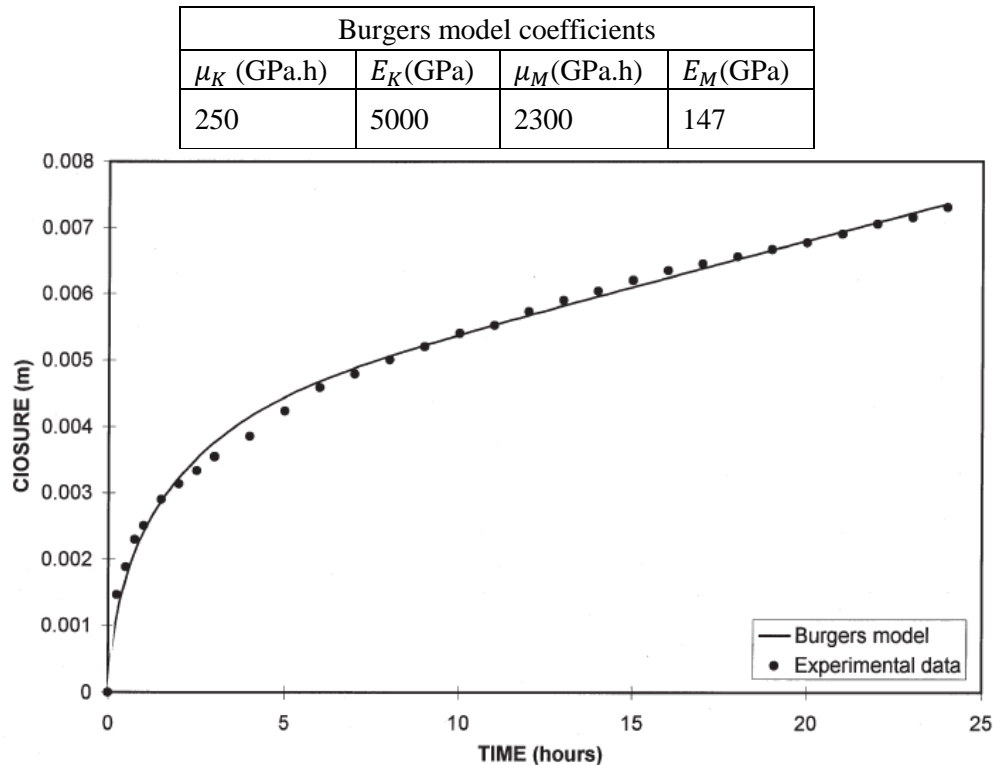


Figure B-10: The Burgers convergence model fitted to the underground closure measurements from Deelkraal gold mine (Malan, *et al.*, 1997).

The value of strain calculated based on the measured closure data and span of the stope. The Excel solver used to fit each of the four rheological models: Burger, Kelvin-Voigt, and Generalized Kelvin-Voigt and Hill-Maxwell to the measured data. Figure B-11 is showing the best fit of each of the four rheological models and the measured data.

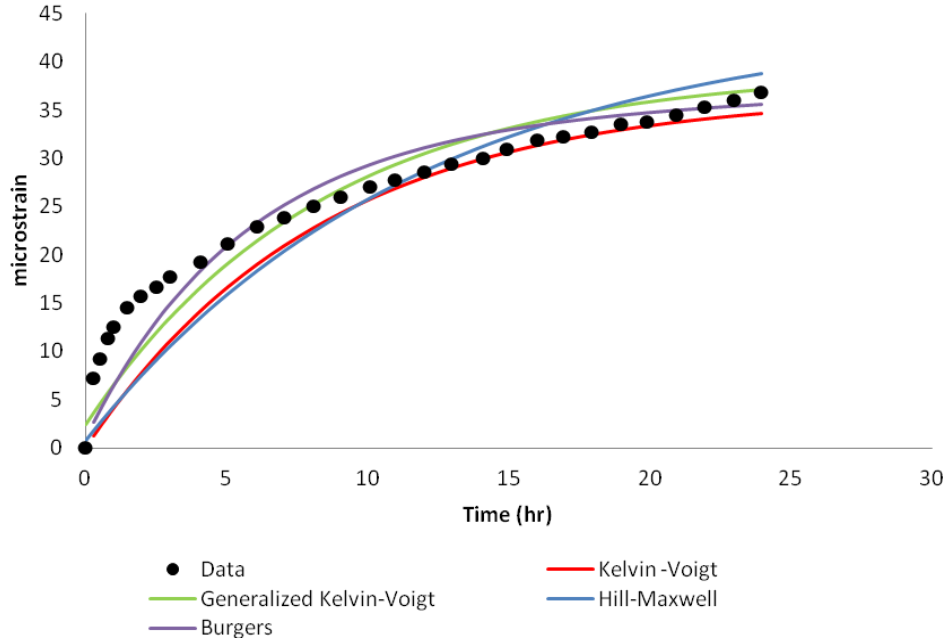


Figure B-11: Rheological models fitted to the calculated strain from the measured closure data from Deelkraal gold mine reported by Malan *et al.* (1997).

Table B-7 provides the back analysed coefficients for each of the models and the minimum R-square.

Table B-7: Back-analyzed coefficients after fitting rheological models to the data presented in Figure B-7.

Kelvin-Voigt	μ_K (MPa.s)		E_K (MPa)		R-square
	120000000000		4000000		0.880602
Generalized Kelvin-Voigt	μ_K (MPa.s)		E_K (MPa)	E (MPa)	R-square
	120000000000		4000000	60000000	0.935606
Burgers	μ_K (MPa.s)	E_K (MPa)	μ_M (MPa.s)	E_M (MPa)	R-square
	30000000000	11000000	54160000000	147000000	0.970602
Hill-Maxwell model	μ_K (MPa.s)		E_K (MPa)	E (MPa)	R-square
	900000000000		19000000	3100000	0.87485

C Appendix 3: Examine3D batch mode processor

The VBA code presented here is to convert the mesh properties that is generated by Rhino (McNeel, 2014) in the format of '*.raw' files to the format of '*.ex3' files which are readable by Examine3D (Curran and Corkum, 1990-8) for computation of the stress field.

Examine3D batch mode processor
by: Dr. Dean Millar
2014

```
Option Explicit

Type MyRhinoPoint
    x As Double
    y As Double
    z As Double
End Type

Type Triangle
    Pt(1 To 3) As MyRhinoPoint
    Ptr(1 To 3) As Integer
End Type

Sub change()
    Dim i As Integer

    For i = 1 To Worksheets("GUI").Cells(14, 4)
        Worksheets("GUI").Cells(18, 4) = Worksheets("FileList").Cells(8 + i, 3) &
        ".raw"
        DriverFor_GetRhinoTriangles (Worksheets("FileList").Cells(8 + i, 3))
    Next i

End Sub

Sub DriverFor_GetRhinoTriangles(ByVal i As String)
    Dim MyPath As String
    Dim MyFile As String
    Dim fileToOpen As Variant
    Dim T() As Triangle
    Dim N() As MyRhinoPoint
    Dim Ans As Variant
    Dim NumObjects As Long
    Dim NumTriangles As Long
    Dim NumNodes As Long

    MyPath = Worksheets("GUI").Cells(17, 4)
    MyFile = Worksheets("GUI").Cells(18, 4)
```

```

Ans = GetRhinoTriangles(MyPath, MyFile, T())
NumObjects = Ans(1) / 2
NumTriangles = Ans(2) / 2
NumNodes = HarvestNodesInTriangles(NumTriangles, T(), N())

fileToOpen = MyPath & "\" & i & ".ex3"

TrialOutput N(), NumNodes, T(), NumTriangles, MyPath, CStr(fileToOpen)

End Sub

Sub TrialOutput(N() As MyRhinoPoint, NumNodes As Long, T() As Triangle,
NumTriangles As Long, MyPath As String, MyFile As String)

    Dim i As Long
    Dim MyString As String
    Dim OStream As Integer
    Dim FileName As String

    FileName = MyPath & "\" & MyFile

    FileName = MyFile

    OStream = FreeFile()
    Open FileName For Output Access Write Shared As OStream

    Print #OStream, "4.0 FILE FORMAT"
    Print #OStream, "EXAMINE3D - A 3D STRESS ANALYSIS PROGRAM"

    Print #OStream, "*" |----|---|----|----|----|----|----|"
    Print #OStream, "*" |DISP|ACC|REST|SOLV|IMOD| FIL| CF |"
    Print #OStream, "*" |----|---|----|----|----|----|----|"

    Dim DISP As String
    Dim ACC As String
    Dim REST As String
    Dim SOLV As String
    Dim IMOD As String
    Dim FILL As String
    Dim CF As String

    DISP = (Worksheets("GUI").Cells(6, 4)) - 1
    ACC = (Worksheets("GUI").Cells(7, 4)) - 1
    REST = (Worksheets("GUI").Cells(8, 4)) - 1
    SOLV = (Worksheets("GUI").Cells(9, 4)) - 1
    IMOD = (Worksheets("GUI").Cells(10, 4)) - 1
    FILL = (Worksheets("GUI").Cells(11, 4)) - 1
    CF = 0.0001

    MyString = " " & " " & " " & " " & _
        CStr(DISP) & " " & " " & " " & " " & _
        CStr(ACC) & " " & " " & " " & " " & _
        CStr(REST) & " " & " " & " " & " " & _
        CStr(SOLV) & " " & " " & " " & " " & _
        CStr(IMOD) & " " & " " & " " & " " & _

```

```

        CStr(FILL) & " " & " " & " " & " " & _
        CStr(CF)

Print #OStream, MyString

Print #OStream, "*" |----|-----|-----|----|-----|----|-----|-----|-----|"
Print #OStream, "*" |NOBJ|NELEM|NNODE|NSOL|IFIELD|KSYM|FCRIT|NCELL|NPLANE|NFREE|"
Print #OStream, "*" |----|-----|-----|----|-----|----|-----|-----|-----|"

Dim NOBJ As Integer
Dim NELEM As Integer
Dim NNODE As Integer
Dim NSOL As Integer
Dim IFIELD As Integer
Dim KSYM As Integer
Dim FCRIT As Integer
Dim NCELL As Integer
Dim NPLANE As Integer
Dim NFREE As Integer
Dim Ans As Variant
Dim NumObjects As Long
NOBJ = NumObjects
NELEM = NumTriangles
NNODE = NumNodes
NSOL = (Worksheets("GUI").Cells(23, 4)) - 1
IFIELD = (Worksheets("GUI").Cells(24, 4)) - 1
KSYM = (Worksheets("GUI").Cells(25, 4)) - 1
FCRIT = (Worksheets("GUI").Cells(26, 4)) - 1
NCELL = (Worksheets("GUI").Cells(28, 4))
NPLANE = (Worksheets("GUI").Cells(29, 4))
NFREE = 0

MyString = " " & " " & _
        CStr(NOBJ) & " " & " " & " " & " " & " " & _
        CStr(NELEM) & " " & " " & " " & " " & " " & " " & _
        CStr(NNODE) & " " & " " & " " & " " & " " & " " & _
        CStr(NSOL) & " " & " " & " " & " " & " " & " " & _
        CStr(IFIELD) & " " & " " & " " & " " & " " & " " & _
        CStr(KSYM) & " " & " " & " " & " " & " " & " " & _
        CStr(FCRIT) & " " & " " & " " & " " & " " & " " & _
        CStr(NCELL) & " " & " " & " " & " " & " " & " " & _
        CStr(NPLANE) & " " & " " & " " & " " & " " & CStr(NFREE)

Print #OStream, MyString

Print #OStream, "*" |-----|-----|-----|"
Print #OStream, "*" |____SIGMA1____|____SIGMA2____|____SIGMA3____|"
Print #OStream, "*" | Value | DipDir/Dip | Value | DipDir/Dip | Value | DipDir/Dip |"
Print #OStream, "*" |-----|-----|-----|"

Dim s1v As Integer
Dim s1dd As Integer
Dim s1d As Integer
Dim s2v As Integer
Dim s2dd As Integer
Dim s2d As Integer
Dim s3v As Integer

```



```

MyString = " " & " " & " " & " " &
    CStr(TS) & " " & " " & " " & " " & " " & " " & " " & " " & " " & " " &
    CStr(FA) & " " & " " & " " & " " & " " & " " & " " & CStr(Co)

Print #OStream, MyString

Print #OStream, "* Nodal Data and Boundary Conditions"
Print #OStream, "* |-----|-----|-----|-----|-----|-----|"
Print #OStream, "* | Node | _____Coordinates_____|"
Print #OStream, "* | No. |     NORTH     |     UP     |     EAST     |"
Print #OStream, "* |-----|-----|-----|-----|-----|-----|"

For i = 1 To NumNodes
    MyString = " " & CStr(i) & " " & " " & CStr(N(i).y) & " " &
CStr(N(i).z) & " " & CStr(N(i).x)           ' Examine3D North-Up-East system
    Print #OStream, MyString
Next
Print #OStream, "* Element Data "
Print #OStream, "* Elem. No. = Element id. "
Print #OStream, "* Obj. No. = Info for which object element belongs to "
Print #OStream, "* Comp. No. = Info for which component element belongs
to "
Print #OStream, "* TYP = 1 for 3-noded linear triangle "
Print #OStream, "*      = 2 for 3-noded constant triangle "
Print #OStream, "*      = 4 for 3-noded quadratic triangle (midnodes
inserted) "
Print #OStream, "* Press Flag = 0 for no applied pressure/traction to
element "
Print #OStream, "*      = 1 for applied pressure to element "
Print #OStream, "*      = 2 for applied traction to element"
Print #OStream, "* Press = 0 if Press Flag is 0"
Print #OStream, "*      = magnitude of pressure if Press Flag is 1"
Print #OStream, "*      = magnitude and direction (normalized NUE
vector) of"
Print #OStream, "*      traction if Press Flag is 2 (4 real values)"
Print #OStream, "* Surf Flag = 0 for an element part of a closed
excavation"
Print #OStream, "*      = 1 for an element part of an open surface"
Print #OStream, "* Color = Info for color of element, currently not
used."
Print #OStream, "* |-----|-----|-----|---|-----|-----|-----|-----|-----|"
Print #OStream, "* |Elem.|Obj. |Comp.|TYP|_Incidences_|Press|Press|Surf|Color|"
Print #OStream, "* | No. | No. | No. |   | 1 2 3 4 |Flag |   |Flag|   |"
Print #OStream, "* |-----|-----|-----|---|-----|-----|-----|-----|-----|"

Dim OBJ_Num As Integer
Dim COMP_Num As Integer
Dim TYP As Integer
Dim PressFlag As Integer
Dim Press As Double
Dim SurfFlag As Integer
Dim ColorString As String

OBJ_Num = 1
COMP_Num = 1
TYP = 1
PressFlag = 0

```

```

Press = 0
SurfFlag = 0
ColorString = "edges=white,faces=gold"

For i = 1 To NumTriangles
    MyString = " " & " " & CStr(i) & " " & " " & CStr(OBJ_Num) & " " & "
" & CStr(COMP_Num) & " " & " " & _
        CStr(TYP) & " " & _
        CStr(T(i).Ptr(1)) & " " & " " & " " & _
        CStr(T(i).Ptr(2)) & " " & " " & " " & _
        CStr(T(i).Ptr(3)) & " " & " " & " " & " " & _
        CStr(PressFlag) & " " & " " & " " & _
        CStr(Press) & " " & " " & _
        CStr(SurfFlag) & " " & " " & " " & _
        CStr(ColorString)
    Print #OStream, MyString
Next

Print #OStream, "* Cell Data"
Print #OStream, "* coordinates in NORTH,UP,EAST format"
Print #OStream, "* numu,numv,numw = dimensions of grid cell"
Print #OStream, "* numu = # between points 0 and 1"
Print #OStream, "* numv = # between points 0 and 3"
Print #OStream, "* numw = # between points 0 and 4"
Print #OStream, "*
          7----6"
Print #OStream, "*
          /|  /|"
Print #OStream, "*
          / | / |"
Print #OStream, "*
          / 4 / 5"
Print #OStream, "*
          / / / /"
Print #OStream, "*
        3--/--2 /"
Print #OStream, "*
        | /  | /"
Print #OStream, "*
        | /  | /"
Print #OStream, "*
        |_____|"
Print #OStream, "*
        0      1"
Print #OStream, "*"
Print #OStream, "* |----|-----|-----|-----|-----|-----|"
Print #OStream, "* | #  | P0 P1 P2 P3 P4 P5 P6 P7 |numu |numv |numw |"
Print #OStream, "* |----|-----|-----|-----|-----|-----|"

Dim num As Integer
Dim P01 As Integer
Dim P02 As Integer
Dim P03 As Integer
Dim P11 As Integer
Dim P12 As Integer
Dim P13 As Integer
Dim P21 As Integer
Dim P22 As Integer
Dim P23 As Integer
Dim P31 As Integer
Dim P32 As Integer
Dim P33 As Integer

num = 1
P01 = Worksheets("GUI").Cells(25, 9)
P02 = Worksheets("GUI").Cells(25, 10)
P03 = Worksheets("GUI").Cells(25, 11)

```

```

P11 = Worksheets("GUI").Cells(26, 9)
P12 = Worksheets("GUI").Cells(26, 10)
P13 = Worksheets("GUI").Cells(26, 11)
P21 = Worksheets("GUI").Cells(27, 9)
P22 = Worksheets("GUI").Cells(27, 10)
P23 = Worksheets("GUI").Cells(27, 11)
P31 = Worksheets("GUI").Cells(28, 9)
P32 = Worksheets("GUI").Cells(28, 10)
P33 = Worksheets("GUI").Cells(28, 11)

MyString = " " & " " & CStr(num) & " " & " " & CStr(P01) & " " &
CStr(P02) & " " & CStr(P03) & " " & " " & _
    CStr(P11) & " " & CStr(P12) & " " & CStr(P13) & " " & " " & _
    CStr(P21) & " " & CStr(P22) & " " & CStr(P23) & " " & " " & _
    CStr(P31) & " " & CStr(P32) & " " & CStr(P33)

Print #OStream, MyString

Dim P41 As Integer
Dim P42 As Integer
Dim P43 As Integer
Dim P51 As Integer
Dim P52 As Integer
Dim P53 As Integer
Dim P61 As Integer
Dim P62 As Integer
Dim P63 As Integer
Dim P71 As Integer
Dim P72 As Integer
Dim P73 As Integer
Dim numu As Integer
Dim numv As Integer
Dim numw As Integer

P41 = Worksheets("GUI").Cells(29, 9)
P42 = Worksheets("GUI").Cells(29, 10)
P43 = Worksheets("GUI").Cells(29, 11)
P51 = Worksheets("GUI").Cells(30, 9)
P52 = Worksheets("GUI").Cells(30, 10)
P53 = Worksheets("GUI").Cells(30, 11)
P61 = Worksheets("GUI").Cells(31, 9)
P62 = Worksheets("GUI").Cells(31, 10)
P63 = Worksheets("GUI").Cells(31, 11)
P71 = Worksheets("GUI").Cells(32, 9)
P72 = Worksheets("GUI").Cells(32, 10)
P73 = Worksheets("GUI").Cells(32, 11)
numu = Worksheets("GUI").Cells(34, 11)
numv = Worksheets("GUI").Cells(35, 11)
numw = Worksheets("GUI").Cells(36, 11)

MyString = " " & " " & CStr(P41) & " " & CStr(P42) & " " & CStr(P43) & "
" & " " & _
    CStr(P51) & " " & CStr(P52) & " " & CStr(P53) & " " & " " & _
    CStr(P61) & " " & CStr(P62) & " " & CStr(P63) & " " & " " & _
    CStr(P71) & " " & CStr(P72) & " " & CStr(P73) & " " & _
    CStr(numu) & " " & CStr(numv) & " " & CStr(numw)

```

```

    Print #OStream, MyString

    Close OStream
End Sub

Function HarvestNodesInTriangles(NumTriangles As Long, T() As Triangle, N()
As MyRhinoPoint) As Long

    Dim NumPoints As Long
    Dim NumNodes As Long
    Dim i As Long
    Dim j As Integer
    Dim NodeIndex As Long

    ReDim N(1 To 3) As MyRhinoPoint

    NumNodes = NumNodes + 1
    ReDim Preserve N(1 To NumNodes) As MyRhinoPoint
    N(NumNodes) = CopyPoint(T(1).Pt(1))
    T(1).Ptr(1) = NumNodes

    NumNodes = NumNodes + 1
    ReDim Preserve N(1 To NumNodes) As MyRhinoPoint
    N(NumNodes) = CopyPoint(T(1).Pt(2))
    T(1).Ptr(2) = NumNodes

    NumNodes = NumNodes + 1
    ReDim Preserve N(1 To NumNodes) As MyRhinoPoint
    N(NumNodes) = CopyPoint(T(1).Pt(3))
    T(1).Ptr(3) = NumNodes
    For i = 2 To NumTriangles          ' Cycle through 2nd and all following
triangles
        For j = 1 To 3                ' Cycle through the 3 points
in the current triangle
            NodeIndex = GetNodeIndex(T(i).Pt(j), N(), NumNodes)      ' See if
the point is already in the list of points, return 0 if not, the index number
if so

            If NodeIndex = 0 Then
                'It's a new node, add it to the list of nodes
                NumNodes = NumNodes + 1
                ReDim Preserve N(1 To NumNodes) As MyRhinoPoint
                N(NumNodes) = CopyPoint(T(i).Pt(j))
                NodeIndex = NumNodes

            End If

            ' Assign the node index to the triangle node pointer variable

            T(i).Ptr(j) = NodeIndex

        Next
    Next

    ' At this stage, we've generated the list of nodes, and assigned the
index number of given nodes to the 3 pointer variables of every triangle

```

```

    ' Return the number of nodes to the calling function

    ReDim Preserve N(1 To NumNodes) As MyRhinoPoint      'Trim the node array
to the final number of nodes found, before passing the argument back

    HarvestNodesInTriangles = NumNodes

End Function

Function GetNodeIndex(P As MyRhinoPoint, N() As MyRhinoPoint, NumNodes As
Long) As Long
    Dim i As Long

    'Set up the comparison test to get out of here as soon as possible
    ' Assume that it is not already listed, until proven wrong

    GetNodeIndex = 0          ' Default value indicating that the node has
not been found in the current listing
    For i = 1 To NumNodes    ' Cycle through the current list of nodes
        If IsSame(P, N(i)) Then
            GetNodeIndex = i
            Exit Function
        End If
    Next
End Function

Function IsNodeListed(P As MyRhinoPoint, N() As MyRhinoPoint, NumNodes As
Long) As Boolean
    Dim i As Long

    'Set up the comparison test to get out of here as soon as possible
    ' Assume that it is not already listed, until proven wrong

    IsNodeListed = False
    For i = 1 To NumNodes    ' Cycle through the current list of nodes
        If IsSame(P, N(i)) Then
            IsNodeListed = True
            Exit Function
        End If
    Next
End Function

Function IsSame(P As MyRhinoPoint, Q As MyRhinoPoint) As Boolean

    ' Set up the comparison tests to get out of here as soon as possible
    ' Assume that it is the same, until proven wrong

    IsSame = True

    If P.x <> Q.x Then
        IsSame = False
        Exit Function
    ElseIf P.y <> Q.y Then
        IsSame = False
        Exit Function
    ElseIf P.z <> Q.z Then
        IsSame = False

```

```

        Exit Function
    End If

End Function

Function CopyPoint(N As MyRhinoPoint) As MyRhinoPoint
    Dim P As MyRhinoPoint

    P.x = N.x
    P.y = N.y
    P.z = N.z

    CopyPoint = P

End Function

Function GetRhinoTriangles(MyPath As String, MyFile As String, T() As
Triangle) As Variant

    Dim FileName As String
    Dim IStream As Integer
    Dim MyString As String
    Dim NumObjects As Long
    Dim NumTriangles As Long
    Dim Ans() As Variant

    ReDim T(1 To 100) As Triangle      ' Start off with space for 100
triangles

    FileName = MyPath & "\" & MyFile

    If (FileName <> "") Then
        IStream = FreeFile()
        Open FileName For Input Access Read Shared As IStream
    Else
        End
    End If

    Do While Not EOF(IStream)
        Line Input #IStream, MyString
        If Mid(MyString, 1, 6) = "Object" Then ' It's a line defining that a
new object is about to be defined
            NumObjects = NumObjects + 1
        Else
            NumTriangles = NumTriangles + 1
            T(NumTriangles) = ParseTriangle(MyString) ' Pass the read in
string to a specially designed function to chop up the text values to numeric
data
            If NumTriangles Mod 100 = 0 Then      ' Ran out of spaces for
more triangles, add another 100 spaces
                ReDim Preserve T(1 To NumTriangles + 100) As Triangle
            End If
        End If
    Loop
    Close IStream ' Close the file containing the triangles

    ReDim Preserve T(1 To NumTriangles) As Triangle ' Trim the array of
triangles down to a length equal to the number of triangles read in.

```

```

ReDim Ans(1 To 2) As Variant

Ans(1) = NumObjects
Ans(2) = NumTriangles

GetRhinoTriangles = Ans      ' Return the number of objects and triangles
read in, if successful.

End Function
Function ParseTriangle(S As String) As Triangle

    Dim i As Long
    Dim SLength As Long
    Dim Vals(1 To 9) As Double
    Dim DatumEnd As Long
    Dim DatumStart As Long
    Dim NumData As Long
    Dim TextValue As String
    Dim T As Triangle

    SLength = Len(S)

    DatumStart = 1
    For i = 1 To SLength
        If Mid(S, i, 1) = " " Or i = SLength Then      ' Data values are
delimited with a space
            DatumEnd = i - 1
            NumData = NumData + 1
            TextValue = Mid(S, DatumStart, DatumEnd - DatumStart + 1)
            Vals(NumData) = CDb1(TextValue)
            DatumStart = i + 1
        End If
    Next

    If NumData = 9 Then      ' The triangle point coordinates have been read
in successfully

        T.Pt(1).x = Vals(1)
        T.Pt(1).y = Vals(2)
        T.Pt(1).z = Vals(3)
        T.Pt(2).x = Vals(4)
        T.Pt(2).y = Vals(5)
        T.Pt(2).z = Vals(6)
        T.Pt(3).x = Vals(7)
        T.Pt(3).y = Vals(8)
        T.Pt(3).z = Vals(9)

    Else
        MsgBox "Failure to read triangle in string: " & S
    End
End If

    ParseTriangle = T      ' Return the triangle to the calling function
End Function

```

	A	B	C	D	E	F	G	H	I	J	K	L	M	N
1														
2														
3														
4														
5														
6														
7														
8														
9														
10														
11														
12														
13														
14														
15														
16														
17														
18														
19														
20														
21														
22														
23														
24														
25														
26														
27														
28														
29														
30														
31														
32														
33														
34														
35														
36														
37														

Analysis Parameters

Calculate displacements: Calculate

Calculate field point accelerations: Don't calculate

Restart analysis: No thanks!

Solver method: GMRES iteration

Integration method: Mixed exact-numerical integration

Field point filtering: Filter field points inside excavation

Convergence / tolerance factor: 0.0001

Number of Files(New): 6

Control Parameters

Path to Rhino files: C:\Users\nsaeidi.CORP\Rhinooutput

Current Rhino file: rhino03.raw

Number of objects: []

Number of boundary elements: []

Number of nodes for boundary elements: []

Far field boundary: Analysis of infinite body

Initial stress field type: Constant initial stress field

Problem symmetry conditions: No symmetry

Failure criterion: Mohr-Coulomb failure criterion

Stress calculations: []

Number of cells defining interior points: 1

Number of planes defining interior points: 0

Stress Field

Component	Magnitude (MPa)	DipDir (°)	Dip (°)
Sigma 1	40	90	0
Sigma 2	30	0	0
Sigma 3	20	0	90

Elastic parameters

Young's modulus (MPa): 69000

Poisson's ratio: 0.26

Mohr-Coulomb Failure Criterion

Tensile strength (MPa): 9.3

Friction angle (°): 59

Cohesion (MPa): 30

Cell data for interior points

	North (m)	Up (m)	East (m)
P0	-375	-315	-60
P1	-375	-315	72
P2	-375	378	72
P3	-375	378	-60
P4	450	-315	-60
P5	450	-315	72
P6	450	378	72
P7	450	378	-60

No. cells east	Num U	44
No. cells up	Num V	231
No. cells north	Num W	275

Figure C-1: The GUI (Graphical User Interface) of the 'Examine3D batch mode processor' VBA code.

D Appendix 4: AutoIt script

The AutoIt script presented here is to automate the following procedure.

1. modeling and meshing n individual stopes in Rhino (McNeel, 2014)
2. exporting their mesh properties in the form of '*.raw' files
3. importing '*.raw' files to 'Examine3D batch mode processor' VBA code to convert to '*.ex3' files
4. loading the '*.ex3' files into the Compute3D (Curran and Corkum, 1990-8) and save computed stress fields for each individual stopes.

AutoIt script
by: Negar Saeidi
2014

```
#cs -----  
  
AutoIt Version: 3.3.12.0  
Author:          myName  
  
Script Function:  
    Template AutoIt script.  
  
#ce -----  
  
; Script Start - Add your code below here  
#include <Excel.au3>  
#include <MsgBoxConstants.au3>  
  
; setting of RHINO  
  
Run('"C:\Program Files\Rhinoceros 4.0\System\rhino4.exe"')  
sleep(5000)  
WinActivate("Untitled - Rhinoceros (Corporativa)")  
WinWaitActive("Untitled - Rhinoceros (Corporativa)")  
Send(" DocumentProperties")  
sleep(1000)  
Send("{Enter}")
```

```

WinActivate("Document Properties","")
WinWaitActive("Document Properties","")
sleep(1000)
Send("u")
sleep(1000)
Send("{TAB}")
sleep(1000)
Send("0.0001")
sleep(1000)
Send("{TAB}")
sleep(1000)
Send("0.001")
sleep(1000)
Send("{TAB}")
sleep(1000)
Send("0.001")
sleep(1000)
send("{Enter}")
sleep(1000)
WinActivate("Untitled - Rhinoceros (Corporativa)")
WinWaitActive("Untitled - Rhinoceros (Corporativa)")
sleep(1000)
Send("Box")
Send("{Enter}")
sleep(1000)
Send("0,0,0{Enter}1{Enter}2{Enter}3{Enter}")
sleep(1000)
WinActivate("Untitled - Rhinoceros (Corporativa)")
WinWaitActive("Untitled - Rhinoceros (Corporativa)")
sleep(1000)
send("selall")
Send("{Enter}")
Send("mesh")
Send("{Enter}")
WinActivate("Polygon Mesh Detailed Options","")
WinWaitActive("Polygon Mesh Detailed Options","")
sleep(1000)
send("{TAB 8}")
sleep(1000)
Send("3")
sleep(1000)
Send("{TAB}")
sleep(1000)
Send("3")
sleep(1000)
Send("{Enter}")
WinActivate("Untitled - Rhinoceros (Corporativa)")
WinWaitActive("Untitled - Rhinoceros (Corporativa)")
sleep(1000)
Send("new")
Send("{Enter}")
sleep(1000)
WinActivate("Rhinoceros 4.0","")
WinWaitActive("Rhinoceros 4.0","")
sleep(1000)
Send("{Enter}")
WinActivate("Save","")

```

```

WinWaitActive("Save", "")
sleep(1000)
Send("C:\Users\nsaeidi.CORP\Desktop\template.raw")
sleep(1000)
Send("{Enter}")
sleep(1000)
WinActivate("Polygon Mesh Detailed Options", "")
WinWaitActive("Polygon Mesh Detailed Options", "")
sleep(1000)
send("{TAB 8}")
Send("3")
Send("{TAB}")
Send("3")
Send("{Enter}")
sleep(1000)
WinWaitActive("Open Template File")
Send("{Enter}")
sleep(1000)
WinActivate("Untitled - Rhinoceros (Corporativa)")
WinWaitActive("Untitled - Rhinoceros (Corporativa)", "")

```

```

#include <Excel.au3>
#include <MsgBoxConstants.au3>
;Reads coordinates of stopes from an Excel file
$FileName=@ScriptDir & '\Stopecoord-P.xlsx'
$CellRange="A1:M12"
if not FileExists($FileName) then
    MsgBox (0,"Excel Data Test","Error: Can't find file " & $FileName)
    Exit
endif
$oExcelDoc = ObjGet($FileName)
If (not @error) and IsObj($oExcelDoc) then
    $oDocument=$oExcelDoc.Worksheets(1)
    $aArray=$oDocument.range($CellRange).value
    If IsArray($aArray) and Ubound($aArray,0)>0 then
        for $z = 0 to ubound($aArray,2)-1
            $sCellValue1 =$aArray[0][$z]
            $sCellValue2 =$aArray[1][$z]
            $sCellValue3 =$aArray[2][$z]
            $sCellValue4 =$aArray[3][$z]
            $sCellValue5 =$aArray[4][$z]
            $sCellValue6 =$aArray[5][$z]
            $sCellValue7 =$aArray[6][$z]
            $sCellValue8 =$aArray[7][$z]
            $sCellValue9 =$aArray[8][$z]
            $sCellValue10 =$aArray[9][$z]
            $sCellValue11 =$aArray[10][$z]
            $sCellValue12 =$aArray[11][$z]
            $sCellValue13 =$aArray[12][$z]

            sleep(1000)
            WinActivate("Untitled - Rhinoceros (Corporativa)")
            WinWaitActive("Untitled - Rhinoceros (Corporativa)")
            sleep(1000)
            Send("polyline")

```

```

Send("{Enter}")
sleep(1000)
Send($sCellValue1)
Send(",")
Send($sCellValue2)
Send(",")
Send($sCellValue3)
Send("{ENTER}")
sleep(1000)
Send($sCellValue4)
Send(",")
Send($sCellValue5)
Send(",")
Send($sCellValue6)
Send("{ENTER}")
sleep(1000)
Send($sCellValue7)
Send(",")
Send($sCellValue8)
Send(",")
Send($sCellValue9)
Send("{ENTER}")
sleep(1000)
Send($sCellValue10)
Send(",")
Send($sCellValue11)
Send(",")
Send($sCellValue12)
Send("{ENTER}")
sleep(1000)
Send("c{Enter}")
WinActivate("Untitled - Rhinoceros (Corporativa)", "")
WinWaitActive("Untitled - Rhinoceros (Corporativa)", "")
sleep(1000)
Send("selcrv")
Send("{Enter}")
sleep(1000)
Send("extrudecrv")
Send("{Enter}")
sleep(1000)
Send("d")
Send("{Enter}")
sleep(1000)
Send("0,0,0{ENTER}0,1,0{ENTER}")
sleep(1000)
Send($sCellValue13)
Send("{ENTER}")
sleep(1000)
Send("selall")
Send("{Enter}")
sleep(1000)
Send("cap")
Send("{Enter}")
sleep(1000)
Send("mesh")
Send("{Enter}")
sleep(1000)

```

```

WinActivate("Polygon Mesh Detailed Options","")
WinWaitActive("Polygon Mesh Detailed Options","")
sleep(1000)
Send("{ENTER}")
WinActivate("Untitled - Rhinoceros (Corporativa)")
WinWaitActive("Untitled - Rhinoceros (Corporativa)")
sleep(1000)
Send("new")
Send("{Enter}")
sleep(1000)
WinActivate("Rhinoceros 4.0","")
WinWaitActive("Rhinoceros 4.0","")
sleep(1000)
Send("{Enter}")
WinActivate("Save","")
WinWaitActive("Save","")
sleep(1000)
Send("negar0" & $z)
sleep(1000)
Send("{Enter}")
sleep(1000)
WinActivate("Polygon Mesh Detailed Options","")
WinWaitActive("Polygon Mesh Detailed Options","")
Send("{ENTER}")
sleep(1000)
WinWaitActive("Open Template File")
Send("{Enter}")
sleep(1000)
WinActivate("Untitled - Rhinoceros (Corporativa)")
WinWaitActive("Untitled - Rhinoceros (Corporativa)","")
Next
Else
Msgbox (0,"Excel Data Test","Error: Could not retrieve data from cell
range: " & $CellRange)
EndIf
$oExcelDoc.close
Else
Msgbox (0,"Excel Data Test","Error: Could not open "& $FileName & " as an
Excel Object.")
Endif

WinActivate("Untitled - Rhinoceros (Corporativa)")
WinWaitActive("Untitled - Rhinoceros (Corporativa)","")
Send("Exit")
Send("{Enter}")

$oExcelDoc=0

Local $oAppl = _Excel_Open()
Local $sWorkbook = @ScriptDir & "\\Examine3D batch mode processor.xls"
Local $oWorkbook = _Excel_BookOpen($oAppl, $sWorkbook)

WinActivate("Microsoft Excel - Examine3D batch mode processor.xls
[Compatibility Mode]","")

```

```

WinWait("Microsoft Excel - Examine3D batch mode processor.xls [Compatibility
Mode]", "")
send("!!{f11}")
send("{f5}")
winactivate("Macros", "")
winwaitactive("Macros", "")
send("{Enter}")

Run('"C:\Program Files\Rocscience\Examine3D\c3.exe"')
sleep(1000)
Winactivate("Compute3D", "")
WinWaitActive("Compute3D", "")
Send("O")
sleep(2000)
WinActivate("Open", "")
WinWaitActive("Open", "")
;winactivate([CLASS:Edit], "")
Send("C:\Users\nsaeidi.CORP\VBAoutput\negar00.ex3")
sleep(1000)
Send("{Enter}")
Send("O")
sleep(2000)
WinActivate("Open", "")
WinWaitActive("Open", "")
Send('"negar01.ex3" "negar02.ex3" "negar03.ex3" "negar04.ex3" "negar05.ex3"
"negar06.ex3" "negar07.ex3" "negar08.ex3" "negar09.ex3" "negar010.ex3"
"negar011.ex3" ')
sleep(2000)
Send("{Enter}")
winactivate("Compute3D", "")
WinWaitActive("Compute3D", "")
Send("c")

```

E Appendix 5: MATLAB script

The MATLAB script presented here undertakes series of stress, strain and stability analysis for feasible schedules of excavating n stopes. It starts with superimposing every individual stress fields (*.res' files, out put of Copmute3D) based on the order which is systematically generated by 'permutation processor' in Appendix 6. It calculates 6 parameters: 1) cumulative stress, 2)cumulative elastic strain , 3) cumulative viscoelastic strain, 4) strength factor, 5)*strainth factor* 6) *viscoelastic strainth factor* at every point within the computational domain, step-by-step for each sequence of excavating stopes and stores them in a database. It also generates time series of each of the 6-aformentioned parameters. At last it studies each stoping schedule based on the 12 (in)stability metrics introduced in Chapter 5 and presents the result in the form of 12 'indicator diagrams' which introduced in Chapter 6 and are presented in Appendix 7.

MAT LAB script
by: Negar Saeidi
2015

```
%Rock mass Properties
young=68000; friction=59; poisson=0.26; cohesion=30;

%Viscoelastic Parameters
eta=40000000; %(MPa.S)
timecoefficient=eta/young; %S

files = dir('C:\Users\Negar\*.res');
numFiles = length(files);
A = [];
for i = 1:numFiles
    file = fopen(files(i).name);
    F = textscan(file, '%*s %f %f %f %f %f %f %f %f %f %f %f %*8c %f %f %f %f %f
%f', 'Delimiter', ' ', 'CollectOutput', true, 'commentStyle', '*');
    fclose(file);
    A = cat(3, A, cell2mat(F));
end
a= length(A(:,1,1)); %number of the grid points
```

```

Permutations= load('perms.txt');
%1 to 6 are third dimension of A()
%Permutations(1,:) are permutationID and Permutations(2:7,:) are stopeID
bp= length(Permutations(:,1)); %number of the grid points
PickedGP=load('Picked Gridpoints - Examine.txt'); %Gridpoints to study
c= length(PickedGP(:,1)); %number of the grid points
%I limit my calculations into to census grid points, introducing a new
%matrice P()
Timetable= load('Schedule 2.txt'); %time label of sequences
t=length(Timetable(:,1)); %time discretization count

%Extracting Picked grid points from '*.res' files
d=1;
for j=1:c
    for k=1:a
        if PickedGP(j,2)==A(k,2,1)
            if PickedGP(j,3)==A(k,3,1)
                if PickedGP(j,4)==A(k,4,1)
                    P(d, :, :)=A(k, :, :);
                    d=d+1;
                end
            end
        end
    end
end

x=1; y=1; %indicator graph counter

Insitu=[30,20,40,0,0,0]; % The assumed in situ stresses!
for l= 1:bp
    % presenting points in different sequences
    for m=1:c
        Ps(m,1:4, :)=P(m,1:4, :);
        for n=1:numFiles
            e=Permutations(l,n);
            if n==1
                Ps(m,5:10,n)=P(m,5:10,e);
            else
                if Ps(m,5:10,n-1)==0
                    Ps(m,5:10,n)=0;
                else
                    Ps(m,5:10,n)=P(m,5:10,e);
                end
            end
        end
    end
end

% Adding up Tensors for different permutations
Stress(:,1:4, :)=Ps(:,1:4, :);
for m=1:c
    for n=1:numFiles
        if n==1 %Step one in sequence of excavations
            Stress(m,5:10,n)=Ps(m,5:10,n);
        else
            if Ps(m,5:10,n)==0
                Stress(m,5:10,n)=0;
            else

```



```

        induced(m,5:10,n)= Ps(m,5:10,n)-Insitu (1,:);
        Stress(m,5:10,n)=induced(m,5:10,n)+ Stress(m,5:10,n-1);
    end
end
end
end

%calculating cumulative principal stress and elastic strain in every
%step of stoping sequences
for o= 1:numFiles
    PStress(:,1:4,o)=Stress(:,1:4,o);
    PStrain(:,1:4,o)=Stress(:,1:4,o);
    for p =1:c
        if Stress(p,5:10,o)==0
            PStress(p,5:7,o)=0;PStrain(p,5:7,o)=0;
        else
            %generating cumulative principal stress for each point in
            every step of each sequence.
            I(p,1,o)=(-1)*(Stress(p,7,o)+Stress(p,5,o)+Stress(p,6,o));

            I(p,2,o)=(Stress(p,7,o)*Stress(p,5,o)+(Stress(p,5,o)*Stress(p,6,o)+(Stress(p,6,o)*Stress(p,7,o))-
            (((Stress(p,10,o))^2)+((Stress(p,8,o))^2)+((Stress(p,9,o))^2)));
            I(p,3,o)=(-
            1)*((Stress(p,7,o)*Stress(p,5,o)*Stress(p,6,o)+(2*(Stress(p,8,o)*Stress(p,9,o)*Stress(p,10,o)))-
            ((Stress(p,7,o)*((Stress(p,8,o))^2)+(Stress(p,5,o)*((Stress(p,9,o))^2)+(Stress(p,6,o)*((Stress(p,10,o))^2)))));
            r=[1 I(p,1,o) I(p,2,o) I(p,3,o)];
            pstress=roots(r);% result is sigma 1,2,3.
            PStress(p,5,o)=max(pstress(:,1)); %maximum
            PStress(p,6,o)=median(pstress(:,1));
            PStress(p,7,o)=min(pstress(:,1)); %minimum
            J2stress(p,1,o)=(1/6)*(((PStress(p,5,o)-
            PStress(p,6,o))^2)+((PStress(p,6,o)-PStress(p,7,o))^2)+((PStress(p,5,o)-
            PStress(p,7,o))^2)); %Deviator Invariant
            PStress(p,8,o)=sqrt(2*J2stress(p,1,o)); % state of deviatoric
            stress
            PStrain(p,5,o)=(PStress(p,5,o)-
            poisson*(PStress(p,6,o)+PStress(p,7,o)))/young;% Cumulative Maximum elastic
            Strain
            PStrain(p,6,o)=(PStress(p,6,o)-
            poisson*(PStress(p,5,o)+PStress(p,7,o)))/young;% Cumulative Intermediate
            elastic Strain
            PStrain(p,7,o)=(PStress(p,7,o)-
            poisson*(PStress(p,6,o)+PStress(p,5,o)))/young;% Cumulative Minimum elastic
            Strain
            J2strain(p,1,o)=(1/6)*(((PStrain(p,5,o)-
            PStrain(p,6,o))^2)+((PStrain(p,6,o)-PStrain(p,7,o))^2)+((PStrain(p,5,o)-
            PStrain(p,7,o))^2)); %Deviator Invariant
            PStrain(p,8,o)=sqrt(2*J2strain(p,1,o)); % state of deviatoric
            stress
        end
    end
end

```

```

end
end

%Threshold calculations (3D MC Criteria)
%Stress at Failure
for o=1:numFiles
    FStress(:,1:4,o)=Stress(:,1:4,o); %Stress failur threshold
    FStrain(:,1:4,o)=Stress(:,1:4,o); %Strain failur threshold
    for p =1:c
        if Stress(p,5:10,o)==0
            FStress(p,5,o)=0; % Deviatoric stress at failure
            FStrain(p,5,o)=0; % Deviatoric strain at failure
        else
            If(p,1,o)=PStress(p,5,o)+PStress(p,6,o)+PStress(p,7,o);
%Stress Invariant
            If(p,2,o)=(PStress(p,5,o)*PStress(p,6,o))+(PStress(p,6,o)*PStress(p,7,o))+(PStress(p,7,o)*PStress(p,5,o));%Stress Invariant
            If(p,3,o)=PStress(p,5,o)*PStress(p,6,o)*PStress(p,7,o);
%Stress Invariant
            Jf(p,1,o)=(1/6)*(((PStress(p,5,o)-PStress(p,6,o))^2)+((PStress(p,6,o)-PStress(p,7,o))^2)+((PStress(p,5,o)-PStress(p,7,o))^2)); %J2
            Jf(p,2,o)=((2/27)*(If(p,1,o)^3))-((1/3)*(If(p,2,o)*If(p,1,o)))+(If(p,3,o));%Deviator Invariant J3
            teta(p,1,o)=(1/3)*(asind((3*sqrt(3)/2)*(Jf(p,2,o)/Jf(p,1,o)^(3/2))));
            FStress(p,5,o)=(((1/3)*If(p,1,o)*sind(friction)))+(cohesion*cosd(friction))/(((cosd(teta(p,1,o)))+(sind(teta(p,1,o))*sind(friction))*(1/sqrt(3))));
%Deviatoric stress at failure
            FStrain(p,5,o)=FStress(p,5,o)/(young/(1+poisson));%Deviatoric strain at failure
        end
    end
end

% time-dependent evaluations
% placing stresses and strains along with time and sequence
o=1;
for q=1:t
    if o<numFiles+1
        timedependent(:,1:4,q)= Stress(:,1:4,o); % #GP, Coordinates
        timedependent(:,5,q)=PStress(:,5,o); %Maximum state of stress
        timedependent(:,6,q)=PStress(:,6,o); %Intermediate state of stress
        timedependent(:,7,q)=PStress(:,7,o); %Minimum state of stress
        timedependent(:,8,q)=PStress(:,8,o); %Deviatoric stress
        timedependent(:,9,q)=PStrain(:,8,o); %Deviatoric strain
        timedependent(:,10,q)=FStress(:,5,o); %Deviatoric stress at failure
        timedependent(:,11,q)=FStrain(:,5,o); %Deviatoric strain at failure
        if q==t
            else
                if Timetable(q+1,1)-Timetable(q,1)==0
                    o=o+1;
                end
            end
        end
    end
end

```

```

        end
        end
    end

    %state of viscoelastic principal strain
    for r=1:c
        shift=1;
        for q=1:t
            if timedependent(r,5:7,q)==0
                timedependent(r,12:15,q)=0;
            else
                if q==1
                    timedependent(r,12,q)= (timedependent(r,5,q)-
                    poisson*(timedependent(r,6,q)+timedependent(r,7,q)))/young; %Maximum
                    Viscoelastic strain
                    timedependent(r,13,q)= (timedependent(r,6,q)-
                    poisson*(timedependent(r,5,q)+timedependent(r,7,q)))/young; %Intermediate
                    Viscoelastic strain
                    timedependent(r,14,q)= (timedependent(r,7,q)-
                    poisson*(timedependent(r,6,q)+timedependent(r,5,q)))/young; %Minimum
                    Viscoelastic strain
                    timedependent(r,15,q)=
                    (1/(young/(1+poisson)))*sqrt((2/6)*(((Insitu(1,1)-
                    Insitu(1,2))^2)+((Insitu(1,1)-Insitu(1,3))^2)+((Insitu(1,2)-
                    Insitu(1,3))^2)));
                    shift=q;
                else
                    if Timetable(q,1)-Timetable(q-1,1)==0
                        timedependent(r,12,q)= timedependent(r,12,q-1);
                    %Maximum Viscoelastic strain
                        timedependent(r,13,q)= timedependent(r,13,q-1);
                    %Intermediate Viscoelastic strain
                        timedependent(r,14,q)= timedependent(r,14,q-1);
                    %Minimum Viscoelastic strain
                        timedependent(r,15,q)=timedependent(r,15,q-1);
                        shift=q;
                    else
                        deltaT=(Timetable(q,1)-
                        Timetable(shift,1))*(24*60*60);% calculating constant load duration in
                        seconds
                        timedependent(r,12,q)= ((-(timecoefficient)*(1-exp(-
                        deltaT/timecoefficient)))*((1/(3*eta))*((1-
                        2*poisson)*(timedependent(r,5,q)+timedependent(r,6,q)+timedependent(r,7,q)))+
                        ((poisson+1)*(2*timedependent(r,5,q)-timedependent(r,6,q)-
                        timedependent(r,7,q)))))); %Maximum Viscoelastic strain
                        timedependent(r,13,q)= ((-(timecoefficient)*(1-exp(-
                        deltaT/timecoefficient)))*((1/(3*eta))*((1-
                        2*poisson)*(timedependent(r,5,q)+timedependent(r,6,q)+timedependent(r,7,q)))-
                        ((poisson+1)*(timedependent(r,5,q)-
                        2*timedependent(r,6,q)+timedependent(r,7,q)))))); %Intermediate Viscoelastic
                        strain
                        timedependent(r,14,q)= ((-(timecoefficient)*(1-exp(-
                        deltaT/timecoefficient)))*((1/(3*eta))*((1-
                        2*poisson)*(timedependent(r,5,q)+timedependent(r,6,q)+timedependent(r,7,q)))-
                        ((poisson+1)*(timedependent(r,5,q)+timedependent(r,6,q)-
                        2*timedependent(r,7,q)))))); %Minimum Viscoelastic strain
                    end
                end
            end
        end
    end

```

```

                                J2vstrain(r,1,q)=(1/6)*(((timedependent(r,12,q)-
timedependent(r,13,q))^2)+((timedependent(r,13,q)-
timedependent(r,14,q))^2)+((timedependent(r,12,q)-timedependent(r,14,q))^2));
%Deviator Invariant
                                timedependent(r,15,q)=sqrt(2*J2vstrain(r,1,q));
%deviatoricviscoelastic strain

                                end
                                end
                                end
                                end
                                end

                                %Stability calculations
for q=1:2:t-1
    b=(q+1)/2;
    stability(:,1:4,b)=Stress(:,1:4,b);
    for r= 1:c
        if timedependent(r,5:7,q)==0
            stability(r,5,b)=0;%Strength Factor
            stability(r,6,b)=0;%Straingth Factor
            stability(r,7,b)=0;%Cumulative Deviatoric strain at failure -
Cumulative State of Deviatoric viscoelastic strain
        else

stability(r,5,b)=timedependent(r,10,q)/timedependent(r,8,q);%Strength Factor

stability(r,6,b)=timedependent(r,11,q)/timedependent(r,9,q);%Straingth Factor
            stability(r,7,b)=timedependent(r,11,q)/timedependent(r,15,q);
%Visco-Straingth Factor
        end
    end
end

    %(in)stability metrics
d=length(stability(1,1,:)); % Number of critical time-schedules to study
% if indicator is greater than 1
for q=1:d
    count(1,1:3)=0;
    d1=2*q-1;
    for b=1:c
        if stability(b,5,q)==0
            count(1,:)=count(1,:)+1;
        else
            if abs(stability(b,5,q))>1
                count(1,1)=count(1,1)+1;
            end
            if abs(stability(b,6,q))>1
                count(1,2)=count(1,2)+1;
            end
            if abs(stability(b,7,q))>1
                count(1,3)=count(1,3)+1;
            end
        end
    end
end
end
end

```

```

        S.F.indicator(x,1)=1;Sr.F.indicator(x,1)=1;
VSr.F.indicator(x,1)=1;%permutations

S.F.indicator(x,2)=Timetable(d1,1);Sr.F.indicator(x,2)=Timetable(d1,1);
VSr.F.indicator(x,2)=Timetable(d1,1);%timetable
    S.F.indicator(x,3)=c-count(1,1); % number of GP with S.F.<1 in each
time interval
    Sr.F.indicator(x,3)=c-count(1,2); % number of GP with S.F.<1 in each
time interval
    VSr.F.indicator(x,3)=c-count(1,3); % number of GP with S.F.<1 in each
time interval
    x=x+1;
end

for q=1:d
    n=0;sum(1,1:3)=0;d2=2*q-1;m=1;
    for b=1:c
        sum(1,1:3)=stability(b,5:7,q)+sum(1,1:3);
        if stability(b,5,q)>0 || stability(b,5,q)<0
            n=n+1;
            pre2(m,1)=stability(b,5,q); % S.F at each time interval at
each grid point
            pre2(m,2)=stability(b,6,q); % Sr.F at each time interval
            pre2(m,3)=stability(b,7,q);% VS.F at each time interval
            m=m+1;
        end
    end
    pre(y,1)=1;pre(y,2)=Timetable(d2,1);
    pre(y,3:5)=sum(1,1:3)/n; %average of S.F, Sr.F and vS.F. at each time
interval
    mi(y,1)=1; mi(y,2)=Timetable(d2,1);
    mi(y,3)=min(pre2(:,1));%min of S.F at each time interval among all
grid points
    mi(y,4)=min(pre2(:,2));%min of Sr.F at each time interval among all
grid points
    mi(y,5)=min(pre2(:,3));%min of vSr.F at each time interval among all
grid points
    ma(y,1)=1; ma(y,2)=Timetable(d2,1);
    ma(y,3)=max(pre2(:,1));%min of S.F at each time interval among all
grid points
    ma(y,4)=max(pre2(:,2));%min of Sr.F at each time interval among all
grid points
    ma(y,5)=max(pre2(:,3));%min of vSr.F at each time interval among all
grid points
    y=y+1;
end

%ploting changes of all curves at each grid point for differen
permutations
for i= 1:c
    k=[i];sequence=[1];
    for q=1:2:t-1
        b=(q+1)/2;
        d(b,1)=Timetable(q,1);
        d(b,2)=timedependent(i,9,q);% State of Elastic Deviatoric strain
        d(b,3)=timedependent(i,11,q);%Elastic Deviatoric strain at failure
    end
end

```

```

    d(b,4)=timedependent(i,8,q); % State of Elastic Deviatoric stress
    d(b,5)=timedependent(i,10,q);% Elastic Deviatoric stress at failure
    d(b,6)=timedependent(i,15,q); %state of viscoelastic deviatoric
strain
    end
    h = figure(k);
    set(h, 'Visible', 'off');
    X=[d(:,1),d(:,1)];
    Y1=[d(:,2),d(:,3)];
    Y2=[d(:,4),d(:,5)];
    Y3= d(:,6);
    [hAx,hLine1,hLine2] = plotyy(X,Y1,X,Y2,@stairs,@stairs);
    set(hAx,'fontsize',7);
    set(hLine1(1),'LineStyle','-','color','b');
    set(hLine1(2),'LineStyle','--','color','b');
    set(hLine2(1),'LineStyle','-','color','m');
    set(hLine2(2),'LineStyle','--','color','m');
    hold on;
    plot(d(:,1),d(:,6),'c');
    set(gca,'fontsize',7)
    hold off;
    hleg1 = legend('State of Elastic Deviatoric Strain','Elastic Deviatoric
Strain at Failure','State of Visco-elastic Deviatoric Strain','State of
Deviatoric Stress','Deviatoric Stress at Failure');
    set(hleg1,'location','southoutside');
    e1= sprintf('Grid Point#%d, Coord(N,U,E):(%d,%d,%d)',Stress(i,1:4,1));
    e2=sprintf('StopeID in sequence:%d,%d,%d,%d,%d,%d',Permutations(1,:));
    e=title({e1,e2});
    set(e,'fontSize',7);
    xl=xlabel('Scheduled Time (days after day 0)');
    set(xl,'fontSize',7);
    yl1=ylabel(hAx(1),'Deviatoric Strain'); % left y-axis
    set(yl1,'fontSize',7);
    yl2=ylabel(hAx(2),'Deviatoric Stress(MPa)'); % right y-axis
    set(yl2,'fontSize',7);
    filename = sprintf('Grid%dPermutation%d-3D.emf', Stress(i,1,1),sequence);
    saveas(h,filename,'emf');
end

end

% generating 'indicator diagrams'

pointsize = 2;h=figure(1);
set(h, 'Visible', 'off');
scatter(S.F.indicator(:,2),S.F.indicator(:,1), pointsize,
S.F.indicator(:,3),'fill');grid on ;
xlim([0 6.5]); ylim([1 bp]); caxis([0 5]);
e= sprintf('Number of grid points with Strength Factor less than one');
title(e);
xlabel('Timetable (days)');
ylabel('Permutations index');
colormap(jet(5));
ch=colorbar;
set(ch,'YTick',[0:1:5]);
filename = sprintf('indicator1-3D.emf');
saveas(h,filename,'emf');

```

```

pointsize = 2;h=figure(1);
set(h, 'Visible', 'off');
scatter(Sr.F.indicator(:,2),Sr.F.indicator(:,1), pointsize,
Sr.F.indicator(:,3),'fill');grid on ;
xlim([0 6.5]); ylim([1 bp]);caxis([0 5]);
e= sprintf('Number of grid points with Straingth Factor less than one');
title(e);
xlabel('Timetable (days)');
ylabel('Permutations index');
colormap(jet(5));
ch=colorbar;
set(ch,'YTick',[0:1:5]);
filename = sprintf('indicator2-3D.emf');
saveas(h,filename,'emf');

```

```

pointsize = 2;h=figure(1);
set(h, 'Visible', 'off');
scatter(VSr.F.indicator(:,2),VSr.F.indicator(:,1), pointsize,
VSr.F.indicator(:,3),'fill');grid on ;
xlim([0 6.5]); ylim([1 bp]);caxis([0 5]);
e= sprintf('Number of grid points with Visco-Straingth Factor less than
one');
title(e);
xlabel('Timetable (days)');
ylabel('Permutations index');
colormap(jet(5));
ch=colorbar;
set(ch,'YTick',[0:1:5]);
filename = sprintf('indicator3-3D.emf');
saveas(h,filename,'emf')

```

%average of S.F, Sr.F and vS.F. at each time interval

```

pointsize = 2;h=figure(1);
set(h, 'Visible', 'off');
scatter(pre(:,2),pre(:,1), pointsize, pre(:,3),'fill');grid on ;
xlim([0 6.5]); ylim([1 bp]);caxis([1.5 3.3]);
e= sprintf('Average Strength Factor');
title(e);
xlabel('Timetable (days)');
ylabel('Permutations index');
colormap(jet(18));
ch=colorbar;
set(ch,'YTick',[1.5:0.1:3.3]);
filename = sprintf('indicator4-3D.emf');
saveas(h,filename,'emf')

```

```

pointsize = 2;h=figure(1);
set(h, 'Visible', 'off');
scatter(pre(:,2),pre(:,1), pointsize, pre(:,4),'fill');grid on ;
xlim([0 6.5]); ylim([1 bp]);caxis([1.5 3.3]);
e= sprintf('Average Straingth Factor');
title(e);
xlabel('Timetable (days)');
ylabel('Permutations index');
colormap(jet(18));

```

```

ch=colorbar;
set(ch,'YTick',[1.5:0.1:3.3]);
filename = sprintf('indicator5-3D.emf');
saveas(h,filename,'emf')

pointsize = 2;h=figure(1);
set(h, 'Visible', 'off');
scatter(pre(:,2),pre(:,1), pointsize, pre(:,5),'fill');grid on ;
xlim([0 6.5]); ylim([1 bp]);caxis([1.5 3.3]);
e= sprintf('Average Visco-Straingth Factor');
title(e);
xlabel('Timetable (days)');
ylabel('Permutations index');
colormap(jet(18));
ch=colorbar;
set(ch,'YTick',[1.5:0.1:3.3]);
filename = sprintf('indicator6-3D.emf');
saveas(h,filename,'emf')

%min of S.F, Sr.F and vS.F. at each time interval

pointsize = 2;h=figure(1);
set(h, 'Visible', 'off');
scatter(mi(:,2),mi(:,1), pointsize, mi(:,3),'fill');grid on ;
xlim([0 6.5]); ylim([1 bp]);caxis([0.4 1.2]);
e= sprintf('Min Strength Factor');
title(e);
xlabel('Timetable (days)');
ylabel('Permutations index');
colormap(jet(16));
ch=colorbar;
set(ch,'YTick',[0.4:0.05:1.2]);
filename = sprintf('indicator7-3D.emf');
saveas(h,filename,'emf')

pointsize = 2;h=figure(1);
set(h, 'Visible', 'off');
scatter(mi(:,2),mi(:,1), pointsize, mi(:,4),'fill');grid on ;
xlim([0 6.5]); ylim([1 bp]);caxis([0.4 1.2]);
e= sprintf('Min Straingth Factor');
title(e);
xlabel('Timetable (days)');
ylabel('Permutations index');
colormap(jet(16));
ch=colorbar;
set(ch,'YTick',[0.4:0.05:1.2]);
filename = sprintf('indicator8-3D.emf');
saveas(h,filename,'emf')

pointsize = 2;h=figure(1);
set(h, 'Visible', 'off');
scatter(mi(:,2),mi(:,1), pointsize, mi(:,5),'fill');grid on ;
xlim([0 6.5]); ylim([1 bp]);caxis([0.4 1.2]);
e= sprintf('Min Visco-Straingth Factor');
title(e);
xlabel('Timetable (days)');
ylabel('Permutations index');

```



```

colormap(jet(16));
ch=colorbar;
set(ch,'YTick',[0.4:0.05:1.2]);
filename = sprintf('indicator9-3D.emf');
saveas(h,filename,'emf')

%max of S.F, Sr.F and vS.F. at each time interval

pointsize = 2;h=figure(1);
set(h, 'Visible', 'off');
scatter(ma(:,2),ma(:,1), pointsize, ma(:,3),'fill');grid on ;
xlim([0 6.5]); ylim([1 bp]);caxis([2.9 3.4]);
e= sprintf('Max Strength Factor');
title(e);
xlabel('Timetable (days)');
ylabel('Permutations index');
colormap(jet(10));
ch=colorbar;
set(ch,'YTick',[2.9:0.05:3.4]);
filename = sprintf('indicator10-3D.emf');
saveas(h,filename,'emf')

pointsize = 2;h=figure(1);
set(h, 'Visible', 'off');
scatter(ma(:,2),ma(:,1), pointsize, ma(:,4),'fill');grid on ;
xlim([0 6.5]); ylim([1 bp]);caxis([2.9 3.4]);
e= sprintf('Max Straingth Factor');
title(e);
xlabel('Timetable (days)');
ylabel('Permutations index');
colormap(jet(10));
ch=colorbar;
set(ch,'YTick',[2.9:0.05:3.4]);
filename = sprintf('indicator11-3D.emf');
saveas(h,filename,'emf')

pointsize = 2;h=figure(1);
set(h, 'Visible', 'off');
scatter(ma(:,2),ma(:,1), pointsize, ma(:,5),'fill');grid on ;
xlim([0 6.5]); ylim([1 bp]);caxis([2.9 6.8]);
e= sprintf('Max Visco-Straingth Factor');
title(e);
xlabel('Timetable (days)');
ylabel('Permutations index');
colormap(jet(26));
ch=colorbar;
set(ch,'YTick',[2.9:0.15:6.8]);
filename = sprintf('indicator12-3D.emf');
saveas(h,filename,'emf')

```

F Appendix 6: Permutation Processor

The VBA code presented here lists out all the ' $n!$ ' permutations of n numbers from one to n into a text file.

Permutation Processor
by: Dr. Dean Millar
2000

```
Option Explicit

Sub permutations()
Dim n As Integer
Dim i As Variant
Dim notdun As Integer
'Open file for output.
'Read n from worksheet
'Set initial permutation {1,2,...,n}
Open "\\MIR-SERV\Personal\nsaeidi\Permutation Difference\perms.txt" For
Output As #1
n = Range("B4")
ReDim x(n)
For i = 1 To n
x(i) = i
Next i
'Notdun=0 iff current permutation is n, n-1, ..., 1
notdun = 1
Do While (notdun)
For i = 1 To n
'Print current permutation
Print #1, x(i);
Next i
'Print line feed
Print #1, ""
'Find next permutation and note whether it is the final one
notdun = permute(x(), n)
Loop
Close
End Sub

Function permute(x(), n)
Dim bigfix As Integer
Dim done As Integer
Dim i As Variant
Dim bigindx As Variant
```

```

Dim descend As Integer
Dim current As Integer
Dim candidx As Variant
Dim temp As Integer
'Creates the next permutation in the "natural sequence"
'Returns 0 if permutation is n, n-1, ..., 1
'Default is to return 1
permute = 1
bigfix = n
'Done = 1 indicates next permutation is complete, 0 not.
done = 0
Do While (done = 0)
done = 1
'Find the index of bigfix
For i = 1 To n
If x(i) = bigfix Then bigindx = i
Next i
descend = 1
If bigindx <> n Then
For i = bigindx To n - 1
If x(i) < x(i + 1) Then descend = 0
Next i
End If
If descend And bigindx = 1 Then permute = 0
If descend Then
'Work left
current = x(bigindx - 1)
candidx = bigindx
'Find element to switch with x(bigindx-1)
For i = bigindx To n
If x(i) > current And x(i) < x(candidx) Then candidx = i
Next i
'Switch them
temp = x(candidx)
x(candidx) = x(bigindx - 1)
x(bigindx - 1) = temp
temp = sort(x(), bigindx)
End If
'End of work left
'Work right
If descend = 0 Then
done = 0
bigfix = findlarg(x(), bigindx + 1)
End If
'End of work right
Loop
End Function
Function findlarg(x(), start)
Dim candid As Integer
Dim ub As Integer
Dim i As Variant

'Finds largest x(i) from i = start to i = n
candid = x(start)
ub = UBound(x)
For i = start To ub
If x(i) > candid Then candid = x(i)

```

```
Next i
findlarg = candid
End Function
Function sort(x(), start)
Dim ub As Integer
Dim i As Variant
Dim j As Variant
Dim temp As Integer

'Sorts x() from i = start to i = n
ub = UBound(x)
For i = start To ub
For j = i To ub
If x(i) > x(j) Then
temp = x(i)
x(i) = x(j)
x(j) = temp
End If
Next j
Next i
End Function
```

G Appendix 7: The 12 ‘indicator diagrams’

The following presents 12 ‘*indicator diagrams*’ showing the (in)stability condition at every step of 720 (=6!) different sequences of excavating 6 stopes.

Indicator 1: number of grid points with strength factor less than one.

As more stopes are excavated, number of grid points with the strength factor less than one increase in all the permutations. This indicator acts more discriminatively as more stopes are excavated e.g. at day 3.5 there are few schedules remained showing zero grid points with strength factor less than one.

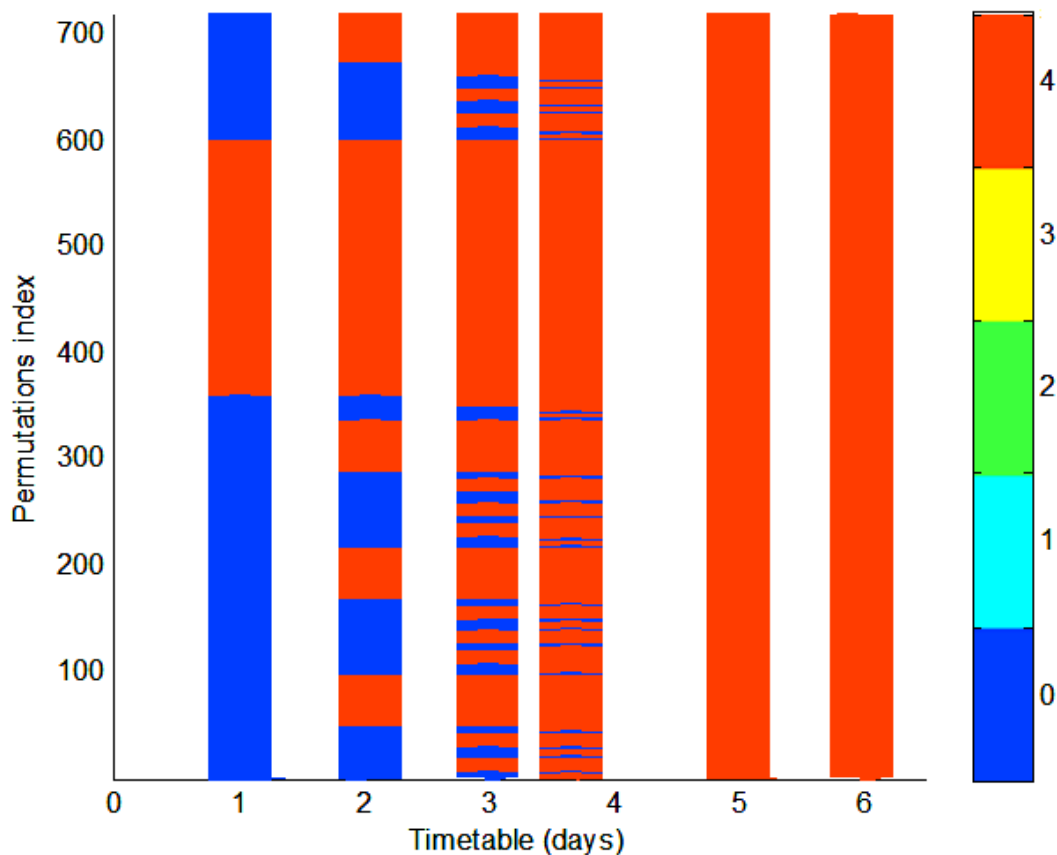


Figure G-1: Indicator 1 - number of grid points with strength factor less than one.

Indicator 2: number of grid points with strainth factor less than one.

This indicator presents the exact same results as indicator number one due to assumption of linear elasticity. As more stopes are excavated, the number of grid points with the *strainth factor* less than one increase in all the permutations. This indicator acts more discriminatively as more stopes are excavated e.g. at day 3.5 there are few schedules remained showing zero grid points with strength factor less than one.

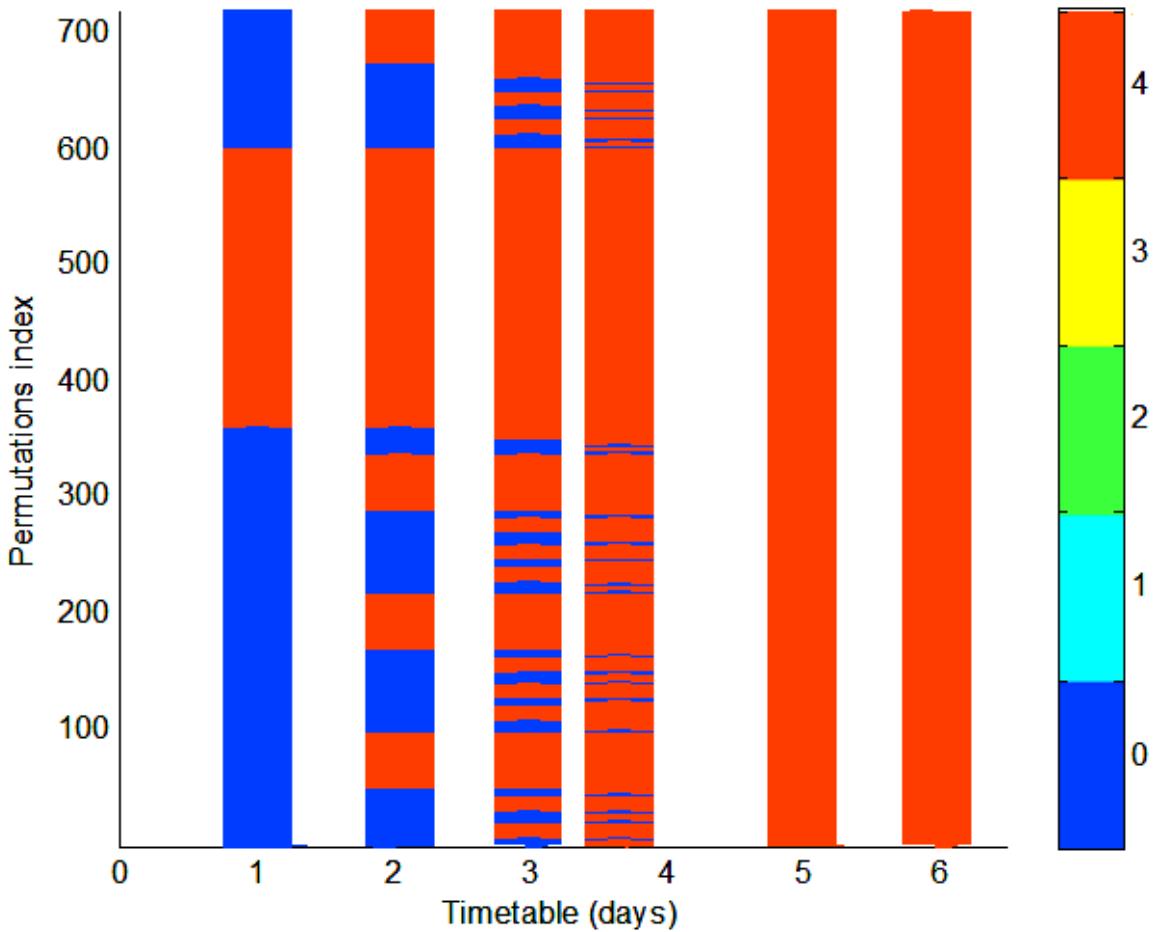


Figure G-2: Indicator 2- number of grid points with strainth factor less than one.

Indicator 3: number of grid points with viscoelasticstrainth factor less than one

This indicator evaluates (in)stability condition in each schedule considering time-dependent response of rock mass in different sequences of excavating stopes. It acts more discriminatively compared to the two previous indicators. As Figure G-1 and Figure G-2 present all the schedules are ranking the same after day 3.5 while Figure G-3 shows that there are schedules remained with zero grid points with VSF less than one at day 5. Moreover, at day 6 there are many schedules which have not reached the maximum of 4 grid points with VSF less than one.

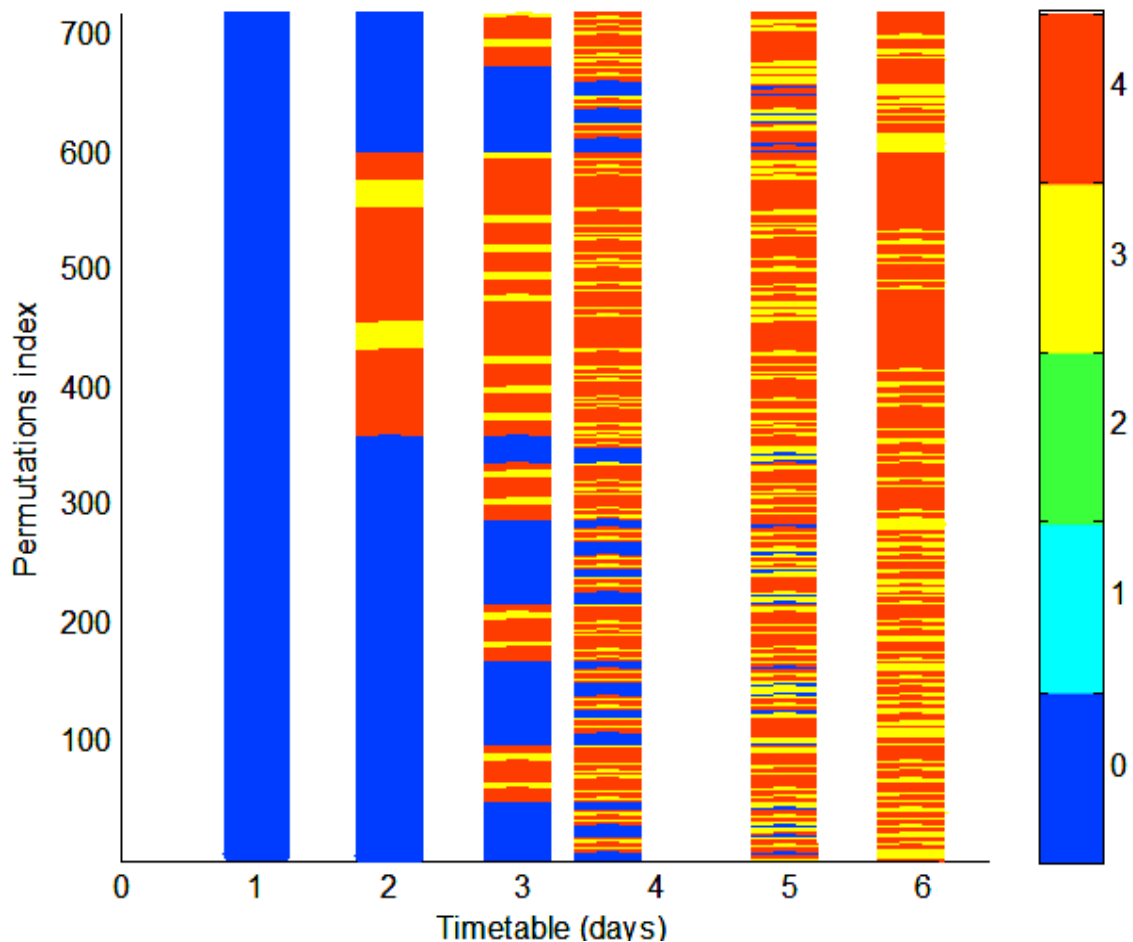


Figure G-3: Indicator 3-number of grid points with viscoelasticstrainth factor less than one.

Indicator 4: Average strength factor over all grid points

As more stopes are excavated the average strength factor over all the grid points decreases. Based on the color paths presented in Figure G-4 the average strength factor decreases more rapidly in some of the schedules and more gradually in some others, but at the end of all the schedules, the average strength factor is around the same number.

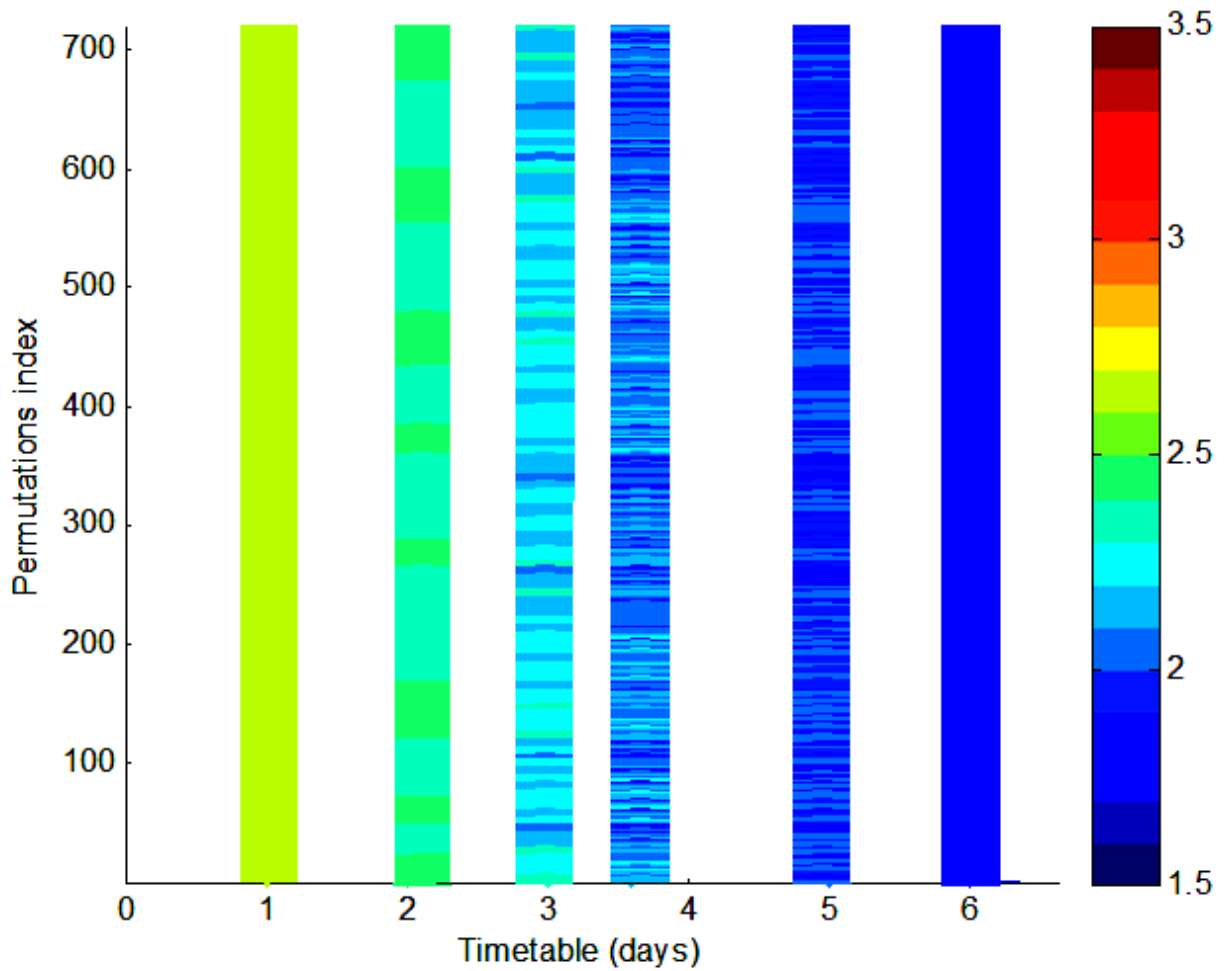


Figure G-4: Indicator 4-Average strength factor over all grid points.

Indicator 5: Average strainth factor over all grid points

This indicator presents the exact same results as the indicator number four due to assumption of linear elasticity. As more stopes are excavated the average strength factor over all the grid points decreases. Based on the color paths presented in Figure G-5 the average strength factor decreases rapidly in some schedules and more gradually in some others, but at the end of all the schedules, the average strength factor is around the same number for all of the 720 schedules.

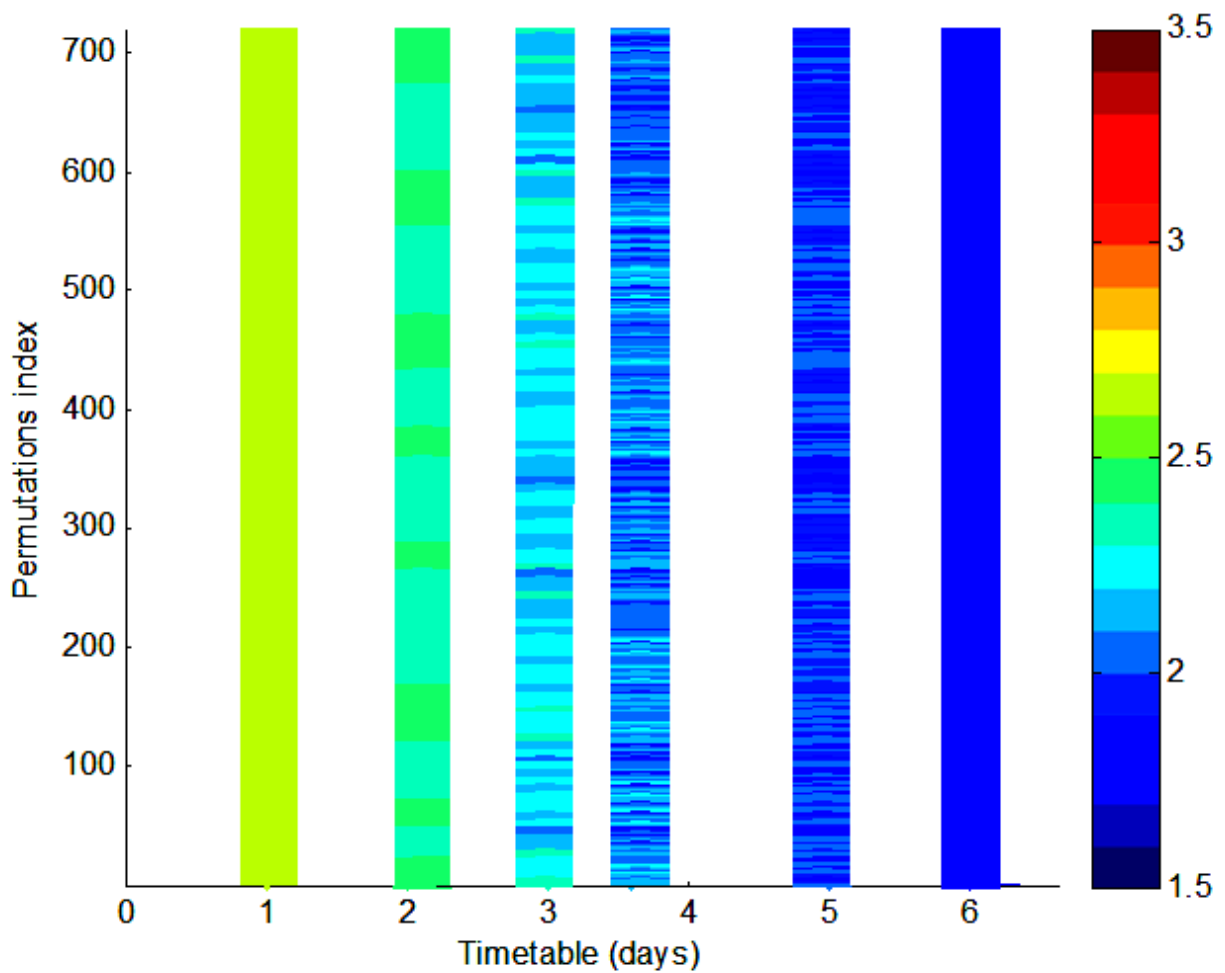


Figure G-5: Indicator 5-Average strainth factor over all grid points.

Indicator 6: Average viscoelasticstrainth factor over all grid points

This indicator evaluates (in)stability condition in each of the schedules considering time-dependent response of the rock mass in different sequences of the excavating stopes. It acts more discriminatively compared to the two previous indicators. This indicator effectively discriminates between the schedules from the day one to the day six while the two latter indicators could not discriminate schedules at the day one and the day six. In addition, it presents a higher stability condition at different steps of each schedule compared to the two previous indicators.

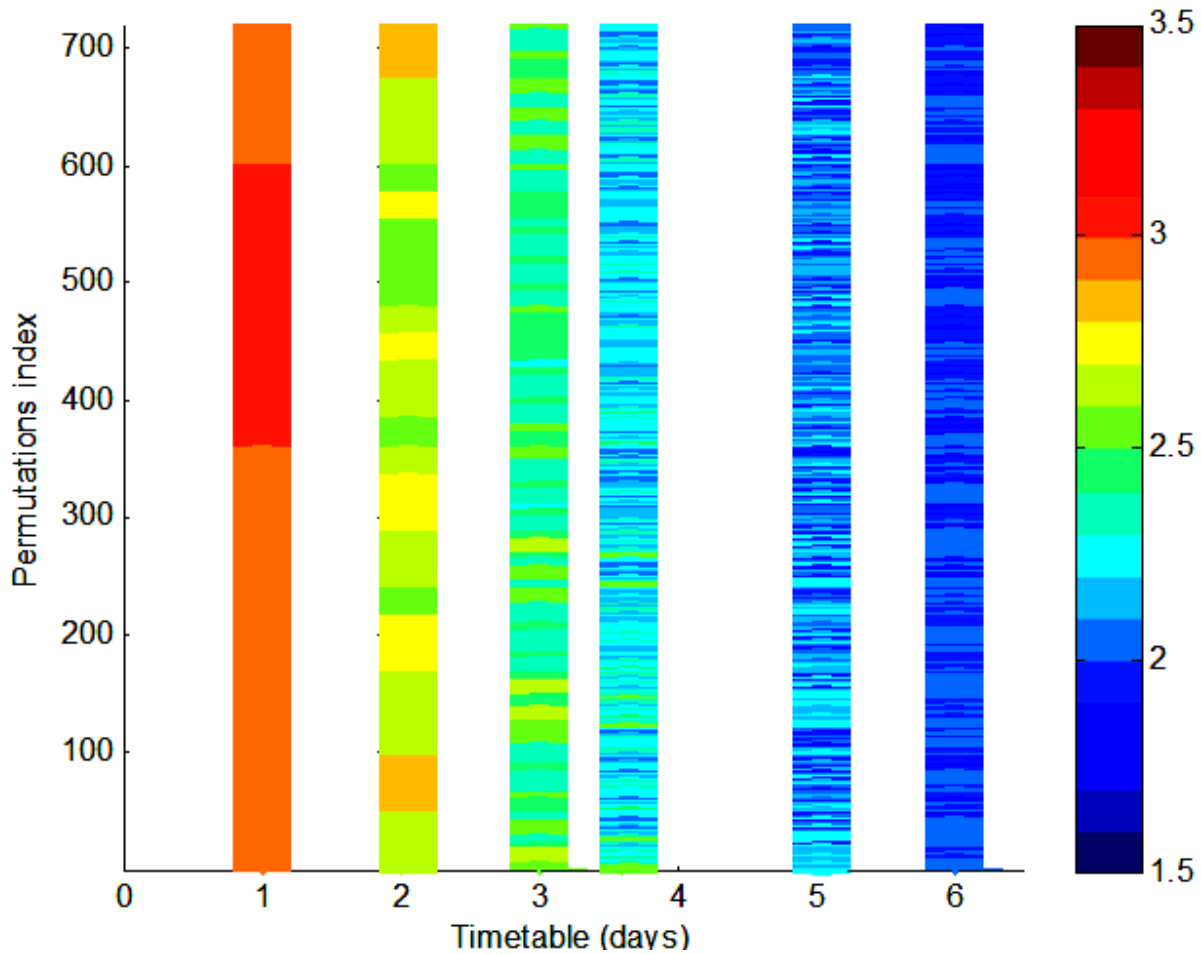


Figure G-6: Indicator 6-Average viscoelasticstrainth factor over all grid points.

Indicator 7: Minimum strength factor over all grid points

As more stope are excavated the minimum strength factor among all the grid points decrease. The results presented in Figure G-7 concurs with the results presented in Figure G-1. At each step of each of the schedules where indicator 1 reported for the grid points with strength factor less than one this indicator reports the minimum strength factor over all grid points with a value of strength factor less than one.

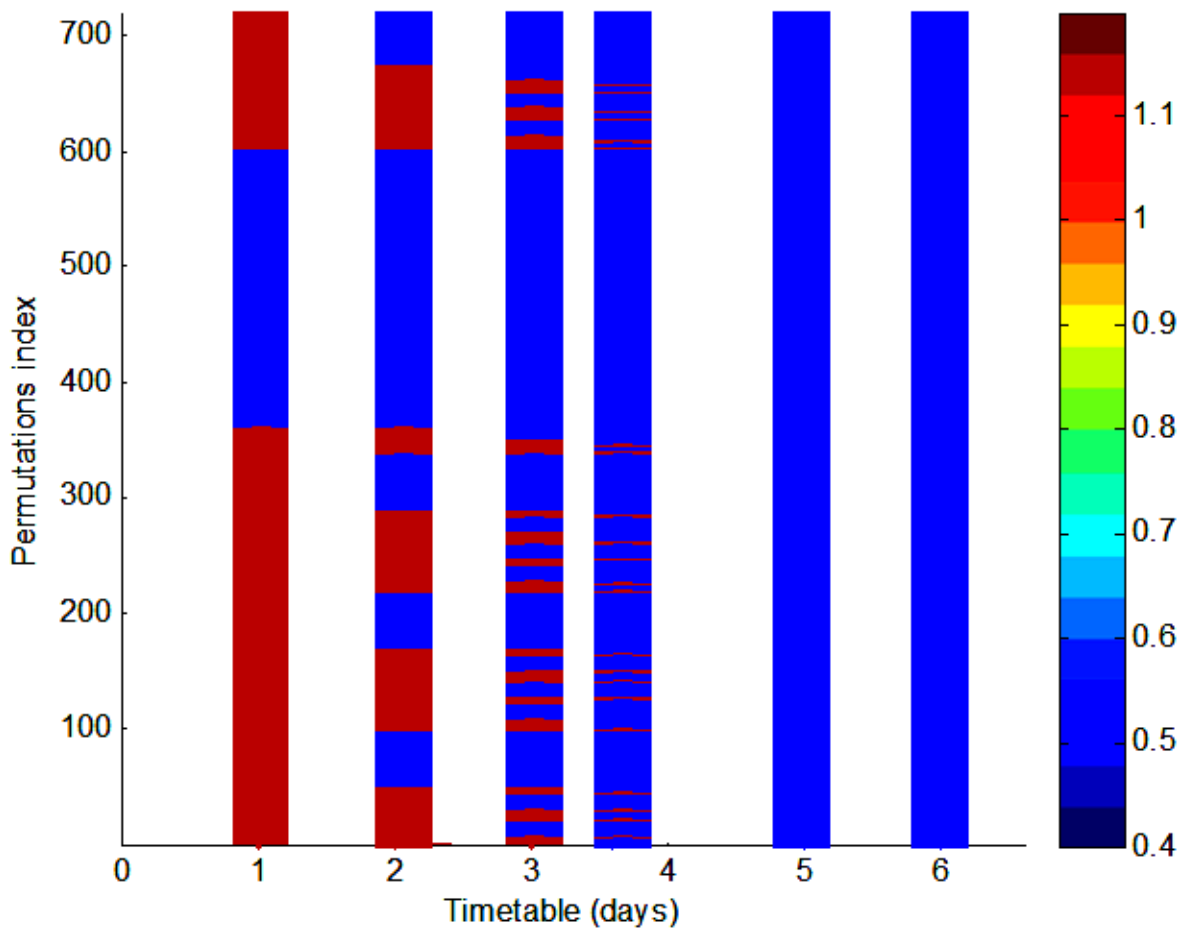


Figure G-7: Indicator 7-Minimum strength factor over all grid points.

Indicator 8: Minimum strainth factor over all grid points

This indicator presents the exact same results as the indicator number four due to the assumption of linear elasticity. As more stope are excavated the minimum strength factor among all the grid points decreases. The results presented in Figure G-8 concur with the results presented in Figure G-2. At each step of each of the schedules where the indicator 1 reorted grid points with strength factor less than one this indicator reports the minimum strength factor over all grid points with a value of strength factor less than one.

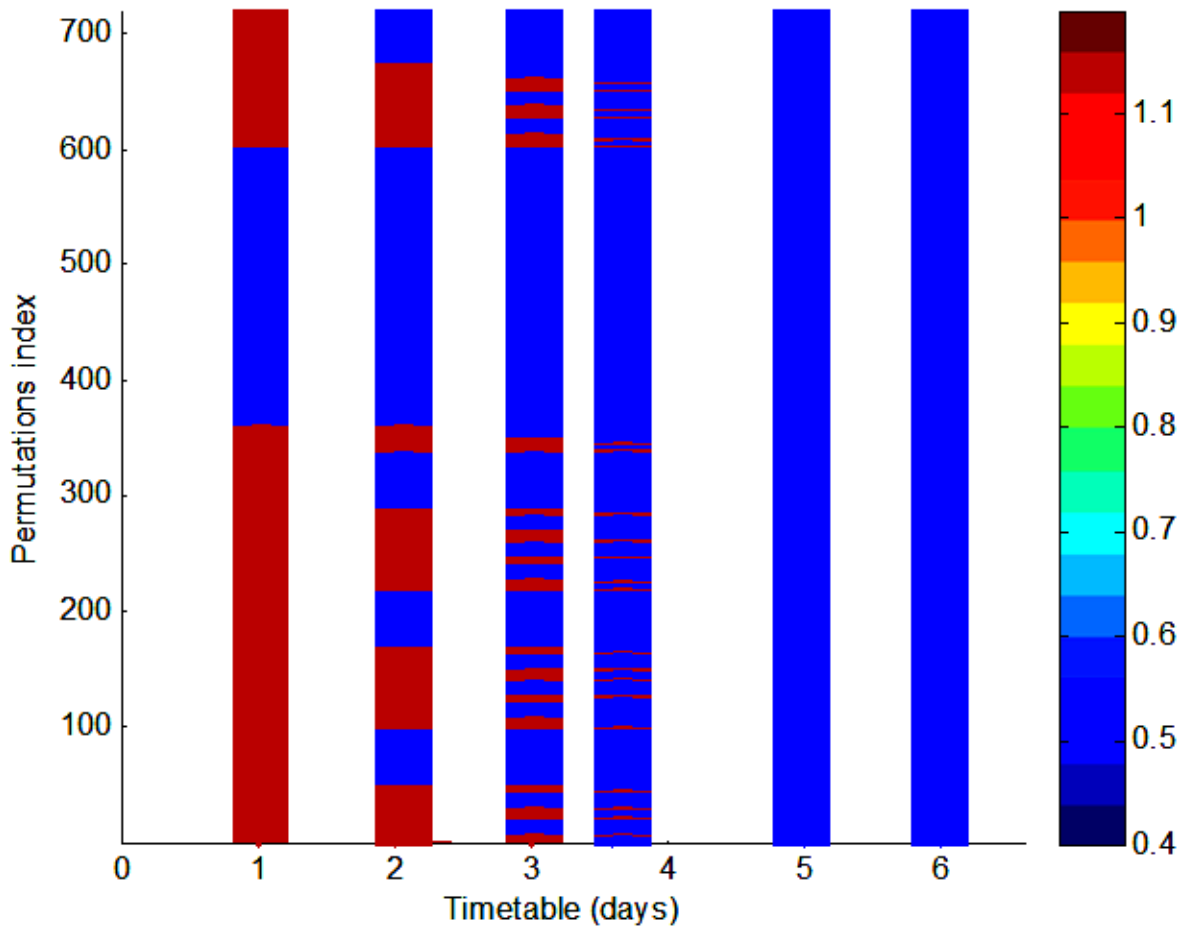


Figure G-8: Indicator 8 - Minimum strainth factor over all grid points.

Indicator 9: Minimum viscoelasticstrainth factor over all grid points

This indicator evaluates (in)stability condition at each step of each of the schedule considering the time-dependent response of the rock mass in different sequences of excavating stopes. This indicator acts more discriminatively compared to the last two. As presented in Figure G-9, at day 5 there are still schedules observed with the minimum *viscoelasticstrainth factor* greater than one. This concurs with the results of the indicator 3 presented in Figure G-3.

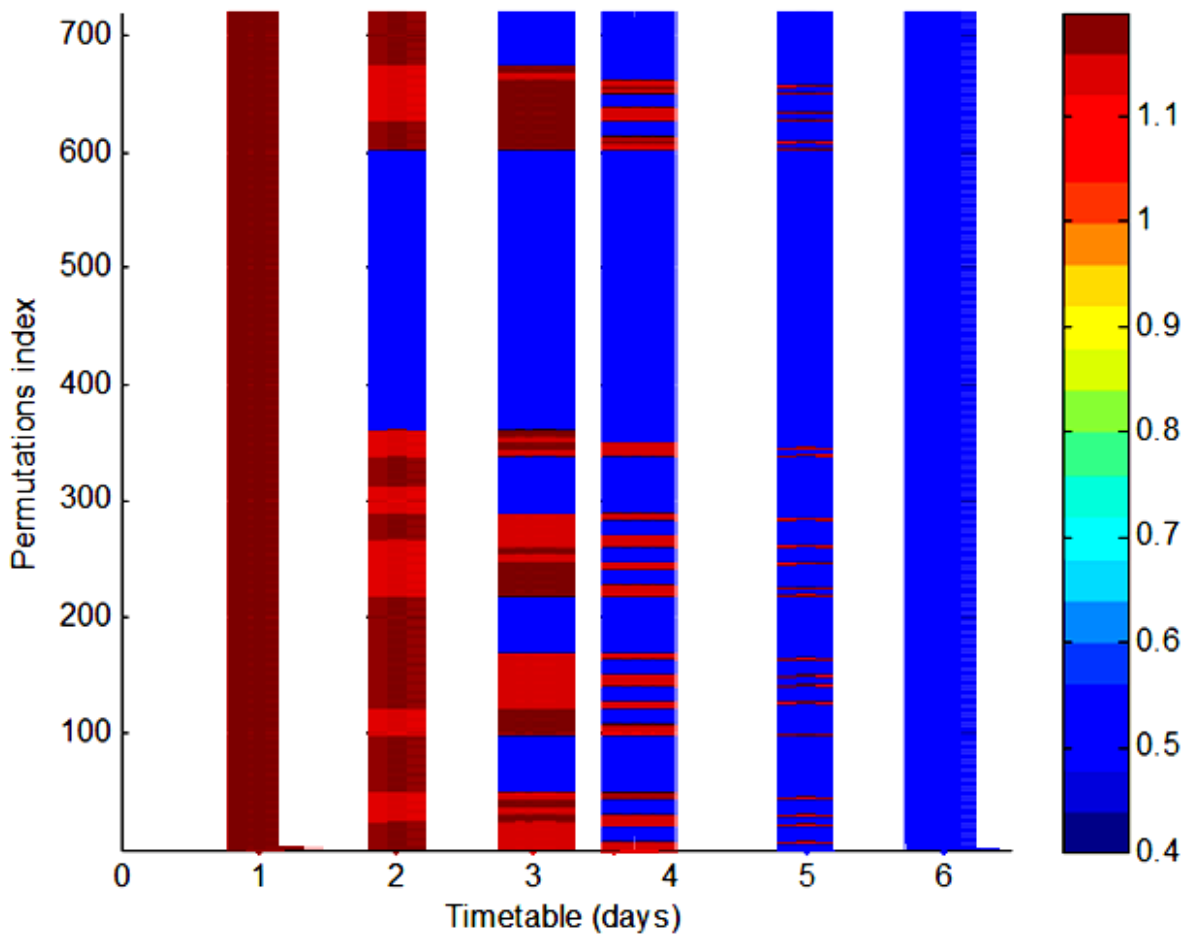


Figure G-9: Indicator 9 - Minimum viscoelasticstrainth factor over all grid points.

Indicator 10: Maximum strength factor over all grid points

This indicator follows different trends in different schedules, the maximum strength factor might increase or decrease as more stopes excavat in different schedules.

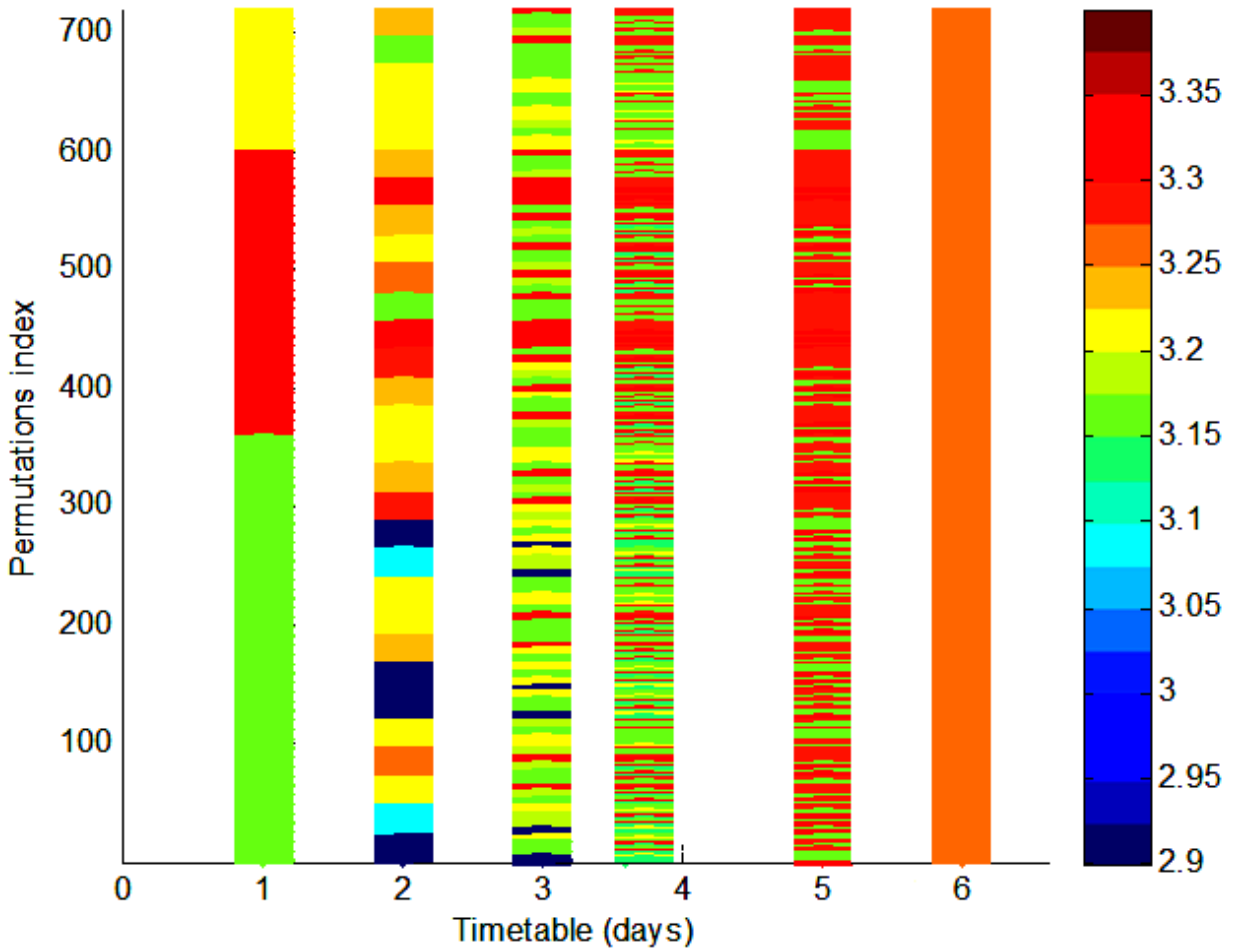


Figure G-10: Indicator 10- Maximum strength factor over all grid points.

Indicator 11: Maximum strainth factor over all grid points

This indicator presents the exact same results as the indicator number four due to the assumption of linear elasticity. Same as the indicator 10, this indicator follows different trends in different schedules, the maximum strength factor might increase or decrease as more stopes are excavated in different schedules.

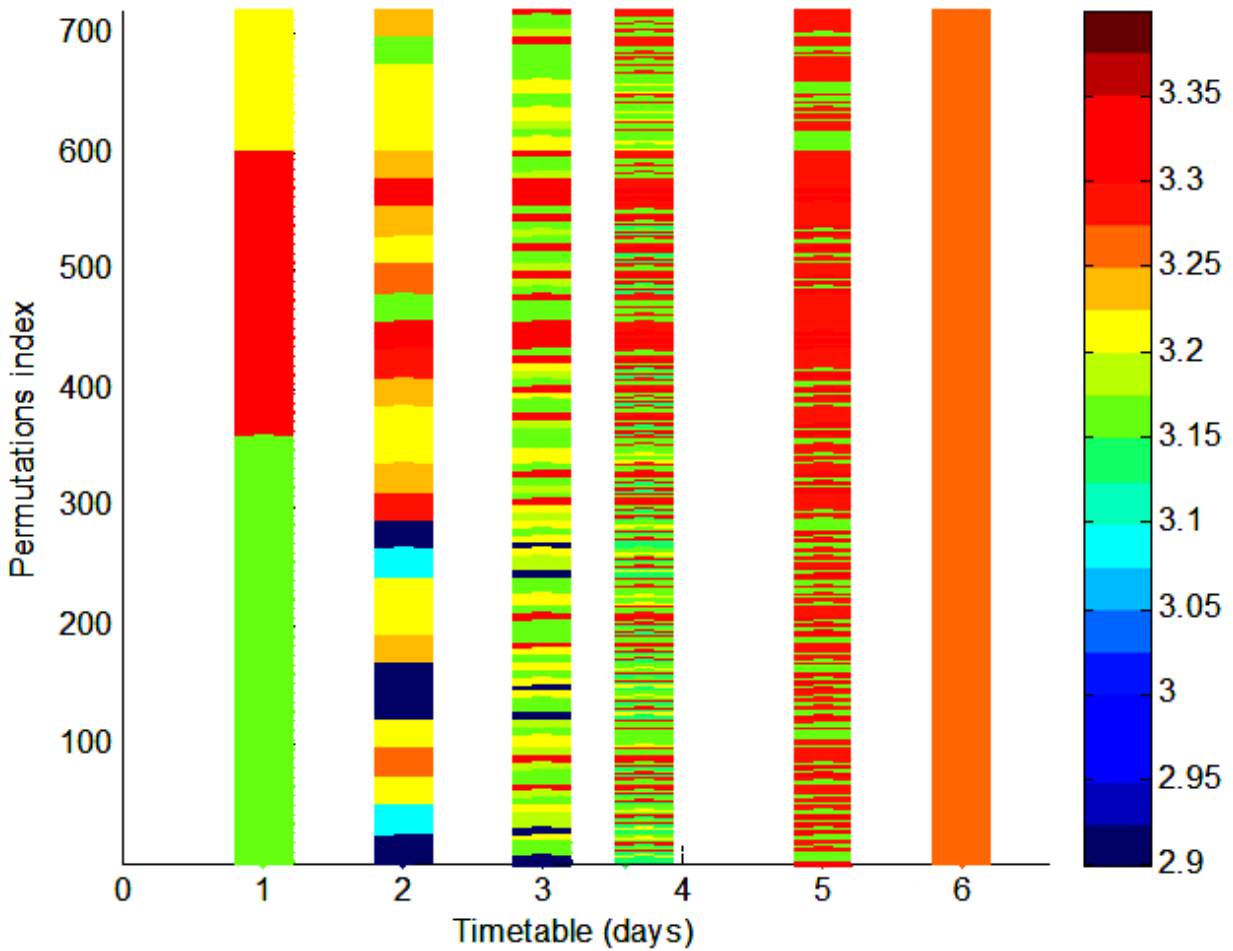


Figure G-11: Indicator 10- Maximum strength factor over all grid points.

Indicator 12: Maximum viscoelasticstrainth factor over all grid points

This indicator evaluates the (in)stability condition at each step of each schedule considering the time-dependent response of rock mass in different sequences of excavating 6 stopes. Comparing this indicator with the last two indicators presents a higher measure of instability.

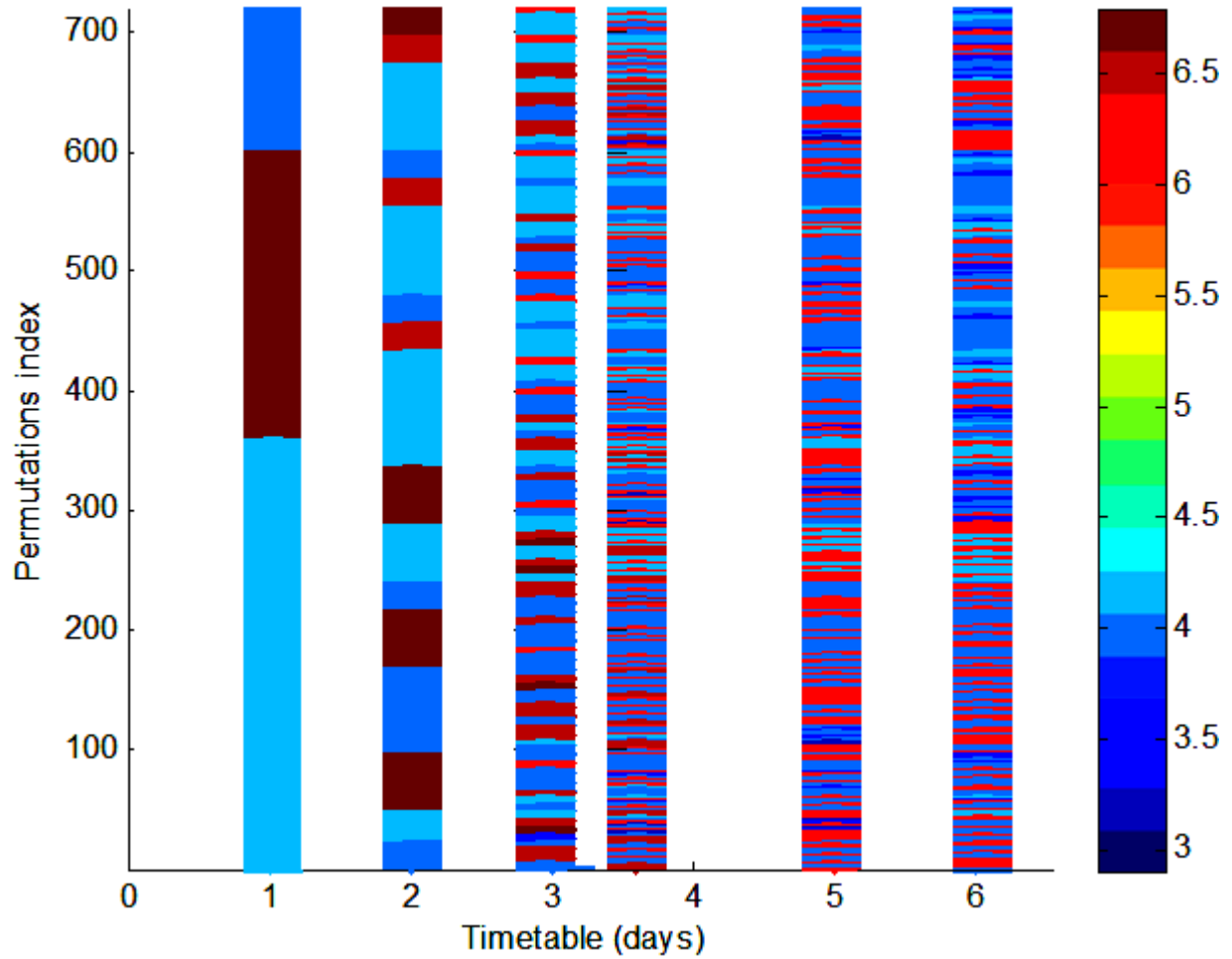


Figure G-12: Indicator 12-Maximum viscoelasticstrainth factor over all grid points.

Curriculum Vitae

Name: Negar Saeidi

**Post-secondary
Education and
Degrees:** University of Tehran
Tehran, Tehran, Iran

2008-2012 B.Sc.

Laurentian University

Sudbury, Ontario, Canada

2013-2015 M.Sc.

Publications:

Saeidi, N., Millar, D., 2015. Response of ore masses to stope sequence variations. Montreal, Quebec, In 13th Int.Congress in Rock Mechanics, ISRM

Saeidi, N., Millar, D., Fava, L. Cai, M., 2014. Towards mining schedule optimisation constrained by geomechanics.Sudbury, Ontario, In 7th International Conference on Deep and High Stress Mining

Azizi, D., Gharabaghi, M. Saeidi, N., 2014. Optimization of the coal flotation procedure using the Plackett-Burmandesign methodology and kinetic analysis. Fuel Processing Technology, Elsevier, Volume 128, pp. 111-118.

Saeidi, N., Noaparast, M., Azizi, D., Aslani, S., Ramadi, A., 2013. A developed approach based on grinding time to determine ore comminution properties. Journal of Mining Environment (JEM), Volume 4, Issue 2, pp. 105-112.